FULL-FIELD EXPERIMENTAL STRESS AND DISPLACEMENT ANALYSES OF ISOTROPIC AND ORTHOTROPIC MATERIALS

by

Yoon Hyuk Ro

A dissertation submitted in partial fulfillment of

the requirements for the degree of

Doctor of Philosophy

(Mechanical Engineering)

at the

UNIVERSITY OF WISCONSIN - MADISON

2019

Date of final oral examination: 04/29/2019

The dissertation is approved by the following members of the Final Oral Committee:

Robert Rowlands, Emeritus, Mechanical Engineering (Co-advisor)

Heidi-Lynn, Professor, Mechanical Engineering (Advisor)

Tim Osswald, Professor, Mechanical Engineering

Lih-Sheng Turng, Professor, Mechanical Engineering

Robert Witt, Associate Professor, Engineering Mechanics and Astronautics

FULL-FIELD EXPERIMENTAL STRESS AND DISPLACEMENT ANALYSES OF ISOTROPIC AND ORTHOTROPIC MATERIALS

Yoon Hyuk Ro

Under the Supervision of Professor Robert Rowlands and Professor Heidi-Lynn Ploeg

At University of Wisconsin − Madison

Abstract

This thesis demonstrates the stress (strain) and displacement determination in important structural members and materials not previously considered. This includes features such as evaluating elastic properties in situ from the applied force rather than from separate tensile coupons and where the coordinate origin is not surrounded by structural materials. Processing experimentally recorded data with an Airy stress function gives reliable results full-field as well as at the edge of geometric discontinuities.

Acknowledgements

All praise, honor and glory to my Lord Jesus Christ for His richest grace and mercy for the accomplishment of this thesis.

First and foremost, I would like to thank my wife Kyung Jin Choi for standing beside me. She had been extremely supportive throughout this entire process and made countless sacrifices to help me get to this point. I also thank my wonderful children: Chloe and Evelyn, for always making me smile.

This journey would not have been possible without the support of my immediate family, my parents, Kwang-Seop Ro and Hyun-Sook Shin, and my brother, Yong-Seok Ro. Their endless love and encouragement throughout my life gave me strength to move forward. Special thanks to my parents-in-law, who stayed with us as we fumbled our way through the early days of parenthood.

I would like to express my sincere gratitude to my advisor Professor Rowlands for the continuous support of my Ph.D study and research, for his patience, motivation, enthusiasm, and immense knowledge. I was very fortunate to have him as a mentor and advisor. I will forever be grateful and never forget our small conversations in the coffee shop.

I am no less grateful to my committee members, Professors Tim Osswald, Lih-Sheng Turng and Robert Witt. I especially want to thank Professor Heidi-Lynn Ploeg for being my official advisor. Finally, some special thanks to my friends who have always been a major source of support and their presence made my stay in Madison unforgettable.

Table of Contents

List of Figures and Tables

List of Symbols

A_o, A_1, A'_1, B_o, C_o, D_o, d_o, B_1, B'_1, a_n, b_n, c_n, d_n, a_n, b_n, c_n, d_n, a'_n, b'_n, c'_n, d'_n	Airy coefficients
$[A]$	Airy Matrix
$\{c\}$	Vector of Airy coefficients
C	Condition number
$\{d\}$	Vector of measured input data
$\{d'\}$	Vector of reconstructed data
E	Modulus of elasticity
E_{11}, E_{22}, E_{33}	Elastic moduli in material directions
f_x, f_y, f_z	Body forces in x-, y-, and z-directions
F	Applied load
$\mathcal{F}$	Airy stress function
$\mathcal{F}(x, y)$	Airy stress function in rectangular coordinate
G_{12}, G_{13}, G_{23}	Shear moduli
H	Height of thick plate
Im	Imaginary part
k	Measure of number of Airy coefficients
K	Isotropic Thermomechanical coefficients (TSA calibration coefficients)
K_1, K_2	Orthotropic Thermomechanical coefficients (TSA calibration coefficients)
K_t	Stress concentration factor

L	Thickness of thick plate
m	Number of measured input values
$[M]$	Matrix consists of S^* input and other known boundary conditions
N	Terminating integer of the summation series
P	Load per thickness
P^*	Concentrated load
q	Number of known stress or displacement conditions
r, θ	Polar coordinates
R	Radius of central circular hole or side circular notch
R^*	Interested region in physical plane or rigid body rotations
Re	Real part
RMS	Root Mean Square
S	First stress invariant trace of stress tensor or isopachic stress (= $\sigma_1 + \sigma_2 = \sigma_{rr} + \sigma_{\theta\theta} = \sigma_{xx} + \sigma_{yy}$)
S^*	Thermoelastic recorded signal (TSA raw data, uncalibrated)
S_1, S_2	Rigid body translations
t	Thickness of plate or time coordinate
$\boldsymbol{T}$	Transformation matrix
u, v, w	Cartesian displacements in x-, y-, and z-directions
u^*, v^*	Measured displacement values inside the region R^*
u_i	Displacement field
W	Width of plate
x, y	Cartesian (rectangular) coordinates

z_1, z_2	Complex variable; $z_j = x + \mu_j y$ for j = 1,2
Δ	Change
ε_{ij}	2nd order strain tensor
ϵ_{xx}, ϵ_{yy}, ϵ_{xy}	Strains in Cartesian coordinate
θ_p	Principal stress direction
μ_k	Roots of characteristic equation associated with the compatibility equation
ν_{12}, ν_{13}, ν_{23}	Poisson's ratio
ρ	Density or ratio of the radial coordinate to hole radius r/a
σ, σ_o	Far-field applied load and normal stresses
σ_1, σ_2, σ_3	Principal stresses
σ_{11}, σ_{22}	Normal stresses in the direction of material symmetry
σ_{ij}	2nd order stress tensor
σ_{max}	Maximum stress
σ_{net}	Nominal stress
σ_{rr}, $\sigma_{\theta\theta}$, $\sigma_{r\theta}$	Stresses in polar coordinate (radial, tangential, and shear stresses)
σ_{xx}, σ_{yy}, σ_{xy}	Stresses in Cartesian coordinate
Σ	Summation
Φ	Airy stress function in real variable for isotropic material
∇^4	Biharmonic operator
\	Backslash operator (MATLAB)

Chapter 1. Introduction

1.1 Background

This research employs experimental techniques to determine full-field individual stress and displacement components in members made from isotropic and orthotropic materials. Optical experimental techniques such as Thermoelastic Stress Analysis (TSA) and Digital Image Correlation (DIC) are utilized to record discrete temperature and displacement information. The information are processed with a stress function to evaluate stresses and displacements. Results are independently validated.

FEA is an attractive engineering tool designed within a Computer Aided Design (CAD) for iterative optimizing design techniques. The advantages of the FEA include ease of performance, no need to carry out an experiment, and the results are generated rapidly. However, FEA necessitates replicating the actual operating conditions, material properties and boundary conditions. The latter are often unknown. Theoretical approaches, which provide closed form and continuous solution, tend to be limited to infinite structures of very simple geometry [1]. Most practical problems involve complicated finite shapes. An important aspect of experimental approaches is capturing the actual exact boundary and loading conditions of the structure. However, traditional experimental approaches such as thermoelastic stress analysis and photoelastic stress analysis do not provide the separate components of stress and often suffer from bad or even unavailable results at and close to the edges of cutouts. These locations are often of the highest interest due to stress concentration. The deficiencies of FEA and analytical approaches when

attempting to replicate the actual boundary and loading conditions motivated the use of full-field hybrid experimental-numerical-analytical approaches. Advantages of the present hybrid methods include that they do not require knowing the external loading/boundary conditions and provide reliable results at the edges of holes of material.

1.2 Hybrid Stress Analysis

The process of combining measured data with the analytical representation of the Airy stress functions is referred to here as the 'Hybrid stress analysis'. The present method demonstrates the analytical ability to stress analyze loaded, finite, elastic engineering members by processing measured information. The in-plane displacements and stresses are evaluated full-field, including at the edge of the geometric discontinuities. The method satisfies equilibrium, strain compatibility and traction-free boundary conditions and it is valid for plane-stress and plane-strain problems assuming no body forces are present.

Experimental information is combined with a series representation of Maxwell's form of an Airy stress function to evaluate the individual stress, strain or displacement components. The Airy stress function, Φ, is derived from conditions of equilibrium and compatibility and is the solution of $\nabla^4\Phi = 0$ [2]. The assumptions associated with this stress function are that there are no body forces and is applicable to plane-stress or plane-strain situations. Derivatives of Airy stress function provide the individual stress components, and associated strain and displacement expressions are available based on elasticity. With orthotropic materials, the stress functions are usually in terms of complex variables. Numerical techniques are utilized to evaluate the coefficients of the Airy stress function from measured data, thereby providing the individual stress, strain or displacement components.

Real world problem often involves complex, finite shapes and complicated boundary conditions but purely analytical solutions tend to be available for only simple, finite geometries subjected to simple loading. The present technique of processing measured data using stress

functions enable one to obtain solutions to complicated, finite shapes subjected to complicated loading. Isotropic or anisotropic materials require knowing the unknown Airy coefficients to stress analyze the structures and the unknown Airy coefficients can be determined using displacement components measured by DIC or isopachic stresses recorded by TSA. The specific form of the Airy stress function for a particular case can depend on conditions of symmetry, whether or not the coordinate origin is within the component, and single-valued stresses, strains and displacements. Based on the geometry and external loading, many of the Airy coefficients can be omitted. This simplifies the Airy stress function hence the associated stress, strain and displacement components. The number of Airy coefficients can often be further reduced depending on finite or infinite geometry, symmetry about specific axis, location of the coordinate's origin, any self-equilibrated boundaries. However, one should be careful reducing the Airy coefficient while analyzing certain cases. For example, Chapter 4 and 5 demonstrate one should retain all the Airy coefficients for hybrid stress analysis method with finite deep U-notched plate where coordinate origin is not surrounded by structure/material.

1.3 Experimental Techniques

The present 'Hybrid stress analysis' method require measured data. Among the numerous full-field experimental methods, photoelasticity (PSA), themoelastic stress analysis (TSA), and optical techniques are non-destructive. Optical techniques include holography, moiré and speckle interferometry, grid methods, and digital image correlation (DIC) [3].

Among the above-mentioned techniques, TSA and DIC are utilized in the present method. PSA requires sensitive coating on opaque materials and optical methods such as digital/electrical speckle pattern interferometry (DSPI) or laser shearography are very sensitive to environmental conditions, rigid body motion, vibration [4] and air-flow which can be difficult to use outside the laboratory. Slight interruption in any of these factors can affect the reliability of the displacement/strain measurements. DIC is based on the principle of tracking common points on two or more images. Advantages of DIC include its minimal surface preparation requirements, ease of implementation, simple testing requirements, capability at various scales [5, 6, 7] and speed [8]. DIC is less sensitive to rigid body motions than some other methods [4]. TSA is another non-destructive technique for full-field stress analysis of loaded members. TSA measures temperature changes and it requires cyclically loading [9]. Advantages of TSA include not requiring differentiating the recorded data and minimal surface preparation.

1.3.1 Thermoelastic Stress Analysis (TSA)

TSA is a non-contacting, non-destructive, and full-field technique. It provides surface stress information of a cyclically loaded component using a sensitive infrared detector [10]. In 1853 Lord

Kelvin [11] was the first to theoretically describe the thermoelastic effect in solids. Compton and Webster [12] experimentally verified Kelvin's theory in 1915. In 1950 Biot [13] modified the basic theory to extend it to anisotropic materials. The first TSA-measurements were done by Belgen [14] in 1967. Mountain and Webber [15] were the first to develop a commercial TSA system. TSA has become an effective experimental tool to assess structural integrity and is used in many studies with developments in infrared cameras and computer processing power.

Theoretical foundation of TSA is based upon thermoelastic effects where a stressed object becomes cooler under tension or warmer in compression. Under elastic, reversible and adiabatic condition, the relationship between temperature variation and stresses remains linear. For materials having a positive coefficient of thermal expansion, thermoelastic temperature variations are positive during compression and negative during expansion [10]. The adiabatic conditions are achieved by cyclically loading the structure such that heat diffusion effects are negligible. If the load causing the volumetric change is removed and the material returns to its original temperature and shape, the process is reversible. The adiabatic condition of the loaded system is monitored by checking the phase-shift between the response and reference signals. Any heat transfer occurring within the test specimen or surface coating will be indicated by a shift between the two signals, i.e., a phase-shift will indicate non-adiabatic response. Adiabaticity can be a major concern in laminated composite structures as there is a possible heat transfer between the adjacent laminate plies as well as high stress gradients at the edge of cutouts.

The thermoelastic equation for isotropic materials is [10],

$$S^* = K\Delta S = K\Delta[\sigma_1 + \sigma_2 = \sigma_{rr} + \sigma_{\theta\theta} \quad = \sigma_{xx} + \sigma_{yy}] \tag{1.1}$$

where K is the TSA calibration factor (or sometimes called isotropic thermoelastic material coefficient) which depends on relevant physical properties of the material, surface condition, and TSA system parameters [3], S is the isopachic value at each point, and S^* is the raw TSA system measured value at the same point. Note that S is in terms of the summation of stresses, so individual components of stress are not provided directly by TSA. Engineering applications such as fatigue or strength theories require information on the individual components of stress and they can be evaluated by hybridizing the TSA information with an analytical and/or numerical tools (Airy stress function and boundary conditions). A common TSA calibration procedure is to experimentally evaluate the test material's thermoelastic coefficient, K. The calibration specimens generally employ a simple geometry and loading. The TSA calibration specimen and test structure must be of the same material and have the same surface coating. Orthotropic materials require testing two calibration coupons, one in each of the two in-plane principal material directions. Chapter 6 and Appendix A6.1 demonstrate acquiring K for orthotropic materials, i.e., glass epoxy, granite epoxy, and loblolly pine wood.

To perform a thermoelastic test, the specimen is cyclically loaded at a suitable frequency to achieve adiabaticity. Applying appropriate cyclic load can result good TSA signals with low signal-to-noise ratio without damaging the specimen [16]. The load-induced temperature variations of the loaded specimen surface are recorded by the infrared camera. A thin black coating is typically applied on the test surface before performing TSA to improve thermal emissivity and reduce reflection of incident radiations from the test object's surface. The coating thickness should

be within 20-30 μm and the loading frequency between 5-200 Hz to avoid non-adiabatic effects and reduced thermoelastic response from the TSA specimen [17].

Unlike DIC, TSA does not involve differentiating the measured data which can be computationally unreliable procedure. TSA can be used to most kinds of materials and it has been successfully performed on metals, metal-alloys, ceramics, composites, polymers, woods, bones, bricks and concretes [17]. Chapter 2 demonstrates stress analyzing on cellulosic composite material using TSA. Limitations and challenges of TSA include image noise, unreliable edge data, and adiabaticity concerns. Inadequate loading frequencies and the surface coating can compromise the adiabatic response. Recorded TSA information at and near edges is typically unreliable, and this is due to the detector having finite spatial resolution. The quality of the TSA-measured edge information is further affected by the applied cyclic loading. An individual point on the specimen surface will generate different radiation signals while occupying different spatial locations.

1.3.2 Previous Research on Hybrid-TSA

The Experimental Mechanics Research Laboratory here at UW-Madison has considerable experience utilizing hybrid-TSA techniques. This technique was utilized to evaluate the individual stresses in structures made of isotropic and orthotropic composite materials by recording the infrared radiation of a cyclically loaded structure to determine the temperature changes which accompany changes in stress. Table 1.1 summarizes some of the important research done in this area with real and complex variables at the UW Experimental Mechanics Research Laboratory.

Table 1.1: Summary of some of the research on TSA carried out at UW-Madison

Topic	1st Author	Year
Partially loaded aluminum half-plane [17]	Huang Y.M	1990
Symmetrical orthotropic plate with circular hole [18]	Feng	1992
Symmetrical orthotropic plate with side notch [19]	S.T. Lin	1995
Symmetrical orthotropic plate with circular hole and crack [20]	J. Rhee	1999
Mixed-mode thermoelastic fracture analysis of orthotropic composites [21]	S.H. Ju	2003
Stress intensity factors for inclined cracks in orthotropic plate [22]	S.H. Ju	2003
Diametrally-loaded disk [23]	B.E. Foust	2011
Plate with a near edge hole subjected to an offset concentrated load [24]	S.J. Lin	2007
Symmetrical plate with circular hole [25, 26]	S.J. Lin	2007
Unsymmetrical loaded plate with central circular hole [24]	S.J. Lin	2007
Nonsymmetrical plate with circular hole [27]	N.S. Joglekar	2009
Plate with two circular holes [28]	A.A. Khaja	2011
Symmetrical plate with elliptical hole [29]	A.A. Khaja	2013
Unsymmetrically-loaded plate with elliptical hole [30]	W.A. Samad	2013
Bolted joint [31]	W.A. Samad	2014
Plate with irregularly-shaped hole [31]	W.A. Samad	2014
Unsymmetrically-loaded plate with irregularly shaped hole [32]	W.A. Samad	2014
Symmetrical orthotropic plate with elliptical hole [33]	A.A. Alshaya	2016
Plate with a near edge hole subjected to a concentrated load using mapping-collocation technique [34]	A.A. Alshaya	2016

Plate with a U-notch subjected to a concentrated load [35]	A.A. Alshaya	2017
TSA of cellulosic manure composite [36]	Y. Ro	2017
Stresses associated with multiple holes [37]	A.A. Khaja	2017
Determination of constitutive parameters in inverse problem using TSA [38]	A.A. Alshaya	2019
Irregularly shaped hole [39]	B. Kalaycioglu	2019

1.3.3 Digital Image Correlation (DIC)

DIC is a non-contacting optical technique to measure full-field 2D or 3D individual components of displacement. It is a computer-based image analysis technique for displacement measurements of a surface having a speckle pattern. The speckle pattern is tracked when the material (structure) deforms by applied load [40].

Gilbert Hobrough first attempted a form of DIC in the early 1950's and the developments of DIC started in the early 1980's. In 1982 Peters and Ranson [41] first proposed the use of DIC-like computer-based image acquisition and deformation measurements. Sutton and colleagues [40, 42, 43] significantly contributed in developing the original concept of DIC with developed numerical algorithms and optically recorded images. Around 2005 DIC made rapid development in the field of experimental mechanics and optics [3] by improving accuracy and efficiency [42]. Bruck et al. [43] subsequently introduced the Newton-Rapson search method which improved the measurement accuracy and computational time. Chen et al. [44] further improved the DIC accuracy by using spline interpolation. Gradient method [45] and curve fitting method [46] are

faster than the Newton-Rapson method but less accurate. Pan et al. [47, 48, 49, 50] made significant contribution in decreasing the computational time of the Newton-Rapson based DIC algorithms.

Advantages of DIC include it is non-contacting and non-destructive; unlike thermoelastic stress analysis, does not involve cyclic loading; is applicable to actual structures without modeling, such as needed with traditional photoelasticity; unlike metal-foil strain gages, it is full-field; benefits from the availability of commercial systems; and is not restricted to a laboratory environment. DIC is a relatively simple but accurate technique. It requires minimal surface preparation and is cost effective compared to other techniques such as speckle interferometry. DIC is applicable to a wide variety of engineering problems, i.e., displacement/strain measurement in diverse range of materials [51], fracture studies to locate crack-tip and monitor crack propagation, detecting damage development in anisotropic members, fatigue [52], structural deflection monitoring, high temperature strain mapping such as in laser welding [53, 54], vibrational analysis, impact studies, infrastructure inspection and assessment and medical image tracking and scanning.

To perform a DIC test, it requires a random speckle pattern to be applied to the specimen surface and the accuracy heavily depends on the quality of the applied speckle pattern. The random pattern works as unique markers to correlate displacement between the undeformed and deformed states of the loaded member. When the structure is loaded, the speckle pattern deforms along with the specimen and it contains deformation information [3]. There are many techniques to generate unique and reproducible speckle patterns. The natural textures of certain material surfaces can serve as the speckle pattern or the latter can be artificially applied by using paints

(spraying/stamping), hand drawing, chemical etching, computer generated images, atomization process, laser-beam and speckle-projections [55]. The most popular way of generating speckle patterns for DIC measurements is the paint spraying technique but it can cause DIC measurement errors [56, 57]. Illumination light fluctuation during specimen loading often induces noise in the images and the measured displacement accuracy decreases with the noise [58]. Like most experimental techniques, traditional DIC analyses suffers from an inability to record reliable information near and at the edges of geometric discontinuities. However, these locations are important because of associated stress concentrations. Conventional DIC, like other displacement-based methods, necessitates differentiating the recorded information to obtain strains and/or stresses.

1.3.4 Previous Research on Hybird-DIC

DIC has been utilized to evaluate the individual stresses in structures made of isotropic and orthotropic composite materials. The Experimental Mechanics Research Laboratory at UW-Madison has considerable experience utilizing hybrid-DIC techniques. Table 1.2 summarizes some of the important research done in this area.

Table 1.2: Summary of some of the research on DIC carried out at UW-Madison

Topic	1st Author	Year
Symmetrical plate with circular hole [59]	A.A. Khaja	2012
Symmetrical plate with elliptical hole [60]	W.A. Samad	2012

Symmetrically loaded metal plate connector in 3-point bending [30]	W.A. Samad	2013
Unsymmetrical structure subjected to a concentrated load [61]	S. Paneerselvam	2014
Symmetrical plate with side circular notches [35]	A.A. Alshaya	2017
Stress Analysis of a Circularly-Perforated Asymmetrical Isotropic Structure [62]	S. Paneerselvam	2017
Circular hole with orthotropic composite plate [63]	N. Fatima	2017
DIC with cellulosic manure composite [64]	Y. Ro	2018

1.4 Summary

TSA and DIC are versatile structural stress assessment techniques. Both experimental methods are non-contact, non-destructive and comparatively simple relative to experimental and specimen requirements. However, each of the method faces some challenges. The cyclic loading requirement of TSA is not always practical for real world and/or industrial applications and differentiating DIC-measured displacement data to obtain strain/stress is not a numerically reliable procedure. Regions close to or along the edges of structural discontinuities typically contain the most critical stresses while recorded data by DIC or TSA provide unreliable information on or near the edge of a geometric discontinuity. Acknowledging the disadvantages of traditional experimental and numerical methods, this thesis demonstrates the ability to determine the individual stresses full-field in a finite plate by hybridizing experimental information with an Airy stress function using 'Hybrid stress analysis' method. All components of strain and stress can be evaluated from the experimentally evaluated Airy coefficients.

Chapter 2. Full-Field Thermoelastic Stress Analysis of Perforated Cellulosic-Manure Composite

2.1 Introduction

This chapter demonstrates ability to determine individual stresses in a loaded, perforated cellulosic manure composite from recorded stress-induced temperature information. Being able to stress analyze green materials such as cellulosic-manure composites addresses several societal issues. These include providing engineering members fabricated from materials which are suitable for developed and developing nations, relieving a troubling by-product of agricultural regions and reducing demands on our landfills. However, most engineering applications of these materials necessitate knowing their structural integrity, e.g., capability to evaluate stresses.

While national or international numbers are unavailable, the State of Wisconsin produces approximately 190 million pounds of manure per day [65]. In addition to posing a troubling agricultural by-product, this material adversely contributes to our landfills and watersheds. However, manure can be an alternative energy source for livestock farmers. An anaerobic digester will partially convert manure to energy in the form of biogas which contains methane. The manure then can be processed with other materials to produce viable, value-added engineering materials for use in the furniture industry, as sandwich structures, sound absorbing panels along highways, replacement for traditional particleboard, insulation board and interior paneling for high-end accommodations fabricated within large shipping crates. With proper fiber refining, it can replace medium density fiberboard (MDF) or mixed with additional recycled paper pulped fibers such as

from recycled corrugated boxes or old newsprint. The manure still retains nutrients that could be used for agricultural applications such as pots or ground cover boards [66]. The USDA Forest Products Laboratory, Madison, WI, has developed methods which can produce cellulosic-manure composite panels having fire and moisture resistant characteristics. Many engineering applications of these materials necessitate knowing their structural integrity, i.e., require being able to evaluate their stresses when loaded.

This chapter determines the stresses in the perforated cellulosic-manure composite plate, figure 2.1.1, from the load-induced temperature information (i.e., thermoelastic stress analysis, TSA) without knowing the constitutive properties or external boundary conditions. The measured thermal data are processed with an Airy stress function and the traction-free conditions are imposed analytically on the edge of the hole. Individual components of stress are determined full-field as well as on the edge of the hole. An advantage of the approach is its ability to evaluate all of the stresses only from measured thermal information.

Alternate candidate methods to experimentally stress analyze members fabricated from green materials include strain gages, moiré, digital image correlation (DIC), electronic speckle pattern interferometry (ESPI) and photoelasticity [10]. Strain gages provide only point-by-point information so such analyses would necessitate bonding, electrically exiting and monitoring many gages. The relatively poor heat conduction and low modulus of cellulosic-manure can also cause commercial metal foil strain gages to be unreliable. Moiré and DIC require applying a pattern to the component. Although displacements have been measured in green materials using electronic speckle (ESPI) [67], the physical set-up needed to record both in-plane displacement components

is cumbersome. To obtain stresses using displacement-based techniques such as moiré, DIC, and ESPI also require differentiating the measured data to obtain strains (which has its own perils), necessitates knowing the constitutive properties. Birefringent-coating photoelasticity is very laborious, time consuming and requires knowing the properties of the coating and composite material. In addition to being applicable for actual structures in their operating environment, TSA provides the stresses without having to either differentiate the measured information or know the constitutive properties.

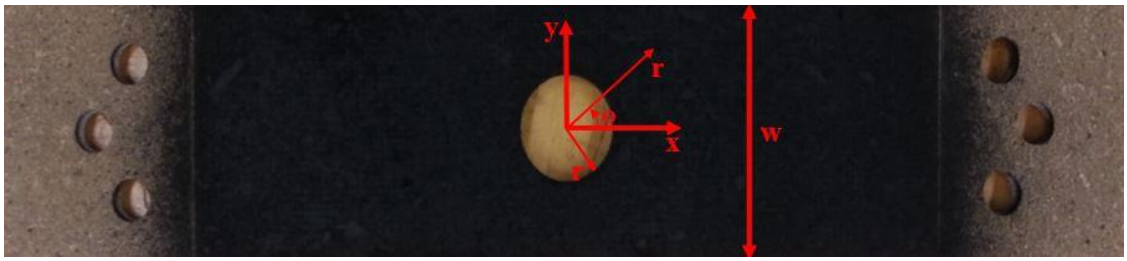

Figure 2.1.1: Black painted perforated cellulosic-manure composite plate (R = 12.7 mm, w = 62 mm, t = 7.2 mm)

2.2 Material Preparation

The initial panel was fabricated from two cellulosic fiber sources: anaerobic digested bovine manure and recycled old corrugated containers. The manure was collected from a farm (figure 2.2.1) and processed through a digester, where it was diluted to 6% solids at a constant temperature of between 38.0 − 39.3° Celsius for 22 to 25 days. During this time the bacteria digests the cellulosic material, while producing methane. The digested manure was screen separated from the bulk of the liquid, leaving a separated solids or fiber content of approximately 25%. This remaining non-digested cellulosic solid content was combined with the recycled corrugated pulp fiber used to form the fibrous mats. The corrugated material came from a local box plant and represents excess cut-offs and industrial scrap material. The received corrugated material was hydro-pulped at approximately 10% solids for 20 minutes to produce a fibrous slurry. The processed manure and paper were combined 1:1 by dry-weight and mixed with water in a forming box to achieve an approximate 2% solids slurry. A mat of randomly oriented fibers was produced by pouring this slurry mixture onto a screen followed by applying a vacuum beneath the screen. The vacuum pulled the water/fiber mixture toward the screen, depositing the fibers on the screen to form a loosely formed fibrous mat. After which, the mat was wet-pressed to remove most of the residual water to produce a relatively thick mat, figure 2.2.2. This mat was subsequently hot-pressed at 160° Celsius at 1.0 MPa until dry. The heat and pressure combined the two fibrous materials to produce a naturally bonded in-plane randomly oriented (isotropic) cellulose-fiber panel. Its in-plane elastic modulus, E, is up to 7 GPa (1.0 Mpsi), which is equal or exceeds that of most commercial hardboards

Figure 2.2.1: Collected manure from a farm

Figure 2.2.2: Wet-formed composite mat prior to the application of heat and pressure

2.3 Experimental Details

Figure 2.1.1 is the image of the tested cellulosic-manure composite specimen. It shows the plate geometry, dimension, orientation and co-ordinate axes. The plate is 30.5 cm (12”) long, 6.2 cm (2.4”) wide, 0.72 cm (0.28”) thick and has a perforated hole of radius with 1.27 cm (0.5”) at the center. The surface of the specimen was sprayed with Krylon Ultra-Flat black paint prior to testing in order provide an enhanced and uniform emissivity surface. The plate was mounted in the loading frame, figure 2.3.1, and loaded sinusoidally between 445 N (100 lbs) and 890 N (200 lbs) at a rate of 20 Hz. The corresponding load-induced temperature information was recorded by a thermoelectrically-cooled infrared DeltaTherm DT1410 camera, figure 2.3.1 (Stress Photonics, Madison, WI, USA; sensor resolution of 256 horizontal by 256 vertical pixels). Figure 2.3.2 is a raw TSA image of the loaded plate recorded over a period of 2 minutes.

The raw TSA image of figure 2.3.2 was subsequently incorporated into MATLAB and, recognizing the mechanical and geometric symmetry about the horizontal and vertical axes through the center of the hole, the measured TSA data were averaged over the four quadrants. Since the specimen was subjected to a uniform, vertical uniaxial stress fields away from the hole and loading grips, the thermo-mechanical coefficient, K, was determined by $S*/(\text{far} - \text{field uniform stress})$, giving K = 184 U / M P a where the symbol U denotes unit-less constant. Figure 2.3.3 shows the uncalibrated TSA image of the raw data, $S*$, processed by MATLAB, whereas figure 2.3.4 displays the calibrated thermogram, S, in MPa, obtained from the evaluated thermo-mechanical coefficient, K, and equation 2.1.

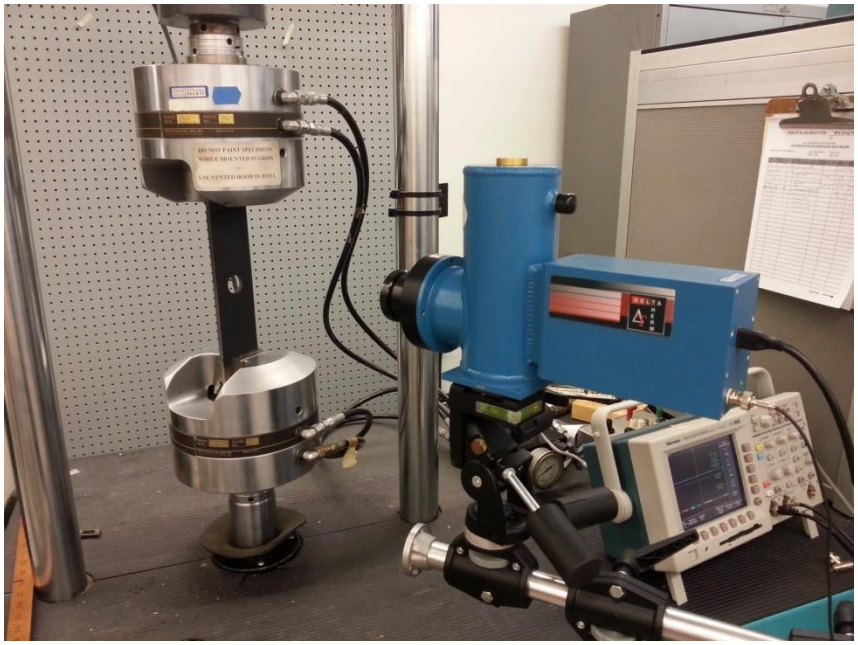

Figure 2.3.1: TSA experimental setup

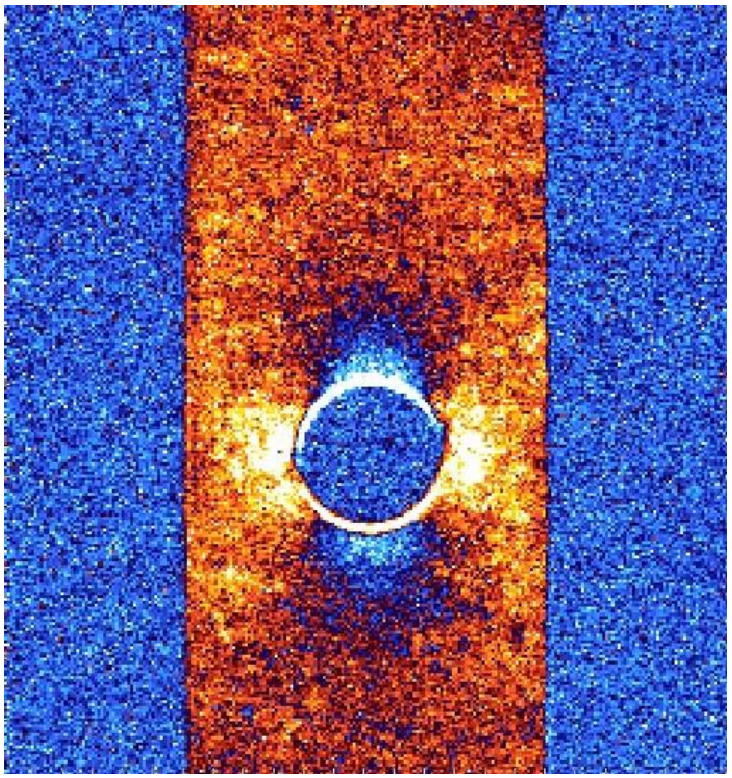

Figure 2.3.2: Raw TSA image by thermoelectrically-cooled infrared DeltaTherm DT1410

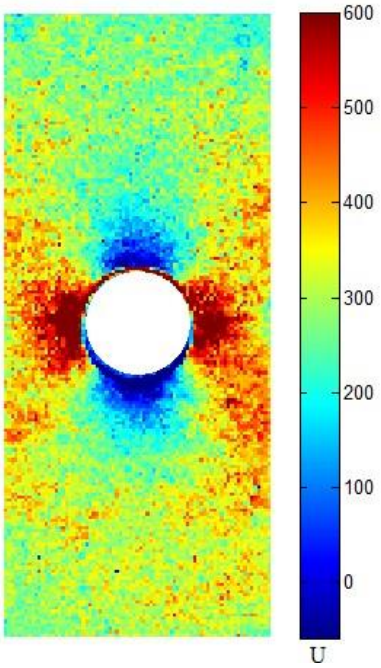

Figure 2.3.3: MATLAB processed uncalibrated raw thermogram, S*, from the vertically loaded tensile plate

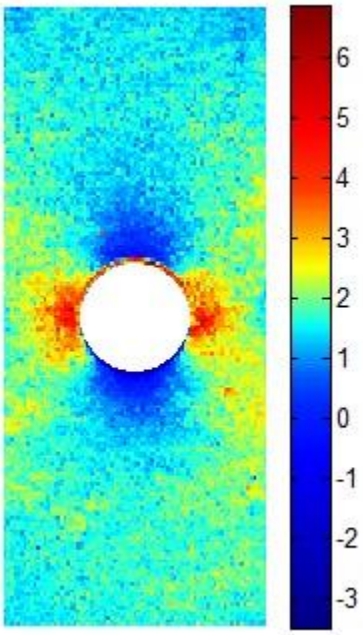

Figure 2.3.4: Thermogram, *S*, from the vertically loaded tensile plate with the calibrated color bar [MPa]

2.4 Relevant Equations

Thermoelastic stress analysis is a non-contact, non-destructive experimental method for determining the full-field stresses in loaded members. The technique enables the stress analysis of actual structures in their operating environment with a sensitivity equal to that of strain gages. No surface preparation is required other than perhaps a flat black paint to provide an enhanced and uniform emissivity. By cyclically loading the structure to satisfy adiabatic reversible conditions, the stresses at a location are related to the stress-induced temperature at that position. One records the temperature data with a sensitive infrared camera.

For plane stress isotropic TSA under cyclic loading condition,

$$S^* = K\Delta S \tag{2.1}$$

where S^* is the recorded signal from the TSA system, K is an experimentally determined thermo-mechanical coefficient, and $S = \sigma_{xx} + \sigma_{yy} = \sigma_{rr} + \sigma_{\theta\theta}$ is the isopachic stress. Using an Airy's stress function and imposing the traction free conditions analytically on the edge of the hole, figure 2.1.1, the expression for the isopachic stress contains all the coefficients which appear in the individual components of stress, σ_{rr}, $\sigma_{\theta\theta}$ and $\sigma_{r\theta}$. By evaluating the Airy coefficients thermoelastically, the individual stress components are available from the measured temperatures alone. The authors are unaware of any previous stress analysis of cellulosic-manure composites.

The method behind determining the state of stress and near the circular hole lies in coupling the Airy's stress function with the measured temperature data by TSA then imposing traction free boundary conditions on the edge of the hole. A general Airy's stress function in polar

coordinates satisfying the biharmonic equation, $\nabla^4\Phi = 0$, equilibrium and compatibility can be written as [10, 68],

$$\begin{aligned}\phi =& a_0 + b_0 \ln r + c_0 r^2 + d_0 r^2 \ln r + (A_0 + B_0 \ln r + C_0 r^2 + D_0 r^2 \ln r)\theta \\ &+ (a_1' r + b_1' r \ln r + \frac{c_1'}{r} + d_1' r^3)\sin\theta + (a_1 r + b_1 r \ln r + \frac{c_1}{r} + d_1 r^3)\cos\theta \\ &+ (A_1' + B_1' r \ln r)\theta \sin\theta + (A_1 r + B_1 r \ln r)\theta \cos\theta \\ &+ \sum_{n=2}^{\infty}(a_n' r^n + b_n' r^{n+2} + c_n' r^{-n} + d_n' r^{2-n})\sin(n\theta) \\ &+ \sum_{n=2}^{\infty}(a_n r^n + b_n r^{n+2} + c_n r^{-n} + d_n r^{2-n})\cos(n\theta)\end{aligned} \tag{2.2}$$

The number of unknown Airy coefficients in equation (2.2) can be reduced significantly in this case due to symmetry. By recognizing that the geometry and loading of the finite plate of figure 2.1.1 are symmetric about *x*- and *y*-axes, each of the inner and outer boundaries is self-equilibrated, and the stresses, strains and displacements must be single values function of θ, the Airy stress function reduces to,

$$\phi = a_0 + b_0 \cdot ln\, r + c_0 \cdot r^2 + \sum_{n=2,4,6...}^{N} \left(a_n \cdot r^n + b_n \cdot r^{n+2} + c_n \cdot r^{-n} + d_n \cdot r^{-(n-2)}\right) \cdot cos\left(n \cdot \theta\right) \tag{2.3}$$

Since,

$$\sigma_{rr} = \frac{1}{r} \cdot \frac{\partial \phi}{\partial r} + \frac{1}{r^2} \frac{\partial^2 \phi}{\partial \theta^2} \tag{2.4}$$

$$\sigma_{\theta\theta} = \frac{\partial^2 \phi}{\partial r^2} \tag{2.5}$$

$$\sigma_{r\theta} = -\frac{\partial}{\partial r} \cdot (\frac{1}{r} \cdot \frac{\partial \phi}{\partial \theta}) \tag{2.6}$$

the individual polar components of stress become

$$\sigma_{rr} = \frac{b_0}{r^2} + 2 \cdot c_0 - \sum_{n=2,4,6\ldots}^{N} \left[\begin{array}{l} a_n \cdot n \cdot (n-1) \cdot r^{(n-2)} \\ +b_n \cdot (n+1) \cdot (n-2) \cdot r^{n} \\ +c_n \cdot n \cdot (n+1) \cdot r^{-(n+2)} \\ +d_n \cdot (n-1) \cdot (n+2) \cdot r^{-n} \end{array} \right] \cdot \cos(n \cdot \theta) \quad (2.7)$$

$$\sigma_{\theta\theta} = -\frac{b_0}{r^2} + 2 \cdot c_0 + \sum_{n=2,4,6\ldots}^{N} \left[\begin{array}{l} a_n \cdot n \cdot (n-1) \cdot r^{(n-2)} \\ +b_n \cdot (n+1) \cdot (n+2) \cdot r^{n} \\ +c_n \cdot n \cdot (n+1) \cdot r^{-(n+2)} \\ +d_n \cdot (n-1) \cdot (n-2) \cdot r^{-n} \end{array} \right] \cdot \cos(n \cdot \theta) \quad (2.8)$$

$$\sigma_{r\theta} = \sum_{n=2,4,6\ldots}^{N} \left[\begin{array}{l} a_n \cdot n \cdot (n-1) \cdot r^{(n-2)} \\ +b_n \cdot n \cdot (n+1) \cdot r^{n} \\ -c_n \cdot n \cdot (n+1) \cdot r^{-(n+2)} \\ -d_n \cdot n \cdot (n-1) \cdot r^{-n} \end{array} \right] \cdot \sin(n \cdot \theta) \quad (2.9)$$

and the Airy coefficients are related to the recorded signal, S^*, and isopachic stress, S,

$$S^* = K \triangle S \quad (2.10)$$

$$\begin{aligned} S &= \left(\sigma_{rr} + \sigma_{\theta\theta}\right) = \left(\sigma_{xx} + \sigma_{yy}\right) = \left(\sigma_1 + \sigma_2\right) \\ &= 4 \cdot c_0 + \sum_{n=2,4,6\ldots}^{N} \left[4 \cdot b_n \cdot \left(n+1\right) \cdot r^n - 4 \cdot d_n \cdot \left(n-1\right) \cdot r^{-n}\right] \cdot cos\left(n \cdot \theta\right) \end{aligned} \tag{2.11}$$

where r is the radius measured from the center of the hole and angle θ is measured counterclockwise from the *x*-axis of figure 2.1.1. R = 12.7 mm is the radius of the hole, and σ_{rr}, $\sigma_{\theta\theta}$, σ_{xx}, σ_{yy}, σ_1, and σ_2 are the orthogonal stress components in the polar, Cartesian rectangular and principal coordinates, respectively. N is the terminating index value of the series and can be any positive even integer up to approaching infinity. c_0, b_n, and d_n are Airy coefficients.

Due to the differentiation of equation (2.4) through (2.6), coefficient a_o of equation (2.3) is not present in the equations (2.7) through (2.9); however, they still involve some coefficients not contained in the equation (2.11) for S. Thus, the separate stress components cannot be derived from thermoelastic data using these equations alone unless traction free condition of $\sigma_{rr} = \sigma_{r\theta} = 0$ on the edge of the hole of figure 2.1.1 are incorporated analytically into the equations. After imposing the traction free condition, the number of coefficients is reduced and the polar stresses are simplified as [69],

$$\begin{aligned} \sigma_{rr} &= \left(\frac{-2 \cdot R^2}{r^2} + 2\right) \cdot c_0 \\ &- \sum_{n=2,4,6\ldots}^{N} \left\{ \begin{array}{l} \left[\left(n-1\right) \cdot r^{(n-2)} \cdot \left(-1\right) \cdot \left(1+n\right) \cdot R^2 + \left(n+1\right) \cdot \left(n-2\right) \cdot r^n + R^{2\cdot(1+n)} \cdot \left(n+1\right) \cdot r^{-(n+2)}\right] \cdot b_n \\ + \left[\left(-1\right) \cdot R^{2\cdot(1-n)} \cdot \left(n-1\right) \cdot r^{(n-2)} + \left(1-n\right) \cdot R^2 \cdot \left(n+1\right) \cdot r^{-(n+2)} + \left(n-1\right) \cdot \left(n+2\right) \cdot r^{-n}\right] \cdot d_n \end{array} \right\} \cdot cos\left(n \cdot \theta\right) \end{aligned} \tag{2.12}$$

$$\sigma_{\theta\theta} = \left(\frac{2\cdot R^2}{r^2} + 2\right)\cdot c_0 + \sum_{n=2,4,6...}^{N} \left\{ \begin{array}{l} \left[\left(n-1\right)\cdot r^{(n-2)}\cdot\left(-1\right)\cdot\left(1+n\right)\cdot R^2 + \left(n+1\right)\cdot\left(n+2\right)\cdot r^n + R^{2\cdot(1+n)}\cdot\left(n+1\right)\cdot r^{-(n+2)}\right]\cdot b_n \\ +\left[\left(n-1\right)\cdot r^{(n-2)}\cdot\left(-1\right)\cdot R^{2\cdot(1-n)} + \left(1-n\right)\cdot R^2\cdot\left(n+1\right)\cdot r^{-(n+2)} + \left(n-1\right)\cdot\left(n-2\right)\cdot r^{-n}\right]\cdot d_n \end{array} \right\}\cdot cos\left(n\cdot\theta\right) \tag{2.13}$$

$$\sigma_{r\theta} = \sum_{n=2,4,6...}^{N} \left\{ \begin{array}{l} \left[\left(n-1\right)\cdot r^{(n-2)}\cdot\left(-1\right)\cdot\left(1+n\right)\cdot R^2 + n\cdot\left(n+1\right)\cdot r^n - \left(n+1\right)\cdot r^{-(n+2)}\cdot R^{2\cdot(1+n)}\right]\cdot b_n \\ +\left[\left(n-1\right)\cdot r^{(n-2)}\cdot\left(-1\right)\cdot R^{2\cdot(1-n)} - \left(1-n\right)\cdot R^2\cdot\left(n+1\right)\cdot r^{-(n+2)} - n\cdot\left(n-1\right)\cdot r^{-n}\right]\cdot d_n \end{array} \right\}\cdot sin\left(n\cdot\theta\right) \tag{2.14}$$

By stress transformation, the stresses of equations (2.12) through (2.14) are converted from polar to rectangular stress components σ_{xx} and σ_{yy} by means of the standard transformation expression,

$$\begin{bmatrix} \sigma_{xx} \\ \sigma_{yy} \\ \sigma_{xy} \end{bmatrix} = \begin{bmatrix} m^2 & n^2 & -2\cdot m\cdot n \\ n^2 & m^2 & 2\cdot m\cdot n \\ m\cdot n & -m\cdot n & m^2-n^2 \end{bmatrix} \cdot \begin{bmatrix} \sigma_{rr} \\ \sigma_{\theta\theta} \\ \sigma_{r\theta} \end{bmatrix} \tag{2.15}$$

$$where\ m\ =\ \cos(\theta)\ \ and\ n\ =\ \sin(\theta)$$

and the rectangular components of stresses are

$$\sigma_{\mathrm{xx}} = \left[\begin{array}{c} \left\{-\cos 2\theta\,\frac{2\,R^2}{r^2} + 2\right\} c_0 \\ + \sum_{n=2,4,\ldots}^{N} \left\{ \begin{array}{c} \left\{ \begin{array}{c} (n+1)(n-1)R^2 r^{n-2}(\cos(n\theta-2\theta)) \\ -(n+1)R^{2(n+1)} r^{-(n+2)}\left(cos(n\theta+2\theta)\right) \\ -(n+1)r^n(n\cos(n\theta-2\theta)-2cosn\theta) \end{array} \right\} b_n \\ + \left\{ \begin{array}{c} (n-1)R^{-2(n-1)}\, r^{n-2}(\cos(n\theta-2\theta)) \\ +(n-1)(n+1)R^2 r^{-(n+2)}\left(cos(n\theta+2\theta)\right) \\ -(n-1)r^{-n}(ncos(n\theta+2\theta)+2cosn\theta) \end{array} \right\} d_n \end{array} \right\} \end{array} \right] \tag{2.16}$$

$$\sigma_{\mathrm{yy}} = \left[\begin{array}{c} \left\{\cos 2\theta \frac{2\,R^2}{r^2} + 2\right\} c_0 \\ + \sum_{n=2,4,\ldots}^{N} \left\{ \begin{array}{c} \left\{ \begin{array}{c} -(n+1)(n-1)R^2 r^{n-2}\cos(n\theta - 2\theta) \\ +(n+1)R^{2(n+1)} r^{-(n+2)} cos(n\theta + 2\theta) \\ +(n+1)r^n (n\cos(n\theta - 2\theta) + 2cosn\theta) \end{array} \right\} b_n \\ + \left\{ \begin{array}{c} -(n-1)R^{-2(n-1)}\, r^{n-2}\cos(n\theta - 2\theta) \\ -(n-1)(n+1)R^2 r^{-(n+2)} cos(n\theta + 2\theta) \\ +(n-1)r^{-n}(ncos(n\theta + 2\theta) - 2cosn\theta) \end{array} \right\} d_n \end{array} \right\} \end{array} \right] \tag{2.17}$$

The Airy coefficients in equations (2.12) through (2.14), (2.16) and (2.17) for the individual stress components are exactly those appearing in the isopachic stress S of equation (2.11). One can therefore evaluate the individual components σ_{rr}, $\sigma_{\theta\theta}$, $\sigma_{r\theta}$, σ_{xx} and σ_{yy} thermoelastically from the measured system signal, S^*. While recorded thermoelastic data at, and adjacent to, an edge are unreliable and recorded thermoelastic information can be noisy, the present technique overcomes these challenges and reliably gives the independent components of full-field stress, including on the edges.

2.5 Data Reduction and Analysis

The coefficients of equations (2.12) through (2.17) were obtained from TSA measured values of $S = (S^*/K)$ at many locations throughout the recorded region. Once the TSA data were acquired as figure 2.3.2, a set of linear isopachic expressions of the form of equation (2.11) and containing the same coefficients as the stress components was formulated as the matrix expression $Ac = d$ of equation (2.18),

$$\begin{bmatrix} S_{r_1,\theta_1}(c_0,b_2,d_2,b_4,d_4\cdots\cdots b_N,d_N) \\ S_{r_2,\theta_2}(c_0,b_2,d_2,b_4,d_4\cdots\cdots b_N,d_N) \\ \vdots \\ \vdots \\ \vdots \\ S_{r_m,\theta_m}(c_0,b_2,d_2,b_4,d_4\cdots\cdots b_N,d_N) \end{bmatrix}_{m\times k} \begin{bmatrix} c_0 \\ b_2 \\ d_2 \\ \vdots \\ b_N \\ d_N \end{bmatrix}_{k\times 1} = \begin{bmatrix} S_1 \\ S_2 \\ S_3 \\ \vdots \\ \vdots \\ S_m \end{bmatrix}_{m\times 1} \tag{2.18}$$

or, in simplified form,

$$[A]_{m\times k}\{c\}_{k\times 1} = \{d\}_{m\times 1} \tag{2.19}$$

where $[A]$ matrix involves m Airy isopachic equations corresponding to radial distance, r, and angle, θ, of the input source locations of S, and vector $\{c\}$ is the set of k unknown Airy coefficient values (i.e., c_0, b_n, d_n). Vector $\{d\}$ is the vector set of m data values of S at the same set of data points used in forming matrix $[A]$. Since measured TSA data typically include some noise and scatter, it is advantageous to use more measured input values than the number of coefficients. Since $m > k$, the least squares method was employed to solve the over-determined matrix expression, $Ac = d$ of equations (2.18) or (2.19).

It is important to determine an appropriate number for k. Too small a value of k can

produce inaccurate results while too many coefficients can cause the Airy matrix of m equations by k coefficients to become unstable or near singular due to computer round off and quantization errors. Recognizing unreliable TSA data at edges, the m = 10,000 TSA values used as input originate at r/R =1.2 (=2.54 mm) away from the edge of the hole, figure 2.5.1.

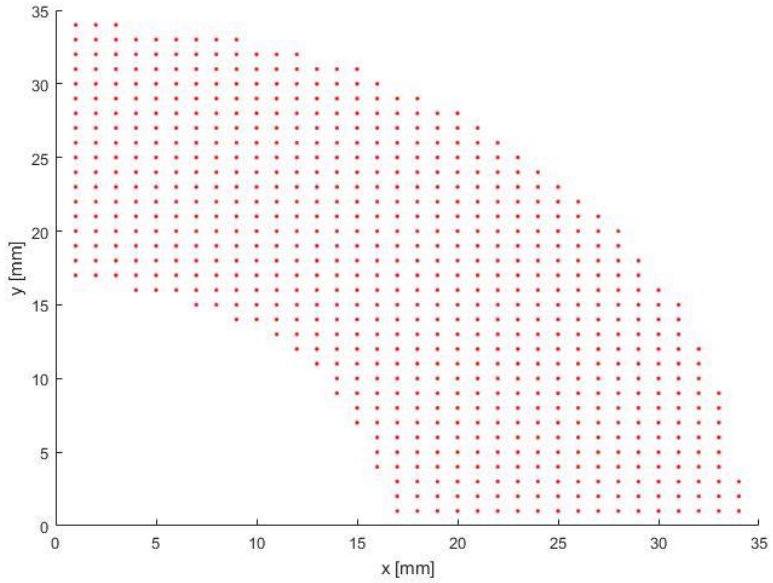

Figure 2.5.1: Source locations of 10,000 measured *S* input for 1.2 ≤ r/R ≤ 2.4

Determining appropriate number for k was achieved by plotting the condition number, C and $\log_{10}C$, of the Airy matrix against the number of coefficients k = 1~ 45, figure 2.5.2 and 2.5.2. It demonstrates that the matrix instability grows exponentially with the number of coefficients, k, increases. Using the smallest number of coefficients which gives sufficient accuracy is therefore desirable.

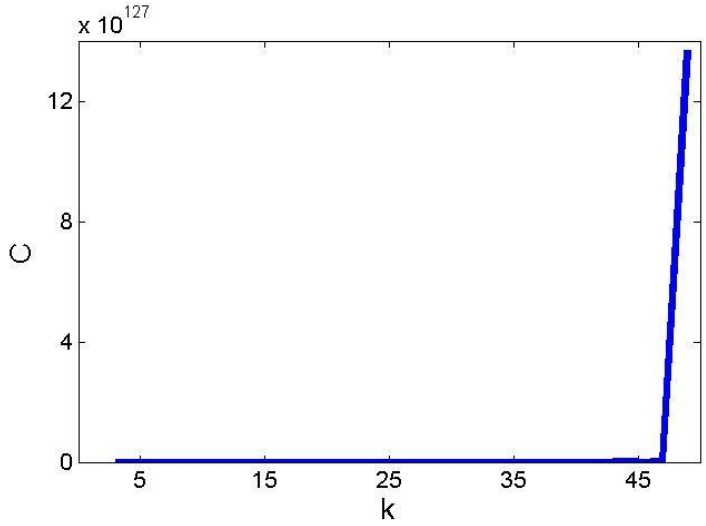

Figure 2.5.2: Airy matrix condition number *C* vs. *k*

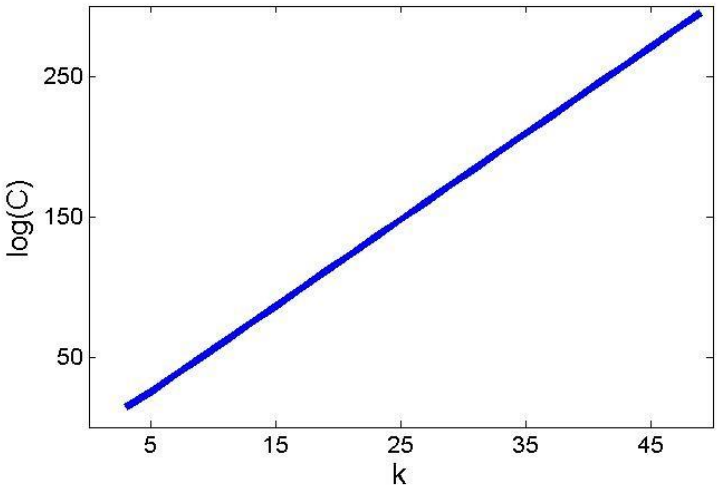

Figure 2.5.3: Log_{10} of *C* vs. *k*

The RMS (root mean square) discrepancy between the experimental values of $\{d\}$ and the calculated isopachic values $\{d'\}$ using the now-determined magnitude of the Airy coefficients was also calculated and plotted in figure 2.5.4. For an over-determined matrix equation of $Ac = d$, solving $c = A\backslash d$ (MATLAB notation) and using the now-known coefficient vector $\{c\}$ in the

original matrix equation will give $Ac = d$, where in general $\{d'\}$ is not exactly the same as the input data $\{d\}$. It is desirable to have the RMS discrepancy of equation (2.20) small for each matrix having a different number of coefficients.

$$(d' - d)_{rms} = \sqrt{\sum_{i=1}^{m} (d'_i - d_i)^2 / m} \tag{2.20}$$

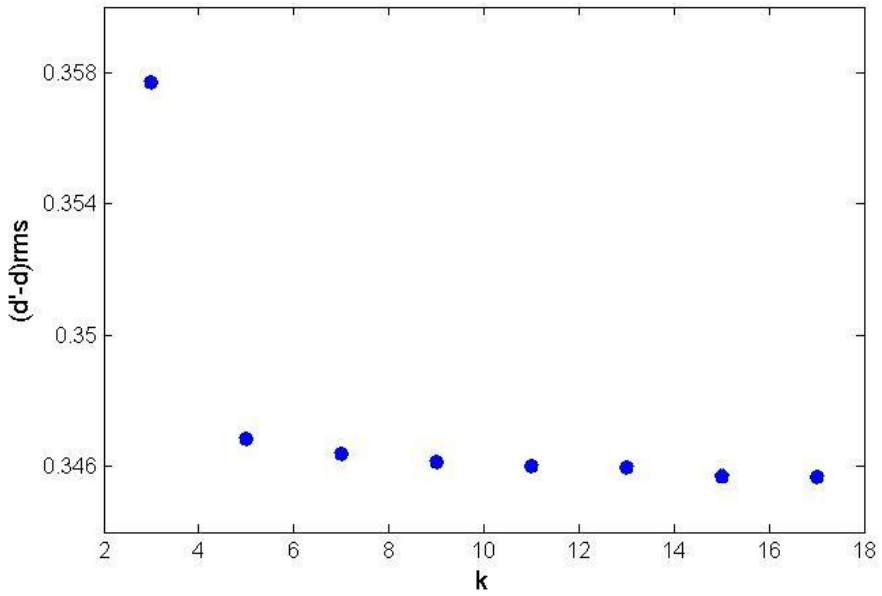

Figure 2.5.4: *RMS* values of (*d'-d*) vs. number of coecients, *k*

Figure 2.5.4 shows the *RMS* values of ($d' - d$) obtained as a function of the number of coefficients, k, from 3 to 17 based on the 10,000 input data from their source locations in figure 2.5.1. The case of $k = 1$ is omitted from figure 2.5.4 since its *RMS* value is 1.22, which is relatively very high compared to others. Data of figures 2.5.2 through and 2.5.4 suggest $k = 7$ is reasonable. Moreover, figure 2.5.4 indicates that $k > 7$ does not show much improvement of the discrepancies

and it would involve more calculations with a larger condition number, C. As discussed previously, using too many coefficients can cause numerical problems. Figures 2.5.5 (a) and (b) compare the normalized experimentally-based and reconstructed S/σ_0 images, further supports using k = 7, where the far-field stress σ_0 = 1.74 MPa is based on the applied load and the gross area of the specimen. The scatter and unreliable information at and near the edge of the hole in the recorded data of figure 2.3.2 is manifested in the messy image of figure 2.5.5 (a). On the other hand, figure 2.5.5 (b) illustrates the smoothing consequences and reliable edge information obtained by processing the measured data with the Airy stress function.

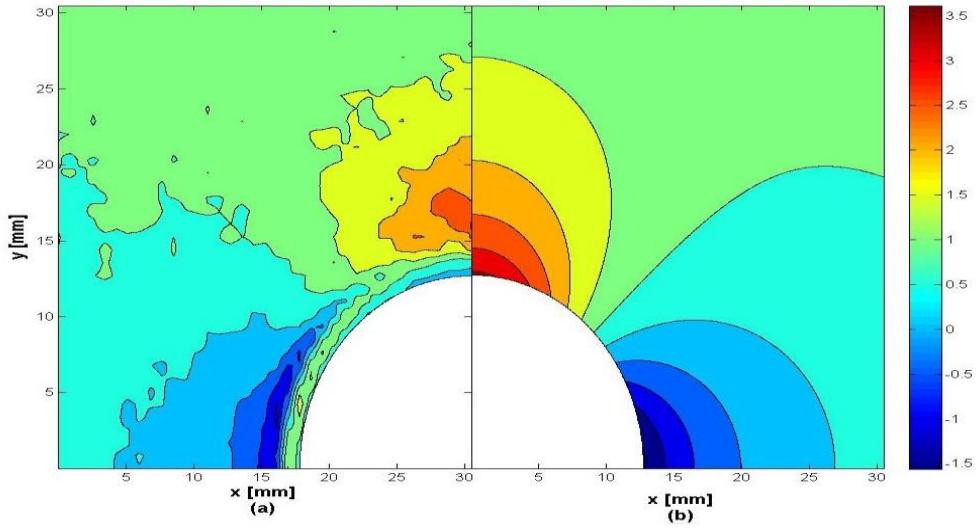

Figure 2.5.5: (a) Experimental and (b) reconstructed (k = 7) normalized isopachic stress, S/σ_0

2.5.1 Further Validation

Figure 2.5.6 compares distribution of normalized TSA-determined isopachic stress with normalized TSA recorded isopachic stress on the boundary of the hole, where r/R equals to 1.25.

Using 7 Airy coefficients, TSA or experimentally determined isopachic stress can be calculated by equation (2.11) and then they are normalized by the far field stress based on the gross area of the specimen. Also, TSA recorded isopachic stress, *S*, is normalized by the far field stress based on the gross area of the specimen. Figure 2.5.7 compares the normalized TSA-determined stress and normalized TSA-recorded stress at *r/R* equals to 2 in the same manner.

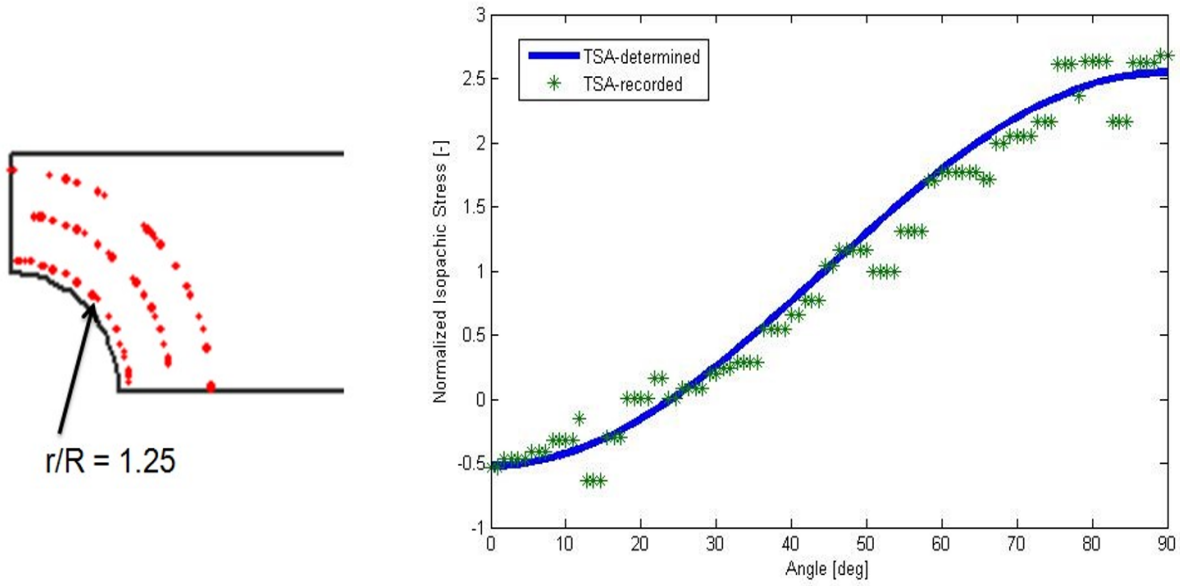

Figure 2.5.6: Comparison between TSA-determined and TSA-recorded normalized isopachic stress, S/σ_0, around the boundary of the hole, r/R = 1.25

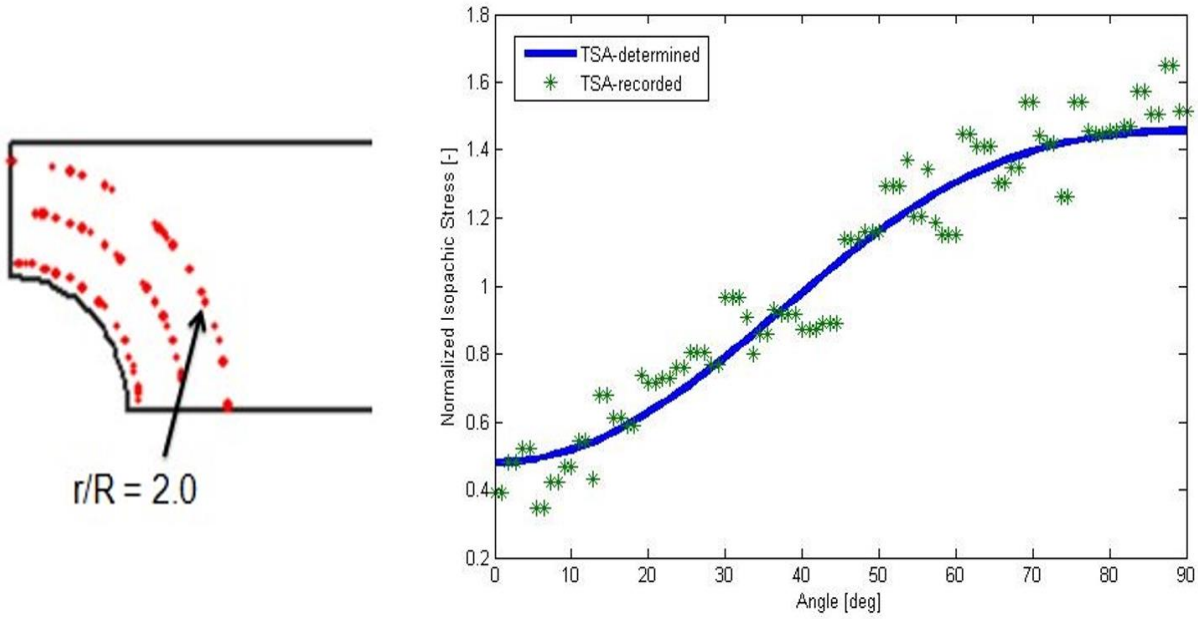

Figure 2.5.7: Comparison between TSA-determined and TSA-recorded normalized isopachic stress, S/σ_0, around the boundary of the hole, r/R = 2.0

Even though the stresses on or near the edge of a geometric discontinuity are usually of greatest importance, it is worth to assess the distance from the hole over which the current analysis is valid. Figure 2.5.8 compares two sets of normalized isopachic stresses, *S*, based on experimentally determined 7 Airy coefficients and recorded raw data on *x* direction from the center of the hole of figure 2.1.1. Because TSA recorded image can be unreliable on the edge of the hole, *x/R* start from 1.20 where *R* is the radius of the hole.

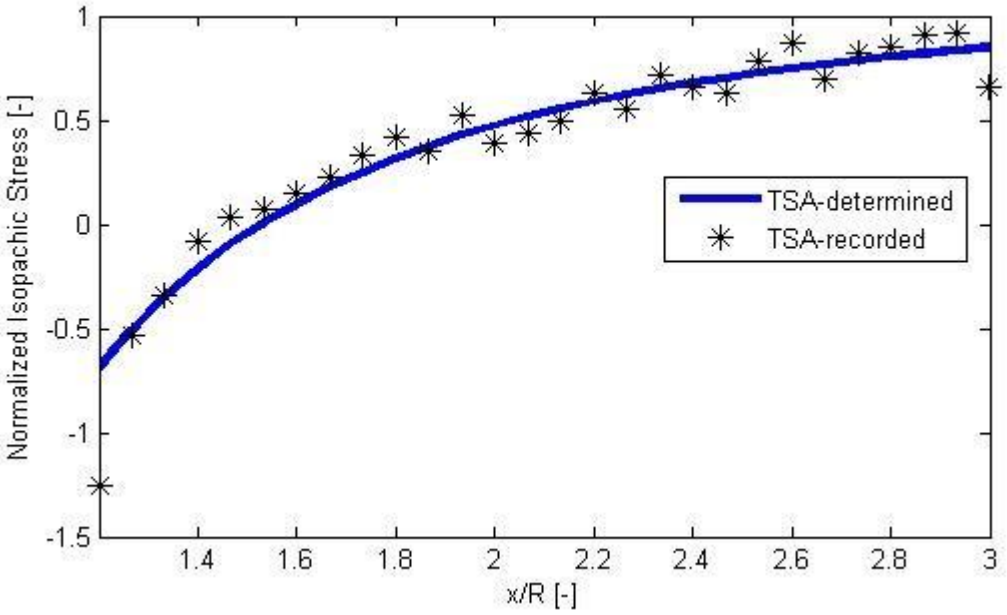

Figure 2.5.8: Comparison of normalized isopachic stress, S/σ_0, along *x*-axis

2.6 Results

Based on the $m = 10,000$ measured values of S^* of figure 2.5.1 and $k = 7$ evaluated coefficients, the individual stresses are available from equations (2.12) through (2.17). Figure 2.6.1 plots the normalized TSA-determined tangential stress based on the gross area of the plate along the edge of the hole. The TSA-evaluated stress concentration factor, K_t, of 3.63 compares with that of 3.77 of based on Young and Budynas [70]. Figures 2.6.2 through 2.6.6 are full-field contour plots where the loading is in the horizontal x-axis [36].

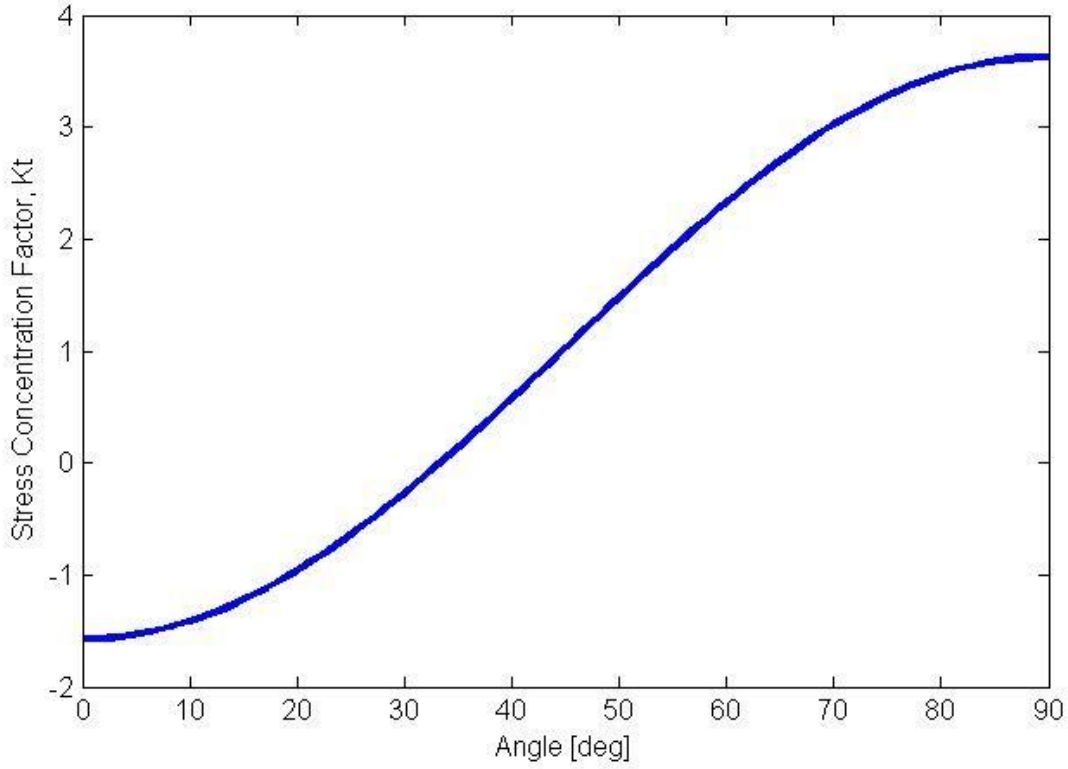

Figure 2.6.1: TSA-determined stress concentration factor, K_t, $\sigma_{\theta\theta}/\sigma_0$ along edge of the hole

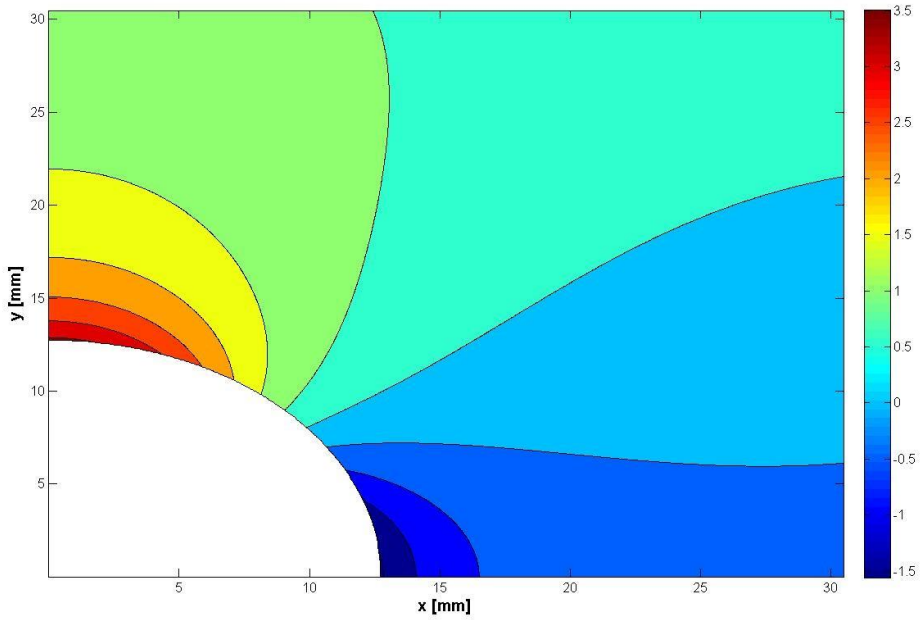

Figure 2.6.2: Experimentally determined stress, $\sigma_{\theta\theta}/\sigma_0$

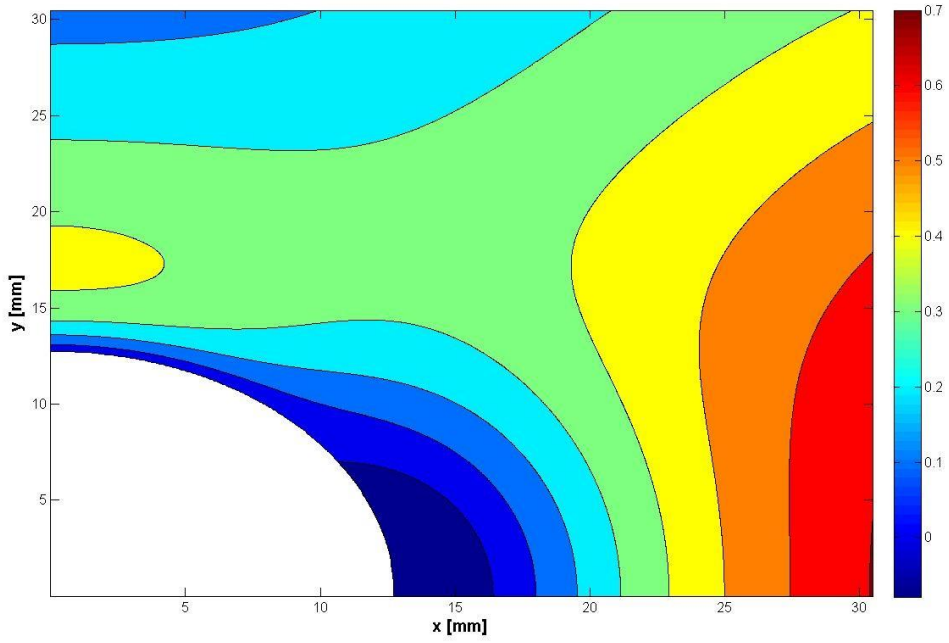

Figure 2.6.3: Experimentally determined stress, σ_{rr}/σ_0

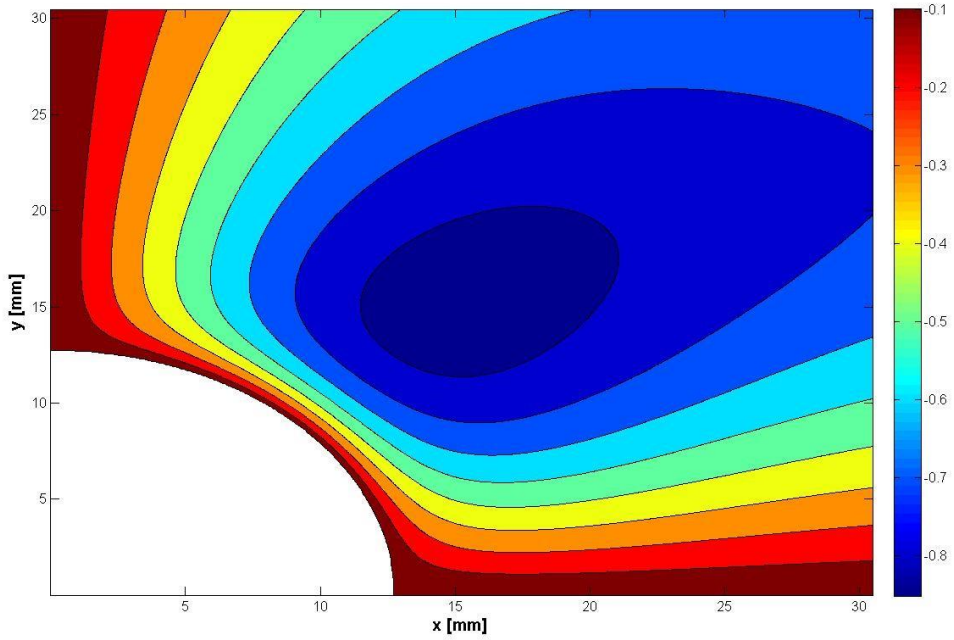

Figure 2.6.4: Experimentally determined stress, $\sigma_{r\theta}/\sigma_0$

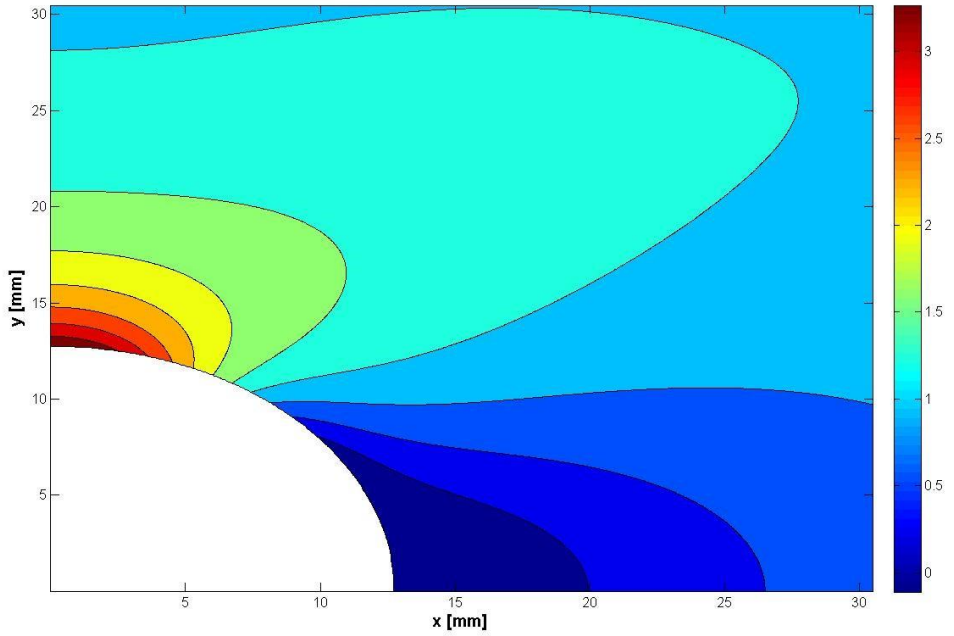

Figure 2.6.5: Experimentally determined stress, σ_{xx}/σ_0

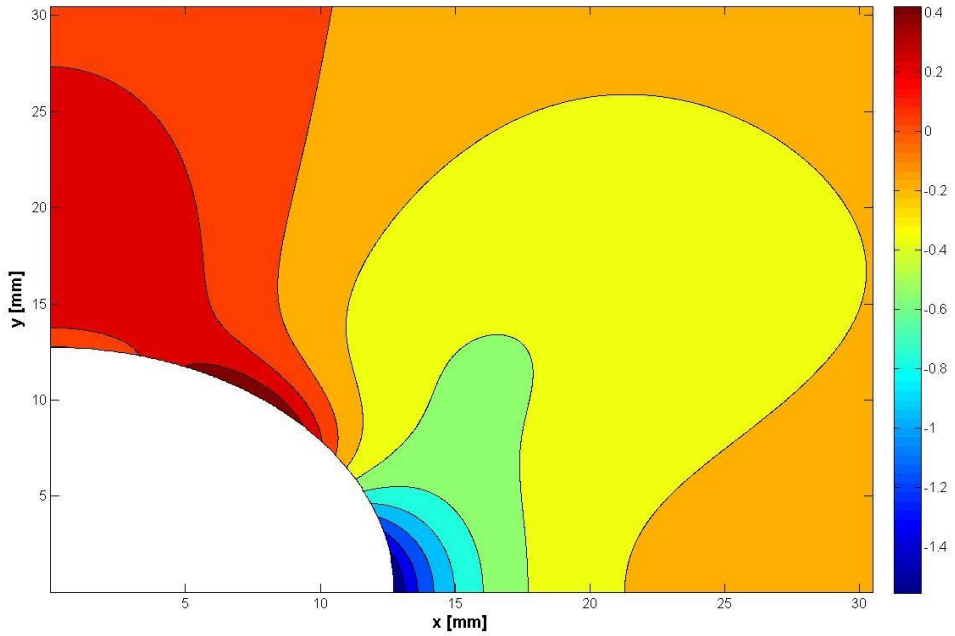

Figure 2.6.6: Experimentally determined stress, σ_{yy}/σ_0

2.7 Summary

By processing the recorded associated temperature information with a stress function, this chapter demonstrates one can stress analyze members fabricated from green materials such as cellulosic-manure composites. In addition to creating a value-added material, this ability addresses a societal problem and eases a major challenge to our landfills. In response to uses for cellulose based manure panels, cellulose fiber composites could have application where ever traditional composites might be used. When it is used as a coarser material, it might be possible that it could be made to perform similar to particleboard. With additional refining of the material, it could be made for replacement of medium density fiberboard (MDF) or also mixed with additional pulped fibers such as recycled corrugated fiberboard, so it could be used for various applications such as furniture. In other applications, the manure still has nutrients that could be used for agricultural applications such as pots or ground cover. While cellulosic materials tend to exhibit decreasing modulus and strength with increased moisture, methods are being developed to prevent this with the present composites. Although the structural integrity of engineering ap- plications of these materials necessitate knowing the stresses, the author is unaware of any previous experimental stress analysis of cellulosic-manure composites.

To determine the individual components of stress of cellulosic manure composite with centrally circular geometric discontinuity in a tensile strip without knowing the constitutive properties, stress induced temperature information was combined with a series representation of the Airy stress function. Recognizing that in notched or perforated members, the most serious stresses usually happen on the edge of the geometric discontinuity; however, measured values are

often unreliable at edges. By employing 10,000 TSA data points which is much greater than unknown coefficients of 7 of Airy stress function, experimental noise and scatter were filtered out. By utilizing TSA-determined coefficients, stress components could be reconstructed as figure 2.6.2 through 2.6.6. The TSA-evaluated stress concentration factor, K_t, around the edge of the hole of 3.63 compares with that of 3.77 based on Young and Budynas, 2002. The present thermoelastic method simultaneously smooths the recorded experimental data and provides the three independent stresses full- field reliably, including on the edge of holes or notches where the serious situations typically occur. While demonstrated presently to the case of a round hole in a finite manure-cellulosic composite tensile plate, the approach is applicable to much more complicated structural situations (e.g., bolted, pinned or nailed holes, or non- isotropic materials).

Chapter 3. Full-Field Stress Analysis of Cellulosic-Manure Composite Plate using Digital Image Correlation

3.1 Introduction

While neither national or international numbers are available, the State of Wisconsin produces approximately 190 million pounds of manure per day [65]. In addition to being a troubling agricultural by-product, this material adversely contributes to our watersheds. However, manure can be processed with other materials to pro- duce value-added engineering materials for use in the furniture industry, as sandwich structures, sound absorbing panels along highways, replacement for traditional particleboard, insulation board and interior paneling for high-end accommodations fabricated within large shipping crates. Manure composites could replace medium density fiberboard (MDF) when mixed with additional pulped fibers from recycled corrugated boxes or old newsprint. The USDA Forest Products Laboratory, Madison, WI. is developing methods to make cellulosic-manure composites both fire and moisture resistant. Many engineering applications of these materials necessitate knowing their structural integrity, i.e., require ability to evaluate the stresses in manure-composite members. A non-destructive and non-contacting method was employed here to determine the individual stresses and displacements full-field in such a composite by processing a single measured component of displacement with a series representation of the Airy stress function. The circularly-perforated cellulosic-manure composite tensile plate was stress analyzed from a digital image correlation (DIC) recorded component of displacement. By combining the measured single component of displacement data with an Airy stress function,

displacement information in the other direction can be evaluated. Moreover, the full-field individual stress components were determined without differentiating the displacement data. The present results agree with those from thermoelastic stress analysis (TSA) [36], finite element analysis (FEM) and theory.

Digital image correlation is a relatively new but prevalently used optical method for recording displacements [40]. Advantages of DIC include the following: it is non-contacting and non-destructive; unlike thermoelastic stress analysis, it does not involve cyclic loading; it is applicable to actual structures without modeling, such as needed with traditional photoelasticity; unlike metal-foil strain gages, it is full-field; it benefits from the availability of commercial systems; and it is not restricted to a laboratory environment. DIC does require the surface of the structure under study to contain a speckle pattern for tracking. Like most experimental techniques, traditional DIC analyses suffers from an inability to record reliable information near and at the edges of geometric discontinuities. However, these locations are important because of associated stress concentrations. Traditional DIC, like other displacement-based methods, necessitates differentiating the recorded information to obtain strains and/or stresses. Purely analytical or numerical methods (finite elements, finite difference) also require knowing the external loading conditions; something which are often unknown in practice. Theoretical approaches tend to be limited to infinite, simple shapes.

Acknowledging the disadvantages of traditional experimental and numerical methods, this paper demonstrates the ability to determine the individual components of stress full-field and on the edge of a hole in a finite, cellulosic-manure composite plate by hybridizing DIC measured

displacement information with an Airy stress function. A particular advantage of the present hybrid approach is its ability to evaluate all of the Airy coefficients from measuring displacement data away from the geometric discontinuity with a reduced number of Airy coefficients by incorporating the traction-free conditions on the edge of the hole analytically. All components of strain and stress can be evaluated from the experimentally evaluated Airy coefficients without differentiating the displacements physically. Furthermore, rather than determining the elastic properties from separate test coupons, they are evaluated from recorded displacement data and force equilibrium.

Strain and stress determination from displacements typically necessitates knowing at least two components of displacement [10]. However, the present approach accomplishes this from recorded information of only a *single* displacement field. This is significant since one can encounter situations where the magnitude or quality of one of the measured in-plane displacement component data is inadequate. Having evaluated the Airy coefficients, the other (which is perhaps experimentally unavailable or inadequate) displacement component can be evaluated, along with all components of stress.

3.2 Experimental Setup and Details

Figure 3.2.1 is the image of the tested cellulosic manure composite specimen showing geometric representation. The specimen is analyzed using digital image correlation technique without knowing any material property prior to the experiment. The plate is 30.5 cm (12”) long, 6.2 cm (2.4”) wide, 0.72 cm (0.28”) thick and has a perforated hole of radius with 1.27 cm (0.5”) at the center. The identical specimen was used and discussed in Chapter 2.

In order to perform DIC test, a speckle pattern has to be applied to the surface of the plate as shown in figure 3.2.1, so the pixel locations of the unloaded plate then can be correlated with those of the loaded plate. The speckle pattern applied to the plate has to be random, exhibiting dark black and bright white and not biased in any one orientation in order to achieve effective correlation. The surface of the raw cellulosic manure composite was initially cleaned and polished using sandpaper and then Krylon Ultra-Flat black paint was applied on the surface to reduce the surface’s reflectiveness. Only one layer of the black paint was applied to minimize unnecessary effect due to the coating thickness such as changing the shape of the surface or increasing shear effects. When the black paint applied on the plate was completely dried, a white speckle pattern using Krylon Ultra-Flat white paint was sprayed onto the surface. This was accomplished by applying consistent pressure to the trigger of the commercial paint bottle container

After the applied speckle pattern of figure 3.2.1 had dried, the specimen was loaded using the MTS Sintech 10/GL screw driven test frame with a 10,000 lb load capacity. Figure 3.2.2 shows the speckle painted cellulosic manure composite plate clamped between the two grips of the MTS machine. When loading the specimen, particular attention was given to avoid any out-of-plane

bending and that was verified by recording three displacement components. The DIC test was performed as shown in figure 3.2.1 using two cameras for 3-Dimensional DIC test. When utilizing two cameras, a separate calibration grid (provided by Correlated Solution with the DIC package) was used to evaluate the displacement data in physical units rather than in pixels. The bottom cross head of the loading machine was fixed and the top cross head moved vertically and the applied static vertical tensile load ranged from 0 N to 500N (112 lbs) with 50N (11 lbs) load increment. At each load increment, digital images were captured simultaneously by the two DIC cameras and recorded using Correlated Solution's Vic Snap software. Subsequently, the recorded images were processed and correlated with Correlated Solution's Vic 3D software to evaluate the displacements for post-processing. Table 3.1 contains the technical information about the DIC system used.

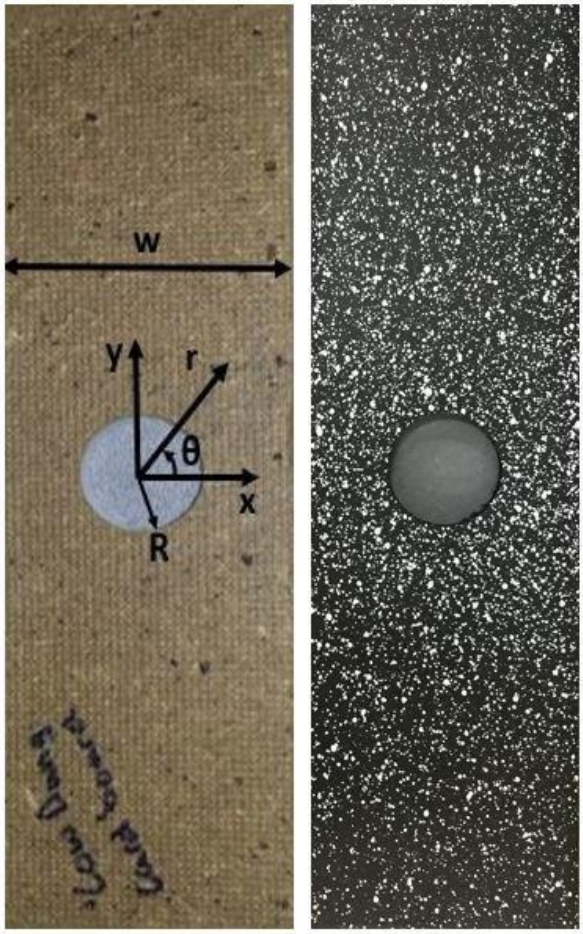

Figure 3.2.1: Perforated cellulosic-manure composite plate (*R* = 12.7 mm, *w* = 62 mm, *t* = 7.2 mm)

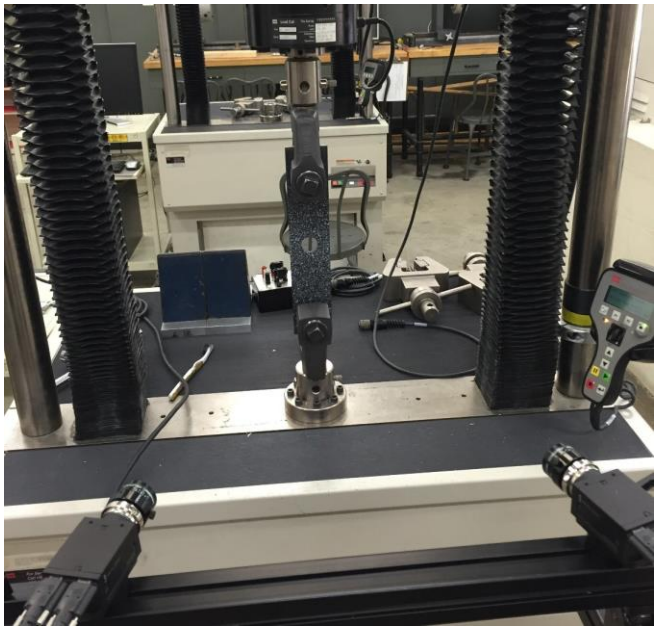

Figure 3.2.2: Specimen loading and DIC recording

Table 3.1: Technical information about the DIC equipment, set-up, and system

Parameter	Information
Technique	Stereo Image Correlation
Cameras*	The Grasshopper (Point Grey Research), Model GRAS-50S5M-C
Imaging sensor*	Sony ICX625 CCD, 2/3", 3.45 *u*m
Lens*	CM120 BK 15 COMPACT- 0901 (focal ratio: 1.9 and focal length: 35 mm)
Sensor/digitization	2448 × 2048 at 15 FPS
Lightening	Ambient white light
Pixel to inch conversion	1 pixel = 0.1 mm
Software*	Vic-Snap software
Subset, step	21,6
Strain Resolution	0.005% (50 microstrain)

* from Correlated Solutions, Inc., Columbia, SC, USA

Figure 3.2.3 shows an actual vertical displacement, *v*, of the specimen produced by Vic 3D software. Since the DIC software's correlation algorithm is unable to track a group of pixels and subsets that do not have any neighboring pixels, displacement information at and near the edge of the hole (the most interested region due to stress concentration factor) are unavailable. To perform the tracking, the subset is shifted until the pattern in the deformed image closely matches that of the reference image.

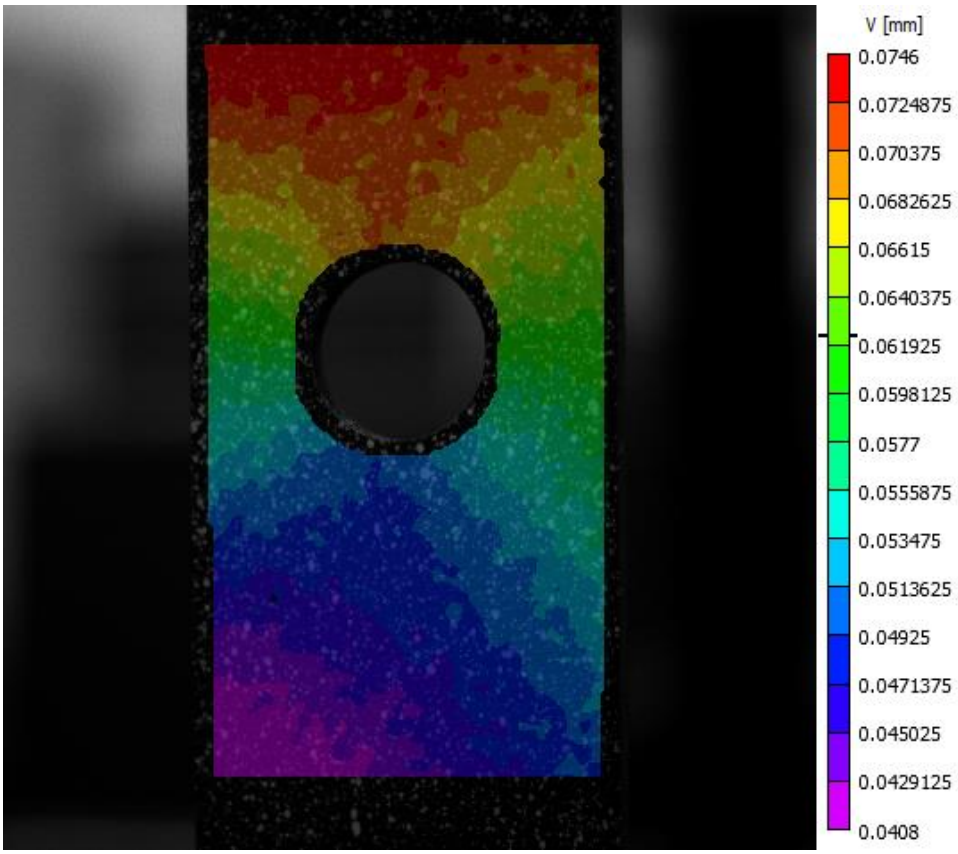

Figure 3.2.3: DIC recorded *v*-displacement data from Vic - 3D with 500 N

3.3 Relevant Equations

For a finite plate having symmetry with respect to both its *x*- and *y*-axes, and its coordinate origin within a cavity, figure 3.1.1, the Airy's stress function in polar coordinates satisfying the biharmonic equation, $\nabla^4 \Phi = 0$, equilibrium and compatibility can be written as [2, 68, 69],

$$\phi = a_0 + b_0 \cdot \ln r + c_0 \cdot r^2 + \sum_{n=2,4,6...}^{N} \left(a_n \cdot r^n + b_n \cdot r^{n+2} + c_n \cdot r^{-n} + d_n \cdot r^{-(n-2)} \right) \cdot \cos\left(n \cdot \theta\right) \qquad (3.1)$$

where r is the radial coordinated measured from the center of the cavity, angle θ is measured counterclockwise from the *x*-axis, figure 3.1.1, and N is the terminating index value of the series. It can be any positive even integer greater than zero.

Upon differentiating equation (3.1), individual stresses can be determined as follows:

$$\sigma_{rr} = \frac{1}{r} \cdot \frac{\partial \phi}{\partial r} + \frac{1}{r^2} \frac{\partial^2 \phi}{\partial \theta^2}$$

$$\sigma_{\theta\theta} = \frac{\partial^2 \phi}{\partial r^2} \qquad (3.2)$$

$$\sigma_{r\theta} = -\frac{\partial}{\partial r} \cdot \left(\frac{1}{r} \cdot \frac{\partial \phi}{\partial \theta} \right)$$

After imposing the traction-free condition of $\sigma_{rr} = \sigma_{r\theta} = 0$ on the edge of the hole of figure 3.1.1 analytically, expressions of the polar component of stresses are [69],

$$\sigma_{rr} = \frac{b_0}{r^2} + 2 \cdot c_0 - \sum_{n=2,4,6\ldots}^{N} \begin{bmatrix} a_n \cdot n \cdot (n-1) \cdot r^{(n-2)} \\ +b_n \cdot (n+1) \cdot (n-2) \cdot r^n \\ +c_n \cdot n \cdot (n+1) \cdot r^{-(n+2)} \\ +d_n \cdot (n-1) \cdot (n+2) \cdot r^{-n} \end{bmatrix} \cdot \cos(n \cdot \theta) \quad (3.3)$$

$$\sigma_{\theta\theta} = -\frac{b_0}{r^2} + 2 \cdot c_0 + \sum_{n=2,4,6\ldots}^{N} \begin{bmatrix} a_n \cdot n \cdot (n-1) \cdot r^{(n-2)} \\ +b_n \cdot (n+1) \cdot (n+2) \cdot r^n \\ +c_n \cdot n \cdot (n+1) \cdot r^{-(n+2)} \\ +d_n \cdot (n-1) \cdot (n-2) \cdot r^{-n} \end{bmatrix} \cdot \cos(n \cdot \theta) \quad (3.4)$$

$$\sigma_{r\theta} = \sum_{n=2,4,6\ldots}^{N} \begin{bmatrix} a_n \cdot n \cdot (n-1) \cdot r^{(n-2)} \\ +b_n \cdot n \cdot (n+1) \cdot r^n \\ -c_n \cdot n \cdot (n+1) \cdot r^{-(n+2)} \\ -d_n \cdot n \cdot (n-1) \cdot r^{-n} \end{bmatrix} \cdot \sin(n \cdot \theta) \quad (3.5)$$

Since DIC provides displacement information (not stresses like TSA), expressions for displacements have to be determined in terms of the Airy coefficients such that DIC measured displacements can be coupled with the analytical displacement Airy equations. From 2D Hooke's law of equation (3.6) and radial and tangential stress of equations (3.3) and (3.4),

$$\frac{\partial u_r}{\partial r} = \epsilon_{rr} = \frac{1}{E}(\sigma_{rr} - \nu\sigma_{\theta\theta}) \tag{3.6}$$

$$\epsilon_{rr} = \frac{\partial u_r}{\partial r} = \frac{1}{E}\left[-\sum_{n=2,4,6\ldots}^{N} \left\{ \begin{array}{c} \{-\frac{2R^2}{r^2}(1+\nu) + 2(1-\nu)\}c_0 \\ \left[\begin{array}{c} -(1+\nu)(n-1)(n+1)R^2 r^{n-2} \\ +(1+\nu)(n+1)R^{2(n+1)} r^{-(n+2)} \\ +(n+1)[(n-2)+\nu(n+2)]r^n \end{array} \right] b_n \\ + \left[\begin{array}{c} -(1+\nu)(n-1)R^{-2(n-1)} r^{n-2} \\ -(1+\nu)(n-1)(n+1)R^2 r^{-(n+2)} \\ +(n-1)[(n+2)+\nu(n-2)]r^{-n} \end{array} \right] d_n \end{array} \right\} \cos(n\theta) \right] \tag{3.7}$$

which upon integrating becomes,

$$u_r = \frac{1}{E}\left[-\sum_{n=2,4,6\ldots}^{N} \left\{ \begin{array}{c} \{\frac{2R^2}{r^2}(1+\nu) + 2(1-\nu)\}c_0 \\ \left[\begin{array}{c} -(1+\nu)(n+1)R^2 r^{n-1} \\ -(1+\nu)R^{2(n+1)} r^{-(n+1)} \\ +[(n-2)+\nu(n+2)]r^{n+1} \end{array} \right] b_n \\ + \left[\begin{array}{c} -(1+\nu)R^{-2(n-1)} r^{n-1} \\ +(1+\nu)(n-1)R^2 r^{-(n+1)} \\ -[(n+2)+\nu(n-2)]r^{-(n+1)} \end{array} \right] d_n \end{array} \right\} \cos(n\theta) + g(\theta) \right] \tag{3.8}$$

where, $g(\theta) = S_1 \cos\theta - S_2 \sin\theta$.

Similarly, from

$$\epsilon_{\theta\theta} = \frac{1}{E}(\sigma_{\theta\theta} - \nu\sigma_{rr}) \tag{3.9}$$

$$\epsilon_{\theta\theta} = \frac{1}{E}\left[\begin{array}{c} \{\frac{2R^2}{r^2}(1+\nu)+2(1-\nu)\}c_0 \\ +\sum_{n=2,4,6\ldots}^{N}\left\{\begin{array}{c}\left[\begin{array}{c}-(1+\nu)(n+1)(n-1)R^2r^{n-2}\\ +(1+\nu)(n+1)R^{2(n+1)}r^{-(n+2)}\\ +(n+1)[(n+2)+\nu(n-2)]r^n\end{array}\right]b_n \\ +\left[\begin{array}{c}-(1+\nu)(n-1)R^{-2(n-1)}r^{n-2}\\ -(1+\nu)(n-1)(n+1)R^2r^{-(n+2)}\\ +(n-1)[(n-2)+\nu(n+2)]r^{-n}\end{array}\right]d_n\end{array}\right\}\cos(n\theta)\end{array}\right] \tag{3.10}$$

Since [2]

$$\begin{aligned}&\frac{1}{r}\frac{\partial u_\theta}{\partial\theta} = \frac{1}{E}(\sigma_{\theta\theta}-\nu\sigma_{rr}) - \frac{u_r}{r} = \epsilon_{\theta\theta} - \frac{u_r}{r}\\ &\Rightarrow \frac{\partial u_\theta}{\partial\theta} = r.\epsilon_{\theta\theta} - u_r\end{aligned} \tag{3.11}$$

$$\frac{\partial u_\theta}{\partial\theta} = \frac{1}{E}\left[\sum_{n=2,4,6\ldots}^{N} n.\left\{\begin{array}{c}\left[\begin{array}{c}-(1+\nu)(n+1)R^2r^{n-1}\\ +(1+\nu)R^{2(n+1)}r^{-(n+1)}\\ +[n(1+\nu)+4]r^{n+1}\end{array}\right]b_n \\ +\left[\begin{array}{c}-(1+\nu)R^{-2(n-1)}r^{n-1}\\ +(1+\nu)(n-1)R^2r^{-(n+1)}\\ +[n(1+\nu)-4]r^{-(n+1)}\end{array}\right]d_n\end{array}\right\}\cos(n\theta)-g(\theta)\right] \tag{3.12}$$

Integrating equation (3.12) gives,

$$u_\theta = \frac{1}{E}\left[\sum_{n=2,4,6\ldots}^{N}\left\{\begin{array}{l}\left[\begin{array}{l}-(1+\nu)(n+1)R^2r^{n-1}\\+(1+\nu)R^{2(n+1)}r^{-(n+1)}\\+[n(1+\nu)+4]r^{n+1}\end{array}\right]b_n\\+\left[\begin{array}{l}-(1+\nu)R^{-2(n-1)}r^{n-1}\\-(1+\nu)(n-1)R^2r^{-(n+1)}\\+[n(1+\nu)-4]r^{-(n+1)}\end{array}\right]d_n\end{array}\right\}\sin(n\theta)\right.$$
$$\left.-S_1\sin\theta - S_2\cos\theta + R^*r\right] \qquad (3.13)$$

In addition to position (r, θ), the displacements given by equations (3.8) and (3.13) depend on the Airy coefficients c_0, b_n, and d_n. Quantities S_1 and S_2 represent rigid body translations and R^* represents a rigid body rotation. With the origin of the coordinate system at the center of the hole, figure 3.1.1, S_1, S_2 and R^* can be equated to zero for a physical plated loaded in a testing machine. With respect to figure 3.3.1, displacement equations (3.8) and (3.13) in polar coordinates can be transformed into Cartesian coordinate system since DIC data are in Cartesian system [71].

$$\begin{aligned} u &= u_\mathrm{r}\cos\theta - u_\theta\sin\theta \\ v &= u_r\sin\theta + u_\theta\cos\theta \end{aligned} \qquad (3.14)$$

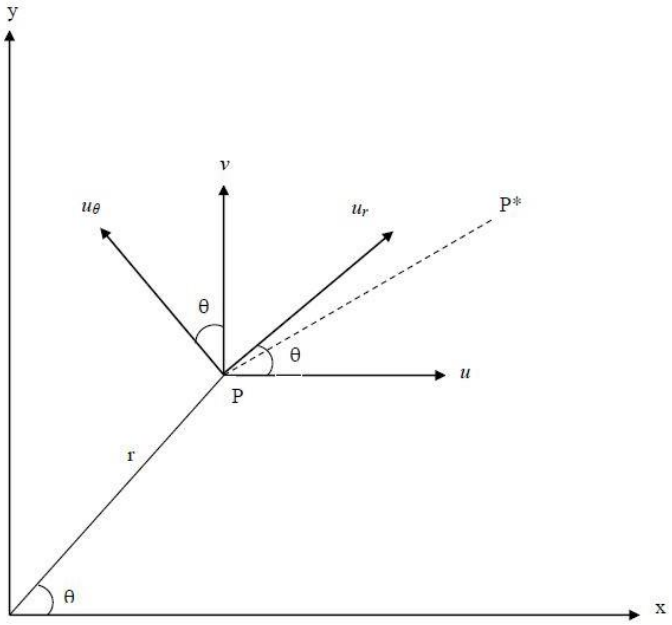

Figure 3.3.1: Displacement components, *u* and *v*, with respect to rectangular Cartesian coordinates (*x*,*y*) and u_r and u_θ with respect to polar coordinates (*r*, θ) when point *P* moves to *P

$$u = \frac{1}{E}\left[\begin{array}{c} \left\{\frac{2R^2}{r}(1+\nu) + 2(1-\nu)r\right\}\cos\theta \cdot c_0 \\ -\sum_{n=2,4,6\ldots}^{N} \left\{ \begin{array}{c} \left[\begin{array}{c} -(1+\nu)(n+1)R^2 \cdot r^{n-1}\cos\big((n-1)\theta\big) \\ -(1+\nu)R^{2(n+1)}r^{-(n+1)}\cos\big((n+1)\theta\big) \\ +\left(\begin{array}{c} (n(1+\nu)\cos\big((n-1)\theta\big) - 2\cos\big((n+1)\theta\big) \\ +2\nu\cos\theta\cos(n\theta) + 2\sin\theta\sin(n\theta) \end{array} \right) r^{n+1} \end{array} \right] b_n \\ + \left[\begin{array}{c} -(1+\nu)R^{-2(n-1)}r^{n-1}\cos\big((n-1)\theta\big) \\ +(1+\nu)(n-1)R^2 \cdot r^{-(n+1)}\cos\big((n+1)\theta\big) \\ -\left(\begin{array}{c} (n(1+\nu)\cos\big((n+1)\theta\big) + 2\cos\big((n-1)\theta\big) \\ -2\nu\cos\theta\cos(n\theta) + 2\sin\theta\sin(n\theta) \end{array} \right) r^{-n+1} \end{array} \right] d_n \end{array} \right\} \end{array} \right] \tag{3.15}$$

$$v = \frac{1}{E}\left[-\sum_{n=2,4,6\ldots}^{N} \left\{ \begin{bmatrix} \left\{\frac{2R^2}{r}(1+\nu) + 2(1-\nu)r\right\}\sin\theta \cdot c_0 \\ (1+\nu)(n+1)R^2 \cdot r^{n-1}\sin\big((n-1)\theta\big) \\ -(1+\nu)R^{2(n+1)}r^{-(n+1)}\sin\big((n+1)\theta\big) \\ -\begin{pmatrix} (n(1+\nu)\sin\big((n-1)\theta\big) + 2\sin\big((n+1)\theta\big) \\ -2\nu\sin\theta\cos(n\theta) + 2\cos\theta\sin(n\theta) \end{pmatrix} r^{n+1} \end{bmatrix} b_n \right. \right. \\ \left. \left. + \begin{bmatrix} (1+\nu)R^{-2(n-1)}r^{n-1}\sin\big((n-1)\theta\big) \\ +(1+\nu)(n-1)R^2 \cdot r^{-(n+1)}\sin\big((n+1)\theta\big) \\ +\begin{pmatrix} (-n(1+\nu)\sin\big((n+1)\theta\big) \\ +2\sin\big((n-1)\theta\big) \\ -2\nu\sin\theta\cos(n\theta) + 2\cos\theta\sin(n\theta) \end{pmatrix} r^{-n+1} \end{bmatrix} d_n \right\} \right] \tag{3.16}$$

Equations (3.15) and (3.16) illustrate that displacements u and v at any polar location $r = (x^2 + y^2)^{0.5}$ and $\theta = \tan^{-1}(y/x)$ are both functions of Airy coefficients c_0, b_n, and d_n. Having assembled the necessary equations, the measured DIC v-displacement data are equated to the analytical formulation of the vertical displacement in equation (3.16). Either displacement equations (u or v) can be used as they both contain all the necessary Airy coefficients. However only v-displacements from DIC is used as their magnitudes are higher than the u-displacements when the specimen is pulled in vertical direction. Equations derived here are valid for any traction-free, circularly perforated member which has mechanical and geometric symmetry about the x- and y-axes and whose coordinate origin is not within the material of the structure.

3.4 Data Reduction and Analysis

DIC measured vertical displacements at many locations throughout the recorded region were imported into MATLAB, figure 3.4.1. Because only the top cross head of the loading machine moves vertically, recorded displacement is unsymmetrical from top to bottom. The unsymmetrical data shown in figure 3.4.1 was converted to the symmetrical data using MATLAB, ie., made equivalent to both top and bottom grips moving vertically apart. Since the geometry and loading are symmetrical about both *x*- and *y*-axes, the so-modified *v*-displacement data were combined throughout the four quadrants into one quadrant as shown in figure 3.4.2. The image was then utilized to evaluate the Airy coefficient from equation (3.16). A total of $m = 6{,}719$ DIC recorded input values of *v*-displacement was utilized and the source locations are identified in figure 3.4.3. DIC VIC-3D software automatically eliminates the unreliable displacement data near the edge of a discontinuity where those locations are of most interest due to stress concentration factor.

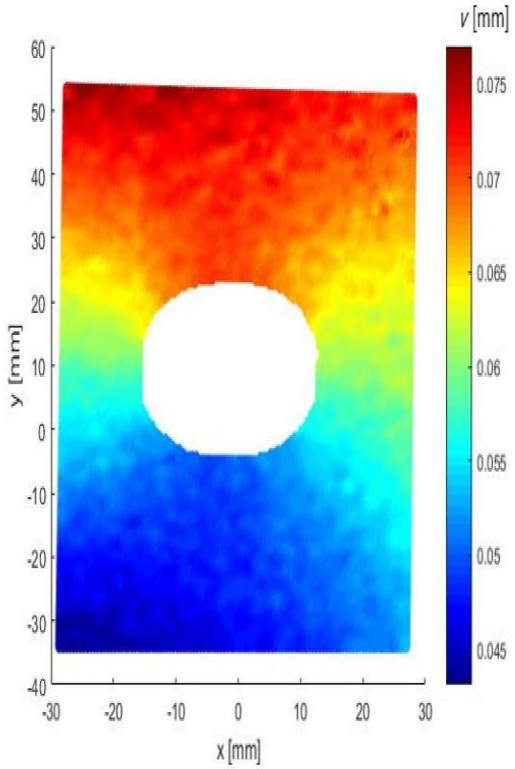

Figure 3.4.1: DIC recorded vertical displacement imported by MATLAB

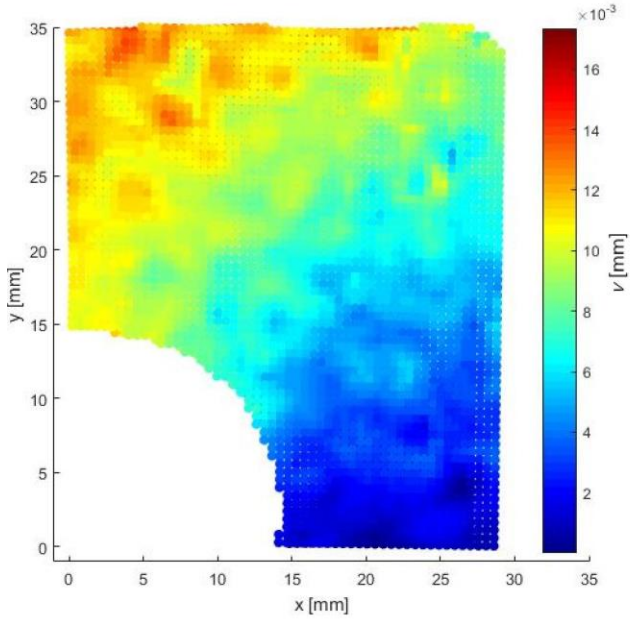

Figure 3.4.2: Vertical displacement image used with Airy stress function

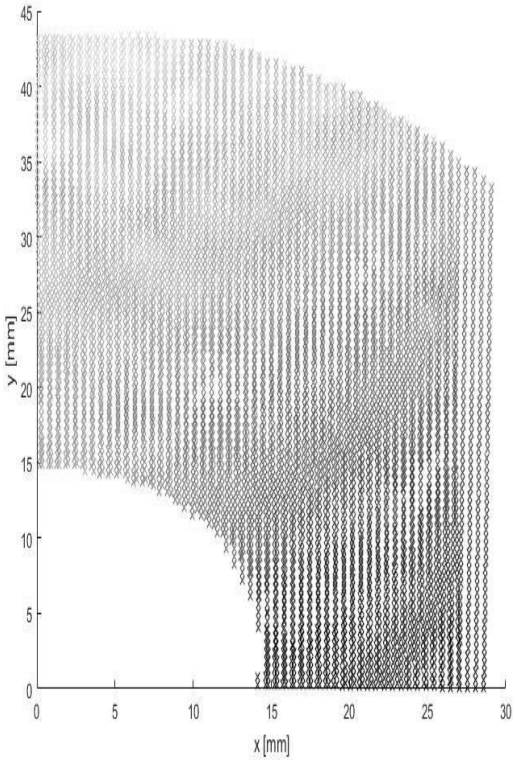

Figure 3.4.3: DIC source locations for *m* = 6, 719 input values

Once the DIC displacement data were acquired, a linear matrix equation $Ac = d$ of equations (3.17) and (3.18) can be formed. Where matrix [A] consists of m Airy v-displacement expressions of the form of equation (3.16), vector $\{c\}$ contains the k unknown Airy coefficients (c_0, b_n, d_n) and vector $\{d\}$ contains the measured DIC v- displacements. There are more equations than the number of unknown, i.e., $m > k$, so equation (3.18) was solved by least-squares using the '\'matrix division operator in MATLAB 2016 (MathWorks, Natick, MA, USA).

$$\begin{bmatrix} v_1(c_0, b_2, d_2, b_4, d_4 \cdots\cdots b_N, d_N) \\ v_2(c_0, b_2, d_2, b_4, d_4 \cdots\cdots b_N, d_N) \\ \vdots \\ \vdots \\ \vdots \\ v_m(c_0, b_2, d_2, b_4, d_4 \cdots\cdots b_N, d_N) \end{bmatrix}_{m\times k} \begin{bmatrix} c_0 \\ b_2 \\ d_2 \\ \vdots \\ b_N \\ d_N \end{bmatrix}_{k\times 1} = \begin{bmatrix} v_1 \\ v_2 \\ v_3 \\ \vdots \\ \vdots \\ v_m \end{bmatrix}_{m\times 1} \tag{3.17}$$

or, in simplified form,

$$[A]_{m\times k}\{c\}_{k\times 1} = \{d\}_{m\times 1} \tag{3.18}$$

When the analysis involves a series representation, the question arises as how many coefficients, *k*, to retain in the series. The number of Airy coefficients to retain was assessed by computing condition number of the matrix [*A*] and the root mean squares (*RMS*) for a series of different number of Airy coefficients. With the value of condition number *C* known, accuracy of the calculations can be approximately determined by identifying how many decimal places are lost during the calculation. The *RMS*, which represents the discrepancy between the calculated vertical displacement data, $\{d'\}$, and measured DIC *v*-displacement data, $\{d\}$. Figures 3.4.4 through 3.4.5 plot the condition number, *C*, logarithm of *C* and *RMS* versus the number of Airy coefficients, *k*, respectively. As can be seen from figures 3.4.4 and 3.4.5, condition number becomes greater as *k* increases, so choosing the smallest possible number of *k* would increase accuracy of the calculation. Figure 3.4.6 indicates that $k = 3$, 5, and 7 would result in less discrepancy whereas $k = 5$ gives the smallest *RMS*. Thus, using $k = 5$ as the number of coefficients would be reasonable.

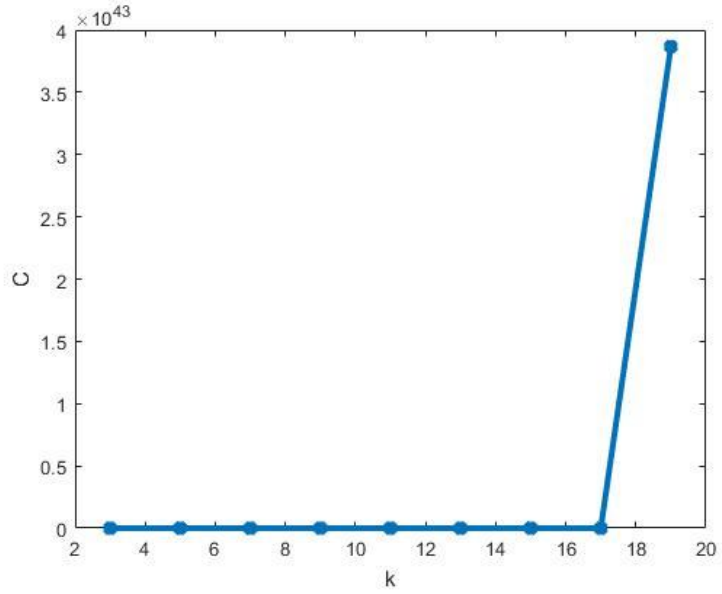

Figure 3.4.4: Condition number, *C*, vs. number of coefficients, *k*, for *m* = 6,719 input values

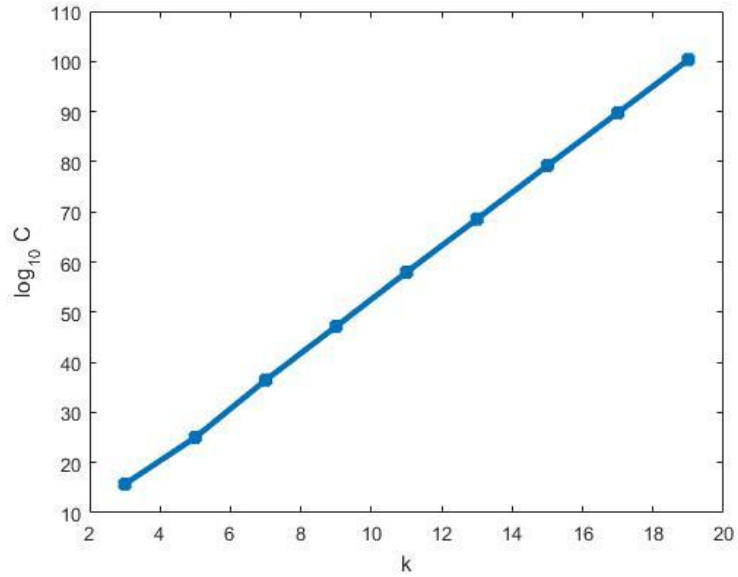

Figure 3.4.5: $\text{Log}_{10}(C)$ vs. number of coefficients, *k*, for *m* = 6,719 input values

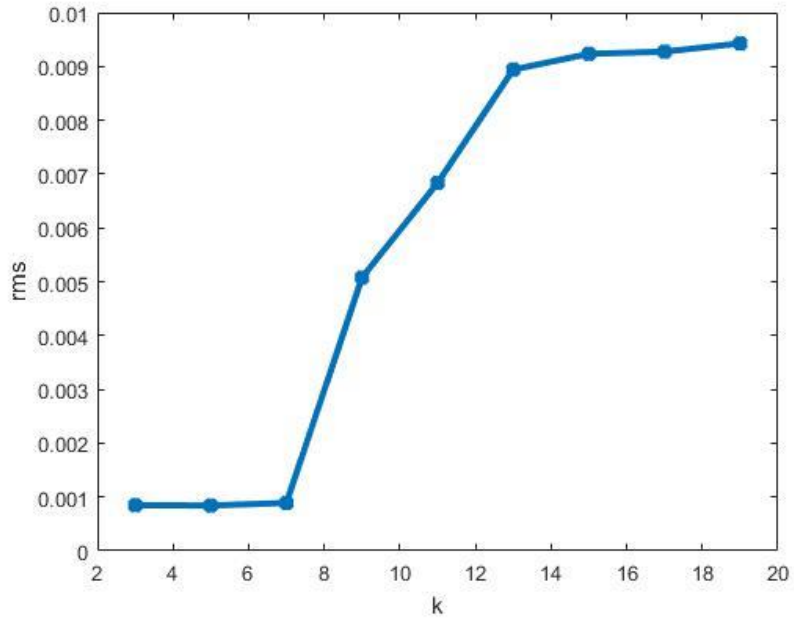

Figure 3.4.6: *RMS* of vertical displacement vs. number of coefficients, *k*, for *m* = 6,719 input values

Solving the overdetermined equation (3.17) with $k = 5$ evaluates all of the Airy coefficient existing in the stress, strain and displacement expressions, equations (3.3) through (3.16). However, matrix $[A]$ requires the values of the Youngs modulus, E, and Poisson ratio, v. These were not well-known, a priori, for this particular cellulosic-manure composite. These quantities were consequently evaluated iteratively using the load equilibrium expression of equation (3.19) where t and w are the plate thickness and width, respectively.

$$F = \int \sigma_{yy} dA = 2 \int_{x}^{w/2} \sigma_{yy} t \, dx \tag{3.19}$$

Taking $v = 0.25$ initially, sets of the Airy coefficients were evaluated iteratively based on 3 GPa $\leq$ E $\leq$ 6 GPa and σ_{yy} of equation (2.17) multiplied by the thickness, and integrated

numerically over the width of the plate, as in equation (3.19). This was done for several different horizontal lines in figure 3.2.1. The vertical stress of equation (2.17) along these horizontal lines was summed by integrating a 5th order polynomial with MATLAB that represents discrete individual values of stress. Figure 3.4.7 is a plot of the total force calculated on these various horizontal lines (from $y = 0$ to 21 mm) for several candidate values of E between 3 and 6 GPa (and $v = 0.25$). Table 3.2 contains the associated average values of the force calculated. Solving the Airy matrix of equation (3.18) with E = 4.8 GPa and $v = 0.25$ satisfies the load equilibrium for the physically applied vertical load of 500 N. The effect of variations in Poisson ratio, v, was also studied. Table 3.3 shows the average values of the computed force for Poisson ratio from 0.2 to 0.4. The effect of these changes in v is negligible. Based on the results of tables 3.2 and 3.3, E = 4.8 GPa and $v = 0.25$ are realistic values by which to relate stress and strain in this material.

Table 3.2: Average force, F, calculated for various values of Young's modulus, E, and assumed $v = 0.25$

E(GPa)	3.0	3.5	4.0	4.5	4.8	5.0	5.5	6.0
F(N)	308.8	360.2	411.8	463.2	494.0	515.8	566.2	617.6

Table 3.3: Average force, F, calculated with various values of Poisson's ratio, v

E(GPa)	0.2	0.25	0.3	0.4
F(N)	493.8	494.0	494.0	493.8

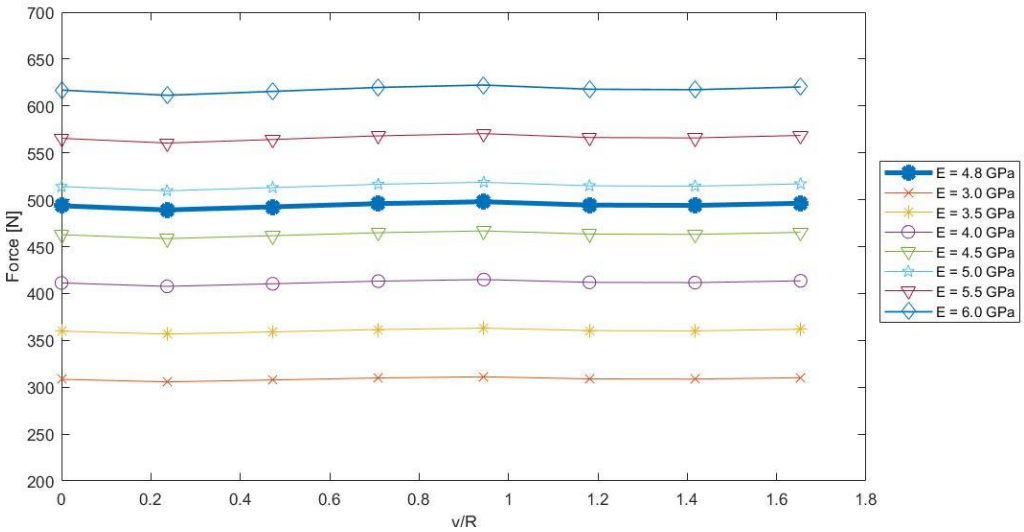

Figure 3.4.7: Forces on each horizontal lines of *y*-axes with different Young's modulus

With the now-determined Young's modulus and Poisson's ratio, vertical displacements are reconstructed with different number of k for the validation purpose in figure 3.4.8. Images of the Airy coefficients k =3, 5, and 7 are fairly uniform with each other and comparable to the experimental data of figure 3.4.2. The image with k = 9, however, is distinctively different from other images. The measured data incorporate some noise and does not provide data near and neighborhood on the edge of the hole as can be seen from figure 3.4.8. The reconstructed images provide smooth contours, free of noise, and most importantly, provide the results right at the edge of the hole.

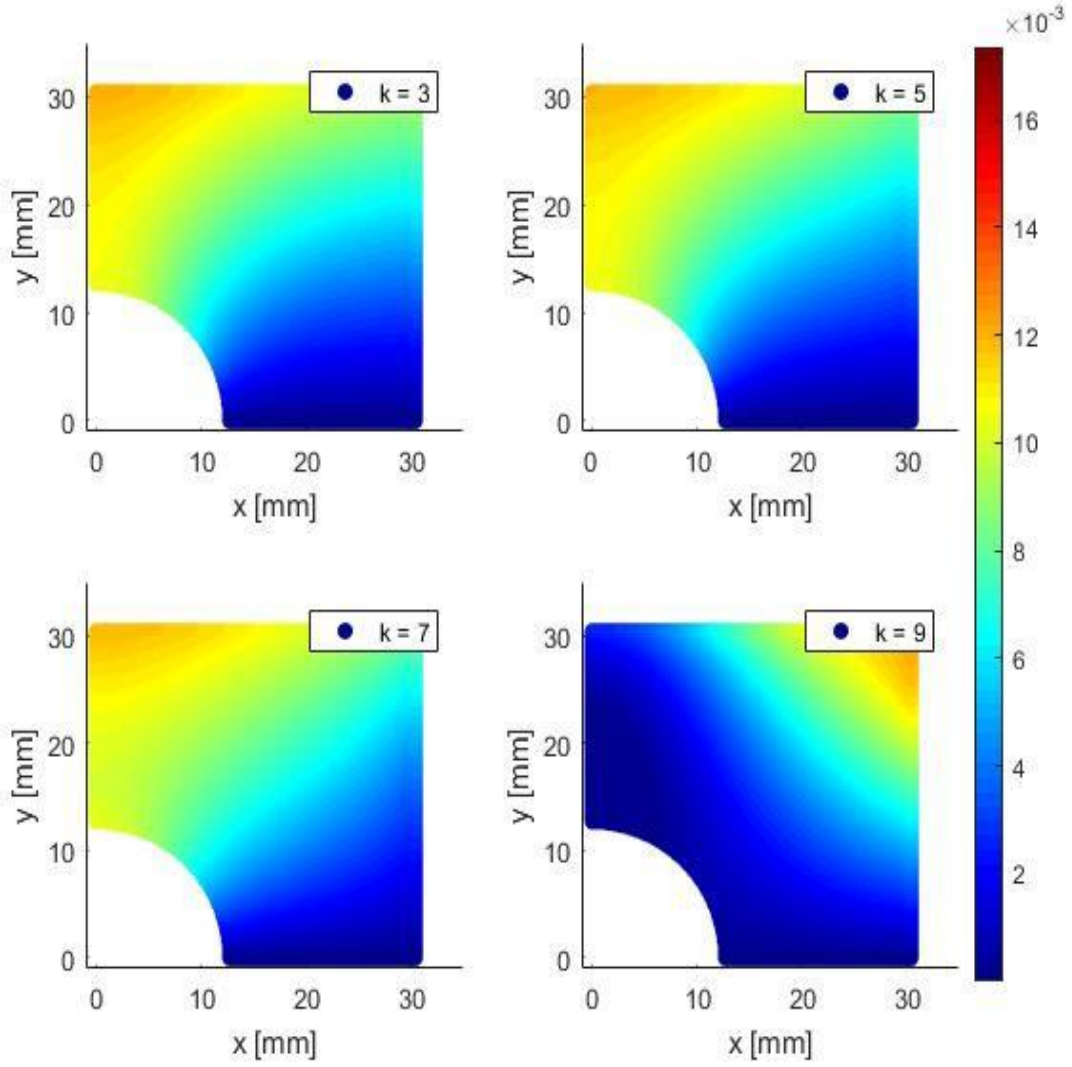

Figure 3.4.8: Comparison of reconstructed vertical displacement images using *k*= 3, 5, 7, and 9

3.5 Finnie Element Analysis

An FEA of the perforated cellulosic-manure composite plate (E = 4.8 GPa, $\nu = 0.25$) was conducted with which to compare the DIC results. Isoparametric elements (ANSYS element type: Plane-82), which have eight nodes per element, were employed. Symmetrical boundary conditions were imposed on the quarter-plate model and a far-field stress, σ_0 = 1.12 MPa (162.4 psi) was applied on the top of the plate. This far-field vertical stress is based on the total applied load of 500 N and the uniform cross-sectional area of the entire plate. A very fine mesh was used around the hole to ensure numerical reliability. The quarter FE model utilized 7,500 elements and 7701 nodes. ANSYS results did not vary by more than 2% with subsequent mesh reduction. The coordinate values for all nodes in the mesh were imported into MATLAB for further analysis and processing.

3.6 Results and Validation

The Hybrid-DIC results obtained from substituting the now-known 5 Airy coefficients into the stress and displacement expressions of equations (3.3) through (3.16) are compared with those predicted from finite element analysis (FEA).

Figure 3.6.1 contains images of vertical displacement of DIC measured, Hybrid- DIC method with now-known Airy coefficients, and ANSYS, respectively. Hybrid- DIC method is based on 6,719 DIC measured vertical displacement values and calculated by equation (3.16) with $k = 5$ evaluated Airy coefficients. The vertical displacement images are plotted on the actual coordinates recorded by DIC for the comparison.

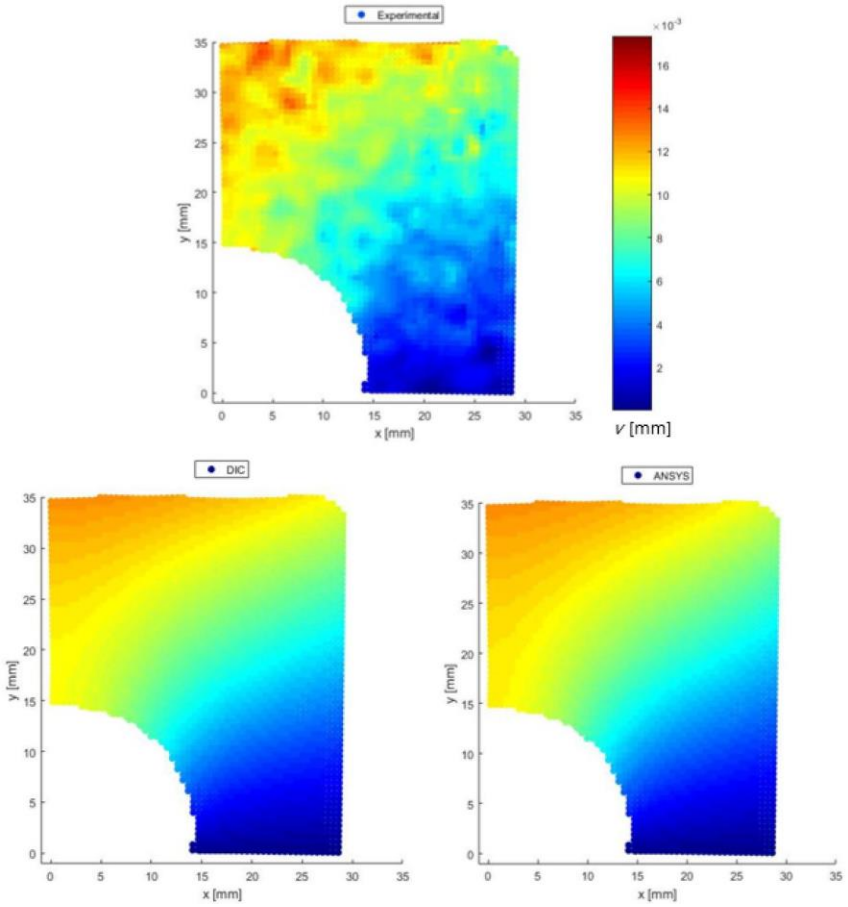

Figure 3.6.1: Contour plots of vertical displacements on DIC-recorded coordinates

Figure 3.6.2 plots the normalized tangential stresses for ANSYS and Hybrid- DIC method along the edge of hole. Normalized stresses are based on the far-field stress (1.12 MPa) and equation (3.4) is used for the tangential stress with the 5 Airy coefficients determined. Stress concentration factor, K_t, of Hybrid-DIC method is evaluated to be 3.61 and compares with that of 3.77 of ANSYS, 3.77 of Young and Budynas [70] and 3.63 of TSA-determined [36].

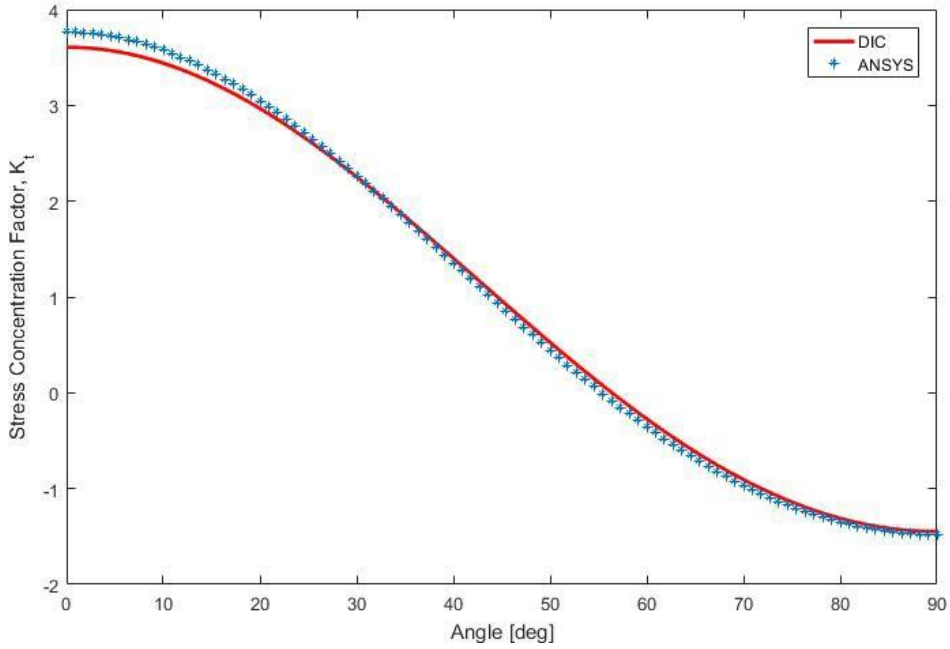

Figure 3.6.2: Normalized tangential stress $\sigma_{\theta\theta}/\sigma_0$ along edge of the hole

Figures 3.6.3 and 3.6.4 compare vertical (v) and horizontal(u) displacement prediction by ANSYS and Hybrid-DIC method. Equations (3.16) and (3.15) with the 5 Airy coefficients were utilized for the Hybrid-DIC method. Even though only the recorded vertical displacement data were utilized to determine the Airy coefficients, the reconstructed horizontal image is comparable to that by ANSYS.

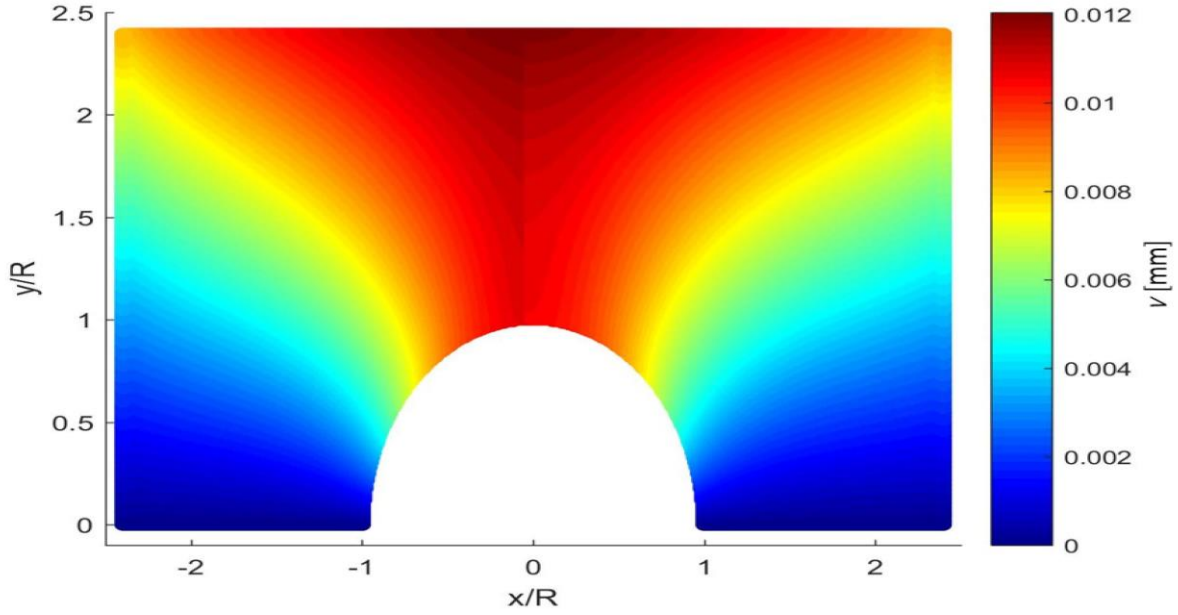

Figure 3.6.3: Contour plot of *v*-displacement for ANSYS (left) and Hybrid-DIC (right)

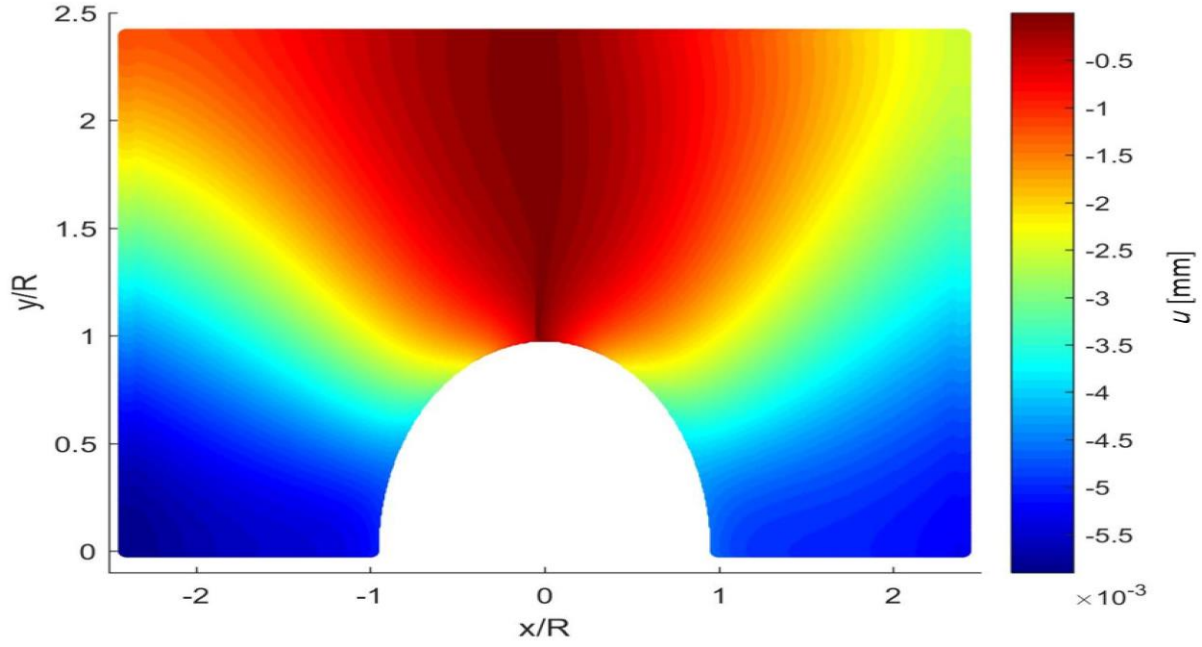

Figure 3.6.4: Contour plot of *u*-displacement for ANSYS (left) and Hybrid-DIC (right)

Figures 3.6.5 through 3.6.10 compare contour plots of normalized full-field stresses predicted by ANSYS and the Hybrid-DIC method. Equations (3.3) through (3.5) are utilized for polar component while equations (2.16) through (2.17) are utilized for rectangular component of stresses.

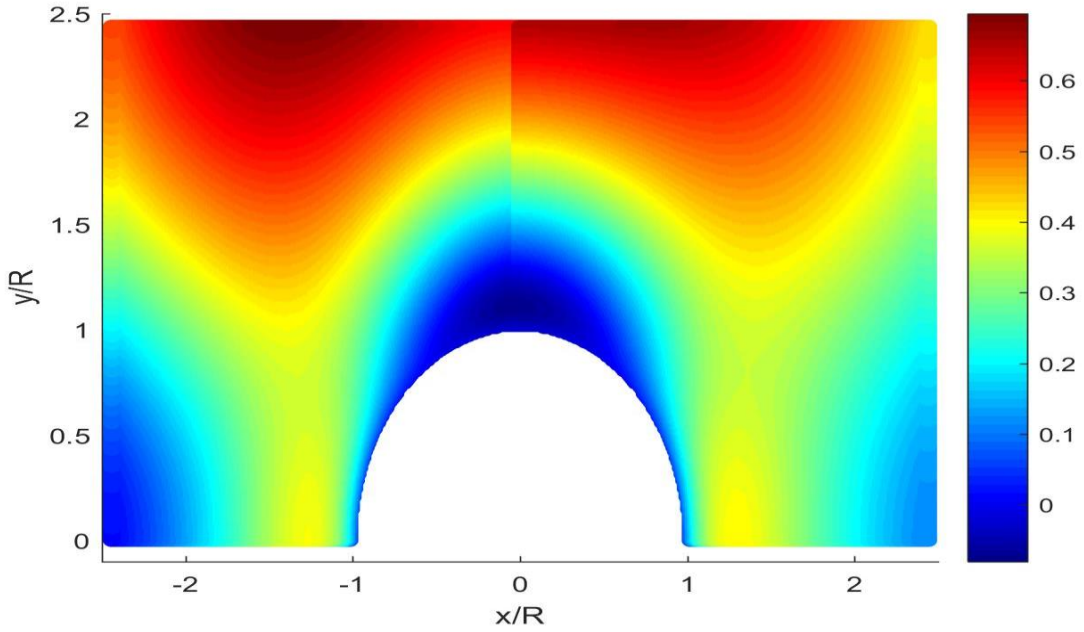

Figure 3.6.5: Contour plot of σ_{rr}/σ_0 for ANSYS (left) and Hybrid-DIC (right)

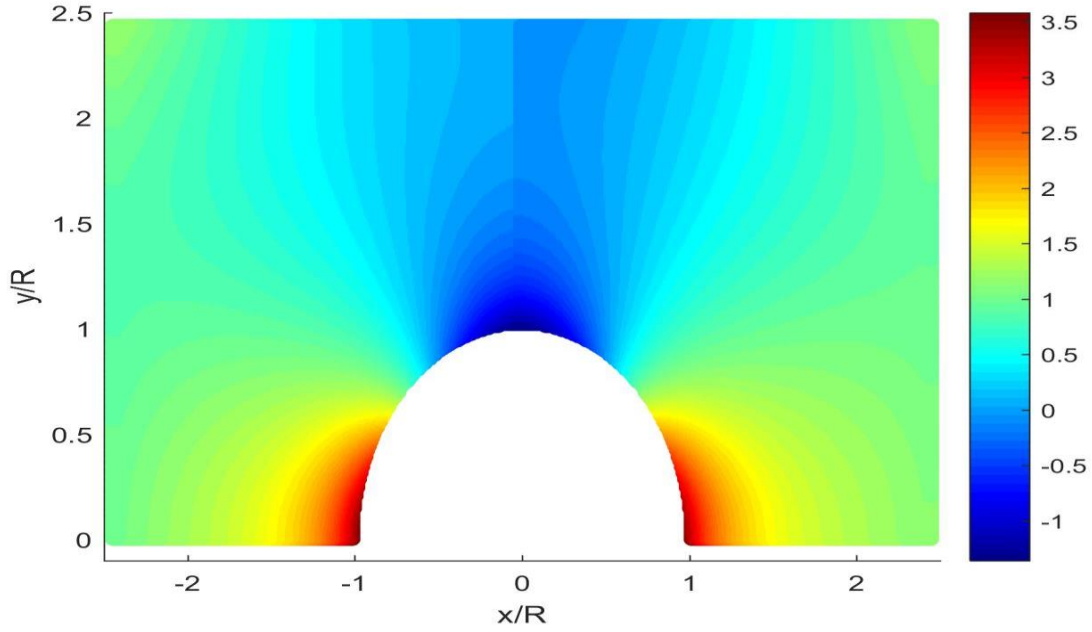

Figure 3.6.6: Contour plot of $\sigma_{\theta\theta}/\sigma_0$ for ANSYS (left) and Hybrid-DIC (right)

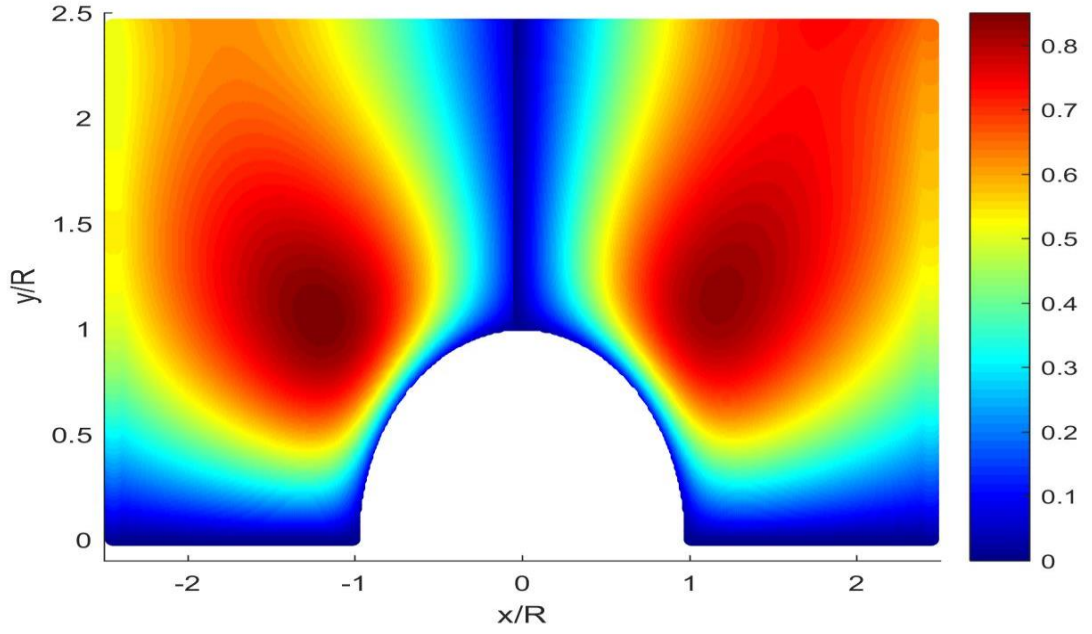

Figure 3.6.7: Contour plot of $\sigma_{r\theta}/\sigma_0$ for ANSYS (left) and Hybrid-DIC (right)

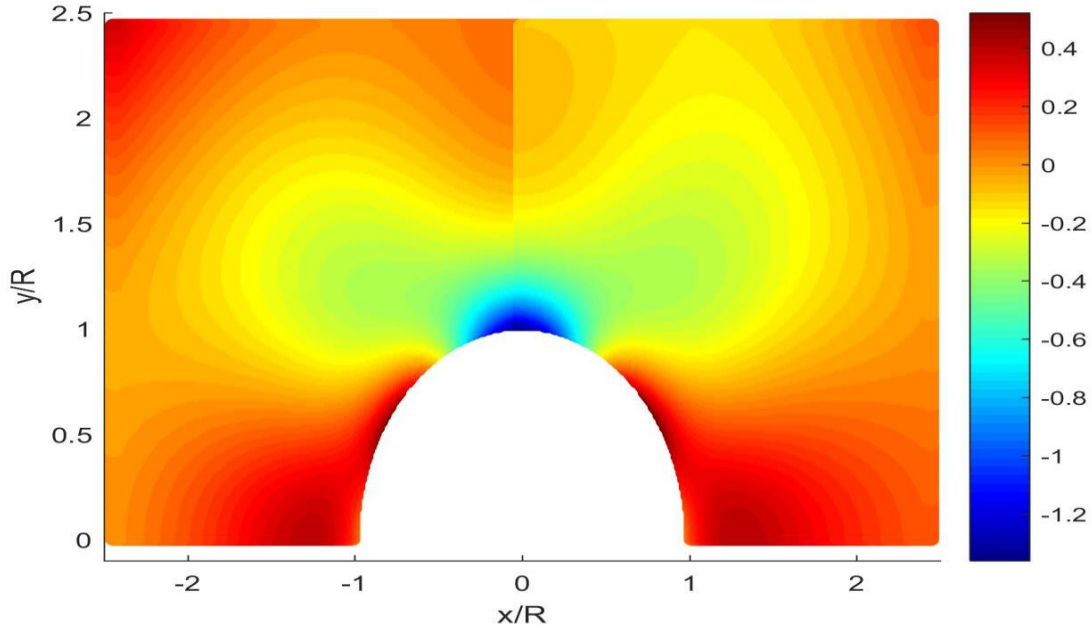

Figure 3.6.8: Contour plot of σ_{xx}/σ_0 for ANSYS (left) and Hybrid-DIC (right)

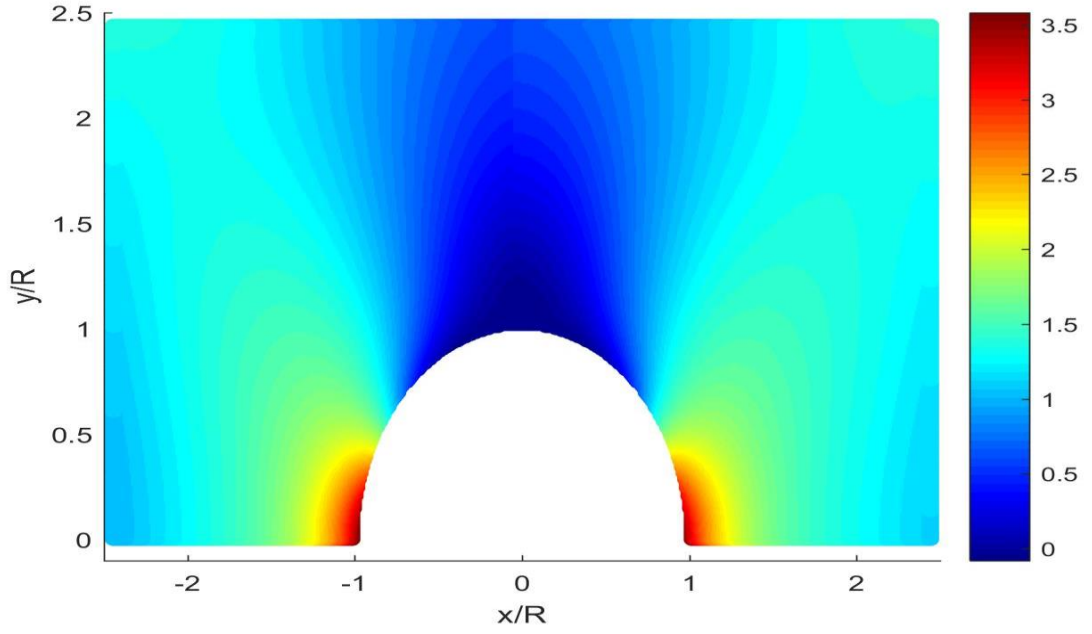

Figure 3.6.9: Contour plot of σ_{yy}/σ_0 for ANSYS (left) and Hybrid-DIC (right)

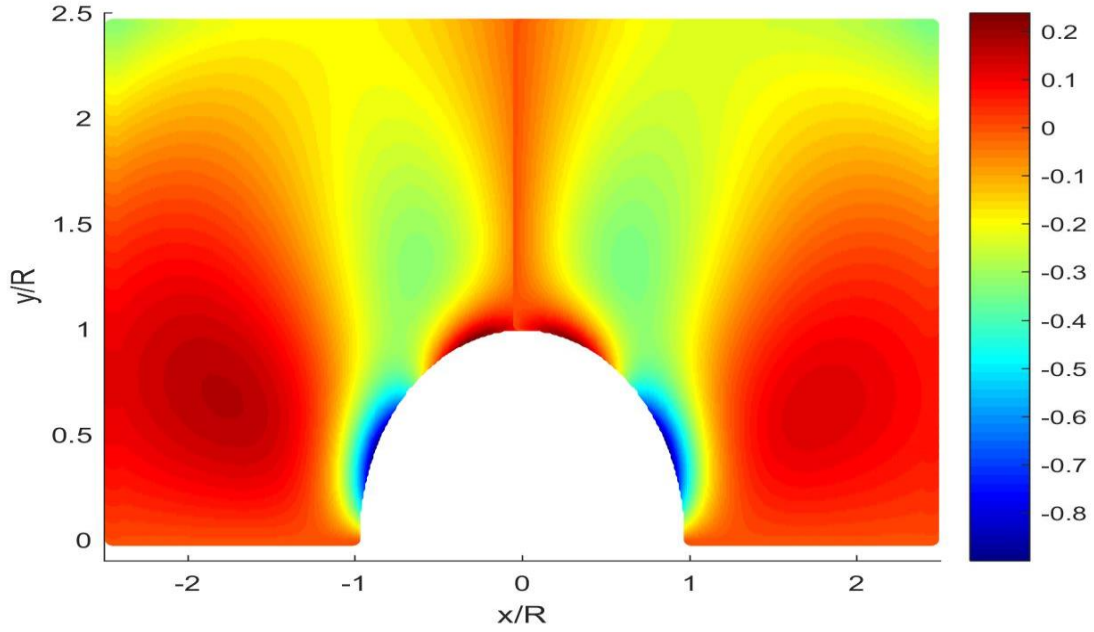

Figure 3.6.10: Contour plot of σ_{xy}/σ_0 for ANSYS (left) and Hybrid-DIC (right)

3.7 Summary

Motivated by the interest in processing troubling agricultural by-products into value-added components, and the associated need to assess their mechanical integrity, this chapter describes the ability to determine stresses in a perforated structure of the material from measured displacement data. The individual stresses on and near the edge of a circular hole in a cellulosic-biowaste composite plate are determined by synergizing the DIC-recorded displacement data with analytical/numerical tools. In addition to the cellulosic-manure composite being an innovative, but highly viable engineering material, the authors are unaware of previous in-situ determination of the constitutive properties without needing experimental stress, strain or displacement data, or applications of DIC to structural components involving such agro/green composites. Present results agree with those from thermoelastic stress analysis, finite element analysis and theory.

This initial photomechanical stress analysis of a cellulosic-manure material intentionally involves a simple geometry and loading. One can build on this experience to address much more complicated cases of cellulosic-based natural composites such as involving large, nonlinear response or highly complicated shapes or loading. DIC-recorded displacements information data could continue under such circumstances to be differentiated into strains, and the stresses obtained from an appropriate stress-strain relationship. Evaluated strains or stresses can be combined with a failure theory to predict structural strength, and present aspects can be used to analyze laminate performance. Unlike with the current relatively simple geometry, imposing boundary conditions for complicated shapes can be done discretely and/or using complex-variable techniques.

Chapter 4. Thermoelastically Determined Individual Stresses in a Deep-Notched Tensile Plate

Abstract

Individual stresses in, and on the edges of, a single deep U-notch in a simply-connected tensile plate, are determined by combining stress-induced thermal information with an Airy stress function. Unlike earlier cases of processing measured data with a stress function, the most convenient coordinate origin lies outside the structure/material. Contrary to published information indicating one should be able to omit many of the coefficients, some of the Airy coefficients cannot be assumed to be zero. Present results are supported by those from FEM, force equilibrium and strain gage data.

4.1 Introduction

Individual stresses are determined experimentally in a finite, tensile loaded aluminum plate containing a single-sided deep U-notch from recorded load-induced thermal information. Under elastic, reversible and adiabatic conditions, the cyclic loading produces an in-phase temperature variation which is linearly proportional to local changes in the normal stresses. As fatigue or strength analyses necessitate knowing the individual components of stress, supplementary experimental methods or measured information are frequently required to separate the stresses. This need is circumvented here in that individual stresses are evaluated throughout the loaded plate without supplementary measured data. Processing the measured thermal data with an Airy stress function and some local known stress conditions simultaneously smooths the measured data, separates the stress components, and evaluates the individual stresses full-field, including at the root of the U-notch (location of highest tensile stress). The present hybrid technique does not presuppose knowledge of the external loading conditions and overcomes the traditional difficulties of erroneous edge data. Reliability of the present results is demonstrated by those from finite elements and strain gage.

The high stresses associated with abrupt geometric discontinuities can significantly influence structural integrity. Traditional experimental approaches such as conventional thermoelastic stress analysis (TSA) do not provide the separate components of stress. However, combining (or hybridizing) experimental information with analytical and numerical tools enables one to overcome the aforementioned challenge. The analytical ingredient of this hybrid approach consists of using the Airy stress function which is based on the sound mechanics foundations of

compatibility and equilibrium. The hybrid approach is applicable to different complicated shapes, various complex loading conditions and inverse problems. The present technique does not presuppose knowledge of the external loading conditions and overcomes the traditional difficulties of unreliable edge data. Particular attention is paid here to determining a realistic number of unknown Airy coefficients. Other candidate experimental approaches include moiré, speckle, holography, grids and digital image correlation. Such displacement-based techniques necessitate differentiating the recorded data (which can be highly unreliable) and require knowing the constitutive material properties to get stresses. On the other hand, thermoelastic stress analysis (TSA) provides the stresses directly without having to differentiate the measured information. The deficiencies of FEA and analytical approaches when attempting to replicate the actual loading conditions motivate use of full-field hybrid experimental-numerical-analytical approach to determine the full-field stresses in continuous form and provide accurate results at the edges of the U-notch. Very few analytical solutions are available for finite geometries and both analytical and numerical techniques require knowing the external loading. The latter is often unknown in practice. Interest in deep side notches is motivated by the fact that such situations can readily initiate a local crack.

A major contribution of this chapter is the demonstrated ability to combine experimental, numerical and analytical techniques for the full-field determination of the separate components of stresses at and in the neighborhood of the U-notch. The most convenient coordinate origin lies outside the structure/material. Notwithstanding the current symmetry, and contrary to previous literature which indicates one should be able to omit many of the coefficients, some of the Airy coefficients cannot assumed here to be zero.

Having first substantiated the numerical stability, reliability and robustness of the least-squares hybrid method using 'simulated' thermoelastic input data from ANSYS, the method is then applied to an actual loaded finite aluminum plate having a single deep U-notch using measured thermal information, figure 4.1.1. Dimensions of the specimen were chosen to ensure essentially plane-stress at the root of the notch (Appendix A4.1). TSA assumes plane stress. The author is unaware of prior utilization of Airy stress function to experimentally evaluate the individual stresses in a loaded material with U-notch using recorded load-induced thermal information. The published literature contains information on double-edged notches, but very little appears to be available for single-edged deep notches.

This study extends the thermoelastic technique into a practical quantitative tool for stress analyzing actual complicated shaped engineering structures in their operating environment. This is accomplished by combining thermoelastic stress analysis (TSA) with an Airy stress function along with discretely imposing local traction-free boundary conditions on the edge of the U-notch and outer free edges of the plate. In view of previously mentioned disadvantages of the FEA, analytical and traditional experimental approaches, this chapter demonstrate the ability to determine the separate components of stress in a finite plate by processing recorded thermal information with an Airy stress function. The present U-shaped notched plate is a simply connected structure. The most convenient location for the coordinate origin of the representing polynomial of the stress function is at the center of the circular end of the notch, i.e., outside of the structure. The author is unaware of any previously published stress function analysis where the coordinate origin lies beyond the boundary of a simply-connected geometry. Resolving this challenge, although it involved numerous ineffective attempts, is significant.

The measured TSA data were digitalized in a matrix form for subsequent processing. The unknown Airy coefficients were determined from the recorded thermal information using least-squares. Although the recorded thermoelastic data at, and near, the edges are unreliable and raw thermoelastic information is inherently noisy, the present technique overcomes these challenges by avoiding the use of recorded data on and near edges and processing the measured interior data with the stress function. Such a technique simultaneously enhances reliability of thermoelastic edge information, smooths the interior measured information, separates the stresses into their three components and evaluates the non-zero stresses along the traction-free boundary (determining stress concentration) without knowing the external loading or material constitutive properties. Because of the previously mentioned scatter in recorded TSA data, it is customary to employ more known quantities (measured thermal data plus known local boundary conditions) than the number of unknown Airy coefficients, and to evaluate the latter using linear least-squares. The resulting TSA-determined stresses are available here on and in the neighborhood of the edge of the notch without knowing the external loading conditions.

All physical stresses are normalized throughout this chapter by applied load over the gross area, i.e., σ_0 = 2670 N / [(88.7 mm) (6.35 mm)] = 4.9 MPa = 715.3 psi.

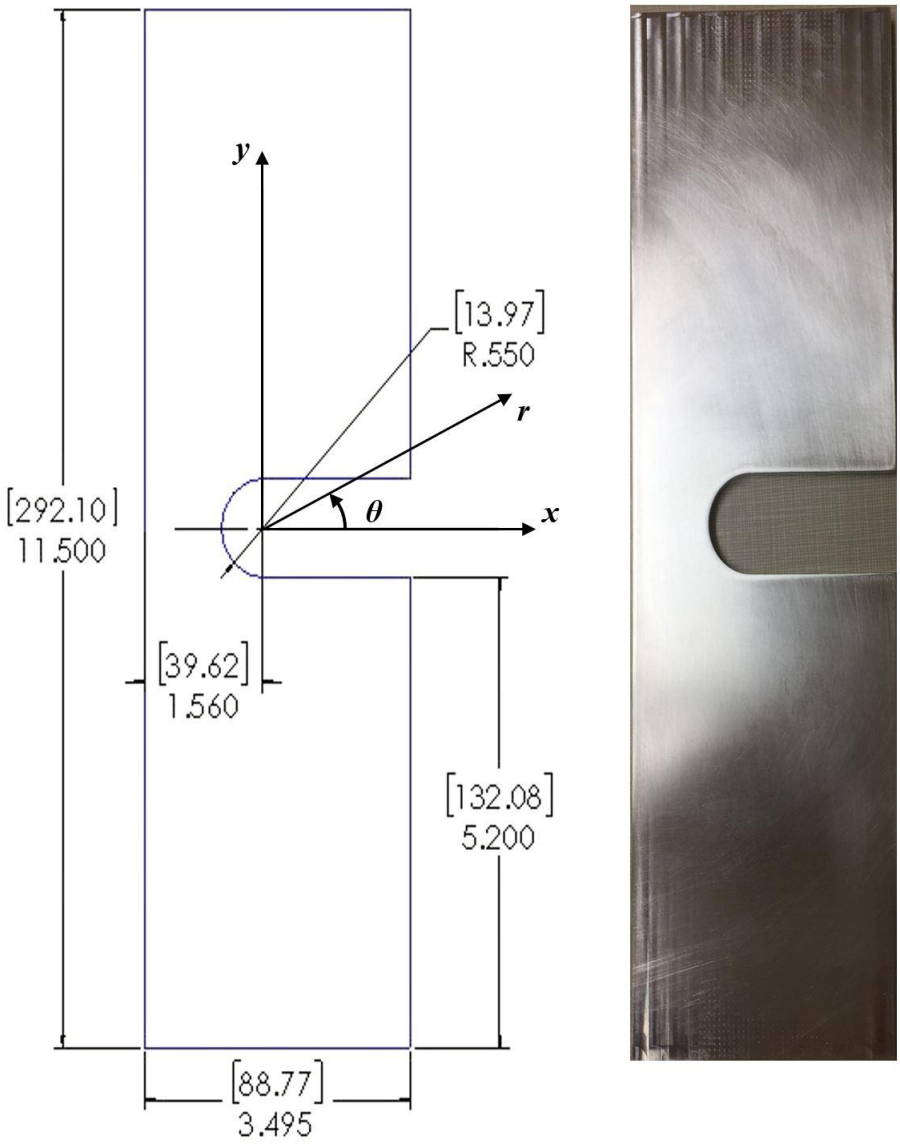

Figure 4.1.1: Plate geometry and dimension (thickness = 6.35 mm = 0.25 inches)

4.2 Related Literature

The author is not aware of any published experimental determination of the individual stresses throughout such a geometry as the present. Related articles include recorded isochromatic fringe patterns around a deep notch [72], analytical investigations of blunt cracks [73, 74], Bowie and Neal's theoretical study of an edge notch in a semi-infinite tensile sheet [75] and References [70, 76, 77] and [78]. Reference [77] involves moiré. Reference [78] applies TSA to a deep notch, but it emphasizes determining the stress concentration factor and does not evaluate individual stresses.

4.3 Relevant Equations

4.3.1. Stresses

The method behind determining the stresses at and in the neighborhood of the notch involves coupling the Airy stress function with the measured thermoelastic stress data and imposing boundary conditions. In isotropic materials and absent body forces, the Airy stress function, Φ, satisfying stress equilibrium and strain compatibility gives the biharmonic equation $\bigtriangledown^4\Phi = 0$. The general solution to the biharmonic equation in polar coordinates is [2]

$$\begin{aligned}\phi =& a_0 + b_0 \ln r + c_0 r^2 + d_0 r^2 \ln r + (A_0 + B_0 \ln r + C_0 r^2 + D_0 r^2 \ln r)\theta \\ &+ (a_1' r + b_1' r \ln r + \frac{c_1'}{r} + d_1' r^3)\cos\theta + (a_1 r + b_1 r \ln r + \frac{c_1}{r} + d_1 r^3)\sin\theta \\ &+ (A_1' + B_1' r \ln r)\theta\cos\theta + (A_1 r + B_1 r \ln r)\theta \sin\theta \\ &+ \sum_{n=2,3,\ldots}^{N} (a_n' r^n + b_n' r^{n+2} + c_n' r^{-n} + d_n' r^{2-n})\cos(n\theta) \\ &+ \sum_{n=2,3,\ldots}^{N} (a_n r^n + b_n r^{n+2} + c_n r^{-n} + d_n r^{2-n})\sin(n\theta)\end{aligned} \tag{4.1}$$

where r is the radial coordinate measured from the origin and θ is measured counter-clockwise from the horizontal $x-$axis. The individual components of stress in polar coordinate are available from

$$\begin{aligned}\sigma_{rr} &= \frac{1}{r}\cdot\frac{\partial\phi}{\partial r}+\frac{1}{r^2}\frac{\partial^2\phi}{\partial\theta^2}\\ \sigma_{\theta\theta} &= \frac{\partial^2\phi}{\partial r^2}\\ \sigma_{r\theta} &= -\frac{\partial}{\partial r}\cdot(\frac{1}{r}\cdot\frac{\partial\phi}{\partial\theta})\end{aligned} \tag{4.2}$$

such that

$$\begin{aligned}\sigma_{rr} =& \frac{b_0}{r^2}+2c_0+d_0(2\ln r+1)+B_0\frac{\theta}{r^2}+2C_0\theta+D_0(2\ln r+1)\theta\\ &+(\frac{b_1}{r}-\frac{2c_1}{r^3}+2rd_1)\sin\theta+(\frac{b_1^{'}}{r}-\frac{2c_1^{'}}{r^3}+2rd_1^{'})\cos\theta\\ &+\frac{2A_1}{r}\cos\theta-\frac{2A_1^{'}}{r}\sin\theta+\frac{B_1}{r}\theta\sin\theta+\frac{B_1^{'}}{r}\theta\cos\theta\\ &+(\frac{2B_1}{r}\ln r)\cos\theta-(\frac{2B_1^{'}}{r}\ln r)\sin\theta\\ &-\sum_{n=2,3,\ldots}^{N}\begin{pmatrix} a_nn(n-1)r^{n-2}+b_n(n+1)(n-2)r^n\\ +c_nn(n+1)r^{-(n+2)}+d_n(n-1)(n+2)r^{-n}\end{pmatrix}\sin(n\theta)\\ &-\sum_{n=2,3,\ldots}^{N}\begin{pmatrix} a_n^{'}n(n-1)r^{n-2}+b_n^{'}(n+1)(n-2)r^n\\ +c_n^{'}n(n+1)r^{-(n+2)}+d_n^{'}(n-1)(n+2)r^{-n}\end{pmatrix}\cos(n\theta)\end{aligned} \tag{4.3}$$

$$
\begin{aligned}
\sigma_{\theta\theta} =& \frac{-b_0}{r^2} + 2c_0 + d_0(2\ln r + 3) - B_0\frac{\theta}{r^2} + 2C_0\theta + D_0(2\ln r + 3)\theta \\
&+ (\frac{b_1}{r} + \frac{2c_1}{r^3} + 6rd_1)\sin\theta + (\frac{b_1^{'}}{r} + \frac{2c_1^{'}}{r^3} + 6rd_1^{'})\cos\theta \\
&+ \frac{B_1}{r}\theta\sin\theta + \frac{B_1^{'}}{r}\theta\cos\theta \\
&+ \sum_{n=2,3,\ldots}^{N} \begin{pmatrix} a_n n(n-1)r^{n-2} + b_n(n+1)(n+2)r^n \\ +c_n n(n+1)r^{-(n+2)} + d_n(n-1)(n-2)r^{-n} \end{pmatrix} \sin(n\theta) \\
&+ \sum_{n=2,3,\ldots}^{N} \begin{pmatrix} a_n^{'} n(n-1)r^{n-2} + b_n^{'}(n+1)(n+2)r^n \\ +c_n^{'} n(n+1)r^{-(n+2)} + d_n^{'}(n-1)(n-2)r^{-n} \end{pmatrix} \cos(n\theta)
\end{aligned} \tag{4.4}
$$

$$
\begin{aligned}
\sigma_{r\theta} =& \frac{A_0}{r^2} + B_0\frac{\ln r - 1}{r^2} - C_0 - D_0(\ln r + 1) + (-\frac{b_1}{r} + \frac{2c_1}{r^3} - 2rd_1)\cos\theta \\
&- (-\frac{b_1^{'}}{r} + \frac{2c_1^{'}}{r^3} - 2rd_1^{'})\sin\theta - \frac{B_1}{r}\sin\theta - \frac{B_1^{'}}{r}\cos\theta - \frac{B_1}{r}\theta\cos\theta \\
&+ \frac{B_1^{'}}{r}\theta\sin\theta \\
&- \sum_{n=2,3,\ldots}^{N} \begin{pmatrix} a_n n(n-1)r^{n-2} + b_n n(n+1)r^n \\ -c_n n(n+1)r^{-(n+2)} - d_n n(n-1)r^{-n} \end{pmatrix} \cos(n\theta) \\
&+ \sum_{n=2,3,\ldots}^{N} \begin{pmatrix} a_n^{'} n(n-1)r^{n-2} + b_n^{'} n(n+1)r^n \\ -c_n^{'} n(n+1)r^{-(n+2)} - d_n^{'} n(n-1)r^{-n} \end{pmatrix} \sin(n\theta)
\end{aligned} \tag{4.5}
$$

Determination of the individual stresses of equations (4.3) through (4.5) necessitates evaluating the unknown coefficients in the Airy stress function (typically referred to as Airy coefficients). The specific form of the Airy stress function for a particular case can depend on

conditions of symmetry, whether or not the coordinate origin is within the component, whether the component is finite or infinite in size (boundedness at origin or infinity), self-equilibrated at individual boundaries, and single-valued stresses, strains and displacements with angle θ. Even though the plate geometry and loading of figure 4.1.1 are symmetrical about the x-axis, most of the coefficients were retained here, i.e., utilized equation (4.1), because the coordinate origin is located outside the boundary of the simply-connected plate. The isopachic stress, $S = \sigma_{rr} + \sigma_{\theta\theta}$, is

$$\begin{aligned} S =& 4c_0 + 4d_0(\ln r + 1) + 4C_0\theta + 4D_0(\ln r + 1)\theta + (\frac{2b_1}{r} + 8rd_1)\sin\theta \\ &+ (\frac{2b_1^{'}}{r} + 8rd_1^{'})\cos\theta + \frac{2A_1}{r}\cos\theta \\ &+ \frac{2B_1}{r}(\theta\sin\theta + \ln r\cos\theta) - \frac{2A_1^{'}}{r}\sin\theta \\ &+ \frac{2B_1^{'}}{r}(\theta\cos\theta - \ln r\sin\theta) \\ &+ 4\sum_{n=2,3,\ldots}^{N}\left[b_n(n+1)r^n - d_n(n-1)r^{-n}\right]\sin(n\theta) \\ &+ 4\sum_{n=2,3,\ldots}^{N}\left[b_n^{'}(n+1)r^n - d_n^{'}(n-1)r^{-n}\right]\cos(n\theta) \end{aligned} \tag{4.6}$$

Notice that S is a function of c_0, d_0, C_0, D_0, b_1, d_1, b'_1, d'_1, A_1, B_1, A'_1, B'_1, b_n, d_n, b'_n, and d'_n whereas the individual stresses are also function of b_0, A_0, B_0, c_1, c'_1, a_n, c_n, a'_n, and c'_n. As a result, one cannot evaluate all the Airy coefficients and therefore not determine the individual stresses from only values of the signal $S^* = K\Delta S$. Therefore, some traction-free boundary and symmetry conditions were also imposed to help evaluate all the coefficients. The Cartesian components of stresses, which will be needed relative to imposing some boundary conditions, are available from the polar stresses according to [34]

$$\begin{bmatrix} \sigma_{xx} \\ \sigma_{yy} \\ \sigma_{xy} \end{bmatrix} = \begin{bmatrix} m^2 & n^2 & -2 \cdot m \cdot n \\ n^2 & m^2 & 2 \cdot m \cdot n \\ m \cdot n & -m \cdot n & m^2 - n^2 \end{bmatrix} \cdot \begin{bmatrix} \sigma_{rr} \\ \sigma_{\theta\theta} \\ \sigma_{r\theta} \end{bmatrix} \tag{4.7}$$

$$where\ m\ =\ \cos(\theta)\ \ and\ n\ =\ \sin(\theta)$$

4.3.2 Boundary Conditions

Recognizing the inability to evaluate all the Airy coefficients from the recorded thermal data, boundary conditions in terms of stresses as shown in figure 4.3.1 were (at least initially) imposed discretely (point-wise) at multiple locations on the traction-free edges of the U-notch. The four conditions can be written as

$$\begin{aligned} &\sigma_{rr}(R,\theta) = \sigma_{r\theta}(R,\theta) = 0, && \frac{\pi}{2} \leq \theta \leq \pi \\ &\sigma_{yy}(x,R) = \sigma_{xy}(x,R) = 0, && 0 \leq x \leq 1.935 \end{aligned} \tag{4.8}$$

where R is the radius of the notch.

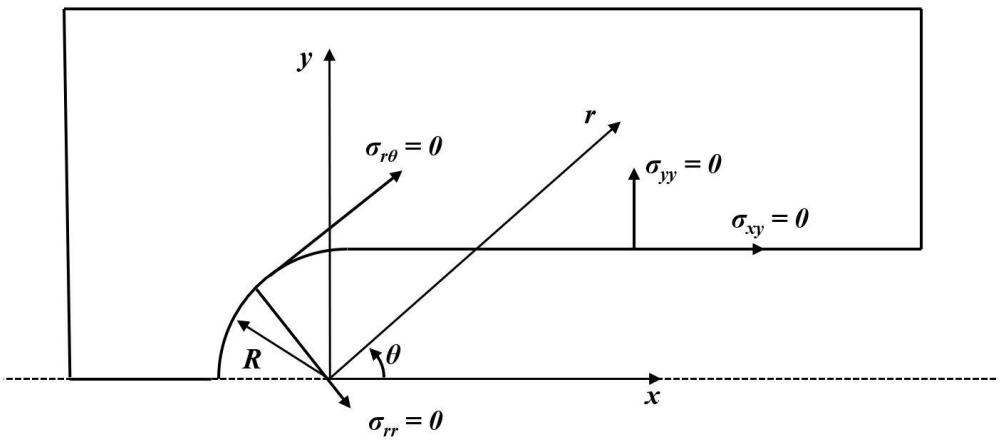

Figure 4.3.1: Imposing traction-free boundary conditions

4.3.3 Coefficient Evaluation

From the recorded thermoelastic data and imposed local boundary conditions, the Airy coefficients were solved by forming a linear system of equation represented in matrix form as $[A]_{(m+h)\times k} \times \{c\}_{k\times 1} = \{d\}_{(m+h)\times 1}$ where m is the total number of measured values of S, h is the number of the imposed stress conditions, and k is the number of unknown Airy coefficients. The matrix $[A]$ consists of the analytical expression of isopachics stress S ($= S^*/K$) of equation (4.6), in addition to h known boundary stress conditions of equations (4.8), as a function of polar coordinates (r, θ). The vector c contains the k unknown Airy coefficients and vector d contains the m measured TSA signal values and the h zeros from the right-hand side of known stress conditions. Like most experimental data, the measured data incorporate some noise which necessitate collecting more measured input values than the number of unknown Airy coefficients. The number of equations, $m + h$, is therefore larger than the number of coefficients, k, which produces an overdetermined system which can be solved using least-squares. The system was solved in MATLAB using the backslash '\' operator.

The number of unknown Airy coefficients, however, can often be reduced by considering factors such as symmetry and/or eliminating any terms that lead to multivalued displacements, strains or stresses. As per discussion of Reference [2], if there is mechanical and geometric symmetry about the x-axis, coefficients A_0, B_0, C_0, D_0, d_0, A'_1, B_1, B'_1, a_n, b_n, c_n, and d_n ($n \geq 1$) should be zero. For a problem requiring single-valued stresses and displacements, $d_0 = B_0 = C_0 = D_0 = B_1 = 0$. If the coordinate origin lies within a simply-connected structure, $b_1 = ((1-\nu)\, A'_1)/2$ and $b'_1 = -(1-\nu)\, A_1/2$. At least if the coordinate origin lies within a simply-connected structure, coefficients A_1, A'_1, b_1, and b'_1 should be zero if there is no resultant force at the origin. On the

other hand, B_0, C_0, D_0, B_1 and B_1' should be retained if the coordinate origin lies outside of a simply-connected structure.

In this chapter, three cases were initially studied: Case A, evaluating coefficients considering only symmetry about x-axis (i.e., A_0, B_0, C_0, D_0, d_0, A'_1, B_1, B'_1, a_n, b_n, c_n, d_n ($n \geq 1$) $\equiv 0$); Case B, in addition to symmetry about x-axis of Case A, assumes $A_1 = A'_1 = b_1 = b'_1 \equiv 0$. At least if the coordinate origin lies within the structure, this is equivalent to no resultant forces at the origin, called fully reduced; Case C retains all of the Airy coefficients appearing in equation (4.1) (i.e., none of the coefficients equal to zero); and Case A*, which is similar to Case A but recognizing the coordinate origin of the plate of figure 4.1.1 is outside of the simply connected structure, one retains B_0, C_0, D_0, B_1 and B'_1.

4.4 Finite Element Model

For comparison with the hybrid-TSA results, an ANSYS finite element analysis (FEA) was prepared of the finite plate of figure 4.4.1 using elastic properties of E = 70 GPa and v = 0.33. Due to the symmetry, only the upper part of the plate was modeled with symmetrical boundary condition applied along the horizontal line of symmetry, y = 0. The physical loading in the hydraulic grips (figures 4.5.1 and 4.5.2) was approximated by a top central concentrated load of 2670 N (600 lbs) and by restricting the end horizontal displacements. Plane 82 isoperimetric element with four nodes were employed. A convergence test was applied until the change in results of maximum stress between two successive meshing was less than 2%. This half-model utilizes 13,300 elements and 13,559 nodes, figure 4.4.1 (b). This image shows the ANSYS-predicted stresses in the plate, illustrates how the restricted horizontal displacements at the end of the plate. Among other considerations, geometry and loading of the figure 4.1.1 were selected so as one could obtain a reliable FEM result with which to compare the experimental results. However, motivation for developing the present ability is to enable stress analysis of cases experimentally which cannot be analyzed numerically; yet FEM is used here. The developed hybrid-TSA method is applicable to more complicated problems which are difficult for FEM, e.g., when do not know the external loading. For example, while industry makes prevalent use of FEM, strain gages are often employed in that environment to obtain the boundary conditions for the FEA.

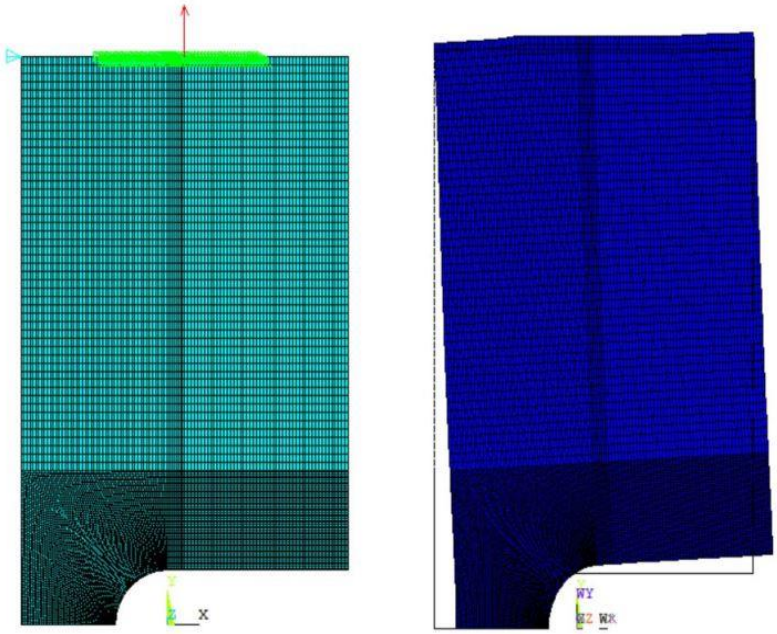

(a) (b)

Figure 4.4.1: (a) FE model with dense meshing adjacent to the U-notch (b) Illustration of restricted horizontal displacements at end of plate

4.5 Experimental Setup and Data Acquisition

4.5.1 Plate Preparation and Loading Condition

The 6.35 mm thick deep U-notched finite-width aluminum plate of figure 4.1.1 plate is 88.77 mm wide, 292.10 mm long and has a 13.97 mm wide deep U-notch, figure 4.1.1. The coordinate origin is at the center of the semi-circular end of the notch and the geometry and loading are symmetric about the horizontal x-axes. The material properties are E = 70 GPa and ν = 0.33. The specimen was initially lightly polished with 400 grit emery cloth paper. A coating of Krylon Ultra-Flat black paint was then applied to provide an enhanced and uniform thermal emissivity. Precaution was taken when sanding the faces of the specimen not to round-off the edges of the notch which could further erode the quality of the thermal information close to the edge of the U-notch. The plate was sinusoidally loaded in a 20-kip capacity MTS hydraulic testing machine at a load range of F = 1780 - 4450 N (400 - 1000 lb), figure 4.5.1. The plate was loaded at different cyclic rates while monitoring the phase information with the DeltaTherm Stress Photonics model DT1410 TSA system software (Stress Photonics, Madison, WI) to ensure that the adiabatic conditions prevailed at the employed loading frequency of 20 Hz. The corresponding load-induced TSA data were recorded using the DeltaTherm system. The camera, which has a sensor array of 256 horizontal by 256 vertical pixels and is cooled with liquid nitrogen, was aligned perpendicular to the surface of the plate, figure 4.5.2.

Figure 4.5.1: Plate testing and TSA recording camera

Figure 4.5.2: Overview of experimental setup

4.5.2 TSA Recording and Calibration

The TSA images (figure 4.5.3) were captured and averaged over two-minute durations, and then exported to MS Excel to convert each pixel into a data point, i.e., a 256 by 256 matrix. To help locate the edges of the plate and determine the pixel size, a thermogram was recorded which also included a transparent flat ruler, figure 4.5.4. Pixel size was determined to be 0.4 mm. Since TSA data typically are unreliable on and near an edge, no recorded TSA information was used within at least three to six-pixel positions (1.2 to 2.4 mm) of the edges of the plate. The thermoelastic calibration coefficient, K, was evaluated from a separate uniaxial tensile coupon of the same material, thickness and coating of the flat black paint and tested on the same day at the same frequency (20 Hz) using the same TSA arrangement as the notched plate, figure 4.5.5. The thermoelastic coefficient was determined to be K = 202 U/MPa (1.3935 U/psi). The unit U is used to signify the raw TSA output, in uncalibrated signal units.

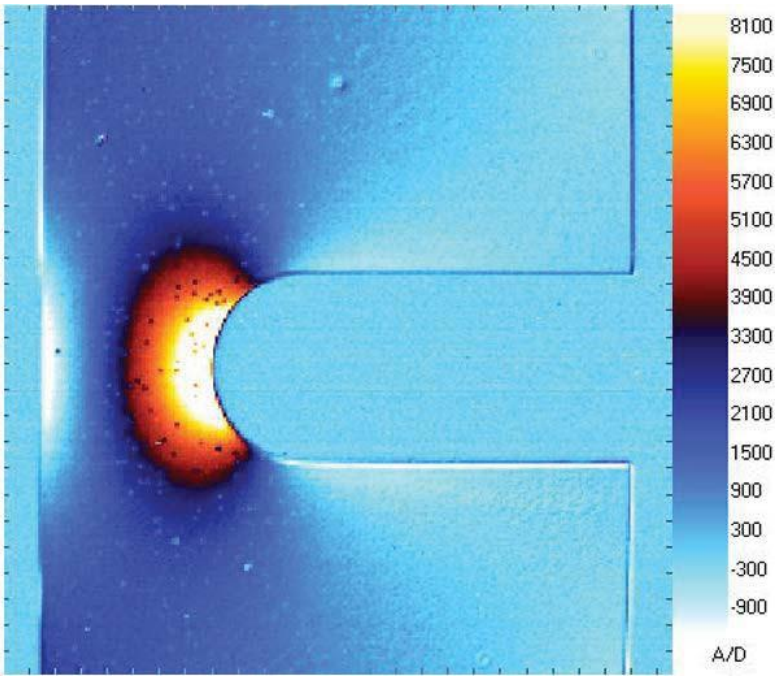

Figure 4.5.3: Recorded TSA image, S^*, of U-notched plate loaded at a range of 2670 N (600 lb) and frequency of 20 Hz

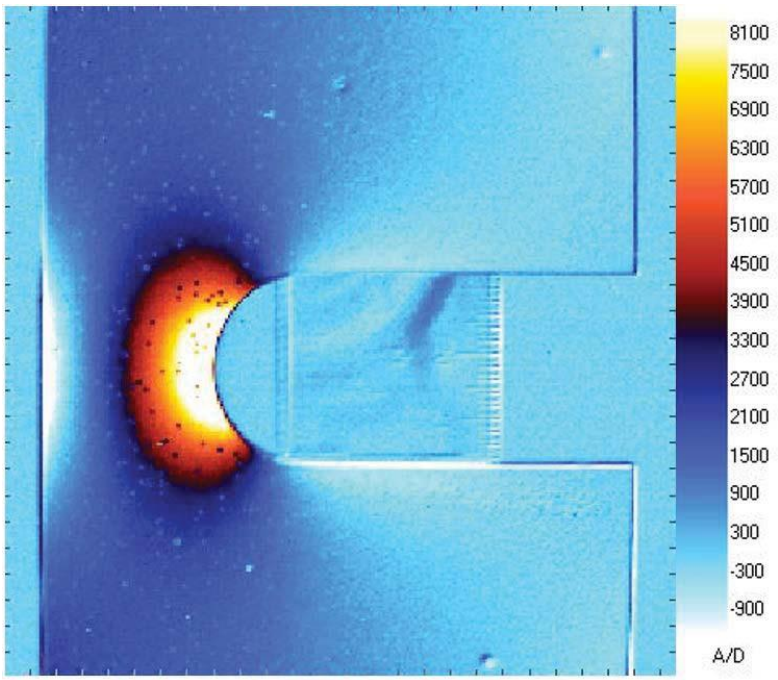

Figure 4.5.4: Recorded TSA image, S^*, containing a transparent scale

Figure 4.5.5: Experimental setup for uniaxial tensile aluminum coupon and TSA image

4.5.3 Data Processing

The individual stresses throughout the region adjacent to the deep U-notch were determined from the recorded thermoelastic data using an Airy stress function. Due to unreliability, the recorded data along and near the edge of the notch were not used. Since the geometry and loading were symmetrical about x-axis, the thermal data were averaged about $y = 0$ and projected into the upper part of the plate. A total of 19,869 thermal values of S^* uniformly located throughout the top shaded area of figure 4.5.6 were utilized. Like most experimental data, the experimental S^* include some noise which necessitates collecting more measured input values than the number of unknown coefficients. In addition to the employed m = 19,869 values of S^*, a total of $h = 500 \times 4 = 2000$ boundary conditions were imposed at 500 equally-spaced discrete points of each of the four relevant expression in equations (4.8) on the edges of figure 4.3.1. A set of linear isopachic expressions of the form of equation (4.8) and boundary conditions were formulated as the matrix expression $[A]\{c\} = \{d\}$ of equation (4.9). Case A assumes coefficients A_0, B_0, C_0, D_0, d_0, A'_1, B_1,

B'_1, a_n, b_n, c_n, d_n ($n \geq 1$) $\equiv 0$, i.e., symmetrical about $y = 0$, while Case B assumes coefficients A_1, $b'_1 \equiv 0$ in addition to those of Case A. The number of equations, $m + h = 21{,}869$, will exceed the number of coefficients, k. The resulting overdetermined system of equations with which to evaluate the unknown coefficients was solved in MATLAB using the backslash '\' operator.

$$\begin{bmatrix} S_{r_1\theta_1}(0, c_0, d_0, 0, \cdots, 0, d'_n) \\ S_{r_2\theta_2}(0, c_0, d_0, 0, \cdots, 0, d'_n) \\ \vdots \\ S_{r_m\theta_m}(0, c_0, d_0, 0, \cdots, 0, d'_n) \\ \sigma_{rr}(b_0, c_0, d_0, 0, \cdots, c'_n, d'_n) \\ \vdots \\ \sigma_{r\theta}(0,0,0, A_0, \cdots, c'_n, d'_n) \end{bmatrix}_{(m+h)\times k} \begin{bmatrix} b_0 \\ c_0 \\ d_0 \\ A_0 \\ \vdots \\ c'_n \\ d'_n \end{bmatrix}_{k\times 1} = \begin{bmatrix} S_1 \\ S_2 \\ \vdots \\ S_m \\ 0 \\ \vdots \\ 0 \end{bmatrix}_{(m+h)\times 1} \tag{4.9}$$

or, in simplified form,

$$[A]_{(m+h)\times k}\{c\}_{k\times 1} = \{d\}_{(m+h)\times 1} \tag{4.10}$$

The subsequent analysis will demonstrate that the described approach is able to evaluate stresses reliably at the edge of the U-notch without using any thermoelastic data on, or very near, the edges. The next section describes how the number of Airy coefficients to retain was determined for three cases.

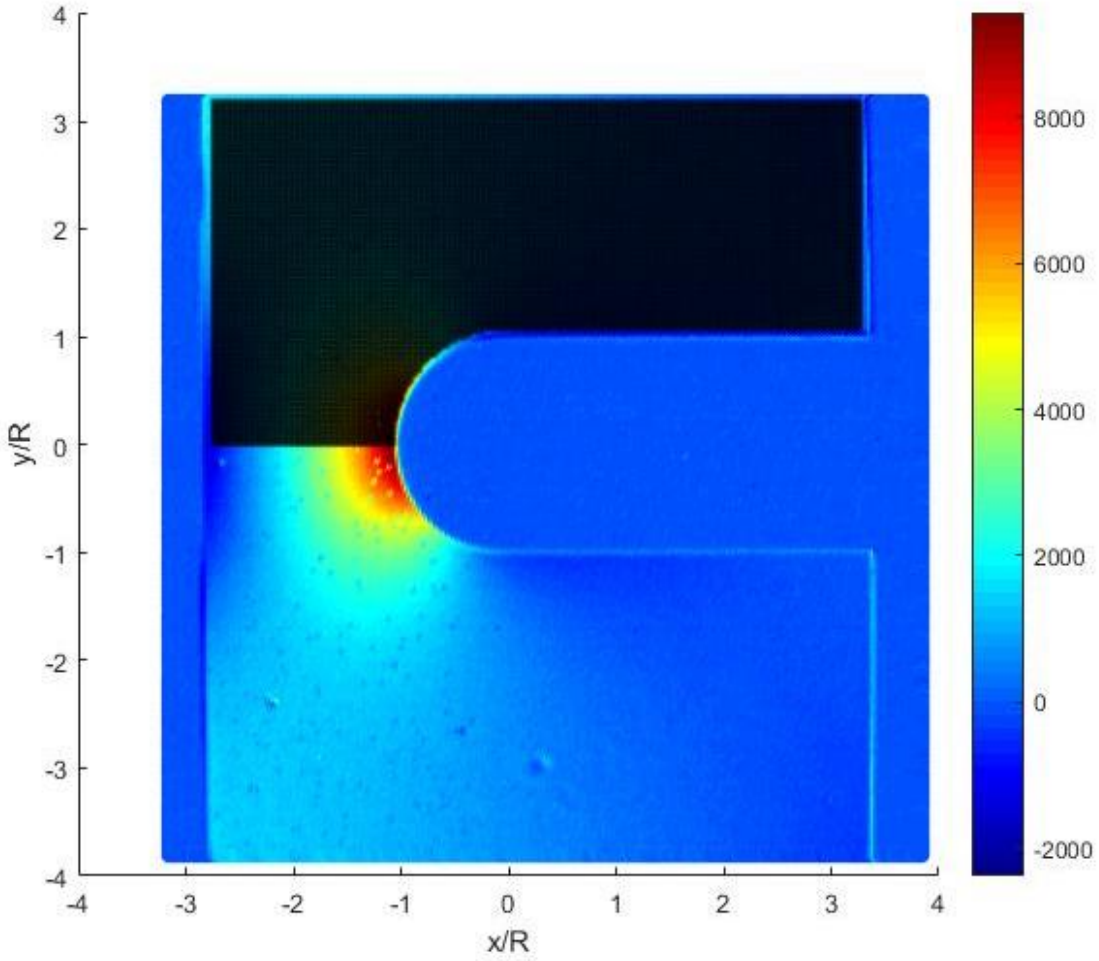

Figure 4.5.6: Source locations of employed S* data (m = 19,869 values)

4.5.4 Evaluating Number of Coefficients to Employ

The $m = 19{,}869$ uniformly distributed input values of S^*, whose source locations are shown in figure 4.5.6, and the 500 equally-spaced imposed stress conditions along the lines of figure 4.3.1 ($h = 2{,}000$) were used to evaluate the $k = 27$ coefficients for Case A, $k = 25$ coefficients for Case B, and $k = 49$ coefficients for Case C (in each case, terminating index, $N = 5$).

The use of $N = 5$ for these cases was determined (based on equation (4.10)) from figures 4.5.7 and 4.5.8. Figure 4.5.7 plots the root mean square (*RMS*) values between $\{d\}$, which contains the recorded values of S^*, and the reconstructed values of $\{d'\} = [A]\{c\}$ of equation (4.11) versus terminating index, N. The plot indicates increased number of coefficients results in less discrepancies for all cases. In addition to figure 4.5.7, load equilibrium was calculated for each N, figure 4.5.8. This was done by averaging the integrated vertical stress, σ_{yy}, multiplied by the thickness across the width of the plate, equation (4.12), for different horizontal lines (from y/R = 0 to 1 with increment of 0.05). The expression for the vertical stress was derived from the relationship between polar and Cartesian components of stress, equation (4.7). The vertical stress along these horizontal lines were summed by integrating an 8^{th} order polynomial with MATLAB that represents discrete individual values of stress. Computed loads are normalized by the physically applied force of 2,670 N and averaged for each terminating index, N. Relative to how many coefficients to employ, it is desirable to use the smallest number of coefficients that gives sufficient accuracy. In addition to requiring potentially more experimental input data, employing more coefficients than necessary can increase computational time and concerns with the condition number of the Airy matrix. The latter could increase the chances of the $[A]$ matrix becoming singular. This is shown with Case A and B of figure 4.5.8 when N exceeds 5, the calculated load equilibrium becomes unstable. On the other hand, for Case C, normalized force is very consistent even with larger terminating index, N.

$$(\boldsymbol{d'} - \boldsymbol{d})_{rms} = \sqrt{\sum_{i=1}^{19,869} \frac{(d_i' - d_i)^2}{19,869}} \tag{4.11}$$

$$F = \int \sigma_{yy}\, dA = \int_x^w \sigma_{yy} t\, dx \tag{4.12}$$

Quantities *t* and *w* are the plate thickness and width, respectively.

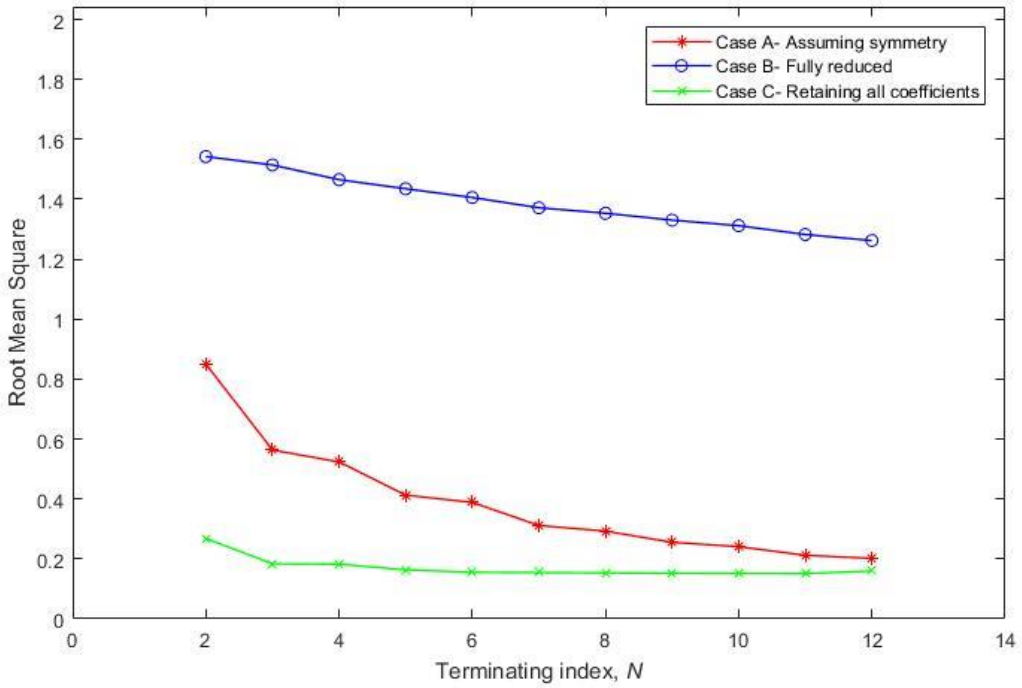

Figure 4.5.7: *RMS* vs terminating index, *N*

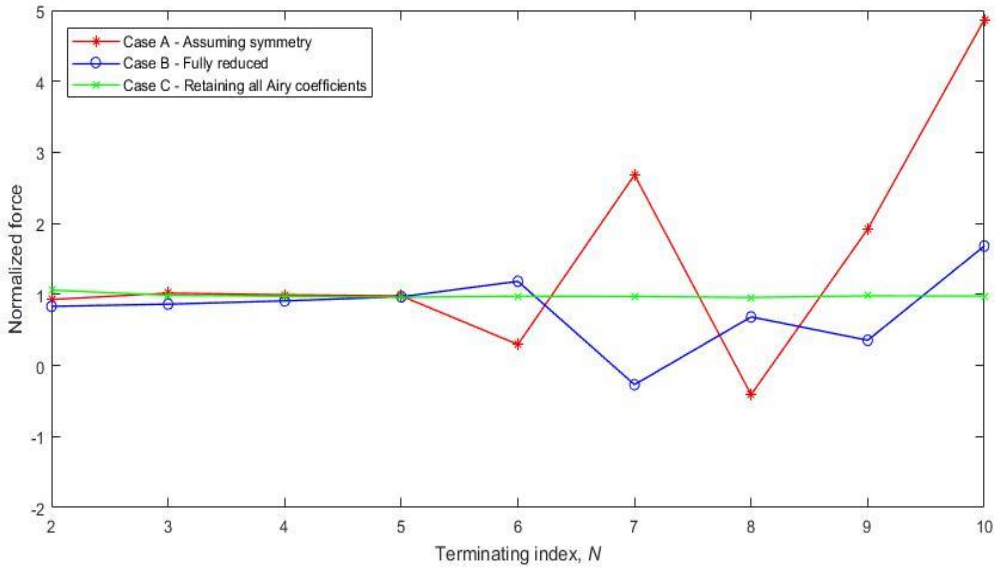

Figure 4.5.8: Average value of normalized forces calculated on the respective horizontal lines of *y*-axis vs terminating index, *N*

4.6 Results

The reconstructed (using the hybrid method, equation (4.10)) results with N =5 for the three cases and experimental values of S data are shown in figure 4.6.1. They are plotted in the same location of the TSA-recorded values of figure 4.5.6 for direct comparison. While reconstructed S values of Case A (assuming symmetry only) and Case C (retaining all coefficients) agree with TSA- recorded S, Case B (assuming symmetry in addition to no resultant force at the origin) shows discrepancies. This was expected by *RMS* plot of figure 4.5.7 where *RMS* values of Case B are much larger than those of Case A or C. Figure 4.6.2 shows normalized S of TSA recorded and reconstructed with hybrid-method using Case C. The upper part of this figure (TSA-recorded) shows noise and unavailable edge data while, due to the numerical processing, the lower part contains smooth and full-field result.

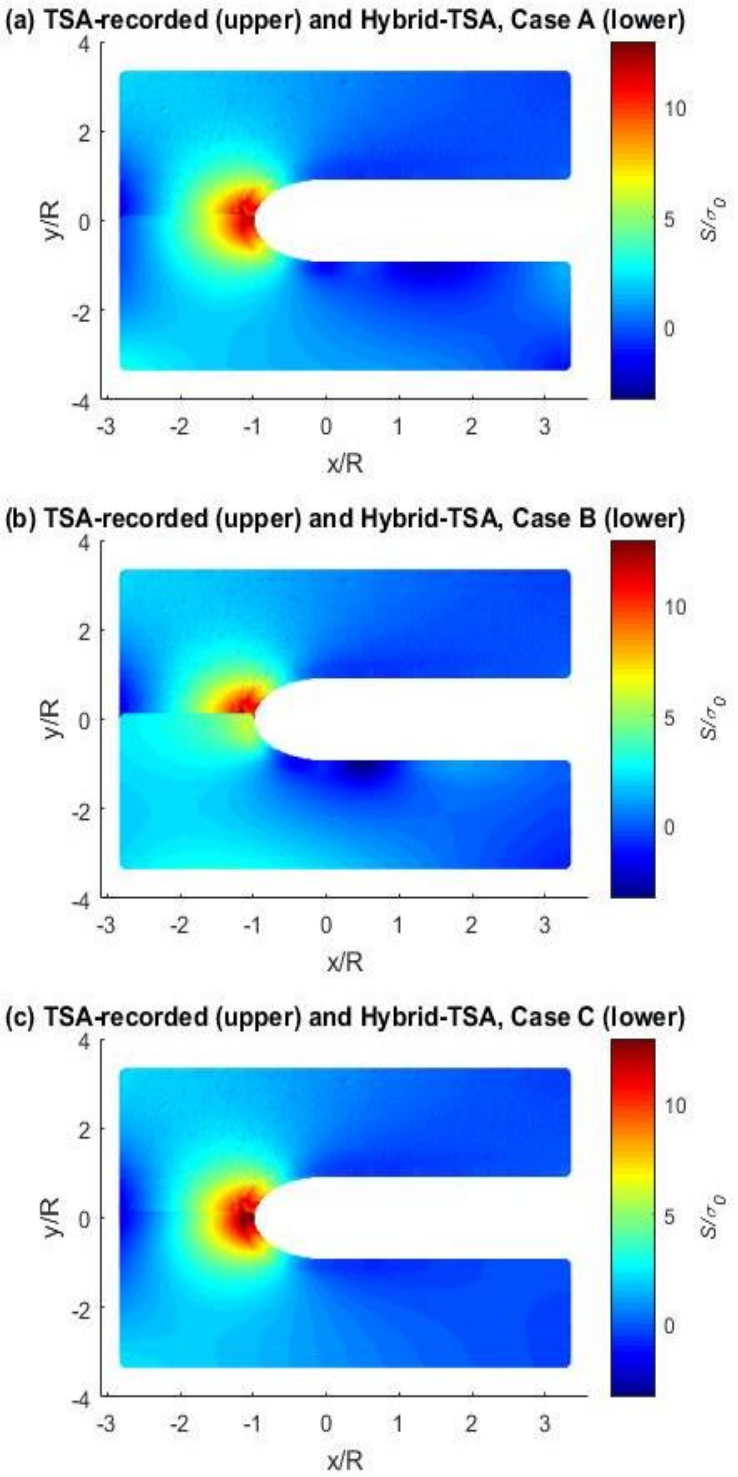

Figure 4.6.1: Normalized isopachic stress, S/σ_0, for TSA-recorded (upper) and reconstructed for hybrid-TSA method with $N = 5$ (lower)

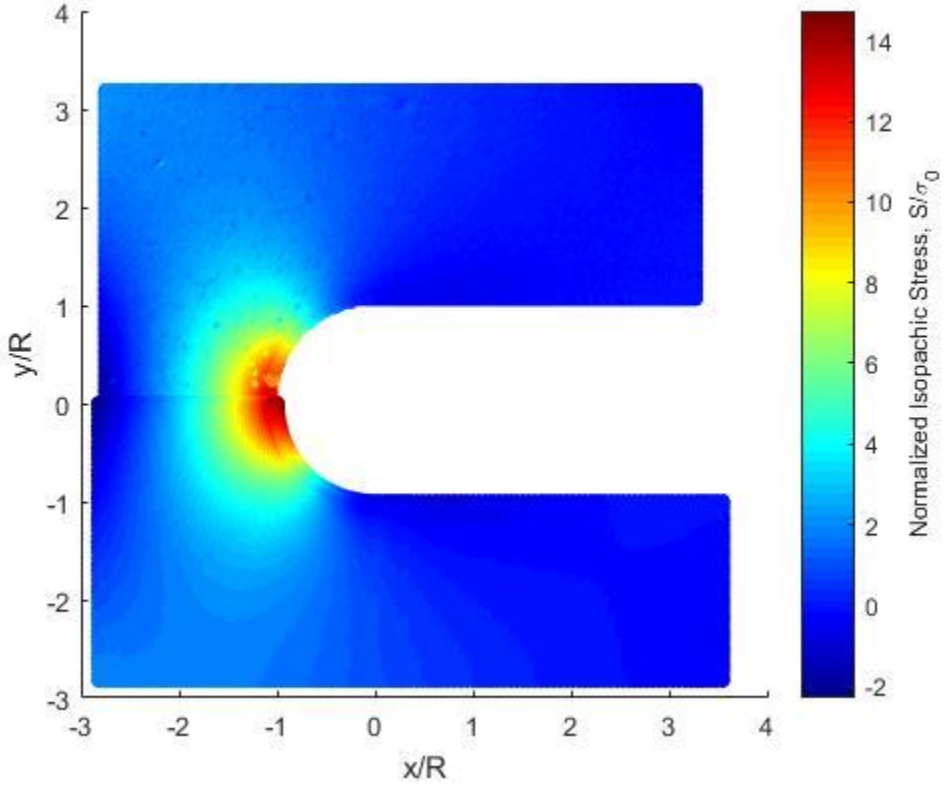

Figure 4.6.2: Normalized isopachic stress, S/σ_0, for TSA-recorded (upper) and reconstructed for hybrid-TSA method (Case C) with $N = 5$ (lower)

4.6.1 Stresses

The normalized tangential stresses determined along the edge of the notch by processing the recorded TSA data with the Airy stress function (i.e., hybrid method) are compared with those from ANSYS in figure 4.6.3. The maximum values of $\sigma_{\theta\theta}$ from hybrid-TSA with Case C and ANSYS agree within 2% of each other while Case B does not agree. Case B follows similar pattern, although it contains some discrepancies. The contour plots of Figures 4.6.4 through 4.6.9 compare the TSA-based individual components of stress with FEM predictions. The TSA-based contours

by Case C agree virtually exactly with ANSYS, including along edges where no input values were employed. The lack of agreement for Case B shown in figure 4.6.3 shows up on the edge of the notch in the contour plots of figure 4.6.4 through 4.6.9 at and near $\theta = 180^{\circ}$.

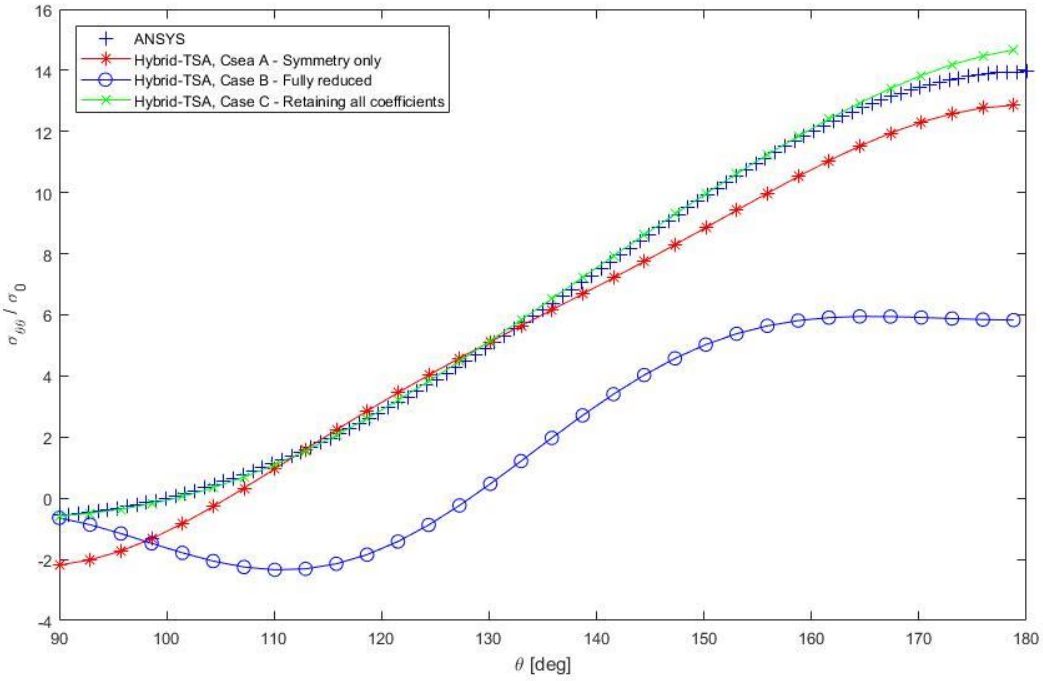

Figure 4.6.3: Normalized tangnetial stress, $\sigma_{\theta\theta}/\sigma_0$, along the edge of the notch

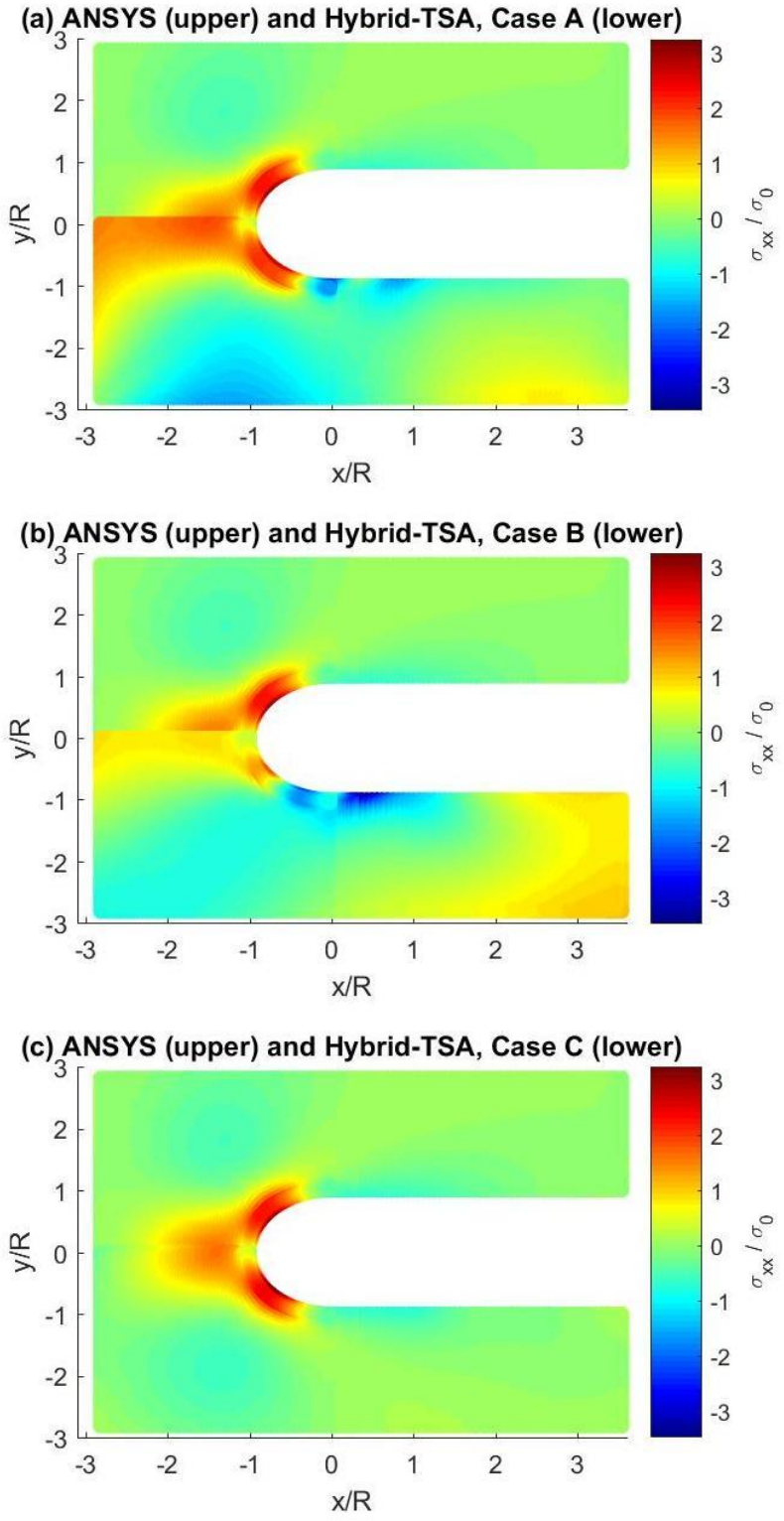

Figure 4.6.4: Normalized horizontal stress, σ_{xx}/σ_0

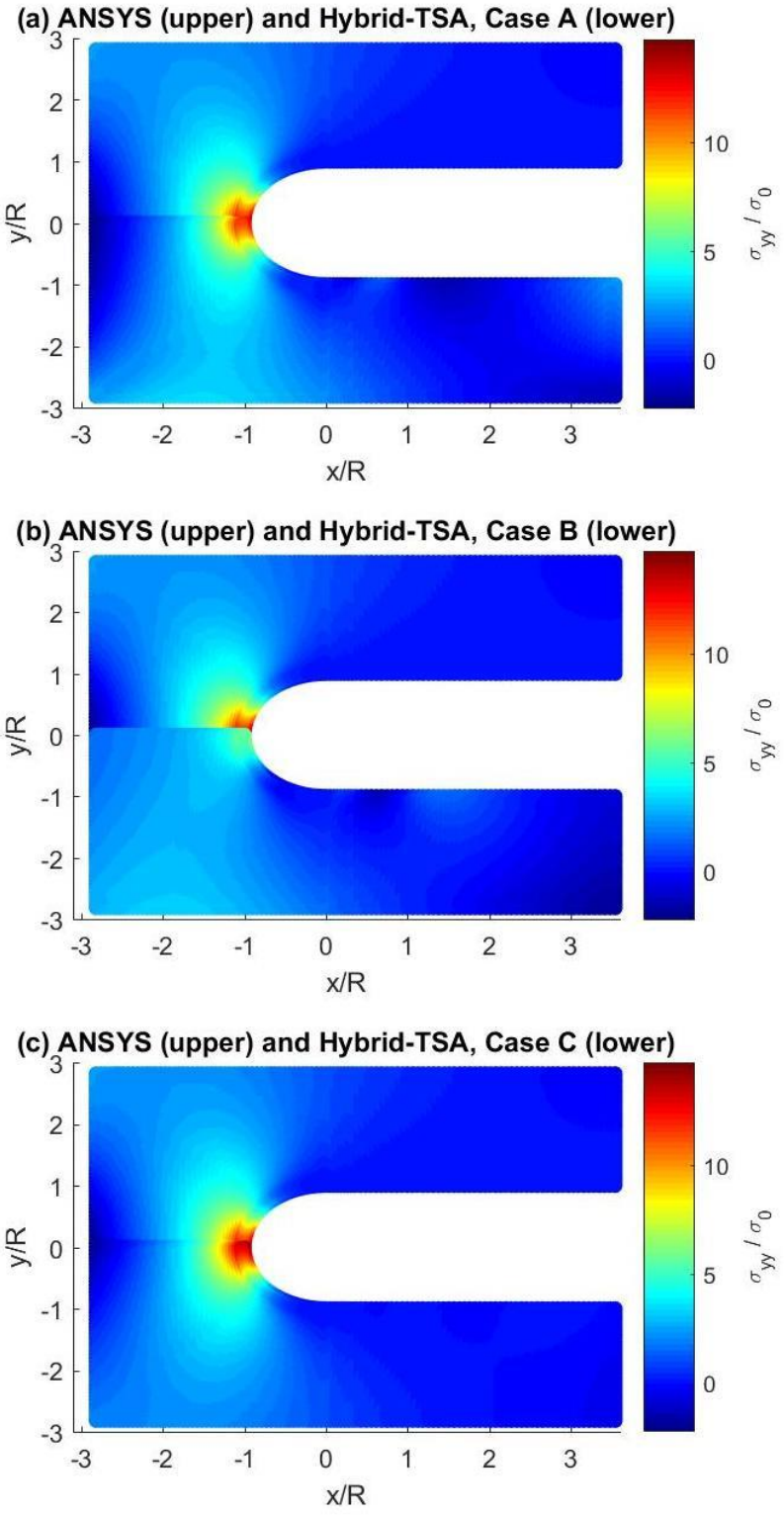

Figure 4.6.5: Normalized vertical stress, σ_{yy}/σ_0

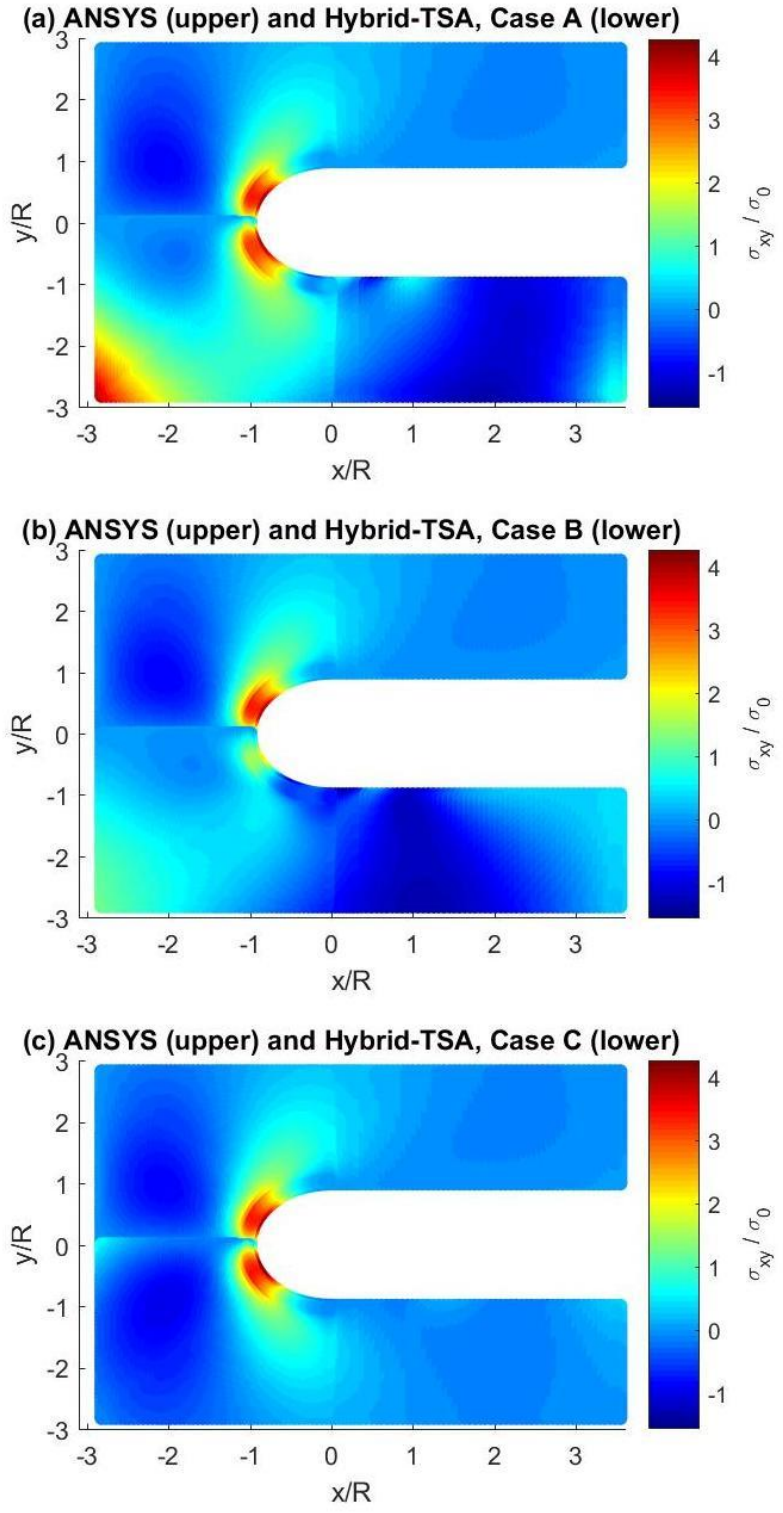

Figure 4.6.6: Normalized shear stress, σ_{xy}/σ_0

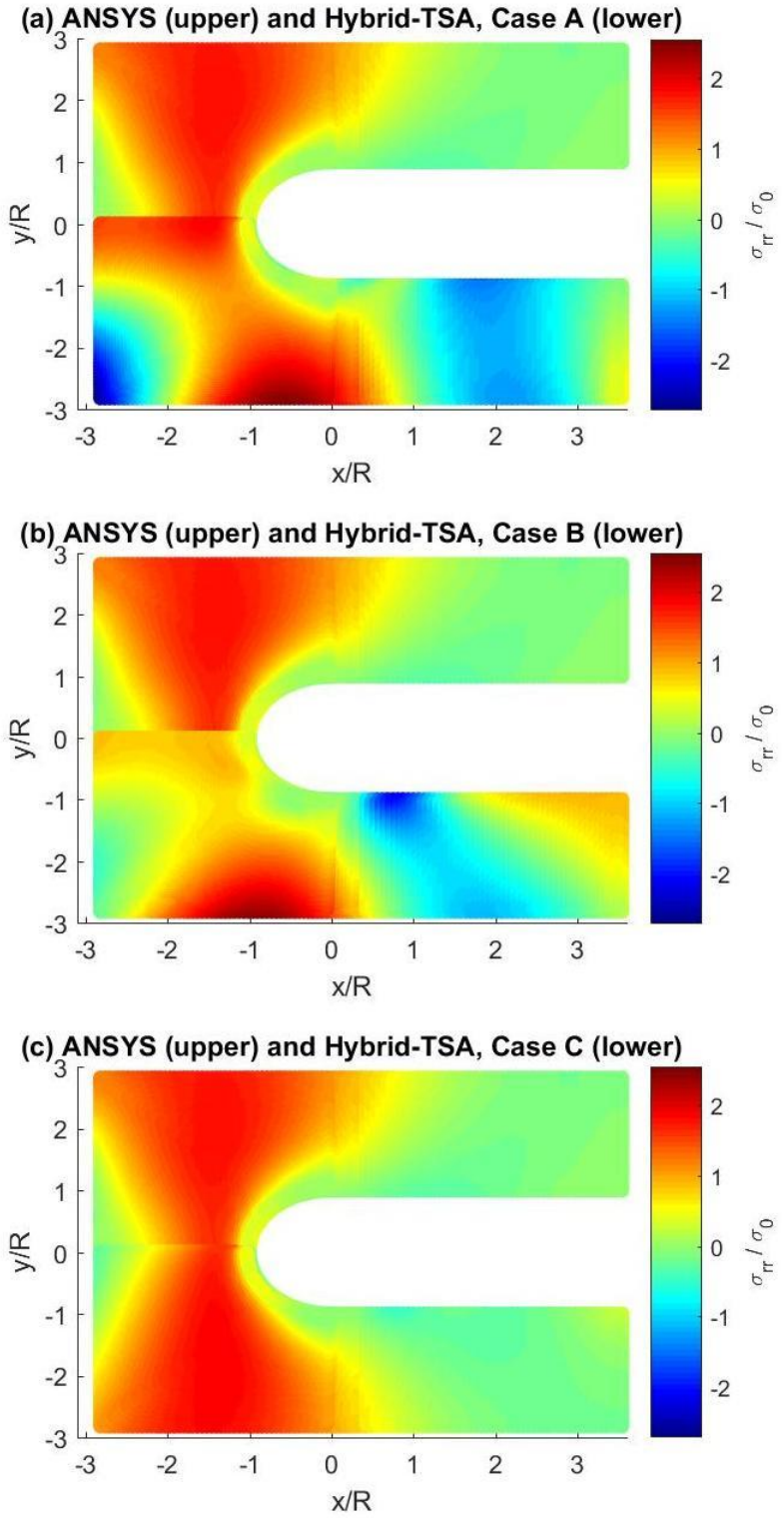

Figure 4.6.7: Normalized radial stress, σ_{rr}/σ_0

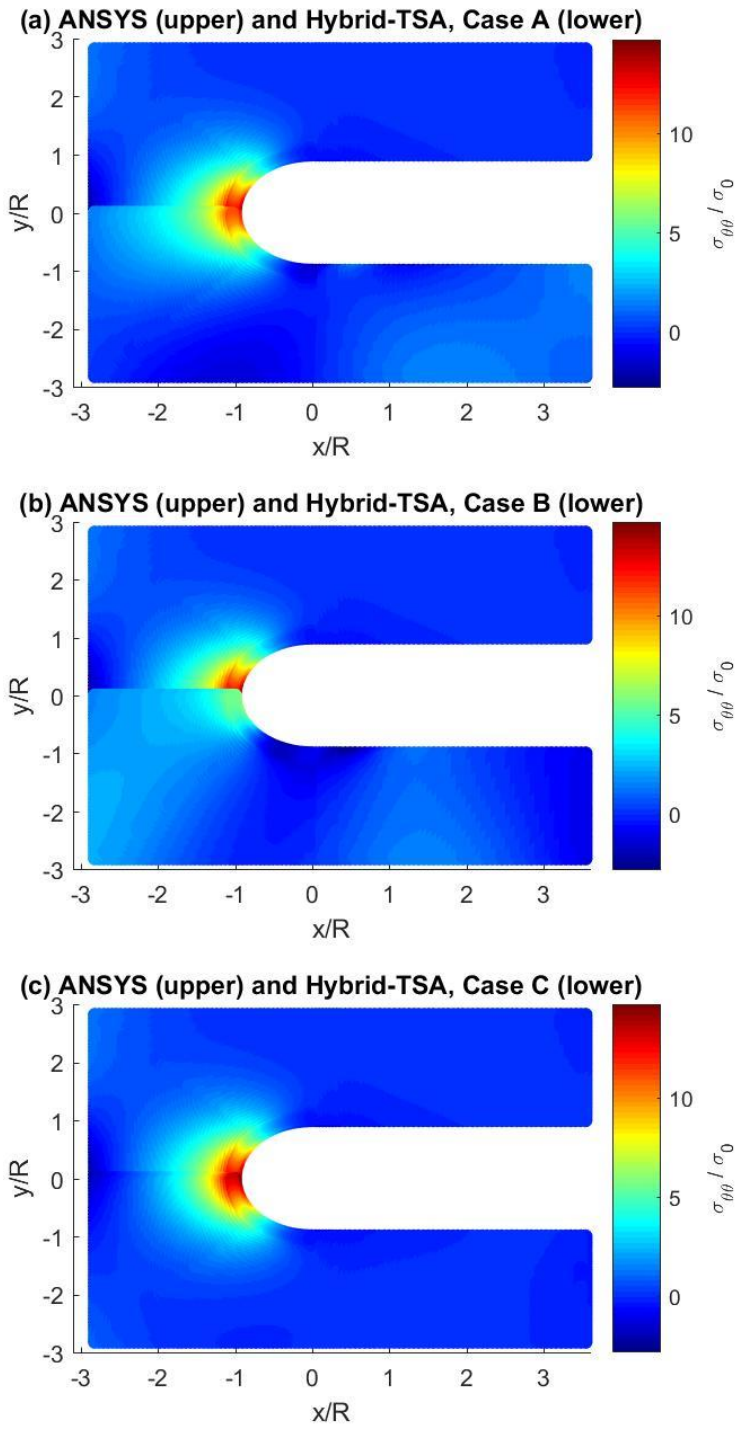

Figure 4.6.8: Normalized tangential stress, $\sigma_{\theta\theta}/\sigma_0$

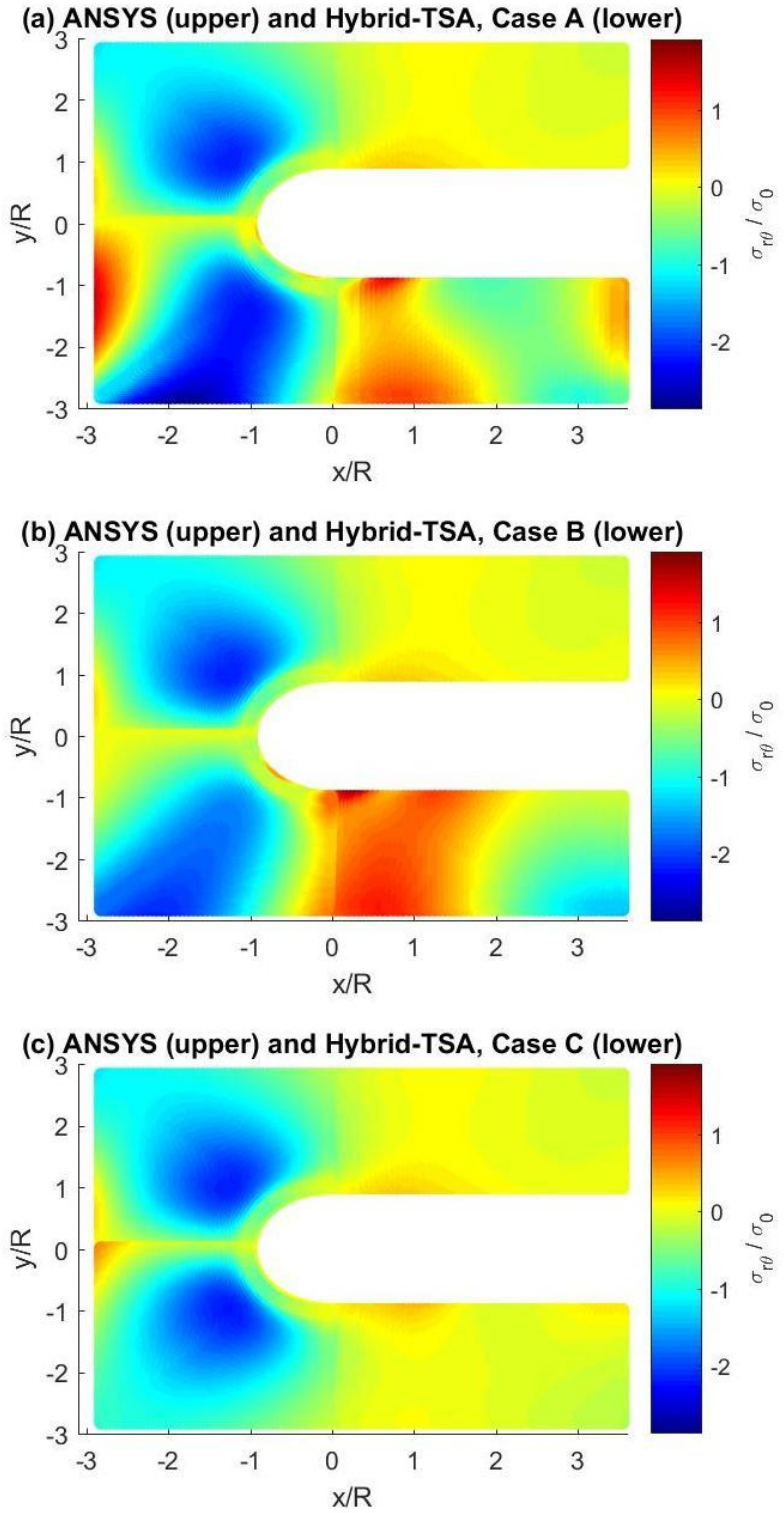

Figure 4.6.9: Normalized shear stress, $\sigma_{r\theta}/\sigma_0$

4.6.2 Force Equilibrium

Figure 4.6.10 is a plot of total force calculated on various horizontal lines (from y/R = 0 to 2.2) using equation (4.12). Computed loads are normalized by the physically applied force of 2,670 N (600 lbs). The average values of these normalized forces are 0.922 for Case A, 0.909 for Case B and 0.986 Case C. The latter again tends to perform the best.

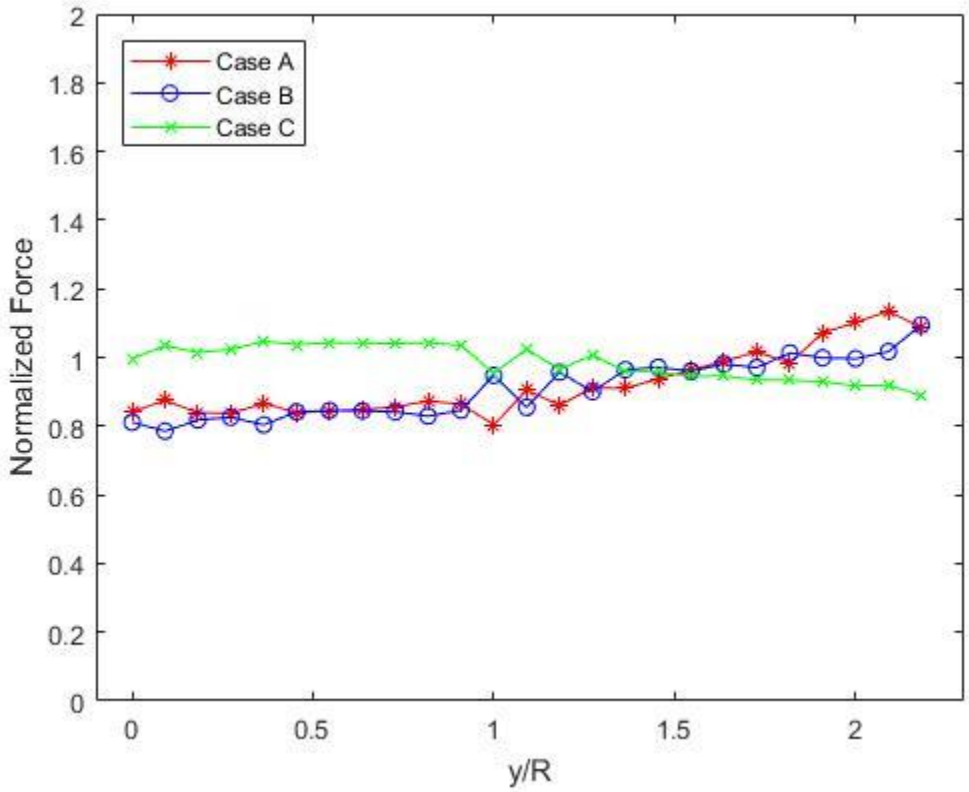

Figure 4.6.10: Normalized forces caluclated on the respective horizontal lines of *y*-axis

4.6.3 Strain Gage

The present hybrid approach was further validated by comparing the hybrid-TSA obtained strains

at a static load of 2670 N with that recorded using a small commercial foil strain gage mounted at $\theta = 180^{o}$ on the curved edge of the notch. A single-element Micro-Measurements strain gage (EA-06-015DJ-120), having gage resistance of 120.0 $\pm$ 0.3% Ω and gage factor of 2.05 ± 1.0%, was mounted at the root of the notch of the plate along line $y = 0$, figures 4.6.11 and 4.6.12. The present gage was mounted using standard strain gage procedures suggested by Vishay Micro-Measurements. The recommended conditioners and neutralizers were used on the aluminum before mounting the gage. M-Bond 610 adhesive (marketed by Vishay Micro-Measurements) was utilized in conjunction with a catalyst (200 Catalyst-C, recommended for use with M-Bond adhesive) for good adhesion. A protective air-drying polyurethane coating, M-Coat, was applied over the gage (and wires) after the adhesive had dried. Although the gage was not 'tuned' for aluminum, it was mounted, and the testing was conducted at room temperature, so no dummy temperature compensating gages were employed.

Figure 4.6.13 contains strain-gage recorded strains for various levels of plate loading. Strain-gage results were recorded under both incremental increasing and decreasing static loading. For comparison, the tangential strains calculated by ANSYS and Hybrid-TSA for Cases A, B and C are marked in figure 4.6.13 at the load of 2670 N. Figures 4.6.14 and 4.6.15 compare normalized tangential and vertical stresses from ANSYS, the three cases of Hybrid-TSA and the strain-gage. A regression line of the strain-gage result was computed and used for calculating stresses at the actual applied load of 2670 N. These current figures again show the poor performance by Case B. Although the stress at $\theta = 180^{o}$ by Case C slightly exceeds the experimental value from the strain gage, from a safety consideration, it is better to over-predict than under-predict.

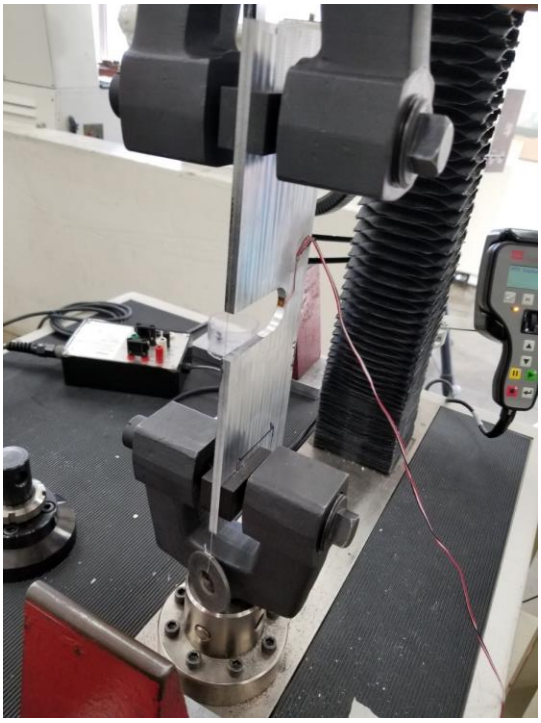

Figure 4.6.11: Strain gage mounted on notch at $\theta = 180^{\circ}$

Figure 4.6.12: Strain gage location

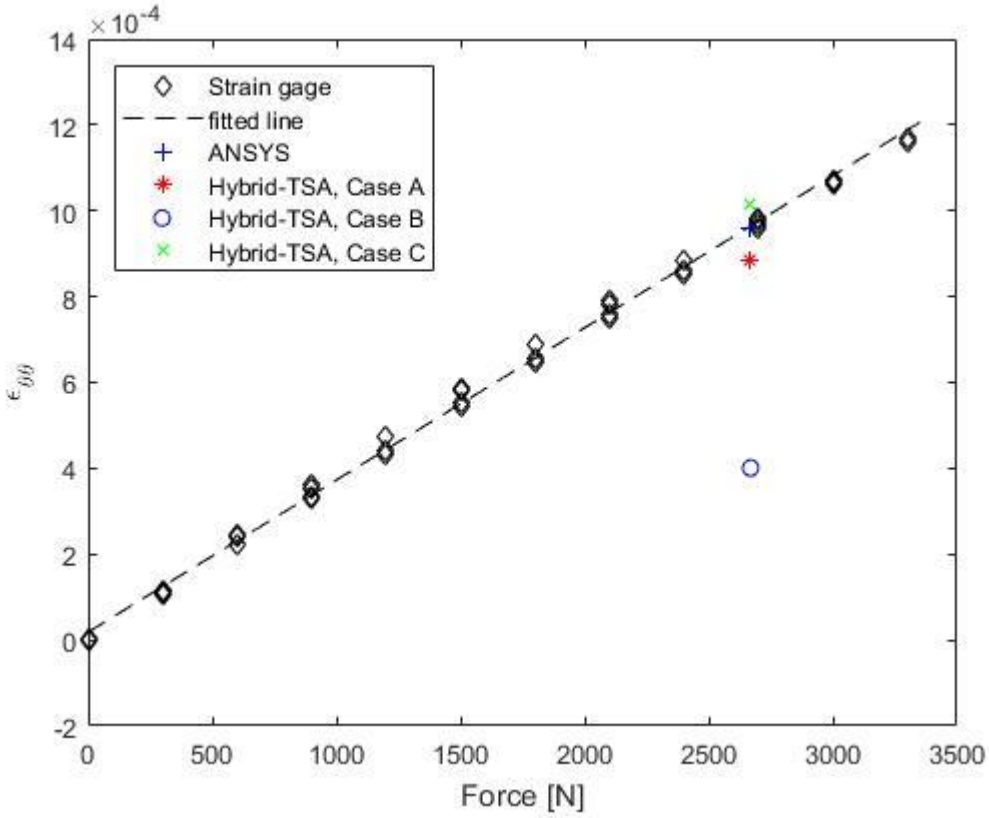

Figure 4.6.13: Strain gage result compared with ANSYS and two cases of Hybrid-TSA

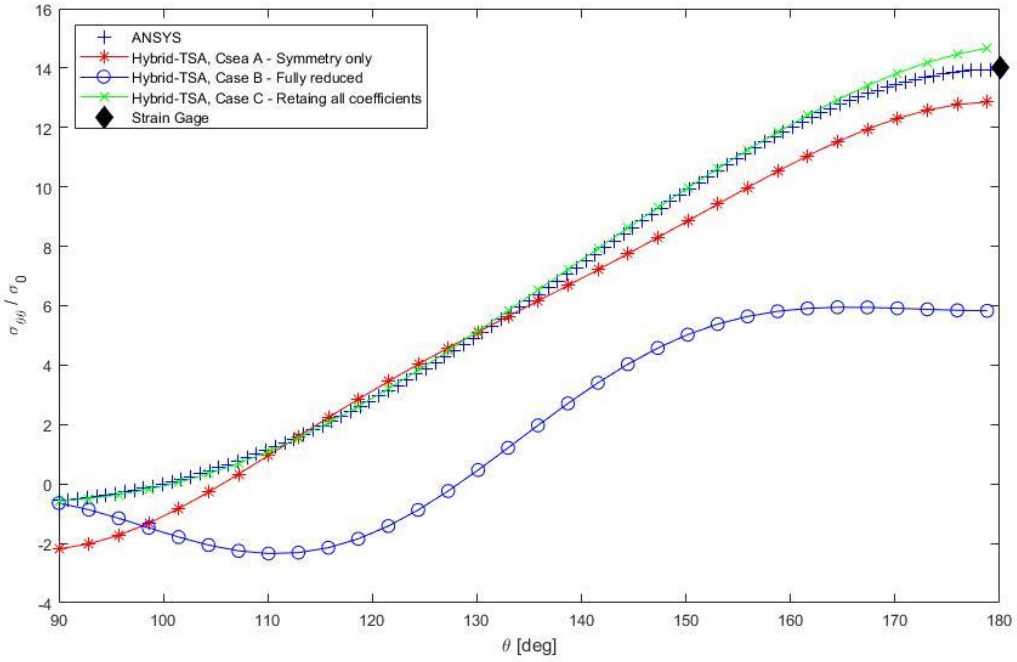

Figure 4.6.14: Normalized tangential stress with strain gage, $\sigma_{\theta\theta}/\sigma_0$

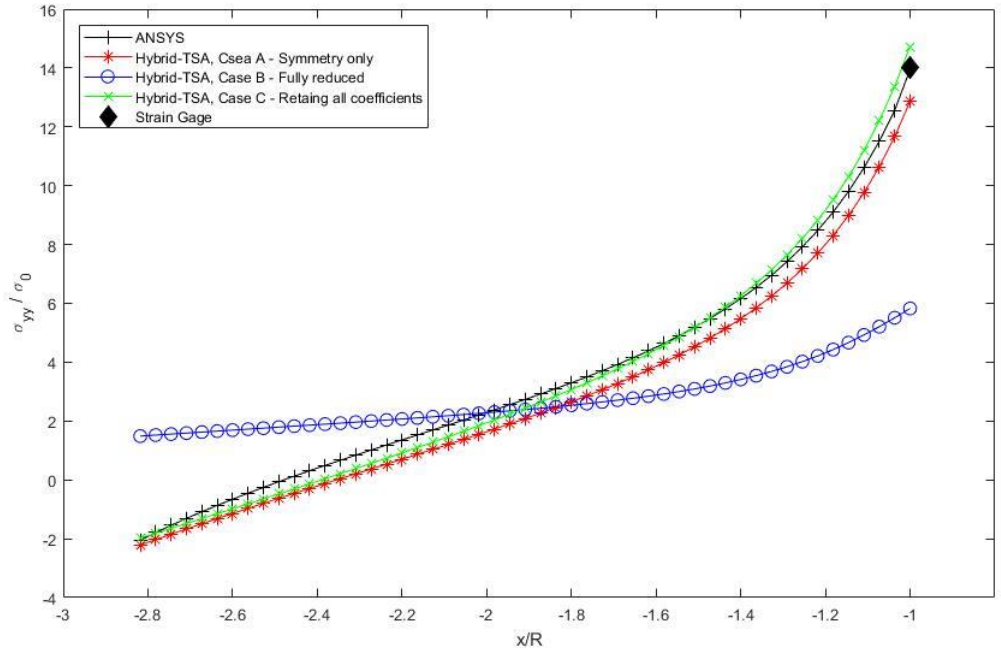

Figure 4.6.15: Normalized vertical stress, σ_{yy}/σ_0, with strain gage at $y = 0$

4.6.4 Symmetry about $y = 0$

TSA recorded isopachic stress, figure 4.5.6, was utilized to evaluate the Airy coefficients and the number of coefficients reduced based on assumption of symmetry with respect to $y = 0$ for both Cases A and B. Figures 4.6.16 through 4.6.18 plot normalized isopachic, radial and tangential stress throughout the plate for these cases to see if they are symmetrical about $y = 0$. Case A and B are symmetrical about $y = 0$. Case C is not. Results of Cases A and B can symmetrically reproduce the bottom half of the plate when only the averaged upper half of the TSA recorded input is utilized. Case C can reconstruct upper half very well while the bottom half is not symmetrical. This is due to not assuming the Airy coefficients related to symmetrical condition equal to zero. Appendix includes results using full-plate input isopachic stress when retaining all Airy coefficients.

A theoretician might adversely view this inability of Case C to provide reliable stresses in both the two halves of this mechanically and geometrically symmetrical structure. However, this is probably not a practical concern since once can visually flip the results of the half plate containing the experimental input data to the other half of the plate.

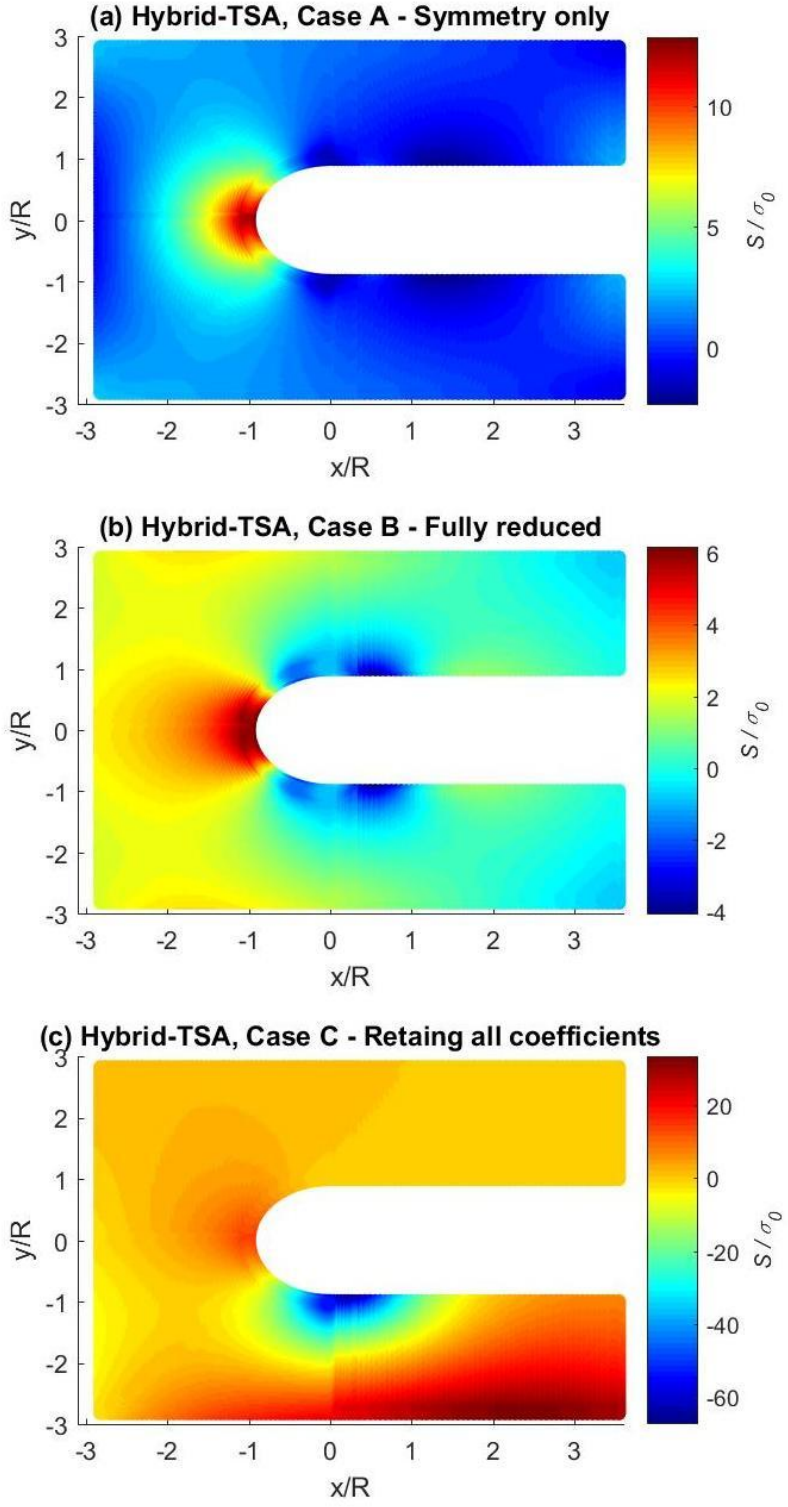

Figure 4.6.16: Normalized isopachic stress, S/σ_0, on entire plate

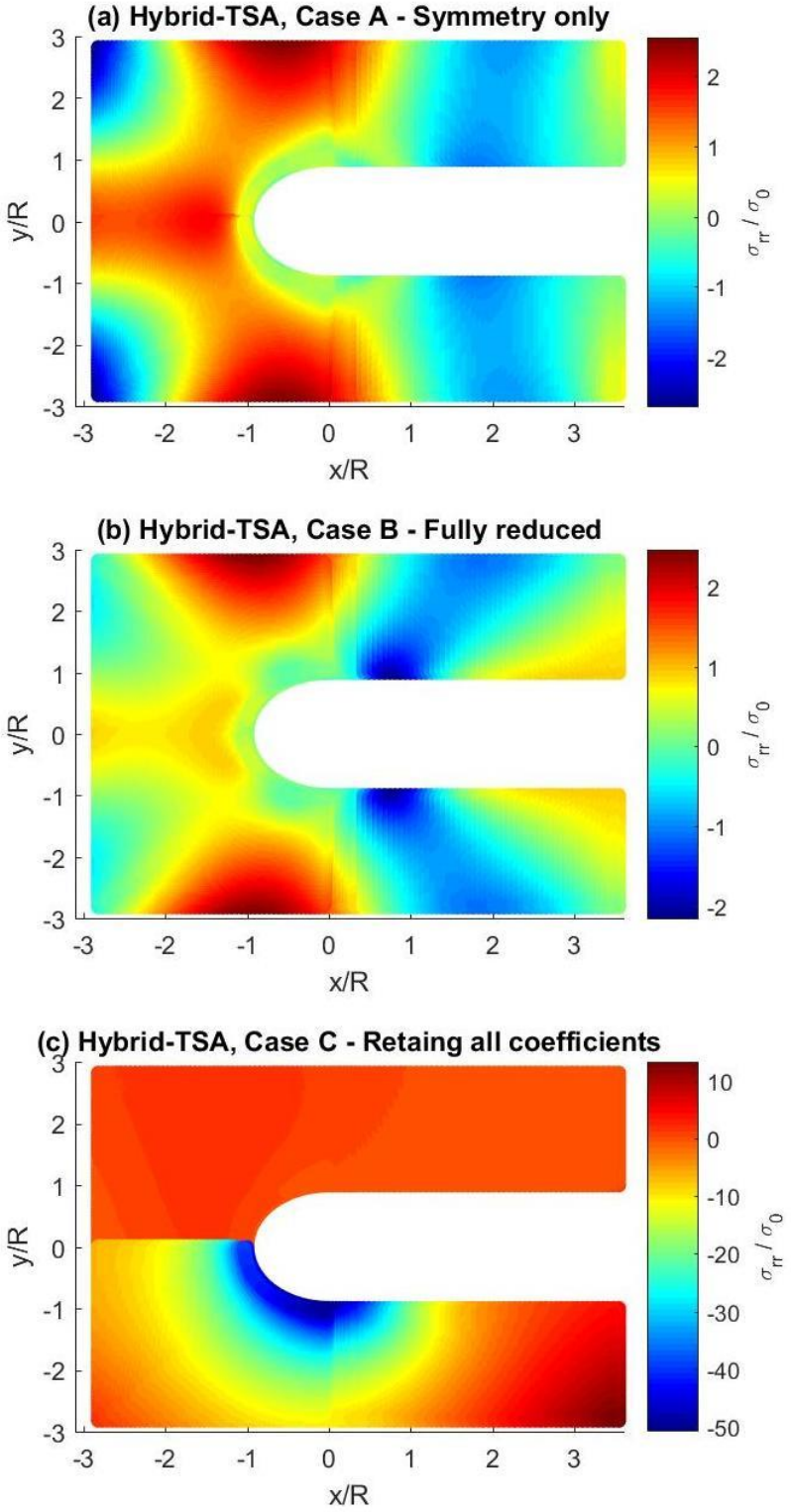

Figure 4.6.17: Normalized radial stress, σ_{rr}/σ_0, on entire plate

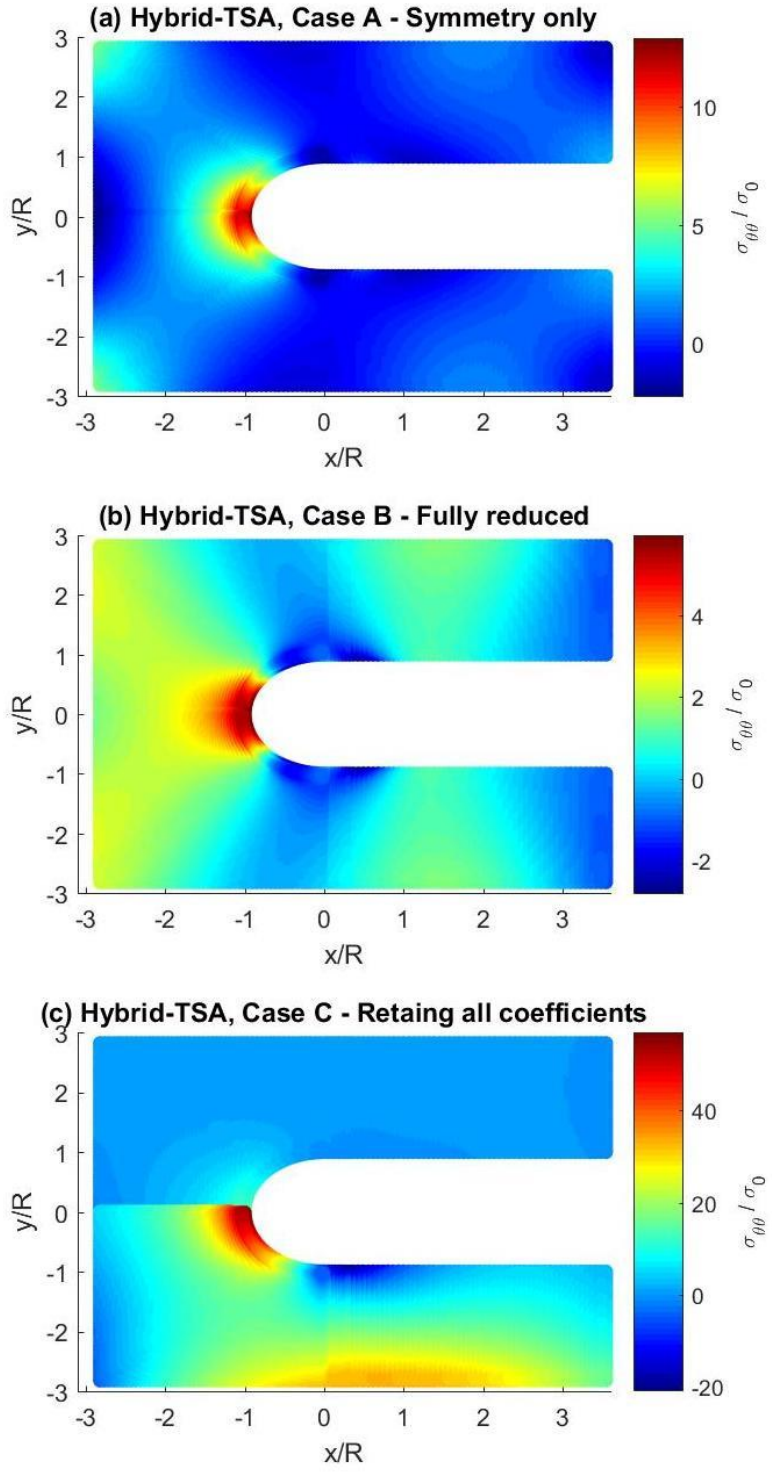

Figure 4.6.18: Normalized tangential stress, $\sigma_{\theta\theta}/\sigma_0$, on entire plate

4.7 Numerical Experiment

To help ensure the equations are correct and that the approach is numerically stable and robust, a numerical-hybrid approach based on Airy stress function was assessed using simulated (rather than TSA measured) input values of S ($=\Delta\sigma_{xx} + \Delta\sigma_{yy}$) from ANSYS.

4.7.1. Data Source Location and Airy Coefficient Evaluation

The results of this numerical experiment are based on m = 8,109 input values of S from ANSYS, figure 4.7.1, in addition to 2,000 boundary conditions ($h = 500 \times 4 = 2{,}000$) along the edges noted in figure 4.3.1. FEM-predicted values of S throughout only the shaded part of figure 4.7.1 are utilized to correlate with TSA recorded data.

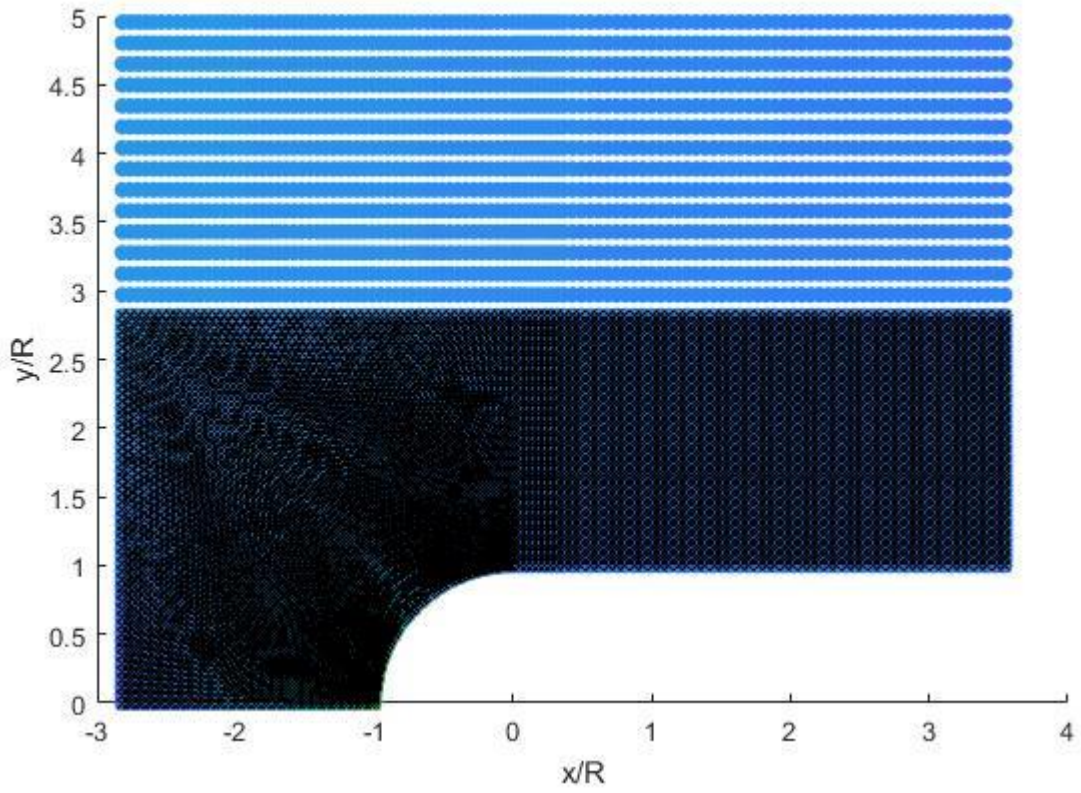

Figure 4.7.1: Source locations of employed data in shaded area (*m* = 8,109 values)

The same method was used to determine the presently appropriate number of Airy coefficients to retain as was employed in section 4.5.4. A total of 27, 25, and 49 Airy coefficients ($N = 5$) were evaluated for the Case A, B and C, respectively. Figure 4.7.2 shows *RMS* values of Cases A, B, and C. As the number of the terminating index, *N*, increases, *RMS* values decrease for all cases. Case B again has significantly higher *RMS* values than the other two cases. Figure 4.7.3 shows average value of normalized forces for increasing *N*. Case C is very stable, however, like for experimental input of figure 4.5.8, Cases A and B tend to be unstable after *N* exceeds 5.

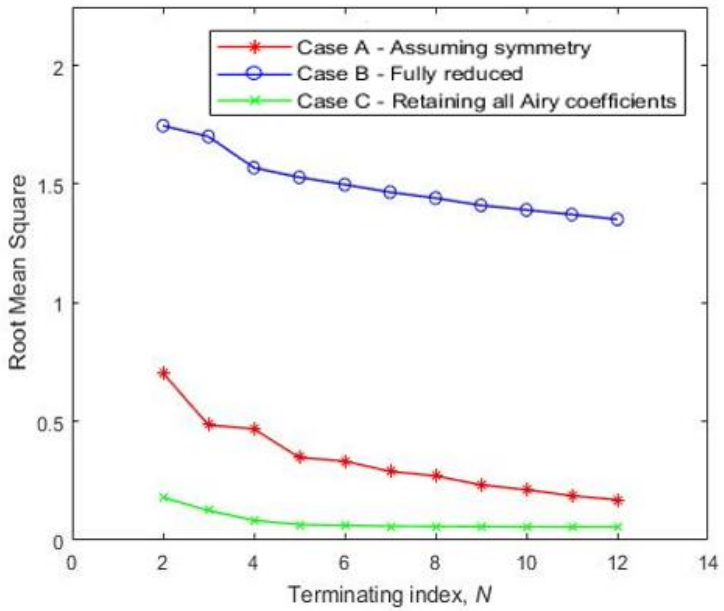

Figure 4.7.2: RMS vs terminating index, *N*

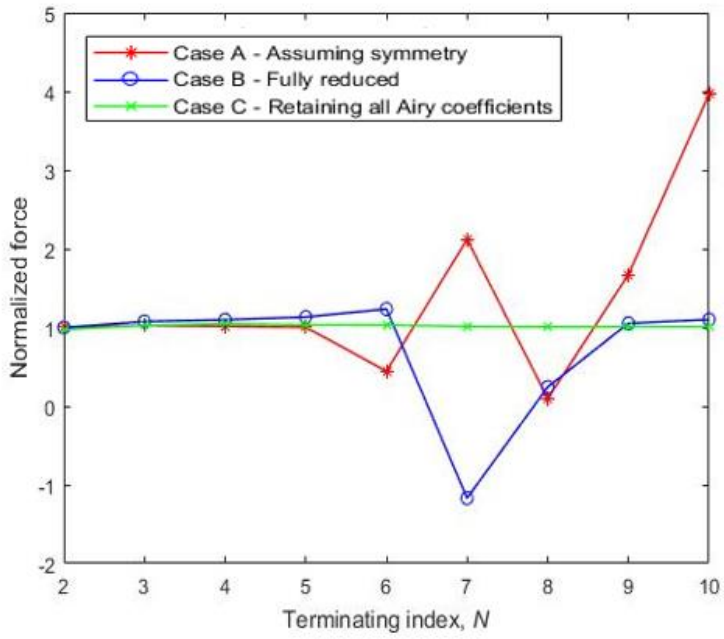

Figure 4.7.3: Average value of normalized forces calculated on the respective horizontal lines of *y*-axis vs terminating index, *N*

4.7.2 Stresses and Results

Figure 4.7.4 correspond to figures 4.6.3 but which was for the recorded TSA input. Case B again performs here badly. Reconstructed results from Case A and C are almost identical to the direct results from ANSYS while results from Case B again shows discrepancies from others. Figure 4.7.5 shows contours of normalized isopachic stress, S/σ_o, of the original ANSYS-simulated (upper) and the three reconstructed cases using hybrid-TSA method (lower). The ANSYS-simulated data is used as input values for evaluating the Airy coefficients (which replaces experimentally recorded data); thus, if the reconstructed stresses agree with the ANSYS-simulated input, the method used in this chapter can be considered to be validated. Figures 4.7.5 to 4.7.11 plot normalized individual components of stress for ANSYS-simulated (upper) and reconstructed using hybrid-TSA methods for the three cases (lower) based on ANSYS-simulated isopachic stress, S. The contour plots of figures 4.7.5 through 4.7.11 again show the poor performance of Case B on the edge of the notch at $\theta = 180^{\circ}$ which is so pronounced in figure 4.7.4.

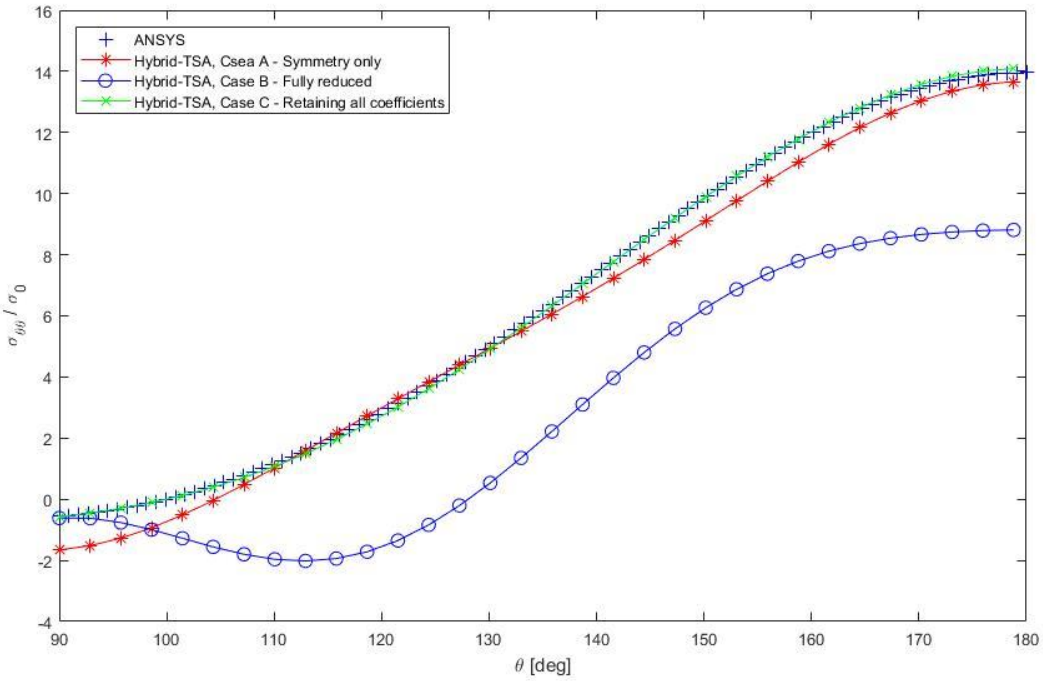

Figure 4.7.4: Normalized tangential stress, $\sigma_{\theta\theta}/\sigma_0$, along the edge of the notch when Hybrid-TSA based on ANSYS simulated input values of *S* and applied boundary conditions

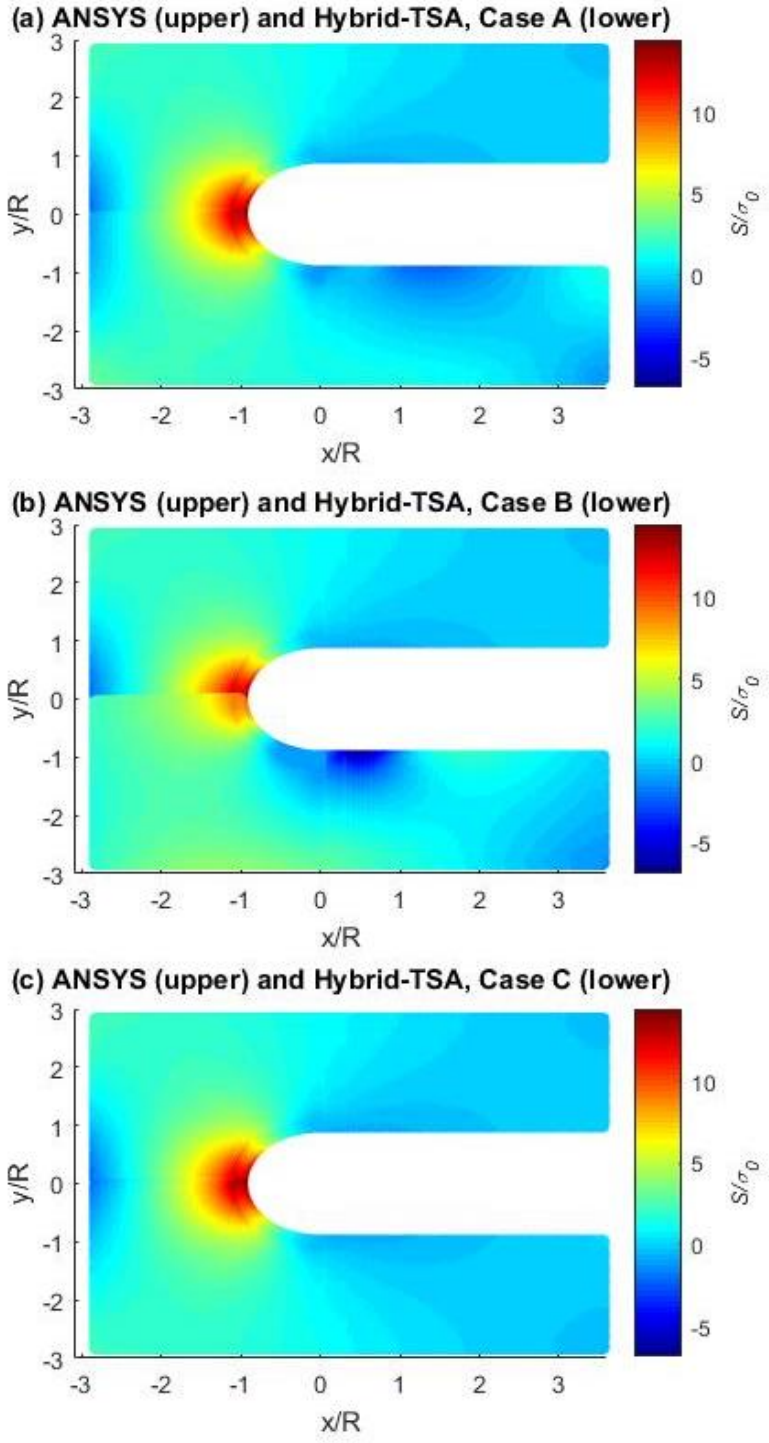

Figure 4.7.5: Normalized isopachic stress, S/σ_0, for ANSYS and reconstructed for hybrid-TSA method for three cases based on ANSYS-simulated input values of S and applied boundary conditions

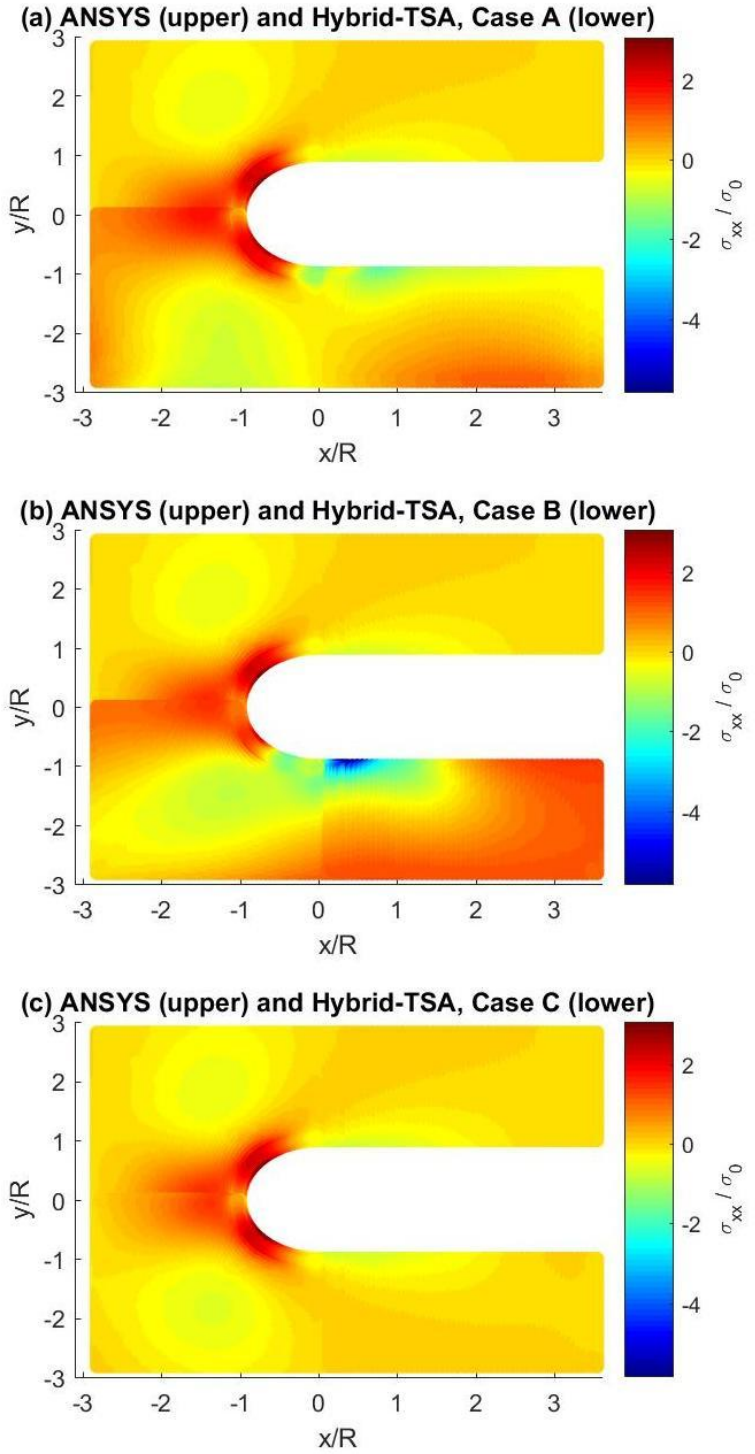

Figure 4.7.6: Normzlized horizontal stress, σ_{xx}/σ_0, for ANSYS and recontructed for hybrid-TSA method for three cases based on ANSYS-simulated input values of S

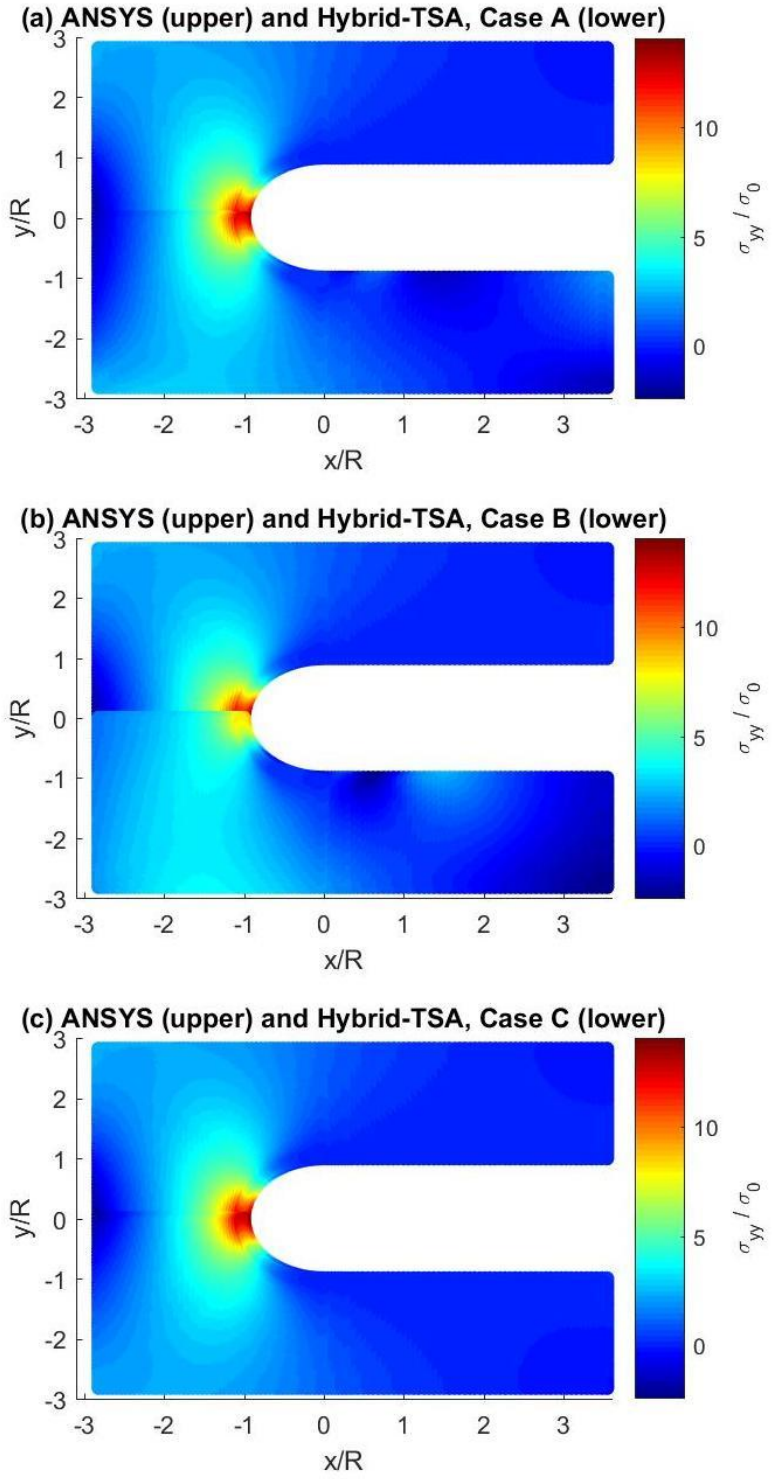

Figure 4.7.7: Normzlized vertical stress, σ_{yy}/σ_0, for ANSYS and recontructed for hybrid-TSA method for three cases based on ANSYS-simulated input values of S

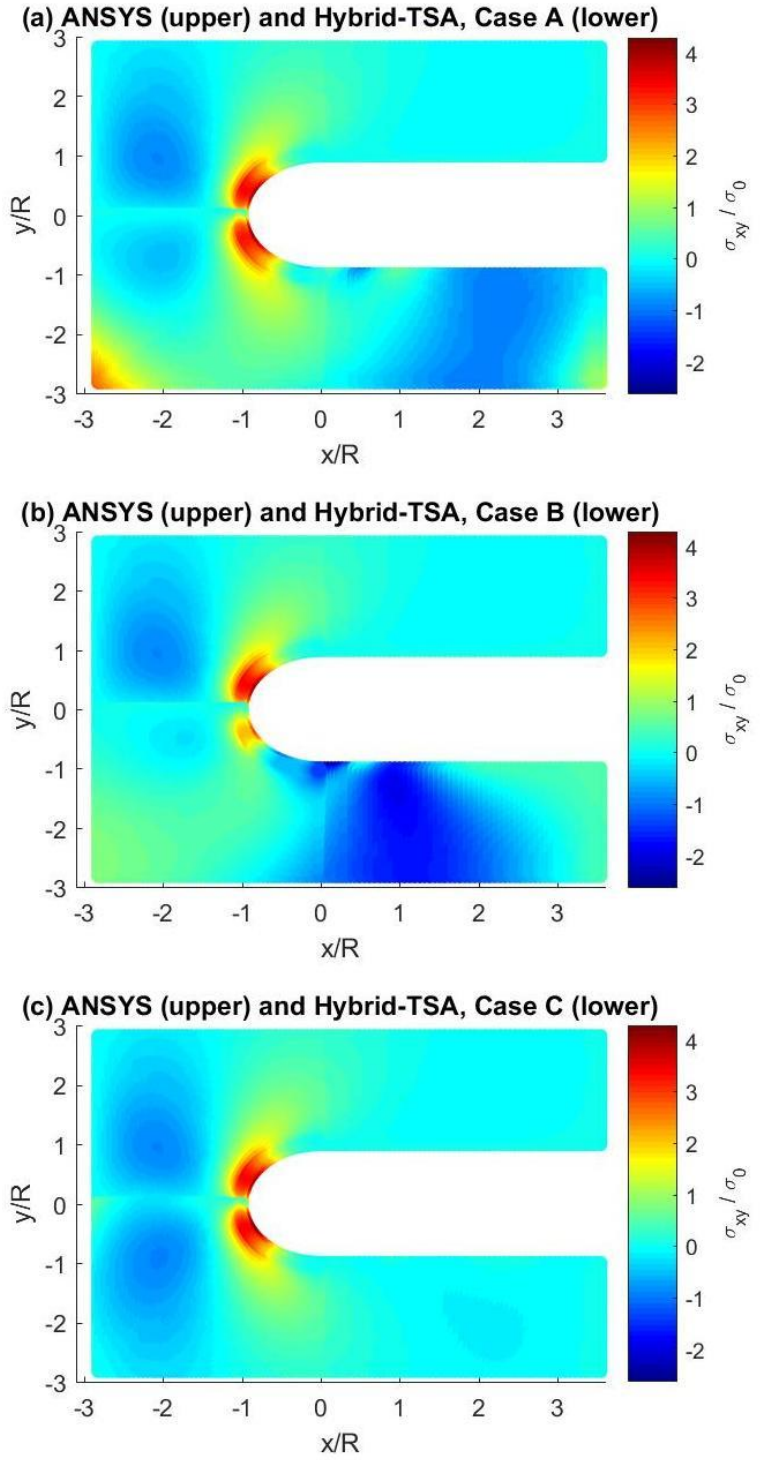

Figure 4.7.8: Normzlized shear stress, σ_{xy}/σ_0, for ANSYS and recontructed for hybrid-TSA method for three cases based on ANSYS-simulated input values of S

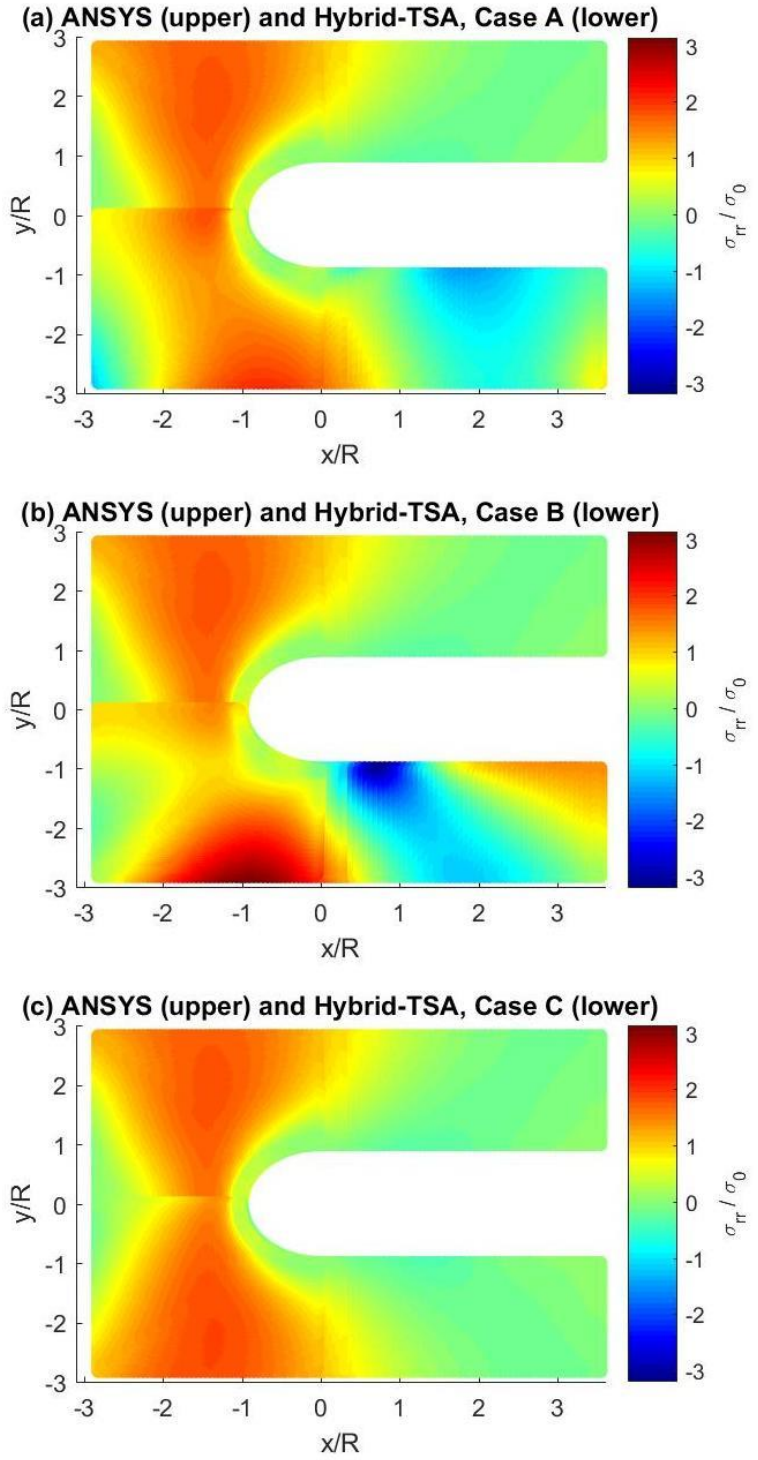

Figure 4.7.9: Normzlized radial stress, σ_{rr}/σ_0, for ANSYS and recontructed for hybrid-TSA method for three cases based on ANSYS-simulated input values of S

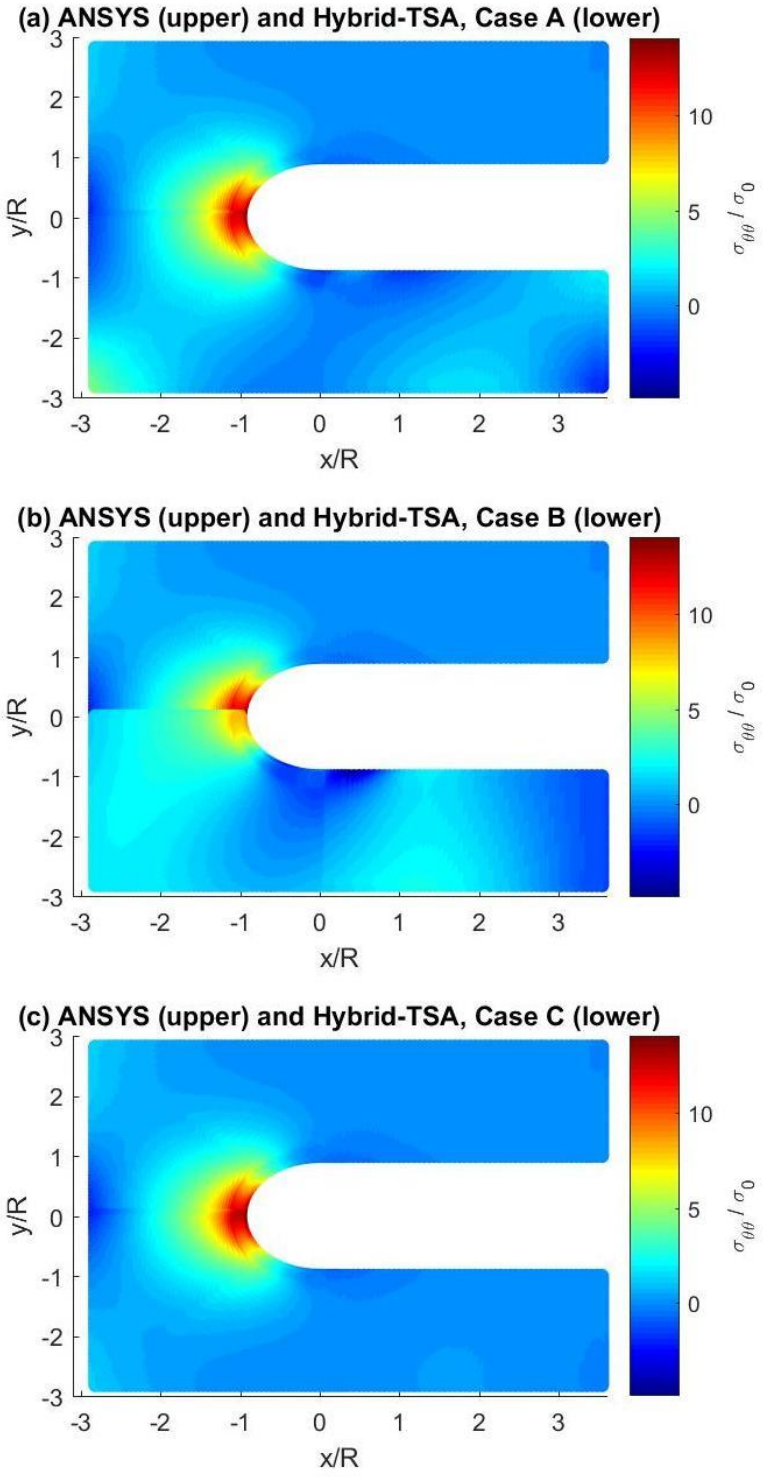

Figure 4.7.10: Normzlized tangential stress, $\sigma_{\theta\theta}/\sigma_0$, for ANSYS and recontructed for hybrid-TSA method for three cases based on ANSYS-simulated input values of S

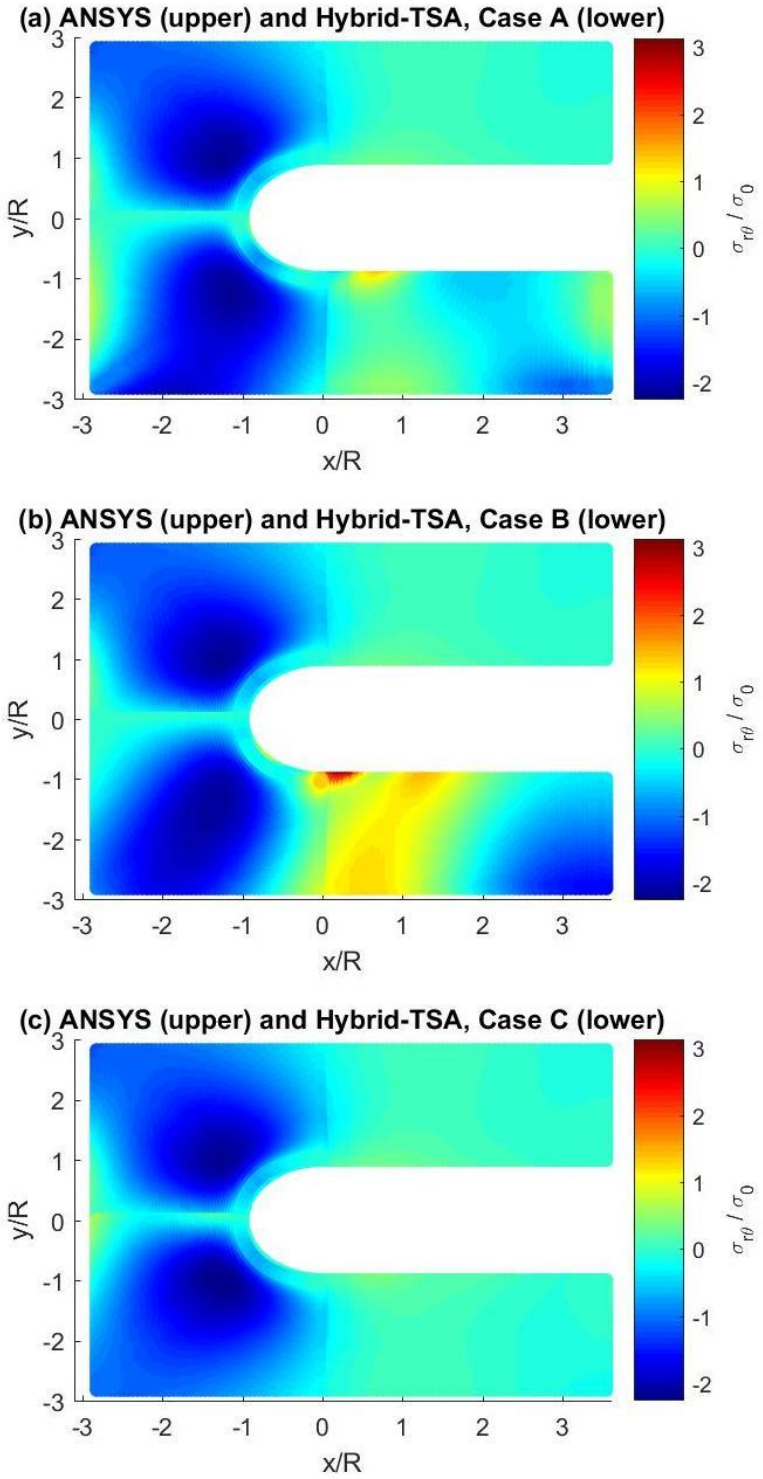

Figure 4.7.11: Normzlized shear stress, $\sigma_{r\theta}/\sigma_0$, for ANSYS and recontructed for hybrid-TSA method for three cases based on ANSYS-simulated input values of S

4.7.3 Force equilibrium

Figure 4.7.12 is a plot of the total force calculated on various horizontal lines (from $y/R = 0$ to 2.2) using equation (4.12). Computed loads are normalized with the physically applied force of 2,670 N and shown in figure 4.7.12 for each of the three cases. The average values of these normalized forces are 0.984, 1.093, and 1.049 for Case A, B, and C, respectively. The story here is similar to that of figure 4.6.10.

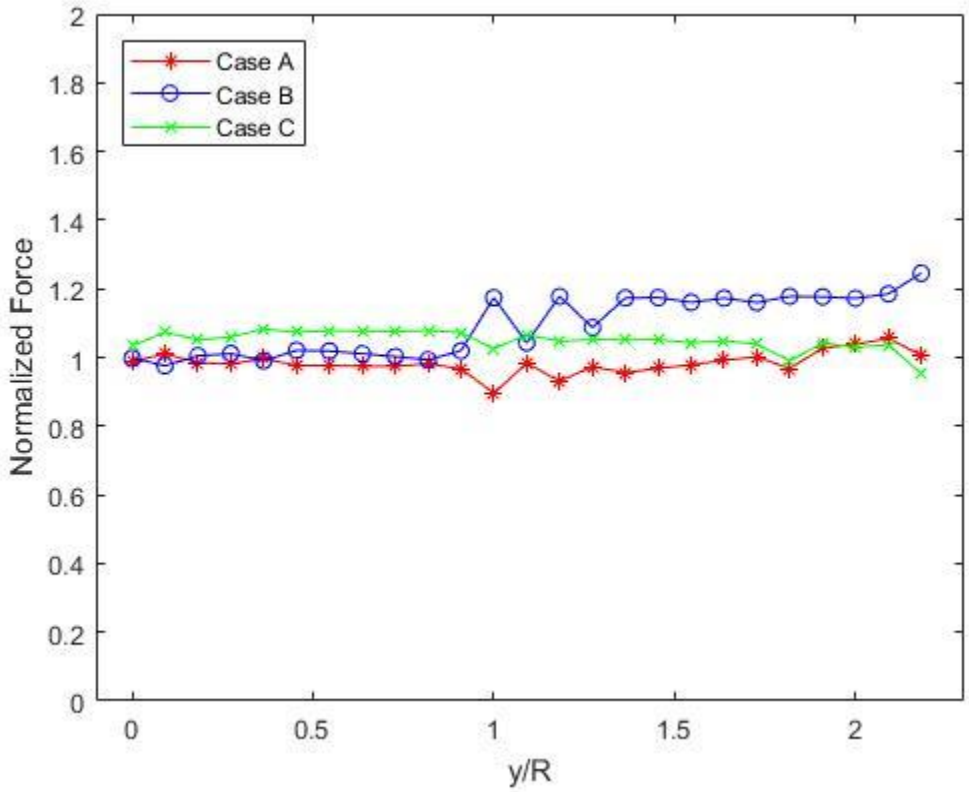

Figure 4.7.12: Force equilibrium on horizontal lines

4.7.4 Effect of Applying Boundary Conditions

The effect of whether or not one discretely applies the boundary conditions associated with figure 4.3.1 was also studied. When evaluating the Airy coefficients, but without applying any of the boundary condition shown in section 4.3.2, the hybrid-TSA method was able to reconstruct S, figure 4.7.13. However, without applying the boundary conditions, the evaluated Airy coefficients could not reconstruct individual stress components. Figure 4.7.14 compares normalized tangential stress for ANSYS and Hybrid-TSA with and without any applied boundary conditions. The latter is not very good since equation (4.6) for isopachic stress does not contain coefficients which appear in expressions of individual components of stress (i.e., b_0, A_0, B_0, c_1, c'_1, a_n, c_n, a'_n, c'_n).

The effect of how many boundary conditions to employ is also studied using similar approach of section 4.5.4. Instead of increasing the terminating index, N, of section 4.5.4, the number of applied boundary condition is increased here. Figure 4.7.15 plots *RMS* of isopachic stress for these cases with increasing number of imposed boundary condition. All three cases are relatively constant with respect to varying number of applied boundary conditions. Figure 4.7.16 shows average normalized force for increasing number of boundary conditions; again, these are very consistent starting from only 100 boundary conditions.

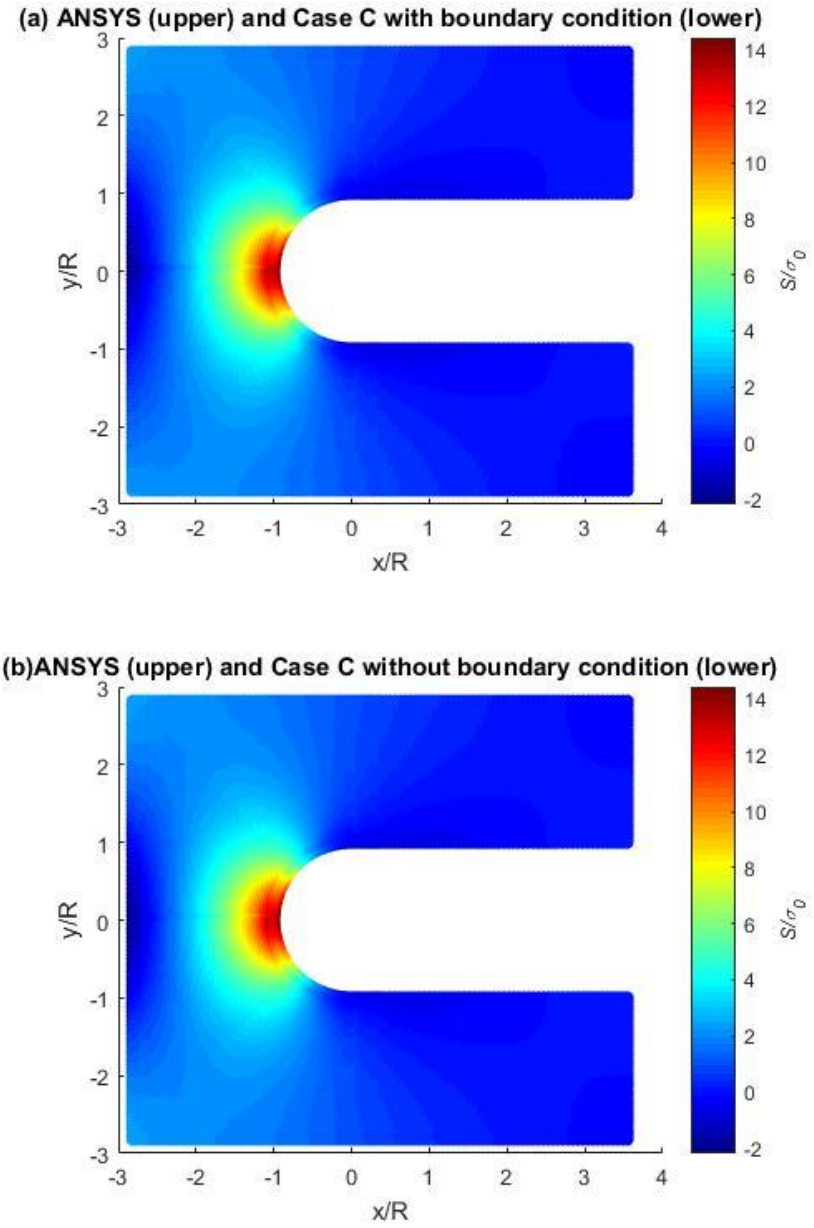

Figure 4.7.13: Normalized isopachic stress, S/σ_0, when Hybrid-TSA with Case C based on ANSYS simulated input values of S with and without applying boundary conditions

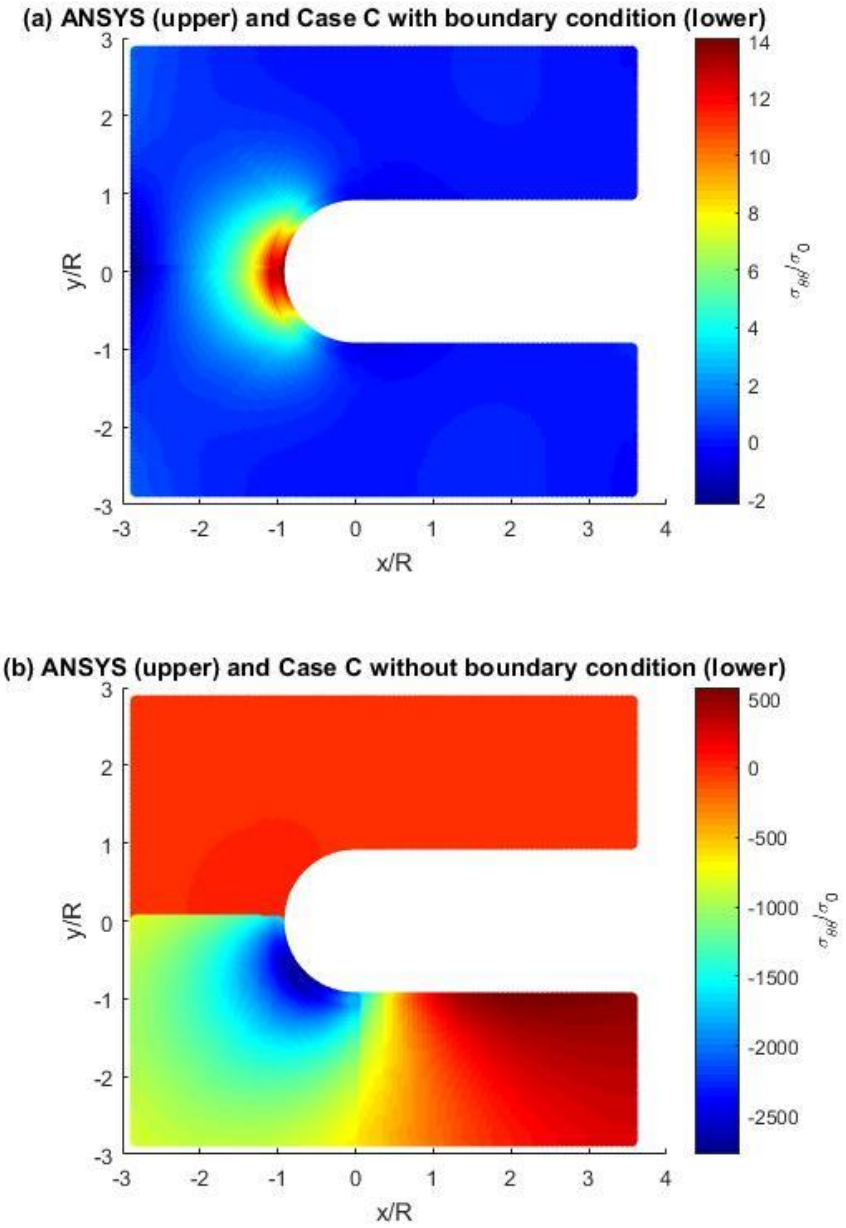

Figure 4.7.14: Normalized tangential stress, $\sigma_{\theta\theta}/\sigma_0$, when Hybrid-TSA with Case C based on ANSYS simulated input values of *S* with and without applying boundary conditions

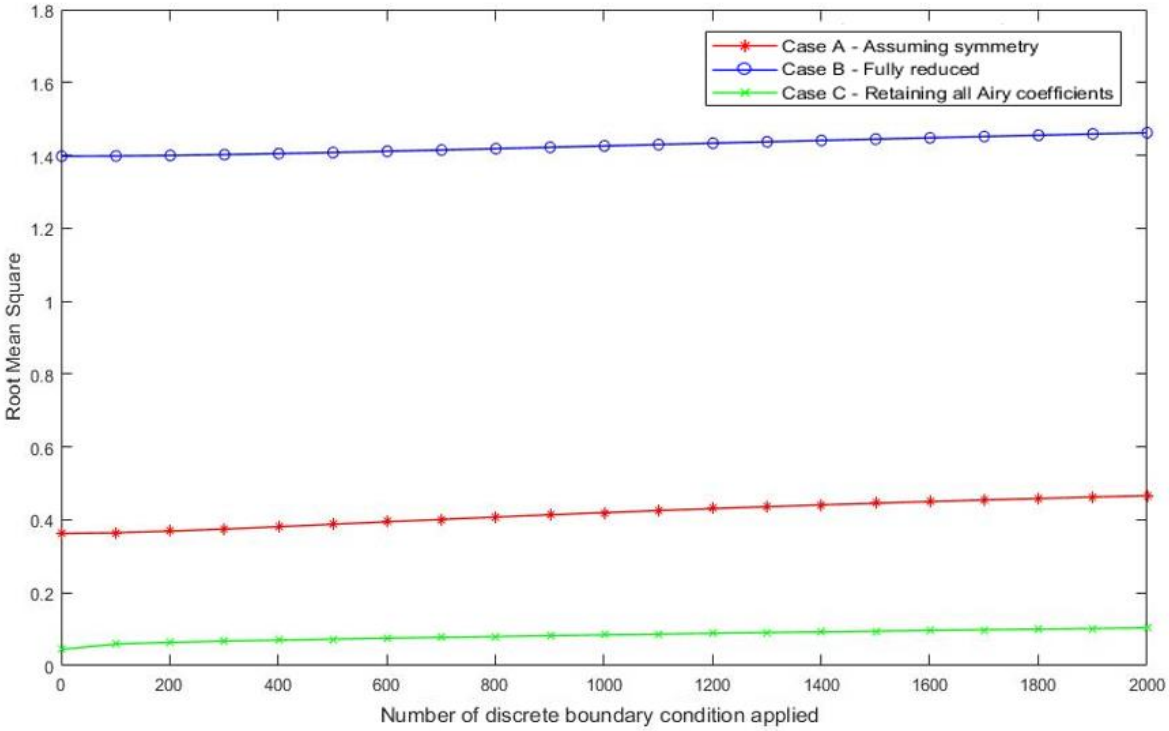

Figure 4.7.15: *RMS* of isopachic stress vs number of boundary condition

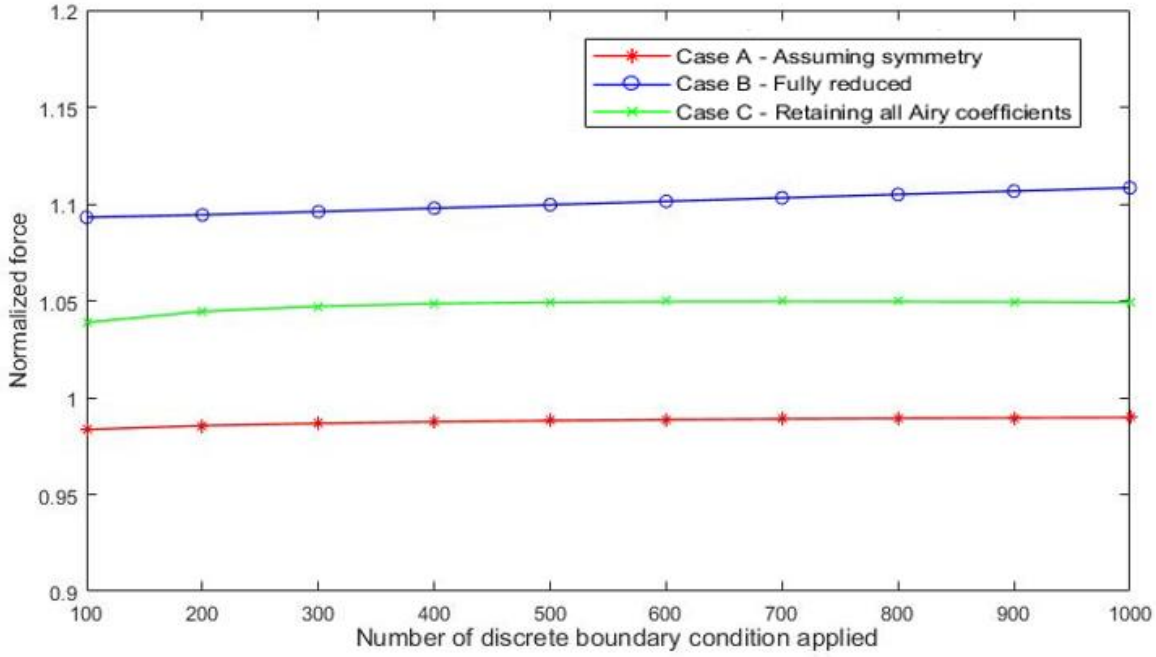

Figure 4.7.16: Average normalized force vs number of boundary condition

4.8 Magnitudes of Airy Coefficients

Tables 4.8.1 and 4.8.2 list the evaluated Airy coefficients of equation (4.6) based on TSA-recorded (Hybrid-TSA) and ANSYS simulated (results of numerical experiment, section 4.7) isopachic stress *S*. The magnitudes of some of the corresponding coefficients of the two tables are quite different from each other while others are reasonably similar. Reference [2] indicates that if there is mechanical and geometric symmetry about the *x*-axis, coefficients A_0, B_0, C_0, D_0, d_0, A'_1, B_1, B'_1, a_n, b_n, c_n, and d_n ($n \geq 1$) should be zero. As highlighted in yellow, these are all satisfied in tables 4.8.1 and 4.8.2 for Cases A and B (where they were imposed). If the coordinate origin lies within the structure, coefficients $do = Bo = Co = Do = B_1 = 0$, and A_1, A'_1, b_1, and b'_1 should also be zero if there is no resultant force at the origin. On the other hand, if the origin does not lie within a simply-connected structure, then B_0, C_0, D_0, B_1 and B'_1 must be included. The latter are zero due to symmetry in Cases A and B in tables 4.8.1 and 4.8.2, but not for Case C. Coefficients A_1 and b'_1 are zero for Case B but non-zero for Case A. If the origin lies within the structure, coefficients A_1, A'_1, b_1, and b'_1 are associated with resultant forces at the origin. However, in this situation the non-zero A_1 and b'_1 of case A occur when the origin lies outside of a simply-connected structure. The physical connotation of A_1, A'_1, b_1, and b'_1 when the origin lies beyond the boundary of a simply-connected geometry is uncertain [2].

Table 4.8.1: Evaluated Airy coefficients based on isopachic stress, *S*, from TSA

	Case A	Case B	Case C		Case A	Case B	Case C		Case A	Case B	Case C
c_0	110.3	255.0	-3,029.6	d_3	0.0	0.0	64.0	a_3	0.0	0.0	14.0
d_0	0.0	0.0	2,787.6	d_4	0.0	0.0	20.3	a_4	0.0	0.0	-4.2
C_0	0.0	0.0	299.1	d_5	0.0	0.0	2.6	a_5	0.0	0.0	-1.0
D_0	0.0	0.0	-164.3	b'_2	-17.8	-19.7	-219.3	c_2	0.0	0.0	90.0
b_1	0.0	0.0	3,296.7	b'_3	10.7	2.3	-15.2	c_3	0.0	0.0	-8.1
d_1	0.0	0.0	-1,070.8	b'_4	-0.7	1.0	3.6	c_4	0.0	0.0	-3.9
b'_1	-1,863.7	0.0	-5,739.2	b'_5	0.8	-0.2	0.0	c_5	0.0	0.0	-0.6
d'_1	186.4	-57.6	510.4	d'_2	3.4	-353.8	-1,030.9	a'_2	321.9	337.0	353.8
A_1	-206.8	0.0	2,337.5	d'_3	66.0	-54.2	-111.0	a'_3	-53.7	-62.5	27.0
B_1	0.0	0.0	-286.9	d'_4	14.7	-23.4	-7.8	a'_4	-23.2	-17.3	10.0
A'_1	0.0	0.0	-2,518.0	d'_5	3.0	-6.3	0.4	a'_5	2.5	5.0	-0.2
B'_1	0.0	0.0	259.8	b_0	-20.7	-130.7	-1,731.2	c'_2	-22.0	56.9	121.8
b_2	0.0	0.0	-126.9	A_0	0.0	0.0	2,938.0	c'_3	-19.7	13.4	20.9
b_3	0.0	0.0	37.5	B_0	0.0	0.0	1,406.3	c'_4	-5.0	6.3	2.1
b_4	0.0	0.0	0.9	c_1	0.0	0.0	538.5	c'_5	-1.0	1.8	0.0
b_5	0.0	0.0	-0.1	c'_1	-365.2	-6.9	-585.2				
d_2	0.0	0.0	-524.4	a_2	0.0	0.0	793.1				

Table 4.8.2: Evaluated Airy coefficients based on isopachic stress, *S*, from ANSYS

	Case A	Case B	Case C		Case A	Case B	Case C		Case A	Case B	Case C
c_0	131.2	374.8	48,075.5	d_3	0.0	0.0	-85.1	a_3	0.0	0.0	-20.4
d_0	0.0	0.0	-35,083.9	d_4	0.0	0.0	-6.7	a_4	0.0	0.0	1.2
C_0	0.0	0.0	-25,844.3	d_5	0.0	0.0	0.6	a_5	0.0	0.0	-0.1
D_0	0.0	0.0	19,581.3	b'_2	-26.0	-44.9	49.8	c_2	0.0	0.0	182.1
b_1	0.0	0.0	6,993.8	b'_3	9.7	5.0	-59.9	c_3	0.0	0.0	31.7
d_1	0.0	0.0	908.6	b'_4	-1.4	2.1	0.9	c_4	0.0	0.0	3.3
b'_1	-1,887.0	0.0	-49,048.8	b'_5	1.1	-0.4	0.1	c_5	0.0	0.0	0.0
d'_1	188.2	-46.8	6,927.1	d'_2	-13.9	-528.9	53.1	a'_2	351.5	467.2	540.6
A_1	-220.8	0.0	-4,426.4	d'_3	62.3	-90.5	-18.0	a'_3	-56.0	-86.3	-16.6
B_1	0.0	0.0	-10,043.4	d'_4	10.9	-35.2	-12.8	a'_4	-8.6	-22.5	0.9
A'_1	0.0	0.0	362.0	d'_5	2.5	-6.3	-1.6	a'_5	-1.0	5.7	0.0
B'_1	0.0	0.0	3,681.4	b_0	-38.8	-203.0	-25,332.0	c'_2	-19.6	87.5	-182.1
b_2	0.0	0.0	-607.0	A_0	0.0	0.0	20,602.9	c'_3	-18.9	22.9	-4.9
b_3	0.0	0.0	3.5	B_0	0.0	0.0	13,116.7	c'_4	-4.1	9.7	2.9
b_4	0.0	0.0	4.0	c_1	0.0	0.0	-1,313.1	c'_5	-0.9	1.9	0.4
b_5	0.0	0.0	-0.1	c'_1	-371.1	1.3	-3,668.7				
d_2	0.0	0.0	-712.0	a_2	0.0	0.0	338.6				

4.8.1 Single-Valueness of Airy Coefficient

The isopachic, radial, tangential, and shear stresses of these three cases (A, B and C) were checked to see if they are single valued. Matrix [A] for each individual component of stress was regenerated for θ+360º and the stresses were reconstructed, figures 4.8.1 to 4.8.4. Cases A and B, where appropriate coefficients were omitted to make these cases symmetrical stress-wise, reproduce the same stresses for original θ and for θ+360º, Case C does not. For single-valued stresses, Airy coefficients $d_0 = B_0 = C_0 = D_0 = B_1 = 0$ must be selected to be zero [2]. The inability of stresses of Case C to be single-valued might be theoretically concerning. However, much less so from a practical point of view.

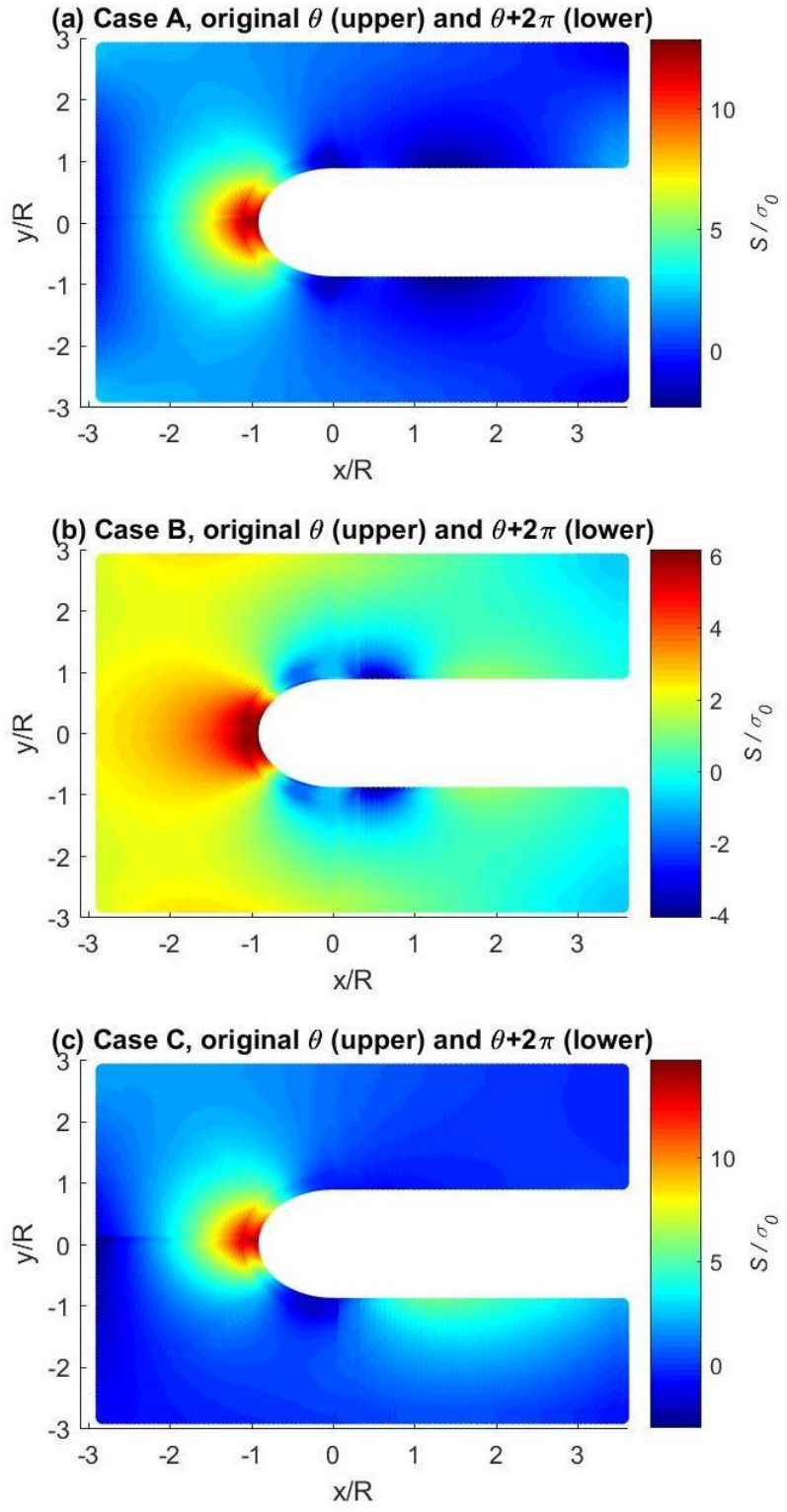

Figure 4.8.1: Normalized isopachic stress, S/σ_0, with original angle, θ (upper) and $\theta+2\pi$ (lower)

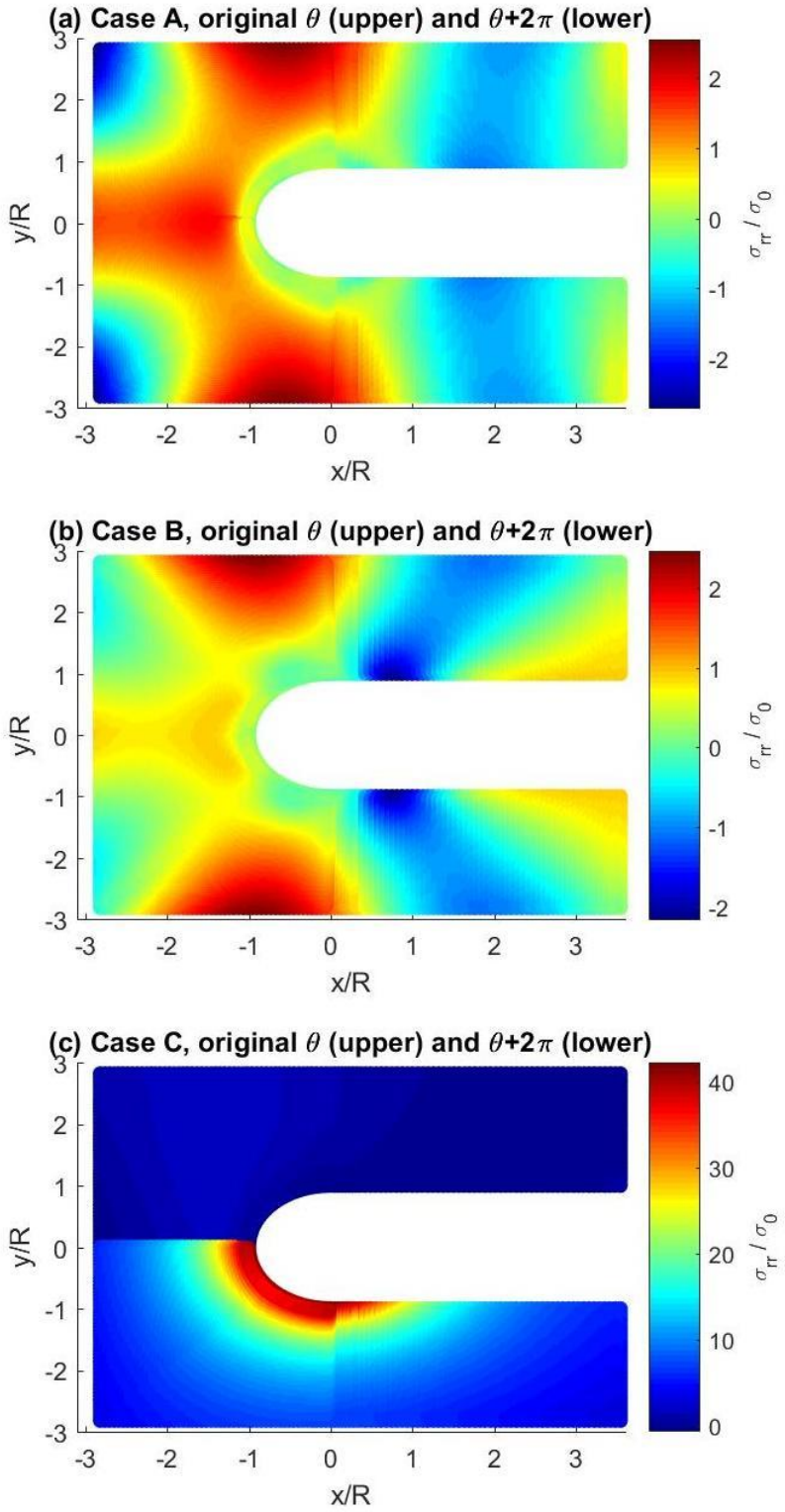

Figure 4.8.2: Normalized radial stress, σ_{rr}/σ_0, with original angle, θ (upper) and $\theta+2\pi$ (lower)

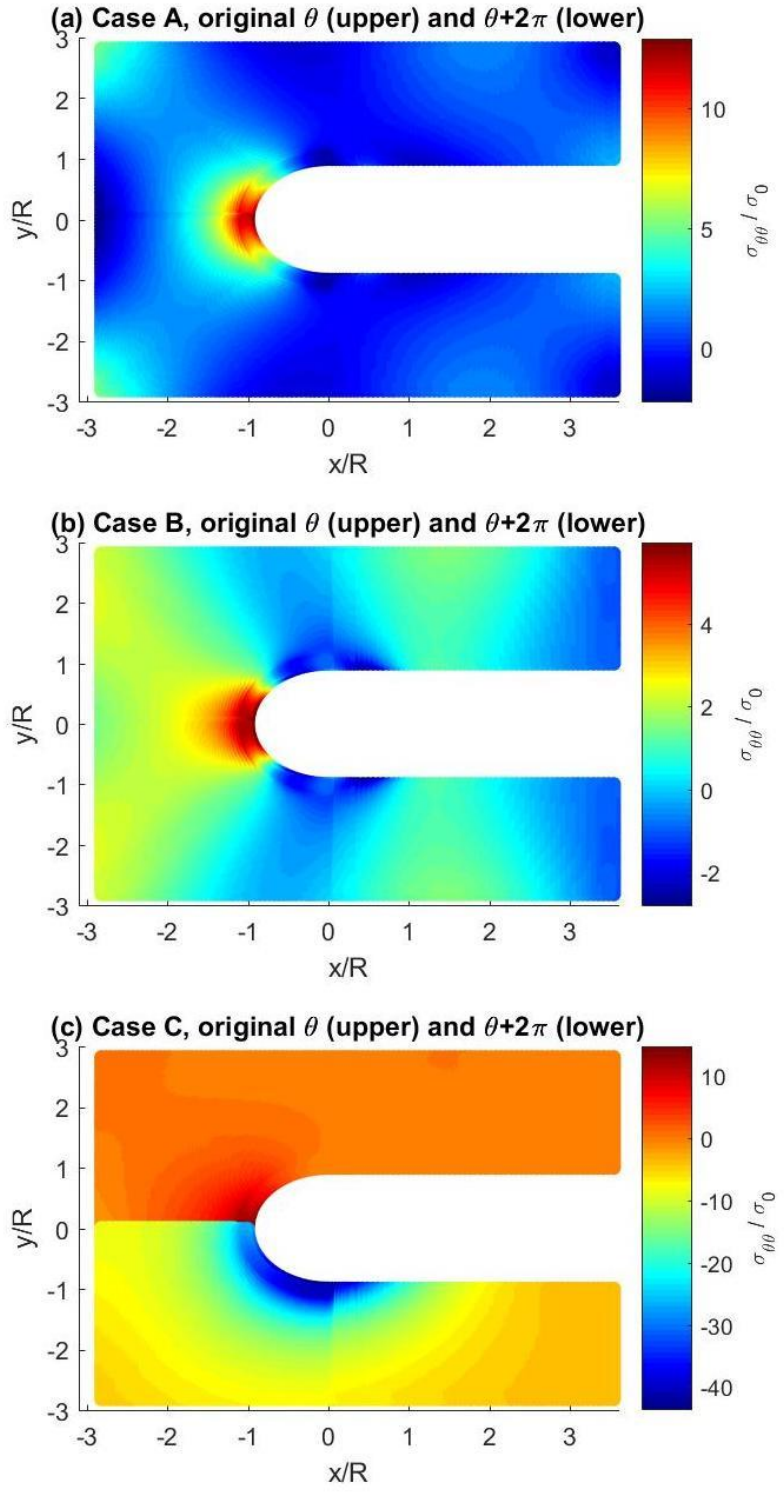

Figure 4.8.3: Normalized tangential stress, $\sigma_{\theta\theta}/\sigma_0$, with original angle, θ (upper) and $\theta+2\pi$ (lower)

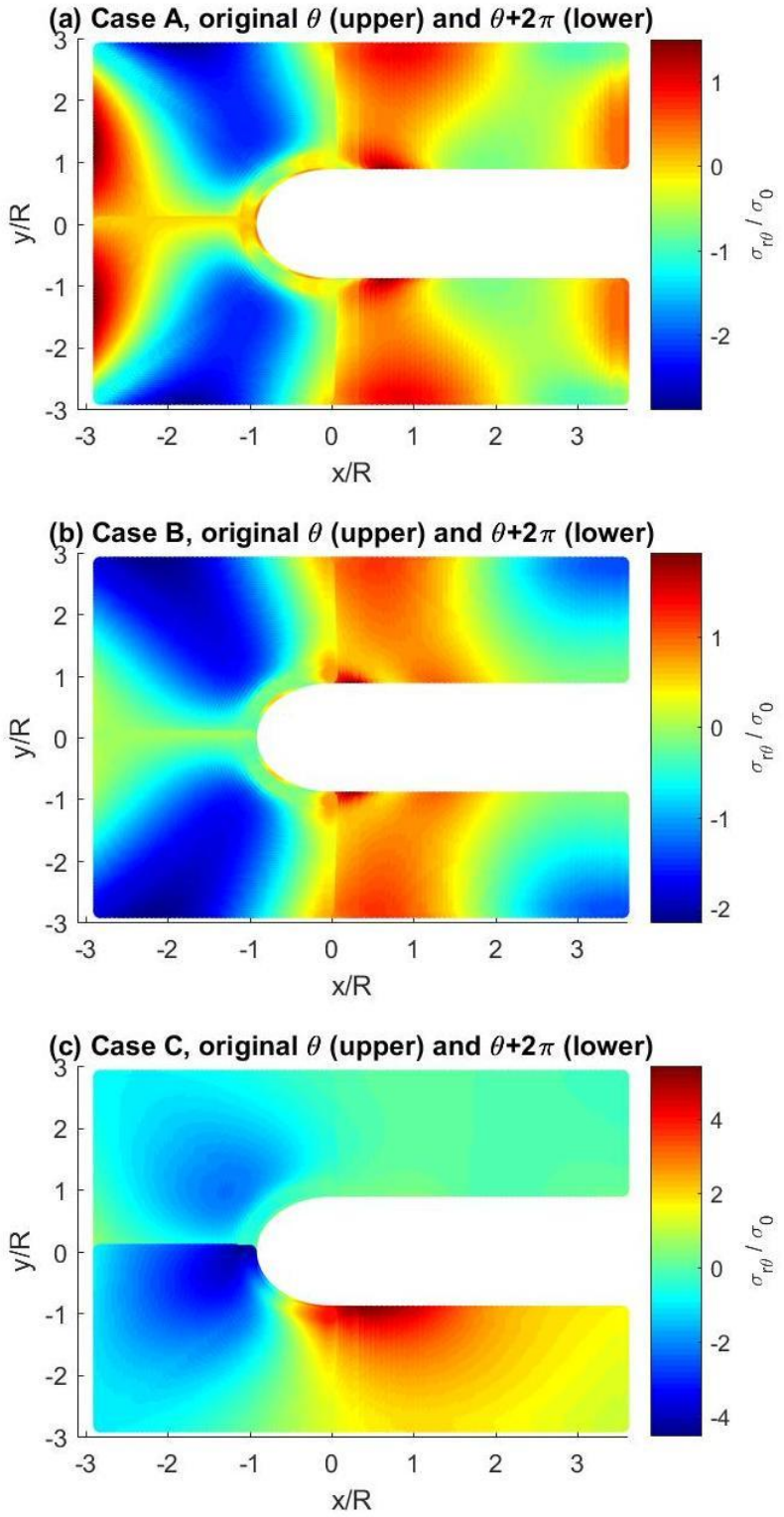

Figure 4.8.4: Normalized shear stress, $\sigma_{r\theta}/\sigma_0$, with original angle, θ (upper) and $\theta+2\pi$ (lower)

4.9 Summary, Discussion and Conclusions

A hybrid method which processes the load-induced TSA information with an Airy stress function, together with applying local conditions discretely, provides the individual stresses at and in the neighborhood of a deeply grooved finite plate. Unlike purely theoretical or numerical methods, knowledge of the external conditions is unnecessary. Employing more measured input values than unknown coefficients filters out experimental noise/scatter and smooths the results. A method was developed to separate reliably the recorded data into individual stresses and to evaluate accurate boundary information even though the recorded TSA data along and adjacent to the edges of the U-notch were not included. TSA results agree with those from FEA, force equilibrium and strain gage.

A series representation of the stress function is assumed, and careful attention was paid to determining which Airy coefficients to retain. The methods utilized here to ascertain how many coefficients to employ are general, not specific to the current data set or example, geometry or loading. The least-square technique was employed to evaluate unknown coefficients of overdetermined systems of equations.

A motivation for developing the present ability is to enable stress analysis of cases experimentally which cannot be analyzed theoretically or numerically, although FEM is used here. The geometry and loading of the plate of figure 4.1.1 are sufficiently simple that one can obtain a reliable FEM result against which to compare the experimental results. However, the developed Hybrid-TSA method is applicable to more complicated problems which are difficult/impossible for FEM, e.g., do not know the external loading. For example, while industry makes prevalent use of

FEM, strain gages are often employed in that environment to obtain the boundary conditions for the FEA.

Reference [2] indicates that if there is mechanical and geometric symmetry about the x-axis, coefficients A_0, B_0, C_0, D_0, d_0, A'_1, B_1, B'_1, a_n, b_n, c_n, and d_n ($n \geq 1$) should be zero. If the coordinate origin lies within a simply-connected structure, coefficients $d_o = B_o = C_o = D_o = B_1 = 0$. At least for a simply-connected structure whose coordinate lies within the structure, coefficients A_1, A'_1, b_1, and b'_1 should also be zero if there is no resultant force at the origin. On the other hand, if the origin does not lie within a simply-connected structure, then B_o, C_o, D_o, B_1, and B'_1 must be included. Several cases were analyzed: Case A, only the symmetry condition is applied, Case B, symmetrical conditions in addition to $A_1 = A' = b_1 = b'_1 = 0$, and Case C retains all of the Airy coefficient without making any assumptions. Overall, Case C compares with ANSYS simulated result better than Case A or B and Case A is better than Case B. Case A reconstructs individual stresses, checks for single-valueness and symmetric about $y = 0$. Case B does not reconstruct isopachic and individual stresses well but checks for single-valueness and symmetry about $y = 0$. Case C reconstruct individual stresses superior to either of the other two cases but does not check for single-valueness and symmetry. Furthermore, the force equilibrium of Case A and C check with applied loading condition. Input data-wise, Case D (see APPENDIX) averages the recorded TSA data about y = 0 and then projects that averaged information into both halves of the plate. This full-plate of input data is processed by a complete stress function (includes all coefficients). Several variations of cases A through D were also conducted. Table 4.9.1 summarizes the various cases (models) considered and their respective outcomes. Of the various cases considered, Case D is superior. The stresses evaluated by model/Case D does are not single-

valued. This might be theoretically troubling but is not deemed a concern. It occurs at least partly because the input data are not perfectly symmetric about y = 0 and they are processed by a numerically fitted polynomial.

A major contribution of this chapter is the demonstrated ability to determine the individual stresses in a finite engineering component by TSA using experimental-numerical-analytical hybrid technique, at, and in the neighborhood of, the boundary of the deep U-notch plate. The author is unaware of any previous research in determining the stresses in a single-sided deep U-notched tensile plate using thermal information and Airy stress function. In fact relatively little stress information seems to be available for single-sided notched plates. This is the first time known to the author when one (i) has succeeded in stress analyzing a simply-connected geometry by processing measured data with an Airy stress function and which involves a coordinate origin that is outside of the component/material, and (ii) has had to employ most of the entire form of the stress function or even to stress analyze a structure by pure theory, i.e., analytically as a boundary-value problem. Having to use the full stress function of equation (4.1) was not expected here a priori. However, in retrospect, having to utilize the complete stress function represents a significant technical contribution as it expands the general hybrid concept of processing measured information with a stress function to more complicate, but realistic/practical, engineering problems. It should be noted that my experience with doubly-connected shapes whose coordinate origin is within the hole (i.e., the origin is surrounded by structure/material), the coefficients one would expect to be zero were zero [36] [64].

Table 4.9.1: Comparison of models/cases evaluated and outcomes

Case	MODEL	RESULTS
A	Recorded TSA data averaged about $y = 0$ and projected into one half of plate. Φ: $A_o = B_o = C_o = D_o = d_o = A'_1 = B_1 = B'_1 = a_n = b_n = c_n = d_n$ (for $n \geq 1$) $= 0$ (symmetry about $y = 0$ for coordinate origin surrounded by structure). Imposed boundary conditions of figure 4.3.1	Stresses symmetrical about $y = 0$. Stresses single-valued. σ_o highly reliable on curved edge of notch. Magnitudes of A_1 and b'_1 large.
B	Recorded TSA data averaged about $y = 0$ and projected into one half of plate. Φ: $A_o = B_o = C_o = D_o = d_o = A'_1 = B_1 = B'_1 = a_n = b_n = c_n = d_n$ (for $n \geq 1$) $= 0$ (symmetry about y = 0 for coordinate origin surrounded by structure) and $A_1 = A'_1 = b_1 = b'_1 = 0$ (no resultant forces at origin when later surrounded by structure). Imposed boundary conditions of figure 4.3.1	Stresses reasonably symmetrical about $y = 0$. Stresses single-valued. σ_o unreliable on curved edge of notch Very few non-zero coefficients.
C	Recorded TSA data averaged about $y = 0$ and projected into one half of plate. Φ: Complete. Imposed boundary conditions of figure 4.3.1	Stresses not symmetrical about $y = 0$ Stresses not single-valued. Virtually all coefficients non-zero, magnitude of many quite big; including A_1, A'_1, b_1 and b'_1. However, several of a_n, b_n, c_n, and d_n (for $n \geq 1$) quite small.
D	Recorded TSA data averaged about y = 0 and projected into both top and bottom halves of plate. Φ: complete. Imposed boundary conditions of figure	Stresses reasonably symmetrical about $y = 0$. Stresses not single-valued. Virtually all coefficients non-zero, magnitude of many quite big. However,

	A4.2.2.	several of a_n, b_n, c_n, and d_n (for $n \geq 1$) quite small. Best of these models for stress analyzing the one-sided deep notched plate.
E	Identical to Case D except omit imposed shear stress along $y = 0$	Results very similar to those for Case D.
F	Repeat D except employ recorded TSA data averaged about $y = 0$ projected into only one half of plate. Φ: $A_o = a_n = b_n = c_n = d_n$ (for $n \geq 1$) = 0 Imposed boundary conditions of figure A4.2.2.	Other than that on the curved edge of the notch, stresses are reasonably symmetrical about $y = 0$. Magnitudes of stresses are so so. Stresses not single-valued.
G	Repeat F except omit imposing shear stress on $y = 0$.	Results essentially same as for Case F.
A*	Identical to Case A except retain B_o, C_o, D_o, B_1 and B'_1 (for when coordinate origin outside of simply-connected structure). Imposed boundary conditions of figure 4.3.1	Since B_o, C_o, D_o, B_1 and B'_1 now significantly non-zero, stresses not symmetrical about $y = 0$. Stresses not single-valued.

Chapter 5. DIC-determined Individual Stresses in a Deep-Notched Tensile Plate

5.1 Introduction

This chapter is similar to Chapter 4 but with DIC-recorded displacement. Cases used in Chapter 4 are again studied; Case A: assumes symmetry bout $y = 0$; Case B: in addition to assumptions of Case A, assumes $b_1 = b'_1 = A_1 = A'_1 = 0$; and Case C: retains all Airy coefficients. Both DIC recorded and ANSYS simulated displacements are utilized for evaluating Airy coefficients. Chapter 3 demonstrated the DIC based Hybrid approach and it utilized only vertical displacement which could reconstruct horizontal displacement. This chapter considers whether that is true if the coordinate original lies beyond the boundary of a simply-connected geometry.

5.2 Relevant Equations

The radial and circumferential displacements, equations (5.1) and (5.2), derived using Hooke's law and integration form individual components of stresses of equations (4.3) through (4.5) [61]. Using equation (5.3), one can transform these displacement equations in polar coordinates to those in Cartesian coordinates. When the plate is loaded physically in a testing machine, the rigid body motions, S_1 and S_2 in equations (5.1) and (5.2) are zero.

$$
\begin{aligned}
u_r = \frac{1}{E}\Bigg[& \frac{-b_0(1+\nu)}{r} + 2c_0(1-\nu)r + d_0[(1-\nu)(2r\ln r - r) - 2\nu r] \\
& - \frac{B_0(1+\nu)\theta}{r} + 2C_0(1-\nu)r\theta \\
& + D_0[(1-\nu)(2r\ln r - r) - 2\nu r]\theta \\
& + \left[(1-\nu)b_1 \ln r + \frac{c_1(1+\nu)}{r^2} + d_1 r^2(1-\nu) - 2d_1\nu r^2\right]\sin\theta \\
& + \left[(1-\nu)b_1' \ln r + \frac{c_1'(1+\nu)}{r^2} + d_1' r^2(1-\nu) - 2d_1'\nu r^2\right]\cos\theta \\
& + 2A_1 \ln r \cos\theta - 2A_1' \ln r \sin\theta \\
& + B_1[(1-\nu)\ln r\,\theta\sin\theta + [\ln r]^2\cos\theta] \\
& + B_1'[(1-\nu)\ln r\,\theta\cos\theta - [\ln r]^2\sin\theta] \\
& - \sum_{n=2,3,\ldots}^{N} \begin{Bmatrix} a_n n(1+\nu)r^{n-1} + \\ b_n[(n-2)+\nu(n+2)]r^{n+1} \\ -c_n n(1+\nu)r^{-(n+1)} - \\ d_n[(n+2)+\nu(n-2)]r^{-n+1} \end{Bmatrix} \sin n\theta \\
& - \sum_{n=2,3,\ldots}^{N} \begin{Bmatrix} a_n' n(1+\nu)r^{n-1} + \\ b_n'[(n-2)+\nu(n+2)]r^{n+1} \\ -c_n' n(1+\nu)r^{-(n+1)} - \\ d_n'[(n+2)+\nu(n-2)]r^{-n+1} \end{Bmatrix} \cos n\theta + S_1\cos\theta \\
& - S_2 \sin\theta \Bigg]
\end{aligned}
\tag{5.1}
$$

$$u_\theta = \frac{1}{E}\Bigg[4d_0 r\theta + 2D_0 r\theta^2$$

$$-\left[b_1(1-\nu)(1-\ln r) + \frac{c_1(1+\nu)}{r^2} + d_1(\nu+5)r^2\right]\cos\theta$$

$$+\left[b_1'(1-\nu)(1-\ln r) + \frac{c_1'(1+\nu)}{r^2} + d_1'(\nu+5)r^2\right]\sin\theta$$

$$-2A_1(\ln r + \nu)\sin\theta - 2A_1'(\ln r + \nu)\cos\theta$$

$$+B_1[1-\nu-(1+\nu)\ln r - [\ln r]^2]\sin\theta \qquad (5.2)$$

$$+B_1'[1-\nu-(1+\nu)\ln r - [\ln r]^2]\cos\theta$$

$$-B_1(1-\nu)(1-\ln r)\theta\cos\theta + B_1'(1-\nu)(1-\ln r)\theta\sin\theta$$

$$-\sum_{n=2,3,..}^{N}\begin{Bmatrix} a_n n(1+\nu)r^{n-1} + \\ b_n[n(\nu+1)+4]r^{n+1} \\ +c_n n(1+\nu)r^{-(n+1)} + \\ d_n[n(\nu+1)-4]r^{-n+1}\end{Bmatrix}\cos n\theta$$

$$+\sum_{n=2,3,..}^{N}\begin{Bmatrix} a_n' n(1+\nu)r^{n-1} + \\ b_n'[n(\nu+1)+4]r^{n+1} \\ +c_n' n(1+\nu)r^{-(n+1)} + \\ d_n'[n(\nu+1)-4]r^{-n+1}\end{Bmatrix}\sin n\theta + S_1\cos\theta - S_2\sin\theta\Bigg]$$

$$u = u_r\cos\theta - u_\theta\sin\theta \qquad (5.3)$$

$$v = u_r\sin\theta + u_\theta\cos\theta$$

5.3 Finite Element Model

The same Finite element model is used here as in section 4.4.

5.4 Plate Preparation and Experimental Setup

The same 6.35 mm thick deep U-notched finite-width aluminum plate of figure 4.1.1 is used for the DIC analysis. The DIC method necessitates having a surface speckle pattern by which the pixel locations of the unloaded plate can be correlated with those of loaded plate. A white speckle pattern (using Ultra-Flat Krylon with paint) was sprayed on the dry black surface. A suitable speckly pattern was achieved by applying a consistent pressure to the trigger of the commercial white paint container, figure 5.4.1.

The upper crosshead of loading machine (20-kip capacity MTS hydraulic testing machine) of figure 5.4.2 was fixed and the bottom crosshead moved vertically downward. Care was taken during testing to avoid out-of-plane motion beyond the Poisson's effect. This was verified by utilizing two cameras, figure 5.4.2, whereby the DIC recorded both the in-plane and the out-of-plane displacement components. When utilizing two cameras, a separate calibration grid (provided by Correlated solution, Inc. with the DIC package) was employed to evaluate the displacement data in physical units rather than in pixels. The plate was statically loaded from essentially 0 N to 4000 N (900 lbs) in 445 N (100 lbs) increments. Results are reported for a load of 2,669 N (600 lbs). Digital images were captured at load increments and saved with the Correlated Solution's VIC Snap software. The recorded images were processed and correlated with Correlated Solution's VIC 3D software to evaluate the displacements for post-processing.

Because the bottom crosshead of the loading machine moves vertically while the top crosshead remains stationary, the recorded displacements of figure 5.4.3 were unsymmetrical from top to bottom. To simulate the longitudinal end of the plate being equally extended, these

unsymmetrical data were converted to have zero vertical displacements at $y = 0$ using MATLAB. The converted top and bottom displacements were normalized with the radius of notch and projected into the upper half and the same data were copied to the lower half of the plate for full-plate information, figures 5.4.5 and 5.4.6.

Table 5.1: DIC Details

Parameter	Information
Technique	Stereo Image Correlation
Cameras*	The Grasshopper (Point Grey Research), Model GRAS-50S5M-C
Imaging sensor*	Sony ICX625 CCD, 2/3", 3.45 um
Lens*	CM120 BK 15 COMPACT- 0901 (focal ratio: 1.9 and focal length: 35 mm)
Sensor/digitization	2448 × 2048 at 15 FPS
Lightening	Ambient white light
Pixel to inch conversion	1 pixel = 0.1 mm
Software*	Vic-Snap software
Subset, step	21,8
Strain Resolution	0.005% (50 microstrain)

* from Correlated Solutions, Inc., Columbia, SC, USA

Figure 5.4.1: White speckle pattern applied on the plate for DIC

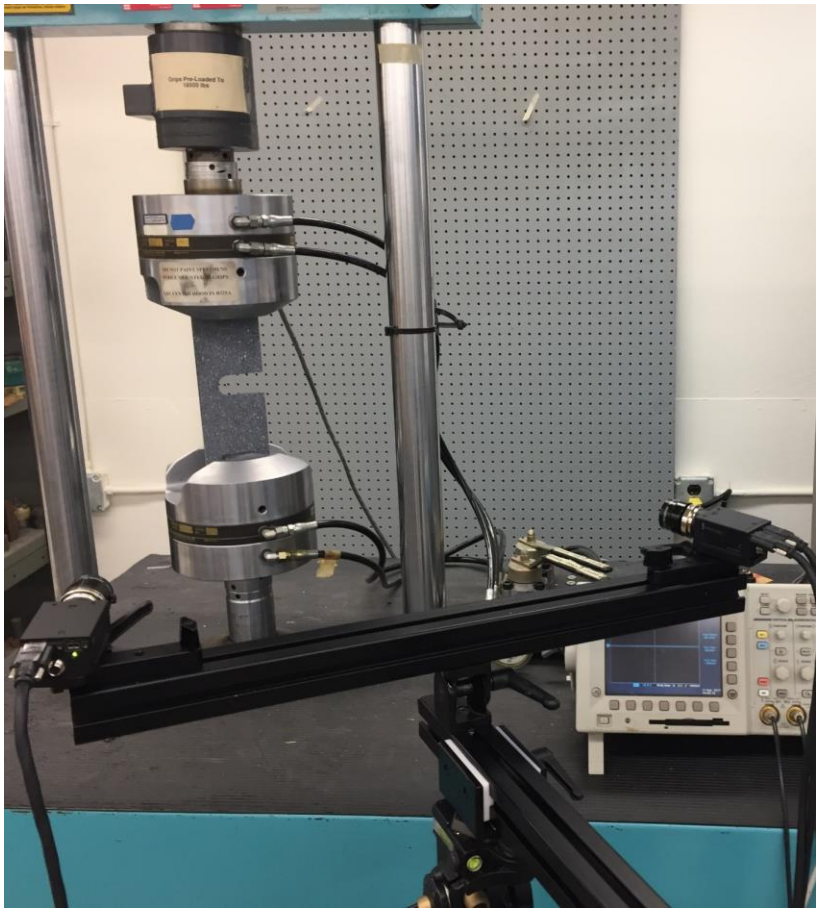

Figure 5.4.2: DIC experimental setup

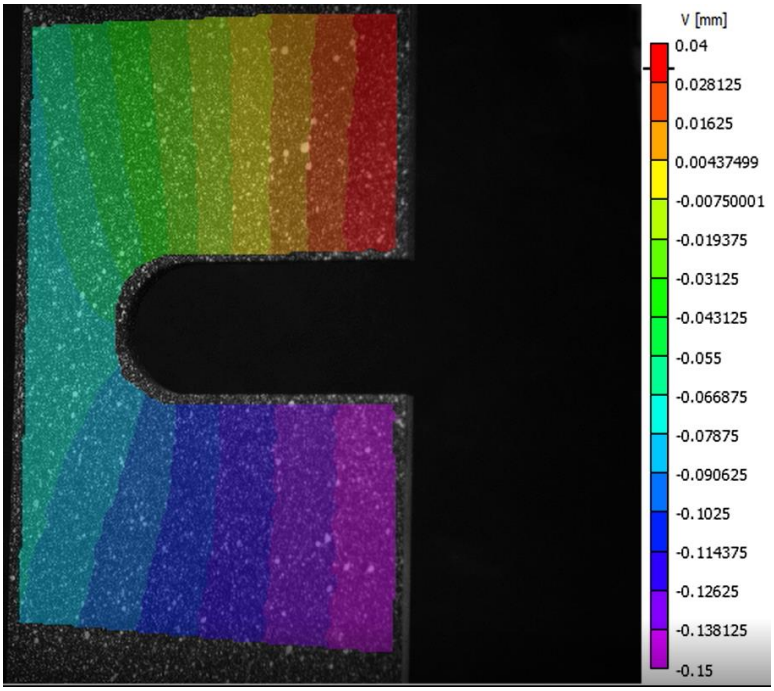

Figure 5.4.3: Raw DIC-recorded vertical displacement

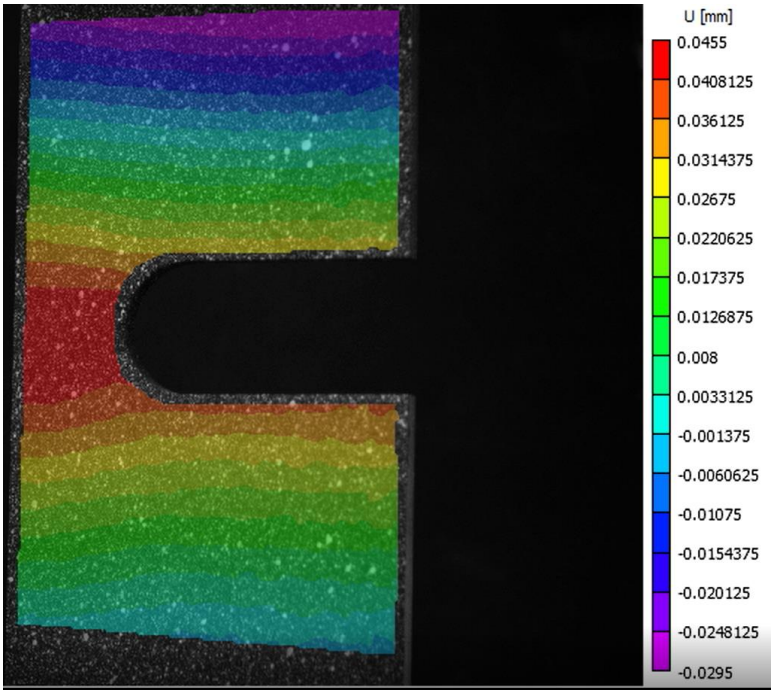

Figure 5.4.4: Raw DIC-recorded horizontal displacement

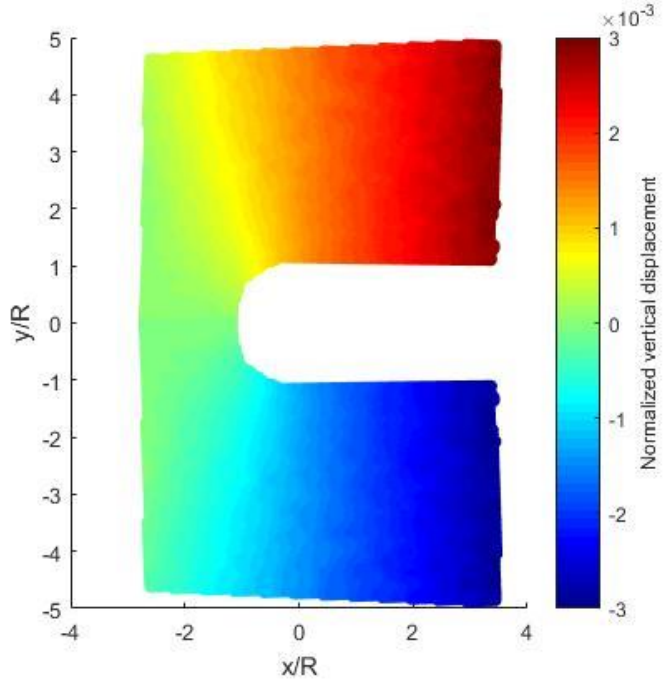

Figure 5.4.5: DIC-recorded vertical displacement

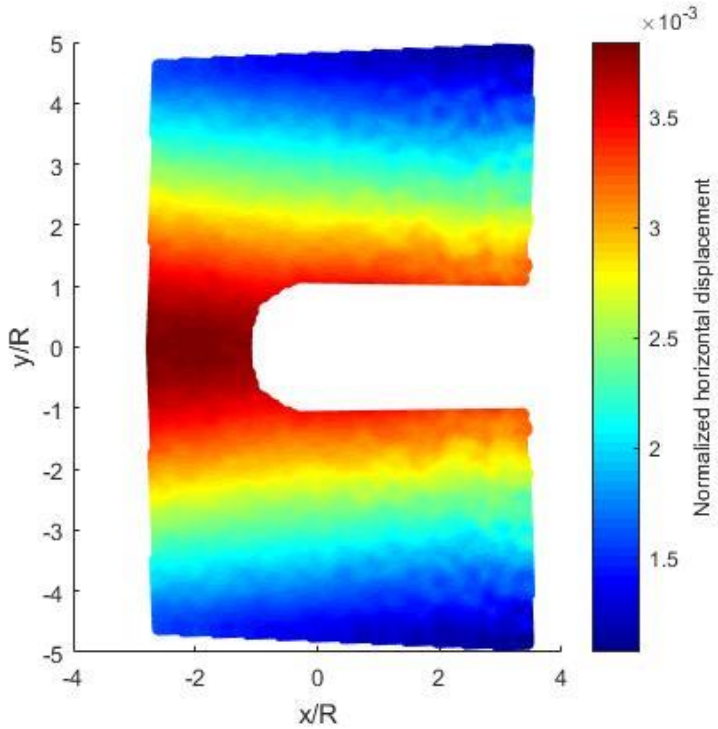

Figure 5.4.6: DIC-recorded horizontal displacement

5.5 DIC-Hybrid

In this section, the upper half plate of DIC recorded displacements are used for evaluating the Airy coefficients. Just to follow Chapter 4's Cases (Case A: evaluating coefficients considering only symmetry about *x*-axis; Case B: in addition to symmetry about *x*-axis of Case A, $b_1 = b'_1 = A_1 = A'_1 = 0$; Case C: retaining all of the Airy coefficient. Also, for each Case, results using only vertical displacement and both components of displacements as input are studied.

5.5.1. Boundary Conditions

Recognizing the inability to evaluate all the Airy coefficients from the recorded displacement data, boundary conditions in terms of stresses as shown in figure 5.5.1 were imposed discretely (point-wise) at locations on the traction-free edges of the U-notch. The two conditions can be written as

$$\sigma_{rr}(R,\theta) = \sigma_{r\theta}(R,\theta) = 0, \qquad \frac{\pi}{2} \leq \theta \leq \pi \tag{5.4}$$

Where *R* is the radius of the notch

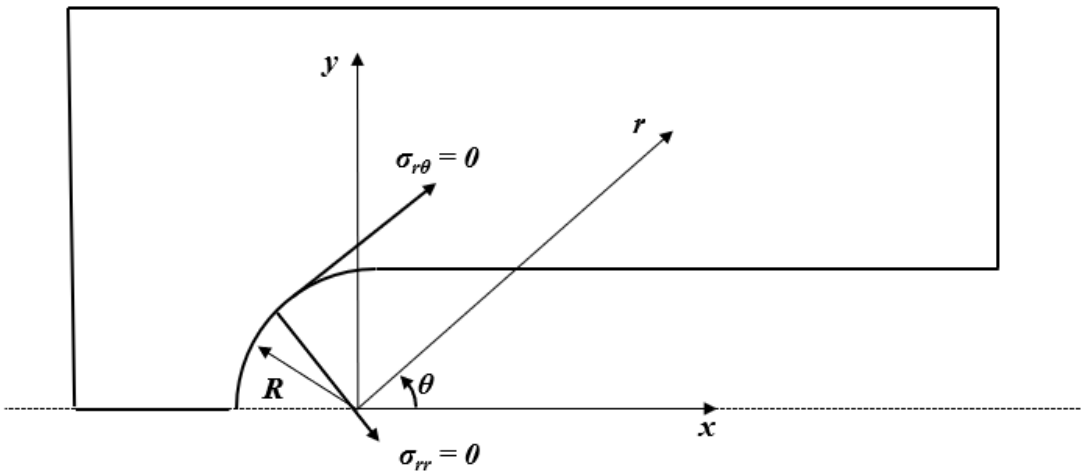

Figure 5.5.1: Imposing traction-free boundary conditions

5.5.2 Coefficient Evaluation

The DIC-measured displacements at many locations throughout the half plate were imported into MATLAB. A total 13,557 source locations utilized are shown in shaded area of figure 5.5.1. At each location, both components of displacements are available. Since the DIC software correlation algorithm is unable to track pixels that do not have any neighboring pixels, the unreliable displacement information at and near the edge of the notch (the most interested region due to stress concentration) was not employed.

In addition to employed values of displacement, a total of $h = 500 \times 2 = 1{,}000$ boundary conditions were imposed at the 500 equally spaced discrete points of figure 5.5.1. A linear matrix equation of the form of $[A]\{c\} = \{d\}$ of equations (5.5) and (5.6) was formed. Matrix [A] of equation (5.6) consists of v- and u-displacement expressions of the form of equations (5.1) and (5.2) in addition to applied boundary conditions, vector $\{c\}$ contains the k unknown Airy coefficients and vector $\{d\}$ contains the DIC-recorded v and u displacements at the coordinates associated with figure 5.5.2. Typical of measured data, the DIC-recorded information contains some scatter. It was consequently advantageous to employ more measured input values than the number of unknown, i.e., $m > k$, so Eq. (5.6) was solved by least-squares using the '\'matrix division operator in MATLAB 2016 (MathWorks, Natick, MA, USA).

$$\begin{bmatrix} v_1(b_0, c_0, d_0 \cdots d'_n) \\ u_1(b_0, c_0, d_0 \cdots d'_n) \\ \vdots \\ v_m(b_0, c_0, d_0 \cdots d'_n) \\ u_m(b_0, c_0, d_0 \cdots d'_n) \\ \vdots \\ \sigma_{r\theta}(b_0, c_0, d_0 \cdots d'_n) \end{bmatrix}_{(m+h)\times k} \begin{bmatrix} b_0 \\ c_0 \\ d_0 \\ A_0 \\ \vdots \\ c'_n \\ d'_n \end{bmatrix}_{k\times 1} = \begin{bmatrix} v_1 \\ u_2 \\ \vdots \\ v_m \\ u_m \\ \vdots \\ 0 \end{bmatrix}_{(m+h)\times 1} \tag{5.5}$$

or in simplified form,

$$[A]_{(m+h)\times k}\{c\}_{k\times 1} = \{d\}_{(m+h)\times 1} \tag{5.6}$$

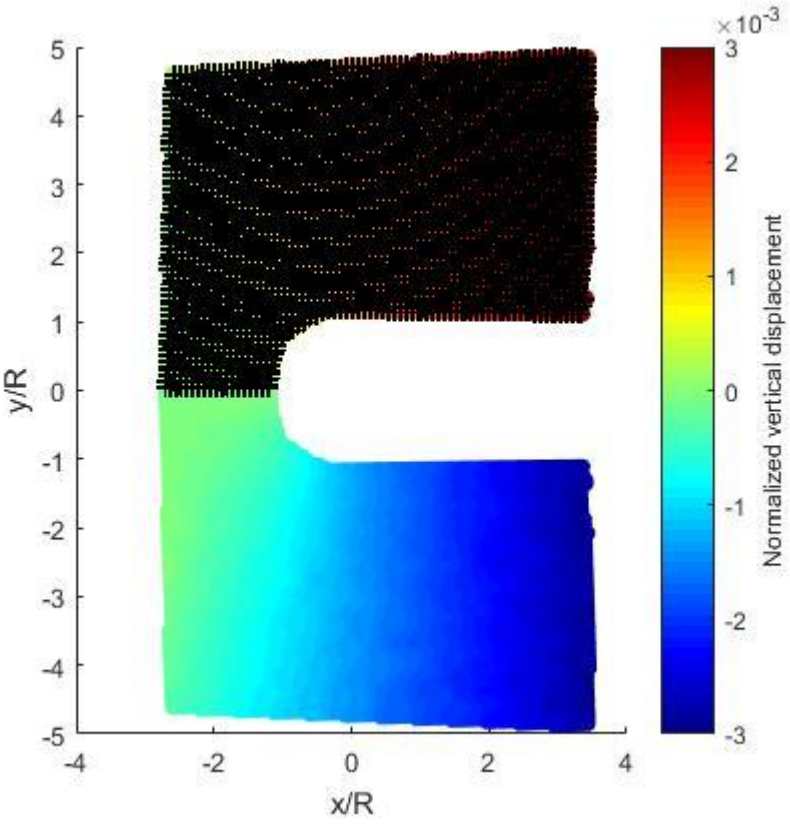

Figure 5.5.2: Source locations of employed displacement data (13,557 locations)

5.5.3 *RMS* of Case A, B and C

The question arises as to how many Airy coefficients, k, to use in the series representation of equation (5.5). The number of these coefficients to retain was assessed by computing the root mean squares (*RMS*) for a series of different number of the coefficients. The *RMS* represents the discrepancy between the calculated vertical displacement data, $\{d'\}$, and measured DIC v-displacement data, $\{d\}$. For each of Cases A, B and C, *RMS* values are plotted in figures 5.5.3 through 5.5.5. Each figure contains two *RMS* plots; one with only input of vertical displacement (m = 13,557) and the other using both components of displacements (m = 27,114). With input of only vertical displacements results in lower *RMS* error for these Cases since the RMS values are between recorded and reconstructed vertical displacement. $N = 6$ is chosen for each of these Cases. Overall, Case C has the lowest *RMS* error.

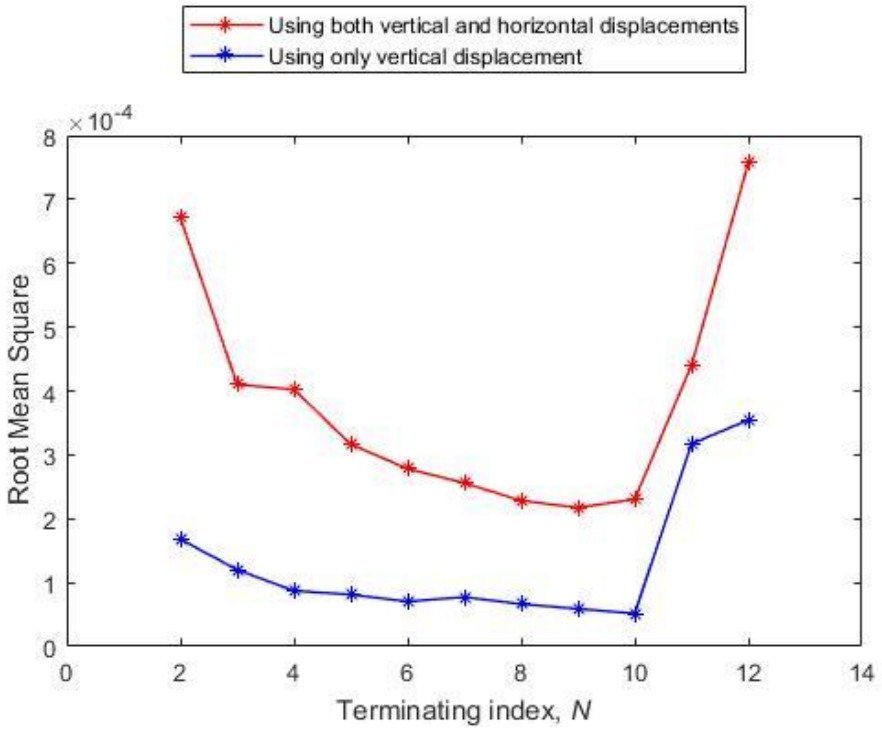

Figure 5.5.3: *RMS* of Case A vs terminating index, *N*

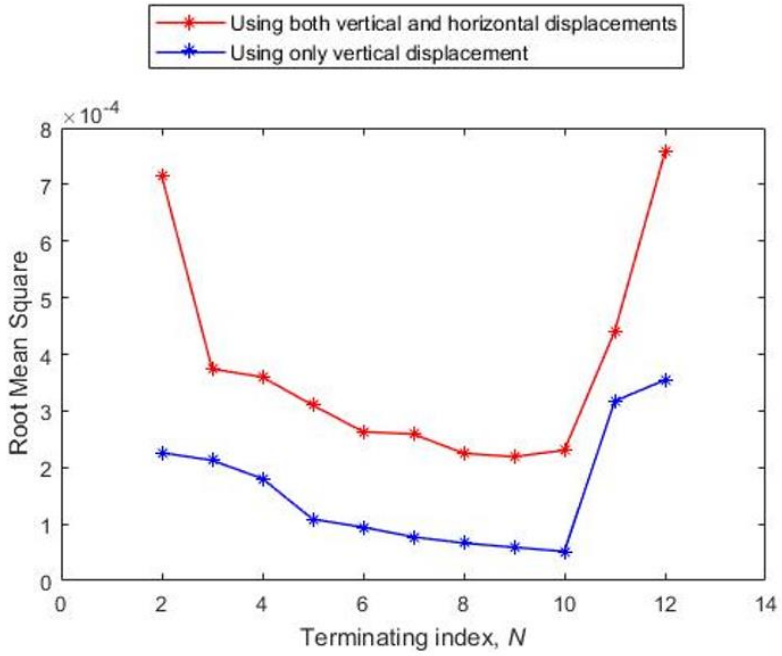

Figure 5.5.4: *RMS* of Case B vs terminating index, *N*

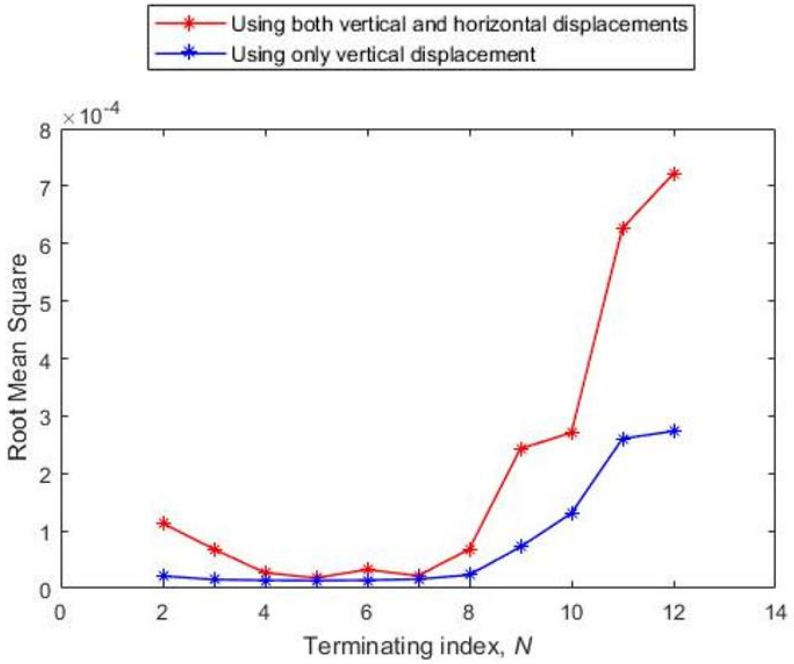

Figure 5.5.5: *RMS* of Case C vs terminating index, *N*

5.5.4 Displacement Reconstruction with Hybrid-DIC

With $N = 6$, both components of displacements are reconstructed for each Case in figures 5.5.6 through 5.5.11. For each contour plot, results with input of both DIC-recorded vertical and horizontal displacement information (m = 13,557+13,557 = 27,154 values) and with input of only vertical displacement information (m = 13,557 values) are shown. The reconstructed displacements (lower in each figure) are compared with DIC-recorded displacements (upper). Cases A and B do not reconstruct any of displacements successfully while Case C using both components of displacements, reconstructs both vertical and horizontal displacements. Case C, with input of only vertical displacements, can reconstruct only vertical displacements. Figures 5.5.10 (a) and 5.5.11 (a) demonstrate most accurate reconstructed displacements. They also predict where no input information was utilized, i.e. along the edge of the notch.

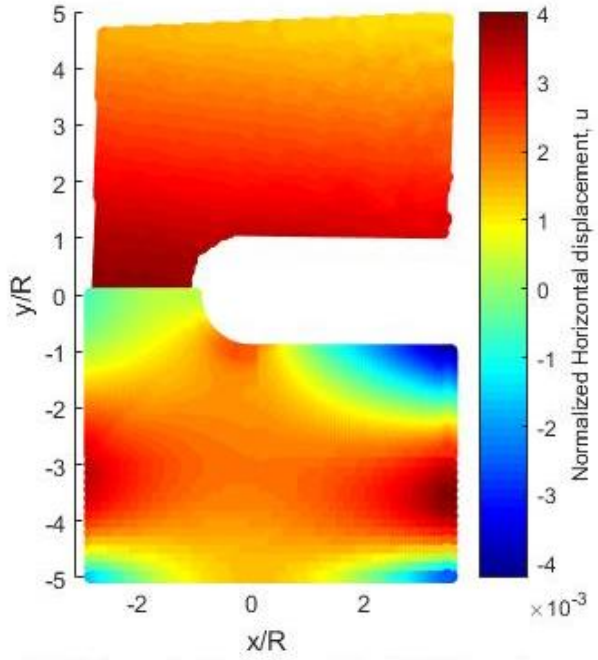

(a) DIC-recorded (upper) and Hybrid-DIC (lower) with input of both components of displacement

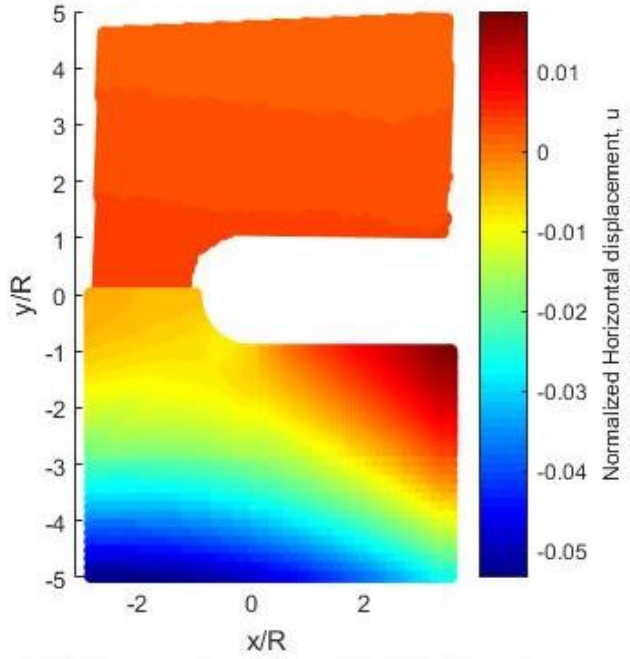

(b) DIC-recorded (upper) and Hybrid-DIC (lower) with input of only vertical displacement

Figure 5.5.6: Horizontal displacement, *u*, for Case A

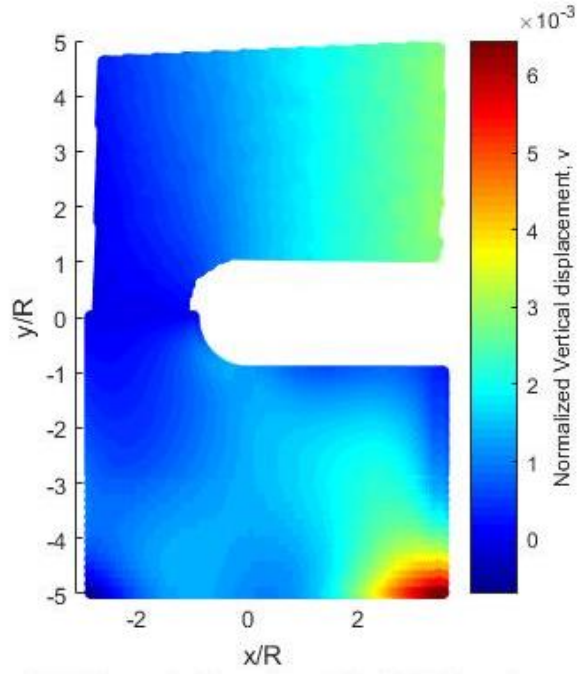

(a) DIC-recorded (upper) and Hybrid-DIC (lower) with input of both components of displacement

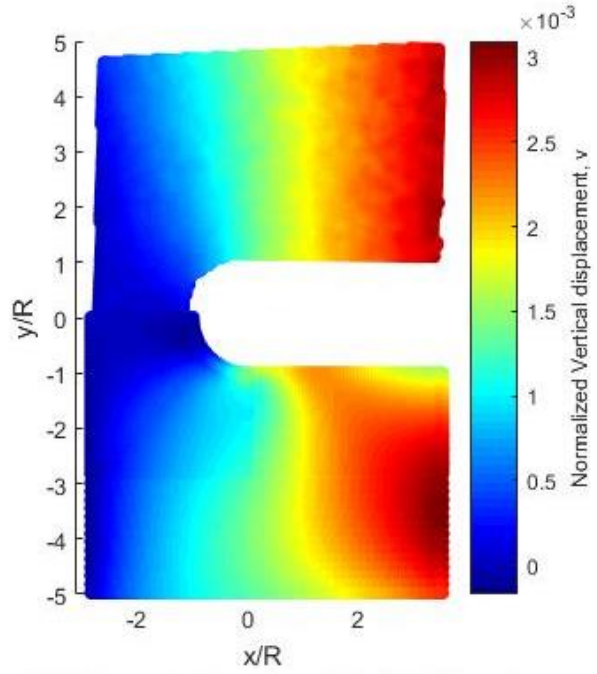

(b) DIC-recorded (upper) and Hybrid-DIC (lower) with input of only vertical displacement

Figure 5.5.7: Vertical displacement, *v*, for Case A

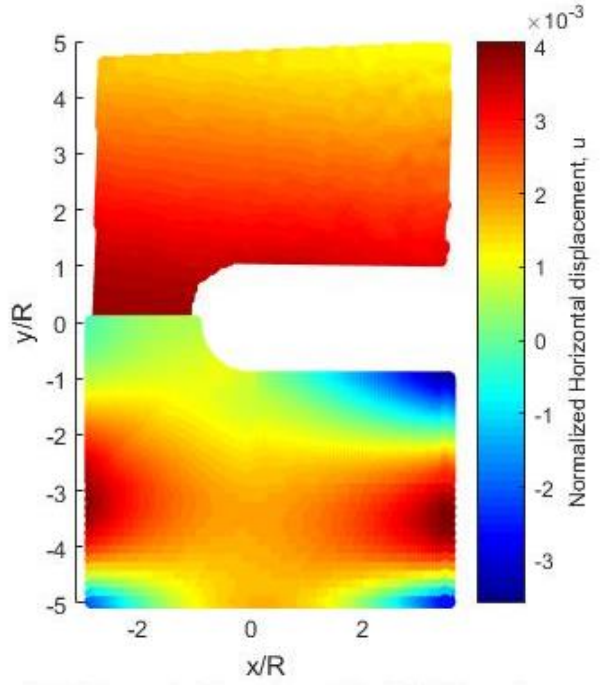

(a) DIC-recorded (upper) and Hybrid-DIC (lower) with input of both components of displacement

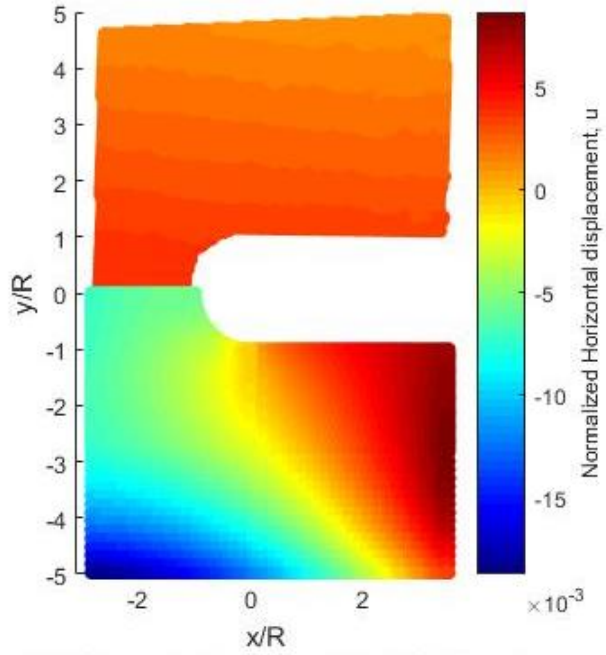

(b) DIC-recorded (upper) and Hybrid-DIC (lower) with input of only vertical displacement

Figure 5.5.8: Horizontal displacement, *u*, for Case B

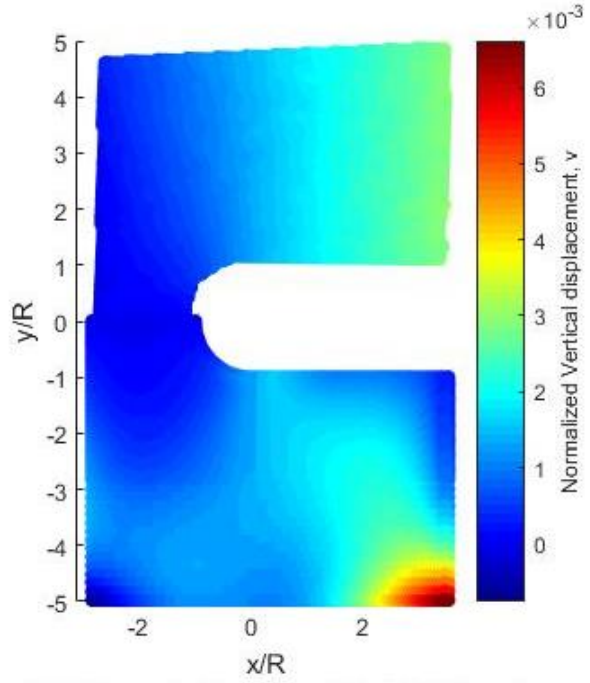

(a) DIC-recorded (upper) and Hybrid-DIC (lower) with input of both components of displacement

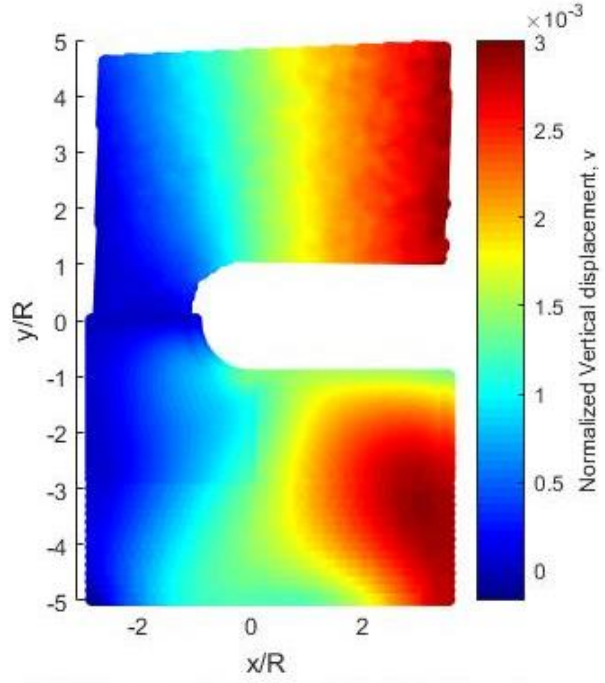

(b) DIC-recorded (upper) and Hybrid-DIC (lower) with input of only vertical displacement

Figure 5.5.9: Vertical displacement, *v*, for Case B

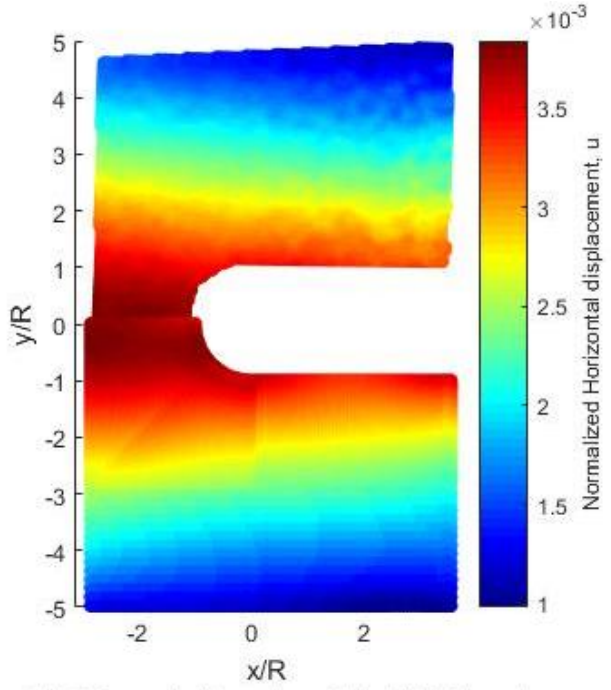

(a) DIC-recorded (upper) and Hybrid-DIC (lower) with input of both components of displacement

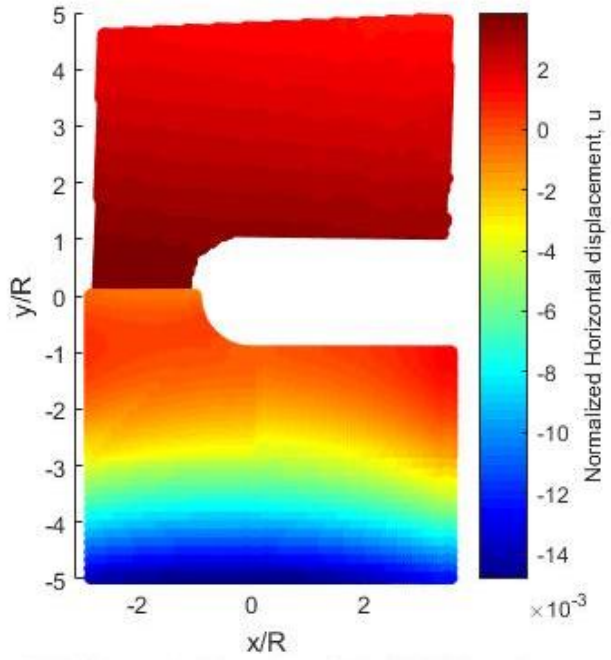

(b) DIC-recorded (upper) and Hybrid-DIC (lower) with input of only vertical displacement

Figure 5.5.10: Horizontal displacement, *u*, for Case C

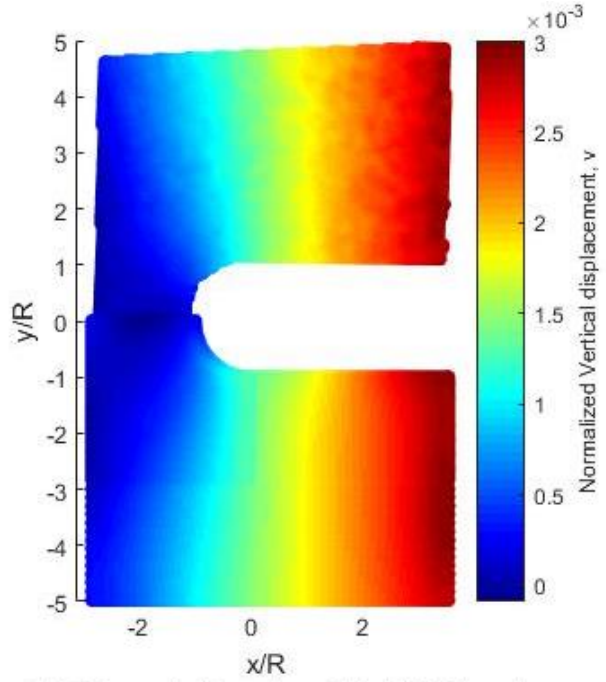

(a) DIC-recorded (upper) and Hybrid-DIC (lower) with input of both components of displacement

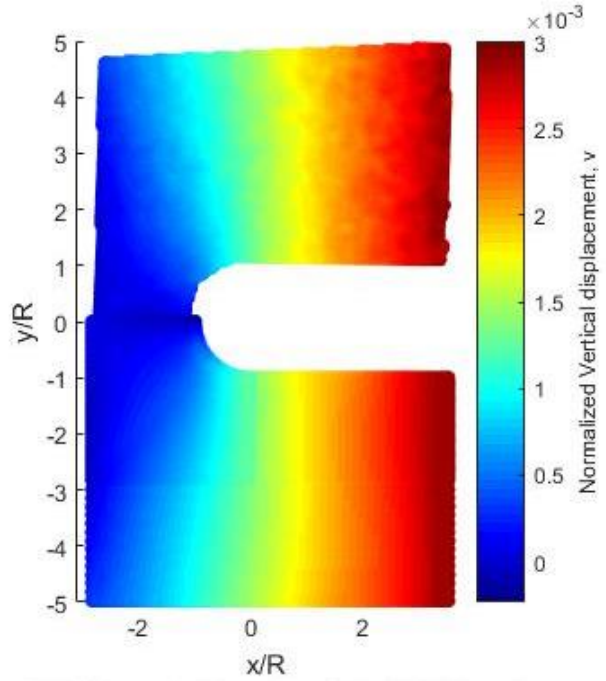

(b) DIC-recorded (upper) and Hybrid-DIC (lower) with input of only vertical displacement

Figure 5.5.11: Vertical displacement, *v*, for Case C

5.5.5 Stress Determination with Hybrid-DIC, Case C

The previous section showed only Case C with inputs of both vertical and horizontal displacements can reconstruct both components of displacements. Thus, individual components of stress are reconstructed with Case C with inputs of both displacements and compared with that of ANSYS, figures 5.5.12 through 5.5.17. All the results are based on $N = 6$ which is equivalent of 57 Airy coefficients.

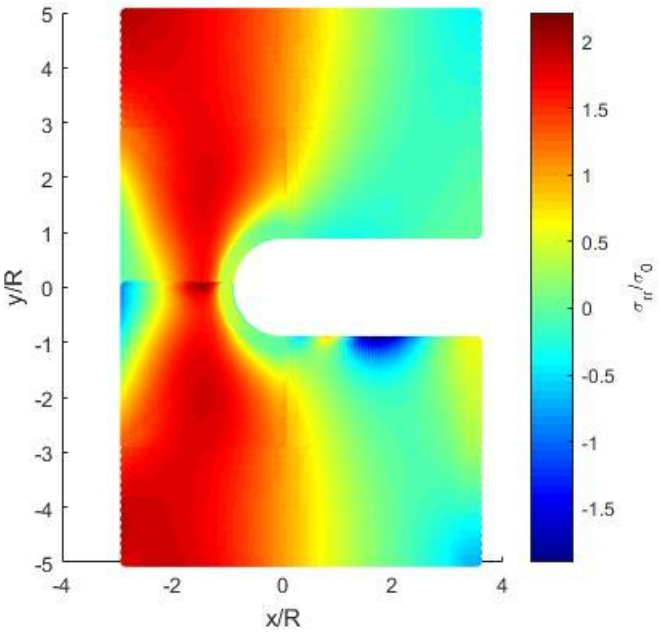

Figure 5.5.12: ANSYS (upper) and Hybrid-DIC (lower) normalized radial stress, σ_{rr}/σ_0

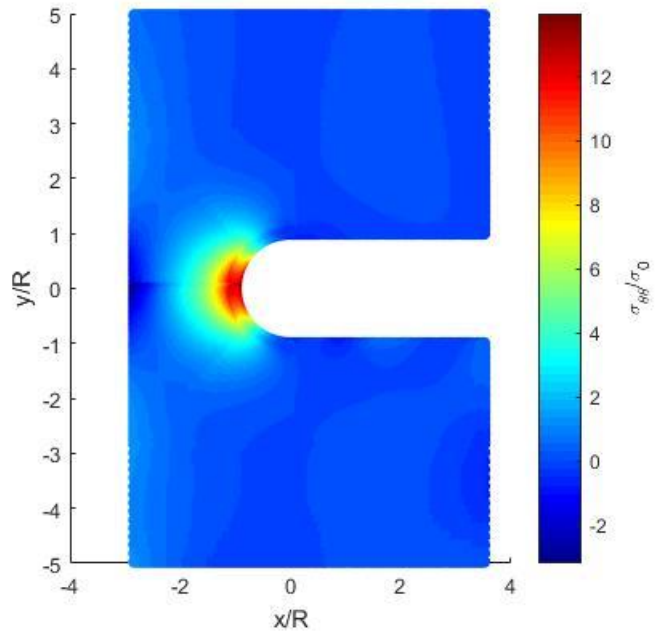

Figure 5.5.13: ANSYS (upper) and Hybrid-DIC (lower) normalized tangential stress, $\sigma_{\theta\theta}/\sigma_0$

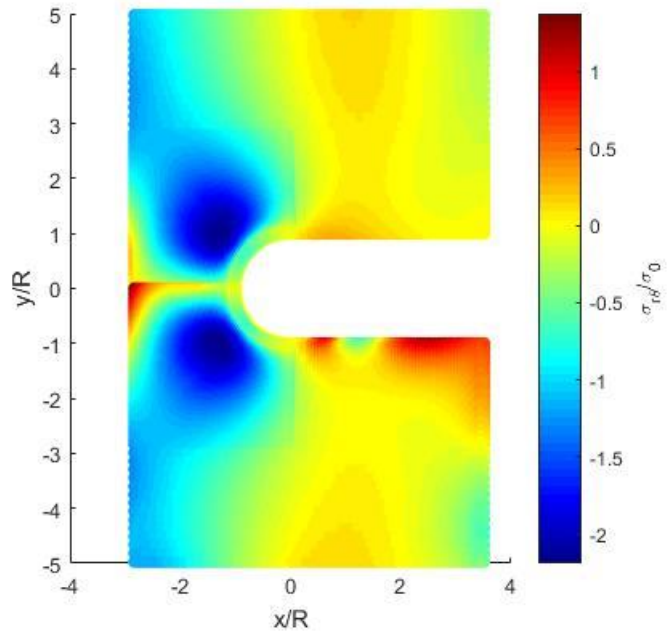

Figure 5.5.14: ANSYS (upper) and Hybrid-DIC (lower) normalized shear stress, $\sigma_{r\theta}/\sigma_0$

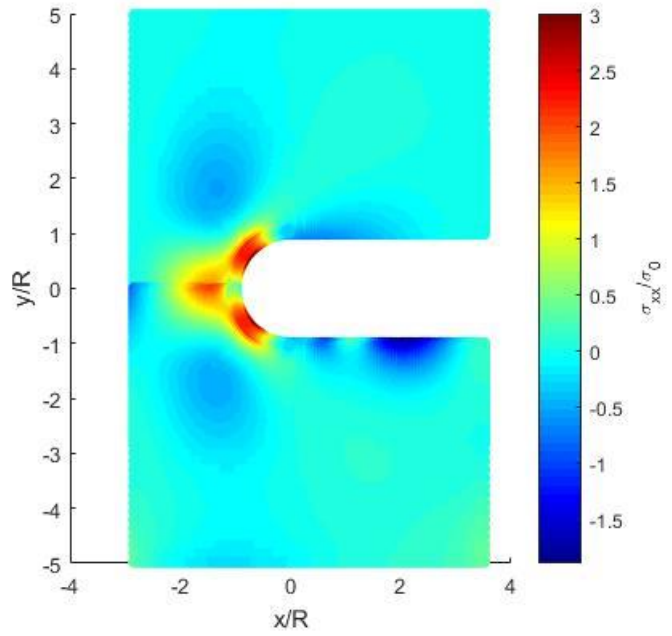

Figure 5.5.15: ANSYS (upper) and Hybrid-DIC (lower) normalized horizontal stress, σ_{xx}/σ_0

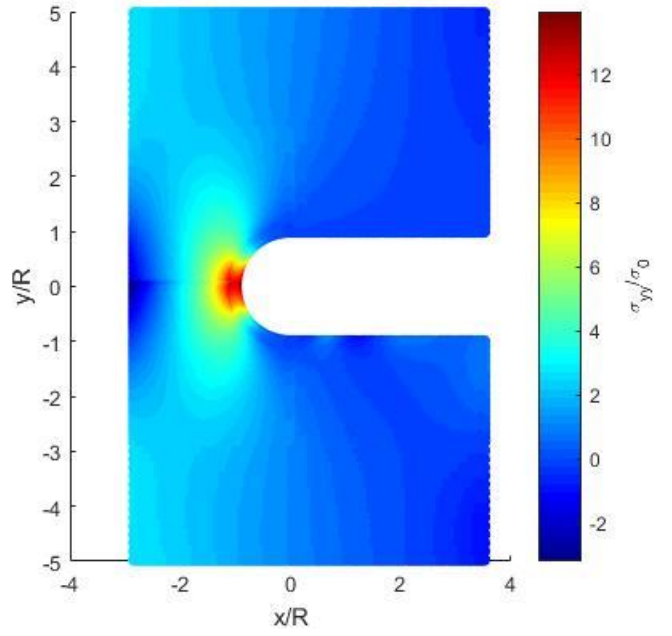

Figure 5.5.16: ANSYS (upper) and Hybrid-DIC (lower) normalized vertical stress, σ_{yy}/σ_0

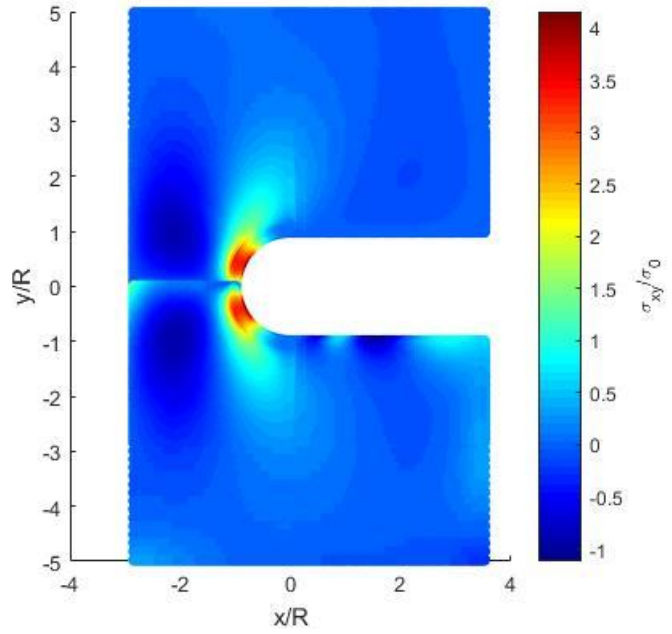

Figure 5.5.17: ANSYS (upper) and Hybrid-DIC (lower) normalized vertical stress, σ_{xy}/σ_0

5.6 Numerical Experiment

To help ensure the approach is numerically stable, a numerical-hybrid approach based on Airy stress function was assessed using simulated (rather than DIC recorded) input values of displacement from ANSYS.

5.6.1 Data Location

ANSYS-simulated displacements (9,635 source locations) are utilized instead of DIC-recorded displacements, figure 5.6.1. The same boundary conditions ($h = 500 \times 2 = 1{,}000$) of figure 5.5.1 are applied as was in the section 5.5.1. FEM-predicted values of displacement throughout only the shaded part of figure 5.6.1 are utilized to correlate with DIC recorded data.

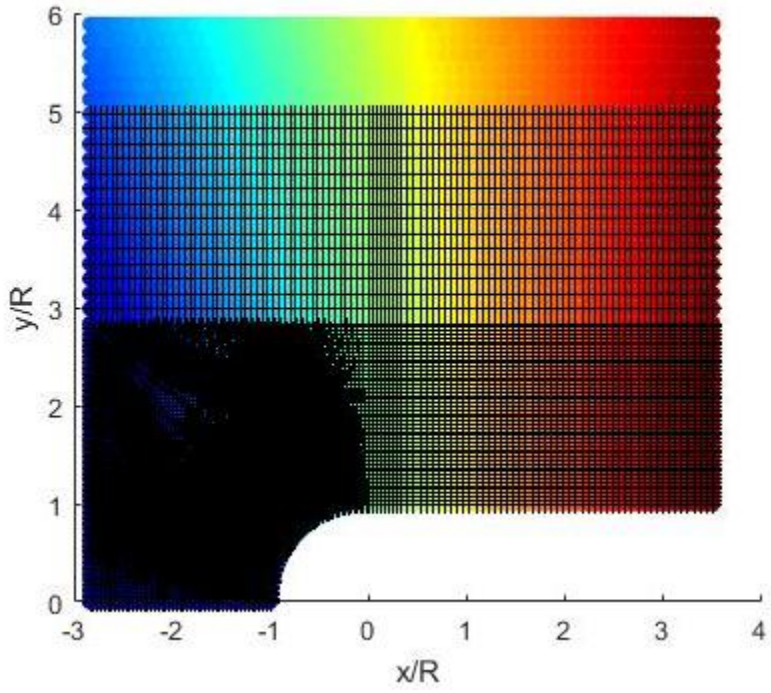

Figure 5.6.1: Source locations of employed data in shaded area (*m* = 9,635 values)

5.6.2 *RMS*

The same method is used to determine appropriate number of Airy coefficients to retain as was in the section 5.5.3, figures 5.6.2 through 5.6.4. *RMS* is between ANSYS-simulated and reconstructed vertical displacement. Figures 5.6.2 and 5.6.3 show *RMS* values are lower with input of only vertical displacement. Compared to *RMS* plots of Hybrid-DIC of figures 5.5.3 through 5.5.5, *RMS* error values are stable even with very high number of Airy coefficients; thus, $N = 11$ is chosen. Again, Case C results in much lower *RMS* error compared to other Cases.

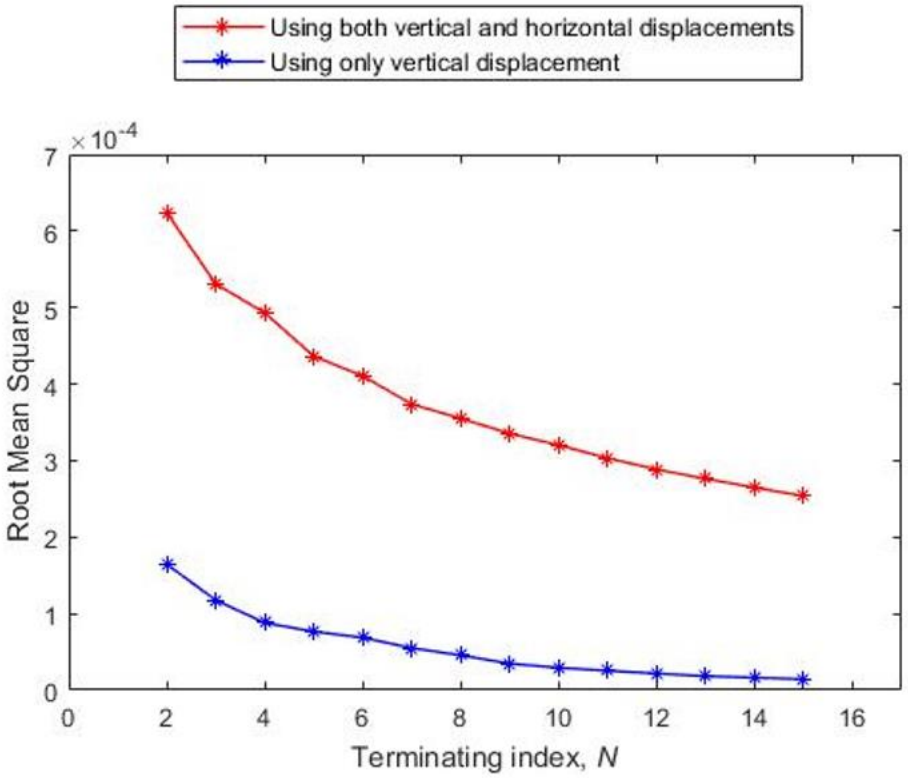

Figure 5.6.2: *RMS* of Case A vs terminating index, *N*

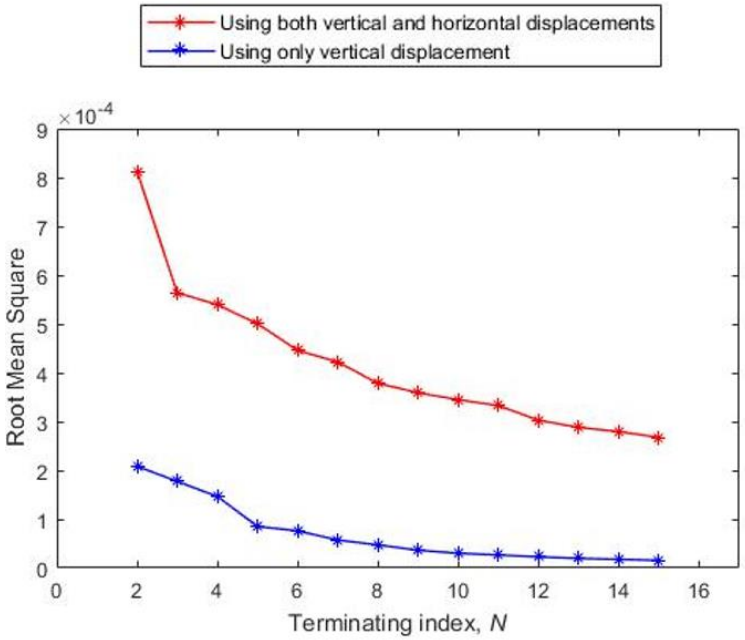

Figure 5.6.3: *RMS* of Case B vs terminating index, *N*

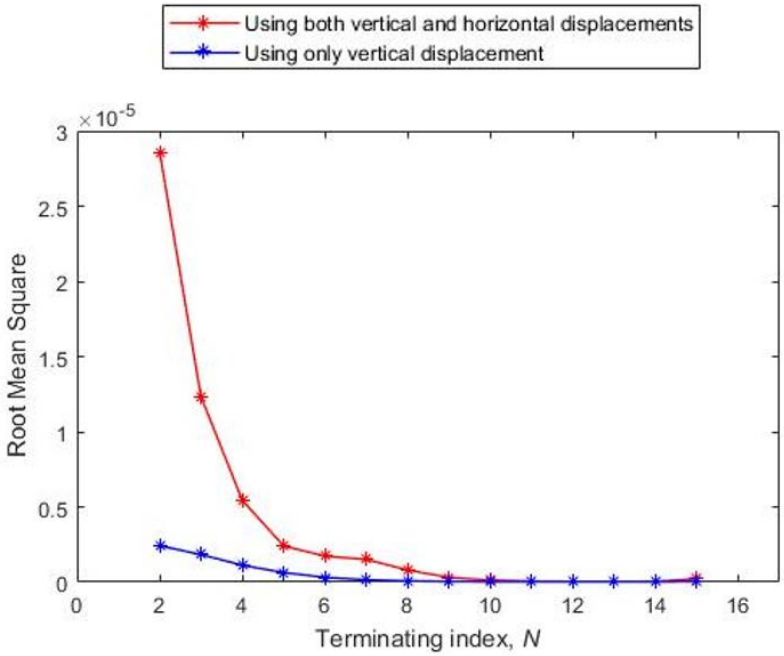

Figure 5.6.4: *RMS* of Case C vs terminating index, *N*

5.6.3 Displacement Reconstruction with Hybrid-ANSYS

Displacements are reconstructed with ANSYS-simulated displacements, figures 5.6.5 through 5.6.10. For each Case, results of both components of displacements are reconstructed with inputs of both displacements and with input of only vertical displacement. With FEM predicted displacements, all Cases can reconstruct vertical displacements with input of only vertical displacement, figures 5.6.6 (b), 5.6.8 (b), and 5.6.10 (b). These results correspond to the *RMS* error plots of the section 5.6.2 where the values are lower with input of only vertical displacements. However, similar to the previous section 5.5.4, only Case C with inputs of both components of displacement can reconstruct both vertical and horizontal components of displacements successfully.

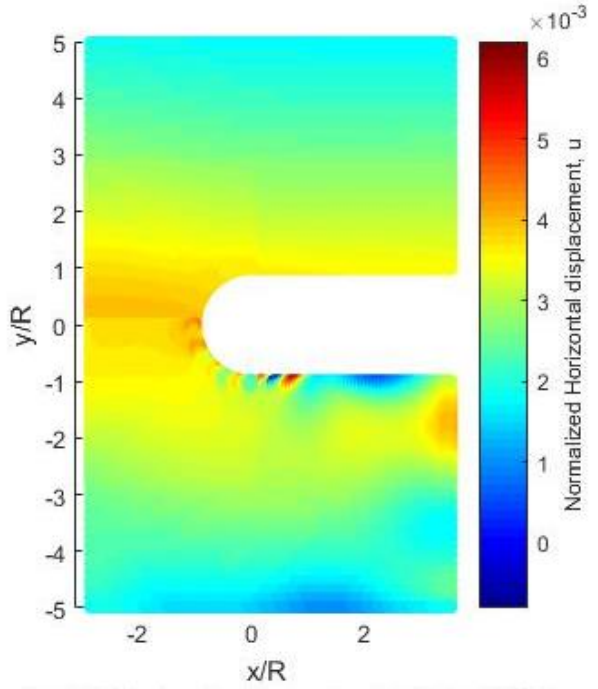

(a) ANSYS-simulated (upper) and Hybrid-ANSYS (lower) with input of both components of displacement

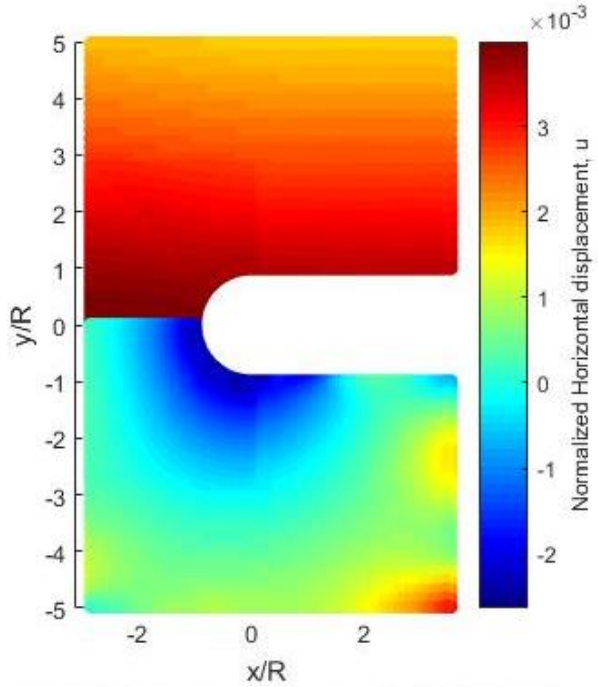

(b) ANSYS-simulated (upper) and Hybrid-ANSYS (lower) with input of only vertical displacement

Figure 5.6.5: Horizontal displacement, *u*, for Case A

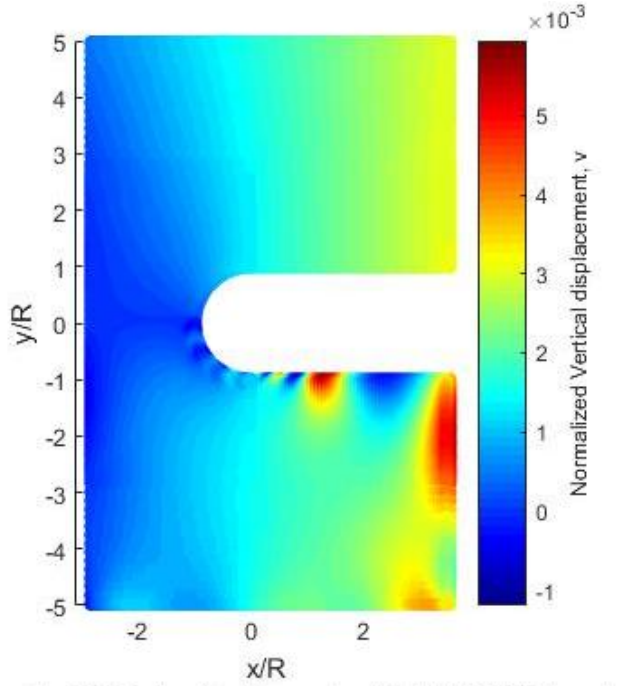

(a) ANSYS-simulated (upper) and Hybrid-ANSYS (lower) with input of both components of displacement

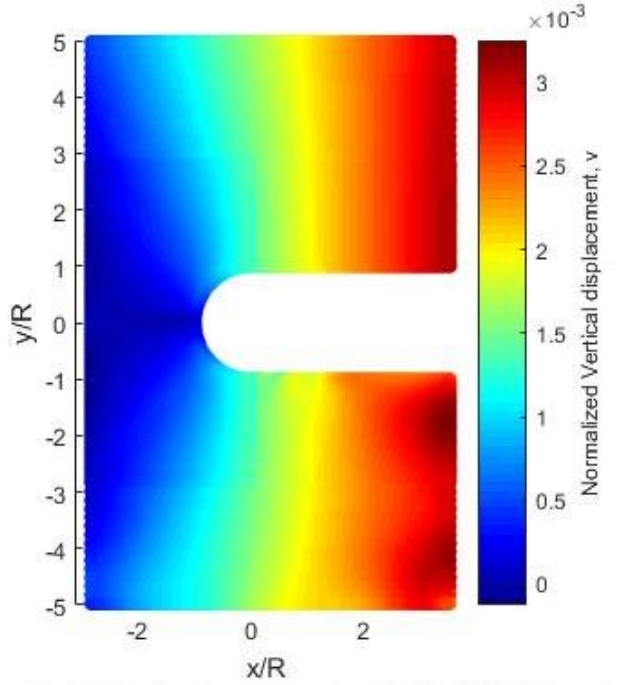

(b) ANSYS-simulated (upper) and Hybrid-ANSYS (lower) with input of only vertical displacement

Figure 5.6.6: Vertical displacement, *v*, for Case A

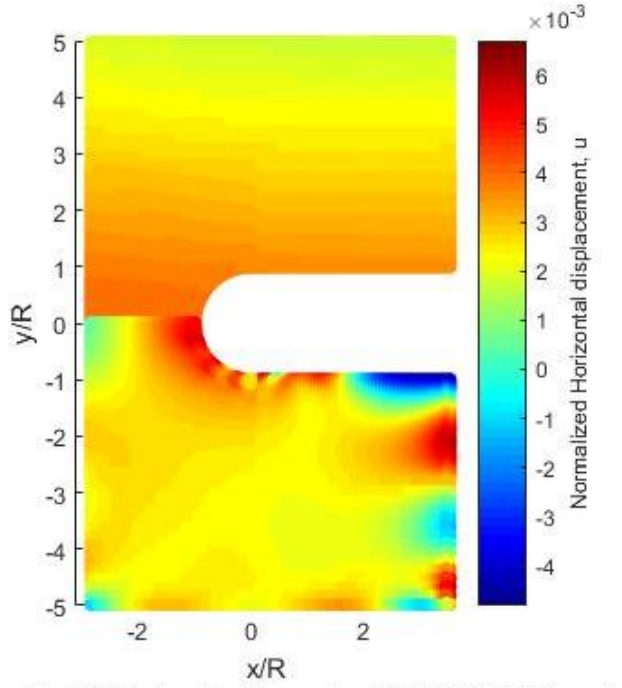

(a) ANSYS-simulated (upper) and Hybrid-ANSYS (lower) with input of both components of displacement

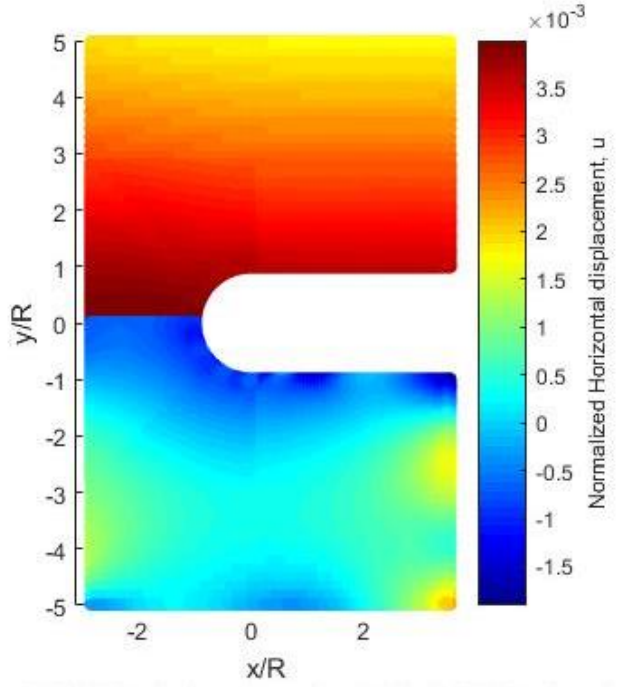

(b)ANSYS-simulated (upper) and Hybrid-ANSYS (lower) with input of only vertical displacement

Figure 5.6.7: Horizontal displacement, *u*, for Case B

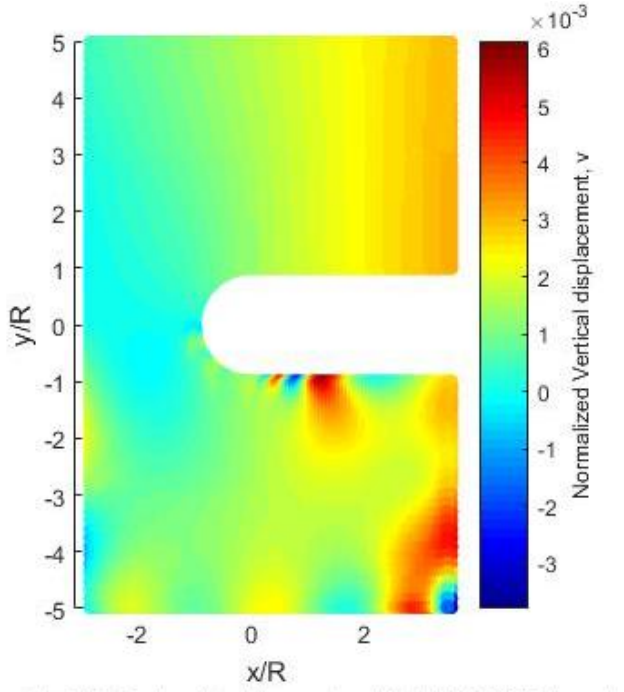

(a) ANSYS-simulated (upper) and Hybrid-ANSYS (lower) with input of both components of displacement

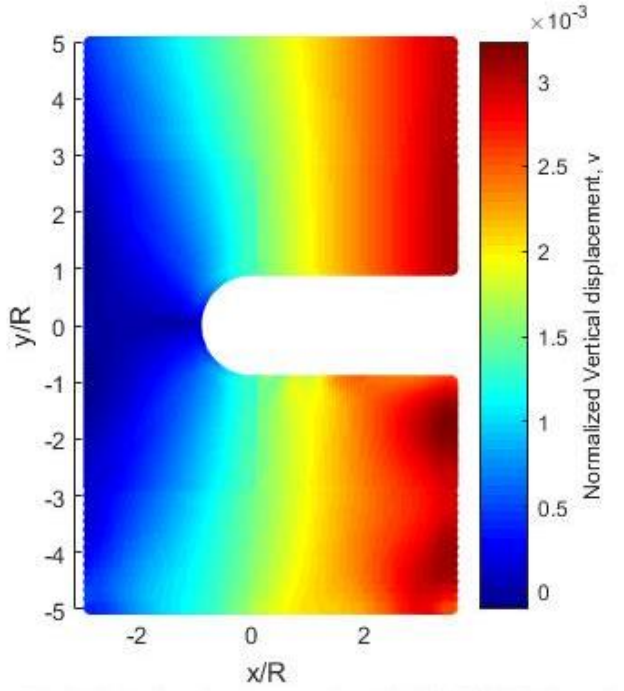

(b) ANSYS-simulated (upper) and Hybrid-ANSYS (lower) with input of only vertical displacement

Figure 5.6.8: Vertical displacement, *v*, for Case B

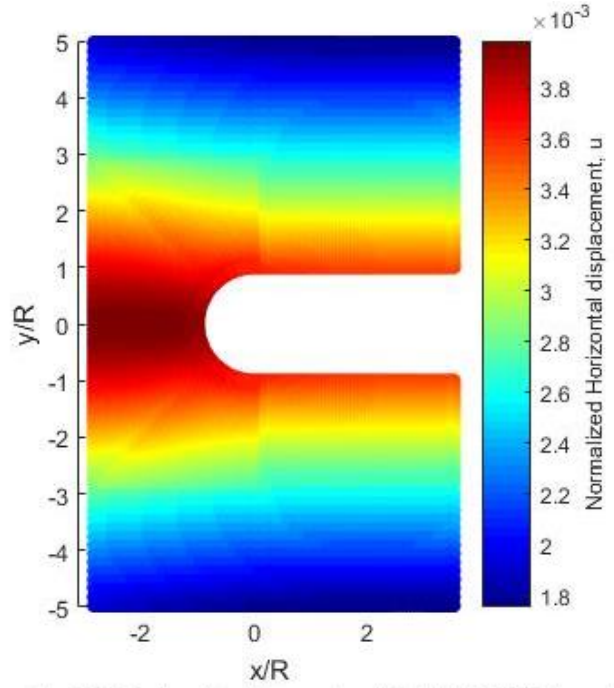

(a) ANSYS-simulated (upper) and Hybrid-ANSYS (lower) with input of both components of displacement

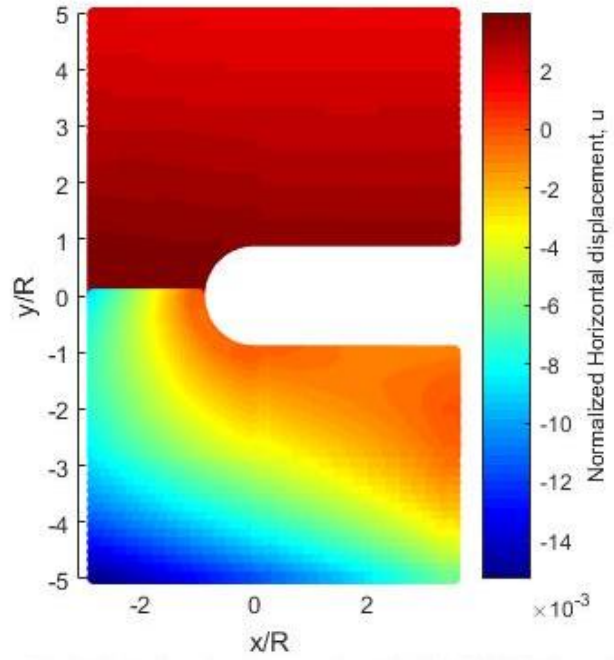

(b) ANSYS-simulated (upper) and Hybrid-ANSYS (lower) with input of only vertical displacement

Figure 5.6.9: Horizontal displacement, *u*, for Case C

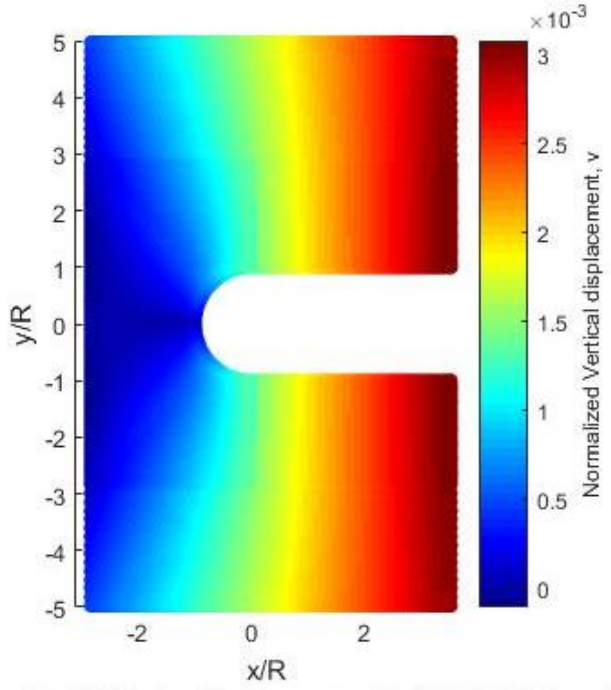

(a) ANSYS-simulated (upper) and Hybrid-ANSYS (lower) with input of both components of displacement

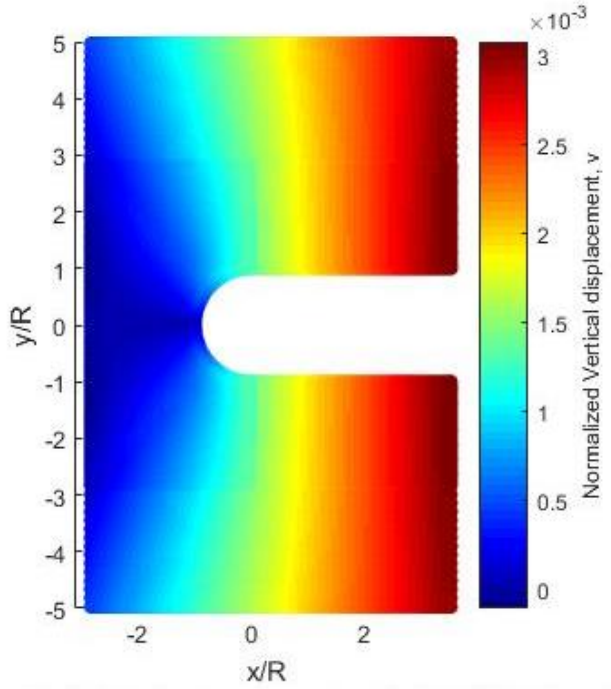

(b) ANSYS-simulated (upper) and Hybrid-ANSYS (lower) with input of only vertical displacement

Figure 5.6.10: Vertical displacement, *v*, for Case C

5.6.4 Stress Determination with Hybrid-ANSYS

Similar to the section 5.5.5, individual components of stress are determined but with the Airy coefficients are evaluated with ANSYS predicted displacements (Hybrid-ANSYS). Again, the stresses are reconstructed with Case C, using both components of displacement and they are shown in figures 5.6.11 through 5.6.16. These figures are compared with that of ANSYS and reconstructed stresses are almost identical to the direct ANSYS predicted stresses.

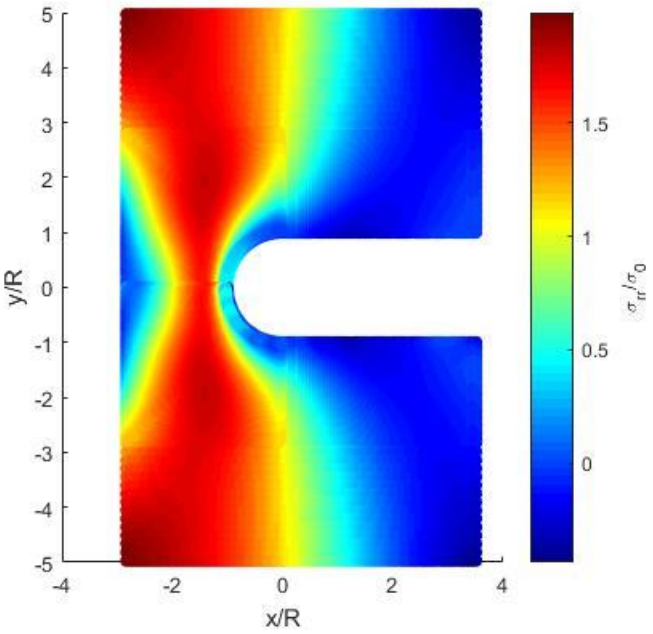

Figure 5.6.11: ANSYS (upper) and Hybrid-ANSYS (lower) normalized radial stress, σ_{rr}/σ_0

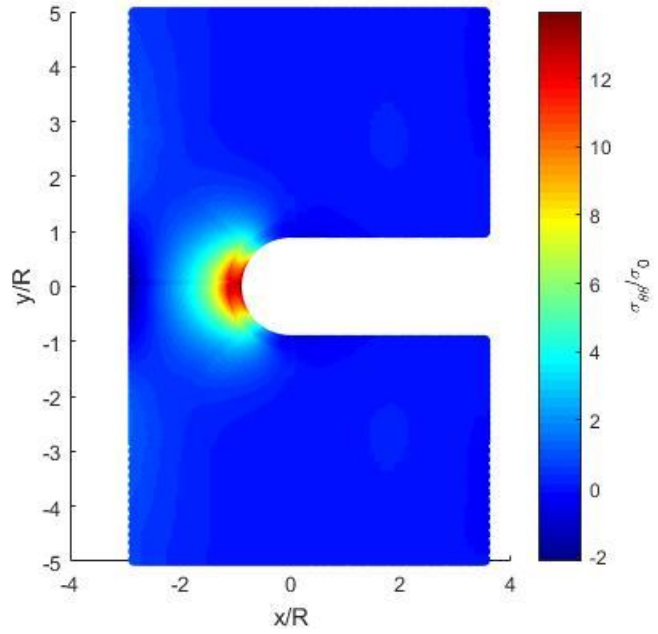

Figure 5.6.12: ANSYS (upper) and Hybrid-ANSYS (lower) normalized tangential stress, $\sigma_{\theta\theta}/\sigma_0$

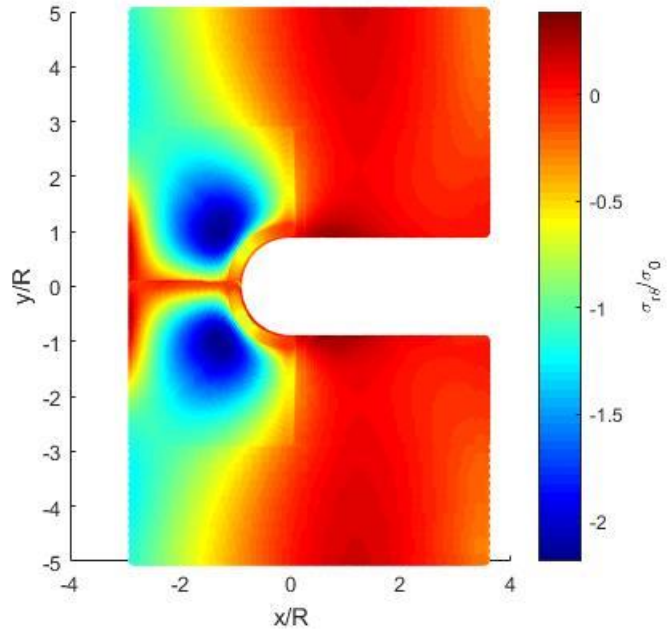

Figure 5.6.13: ANSYS (upper) and Hybrid-ANSYS (lower) normalized shear stress, $\sigma_{r\theta}/\sigma_0$

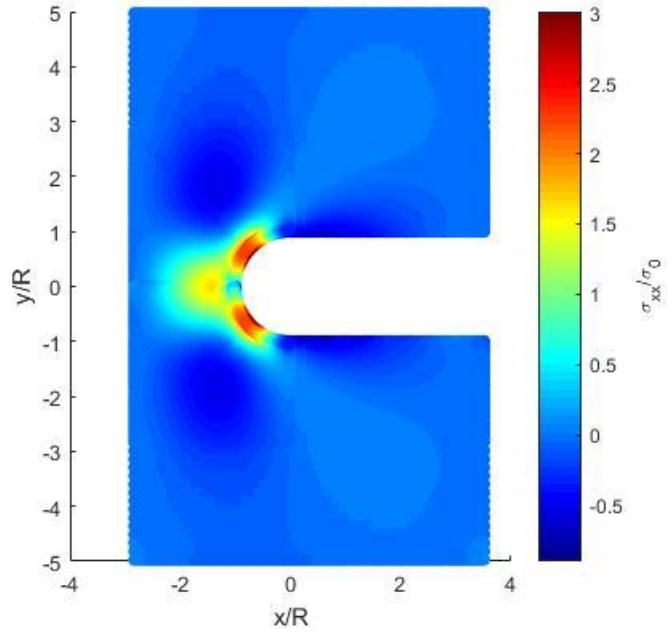

Figure 5.6.14: ANSYS (upper) and Hybrid-ANSYS (lower) normalized horizontal stress, σ_{xx}/σ_0

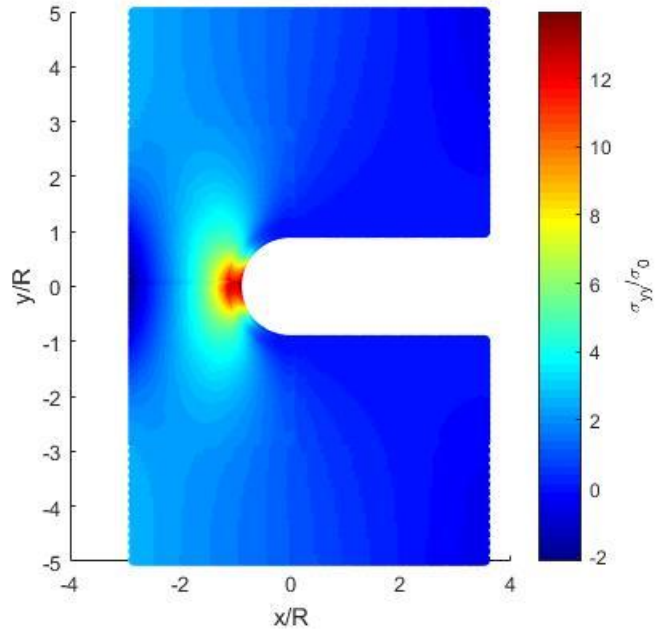

Figure 5.6.15: ANSYS (upper) and Hybrid-ANSYS (lower) normalized vertical stress, σ_{yy}/σ_0

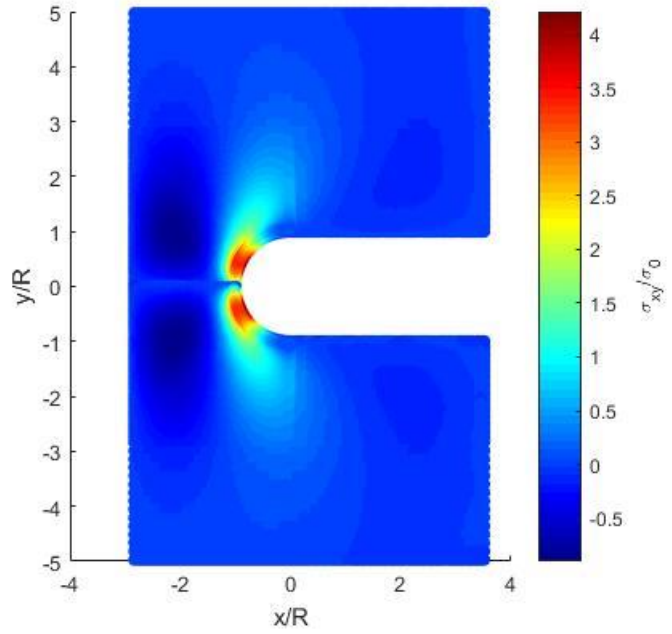

Figure 5.6.16: ANSYS (upper) and Hybrid-ANSYS (lower) normalized vertical stress, σ_{xy}/σ_0

5.7 Results

Some of results using Hybrid-methods with Case C and input of both components of displacements, are shown here and compared with the direct result of ANSYS. Both Hybrid-DIC and Hybrid-ANSYS results of the sections 5.5 and 5.7 are utilized.

5.7.1 Stress Around the Notch

Figure 5.7.1. shows the normalized tangential stresses evaluated for Hybrid-DIC and Hybrid-ANSYS along the end edge of the notch and compared with that of ANSYS. Figure 5.7.2 shows normalized radial and shear stresses around the notch to check if they are essentially zero.

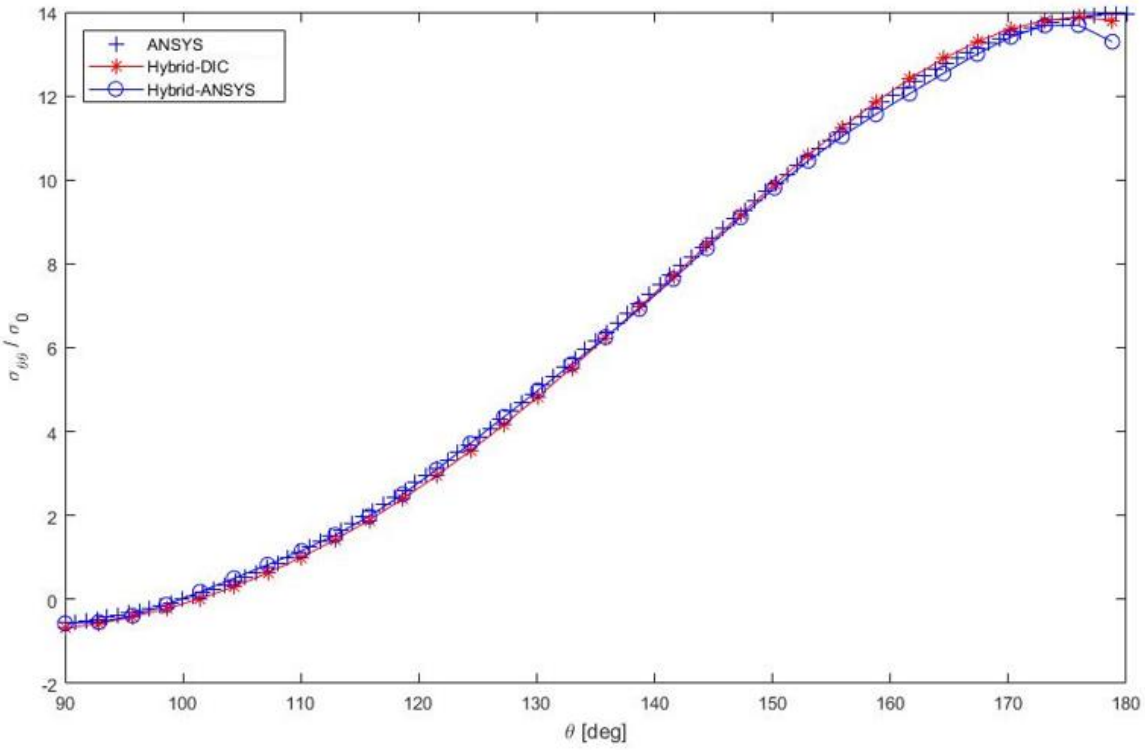

Figure 5.7.1: Normalized tangnetial stress, $\sigma_{\theta\theta}/\sigma_0$, along the edge of the notch

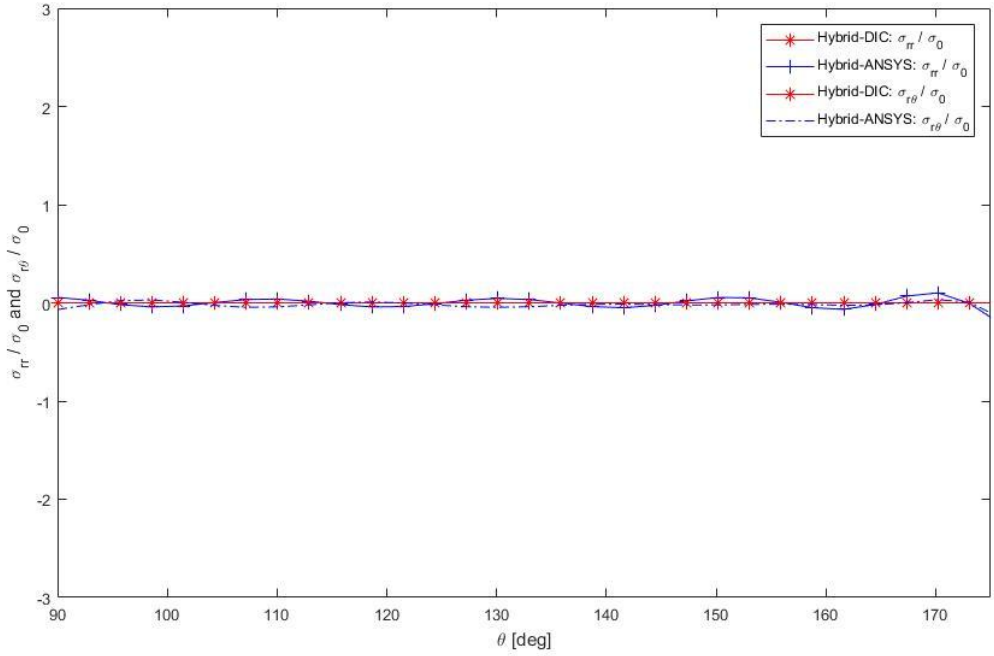

Figure 5.7.2: Normalized radial and shear stress, σ_{rr}/σ_0 and $\sigma_{r\theta}/\sigma_0$, along the edge of the notch

5.7.2 Force Equilibrium

For various horizontal lines (from $y/R = 0$ to $y/R = 2.2$ with increments of 0.1) of the upper half plate, vertical stresses were evaluated, multiplied by the thickness, and integrated numerically over the width of the plate for Hybrid-DIC and Hybrid-ANSYS. The forces calculated are normalized with physically applied load of 2,670 N and shown in figure 5.7.3. The average values of these normalized forces are 1.07 for Hybrid-DIC and 1.03 for Hybrid-ANSYS.

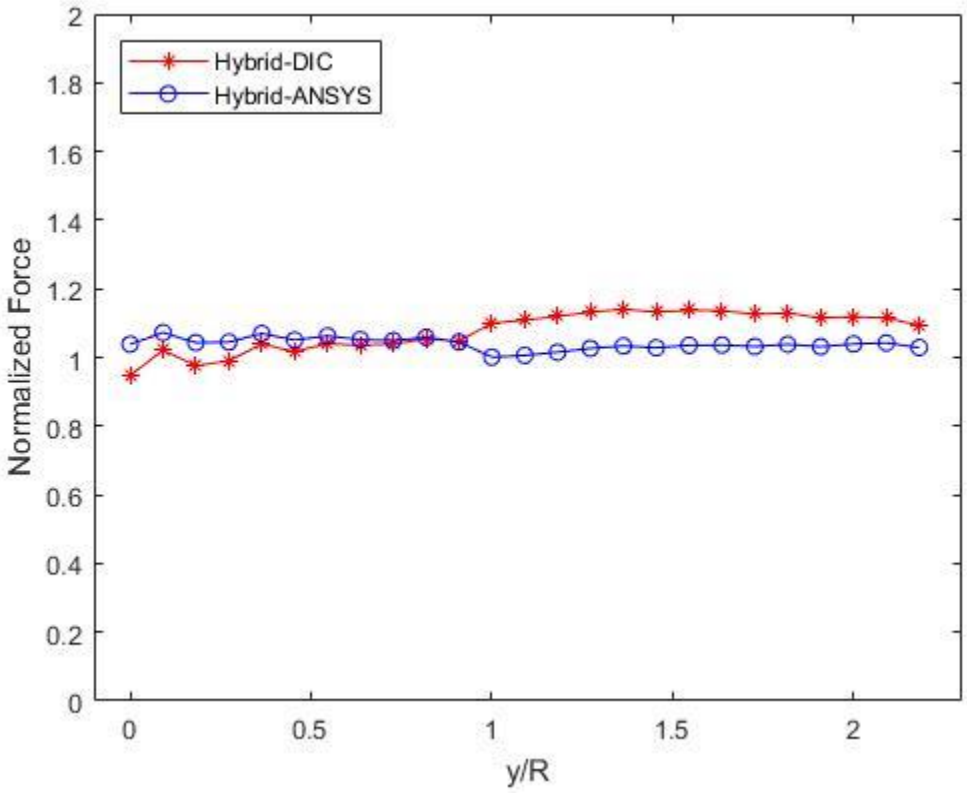

Figure 5.7.3: Forces on each horizontal line of *y*-axes

5.7.3 Airy Coefficients

Tables 5.7.1 and 5.7.2 list the evaluated Airy coefficient based on DIC-recorded(Hybrid-DIC with $N = 6$) and ANSYS simulated (Hybrid-ANSYS with $N = 11$) displacements.

Table 5.7.1: Evaluated Airy coefficients of Hybrid-DIC

c_0	11348.8	d_4	-76.4	a_3	-338.9
d_0	-3230.3	d_5	-11.4	a_4	-70.2
C_0	-5945.0	d_6	-0.1	a_5	4.6
D_0	2710.0	b'_2	-632.0	a_6	1.8
b_1	5742.6	b'_3	71.8	c_2	-539.1
d_1	-1720.5	b'_4	37.6	c_3	-44.3
b'_1	-10699.3	b'_5	-0.9	c_4	21.0
d'_1	-180.1	b'_6	-0.3	c_5	3.7
A_1	0.0	d'_2	-200.2	c_6	0.1
B_1	-4387.6	d'_3	444.0	a'_2	1671.7
A'_1	0.0	d'_4	51.6	a'_3	76.7
B'_1	1163.8	d'_5	-5.1	a'_4	-52.2
b_2	215.6	d'_6	-0.8	a'_5	-18.1
b_3	186.1	b_0	-5158.7	a'_6	0.2
b_4	-12.8	A_0	5344.6	c'_2	-27.3
b_5	-4.7	B_0	1335.2	c'_3	-142.1
b_6	0.0	c_1	-1005.5	c'_4	-20.6
d_2	1775.4	c'_1	1443.3	c'_5	0.9
d_3	73.3	a_2	-399.2	c'_6	0.2

Table 5.7.2: Evaluated Airy coefficients of Hybrid-ANSYS

c_0	1493.2	b'_3	-436.1	a_{11}	0.0
d_0	-1555.6	b'_4	-18.3	c_2	5548.8
C_0	0.1	b'_5	47.3	c_3	1988.4
D_0	-0.3	b'_6	-9.6	c_4	-985.3
b_1	-0.1	b'_7	-1.6	c_5	-878.4
d_1	789.3	b'_8	1.0	c_6	-194.0
b'_1	-3.9	b'_9	0.0	c_7	-3.8
d'_1	2130.6	b'_{10}	0.0	c_8	13.9
A_1	0.0	b'_{11}	0.0	c_9	8.7
B_1	-0.7	d'_2	-3838.2	c_{10}	1.6
A'_1	0.0	d'_3	4466.6	c_{11}	0.0
B'_1	1.4	d'_4	4227.9	a'_2	885.9
b_2	-1046.6	d'_5	-884.7	a'_3	-2448.0
b_3	-108.5	d'_6	-1832.8	a'_4	-780.0
b_4	158.3	d'_7	-306.8	a'_5	365.6
b_5	-10.6	d'_8	201.5	a'_6	158.4
b_6	-10.7	d'_9	63.7	a'_7	-25.4
b_7	4.0	d'_{10}	0.2	a'_8	-10.4
b_8	0.1	d'_{11}	-0.8	a'_9	0.7
b_9	-0.2	b_0	5147.5	a'_{10}	0.2
b_{10}	0.0	A_0	0.0	a'_{11}	0.0
b_{11}	0.0	B_0	1.7	c'_2	-529.6
d_2	5747.4	c_1	4080.8	c'_3	3034.9
d_3	4345.9	c'_1	-7460.2	c'_4	1729.7
d_4	-2595.7	a_2	-4648.0	c'_5	12.3

d_5	-3207.1	a_3	-1065.6	c'_6	-237.3
d_6	-81.0	a_4	1032.0	c'_7	-92.3
d_7	751.5	a_5	405.3	c'_8	-27.2
d_8	191.4	a_6	-107.1	c'_9	-3.4
d_9	-27.8	a_7	-46.9	c'_{10}	0.9
d_{10}	-11.3	a_8	4.7	c'_{11}	0.2
d_{11}	-0.4	a_9	1.6		
b'_2	277.6	a_{10}	-0.1		

5.7.3 Ability to Reconstruct the Other Half-plate

Vertical displacement and tangential stress are reconstructed on the full plate using evaluated Airy coefficients. Since only the upper half plate is used as input for evaluating Airy coefficients for Hybrid-DIC and Hybrid-ANSYS, figures 5.7.4 and 5.7.5 show they cannot reconstruct the other lower half.

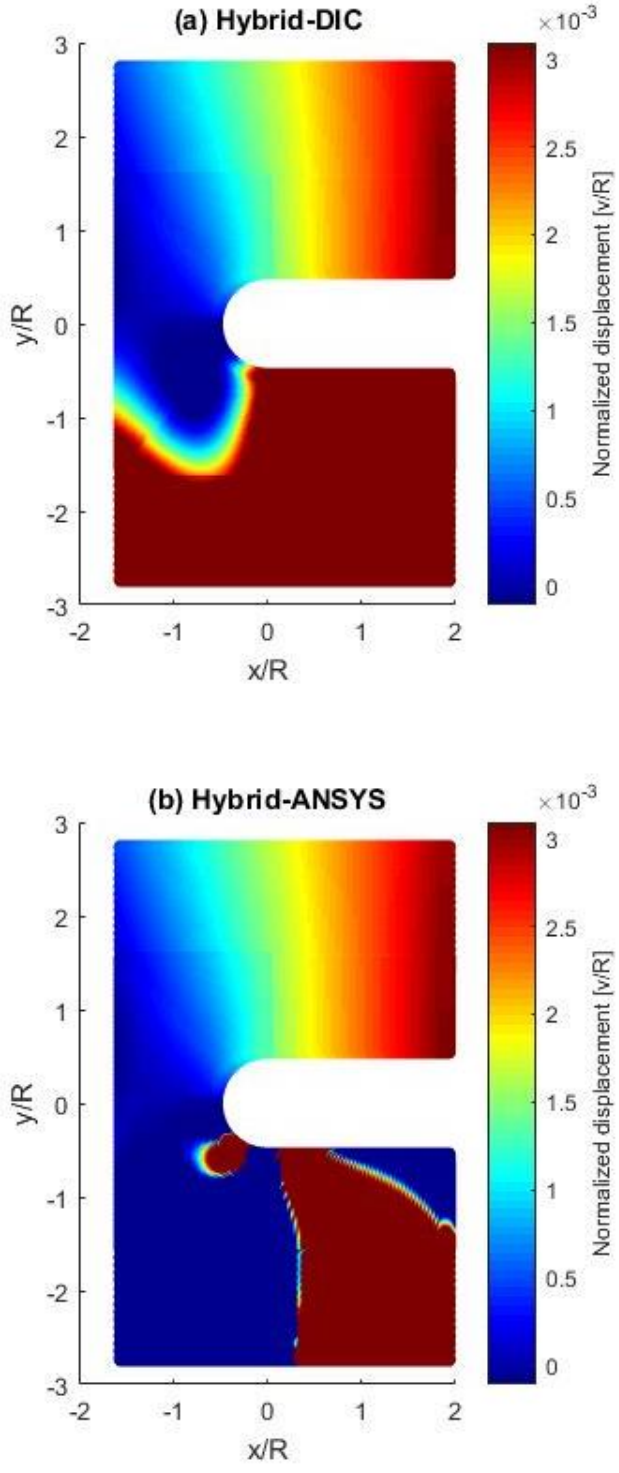

Figure 5.7.4: Vertical displacement reconstruced for full plate

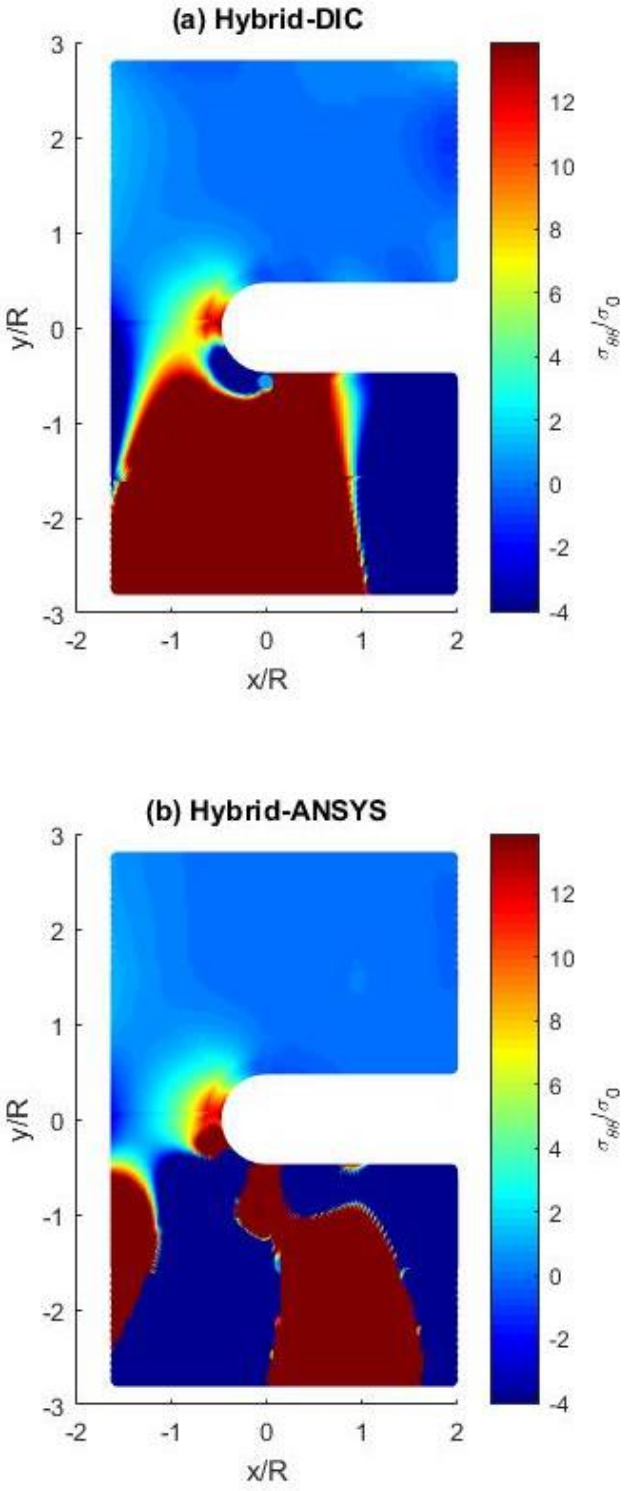

Figure 5.7.5: Tangential stress reconstruced for full plate

5.7.4 Single-valuness

Figures 5.7.6 and 5.7.7. show vertical displacements and tangential stress evaluated for the original θ (on the upper half) and θ+360º (on the lower half) to check if results are single-valued. Both Hybrid-DIC and Hybrid-ANSYS do not result in single-valuness for vertical displacement. Interestingly however, the ANSYS-Hybrid plotted tangential stress with θ+360º almost identical with original θ, figure 5.7.7 (b).

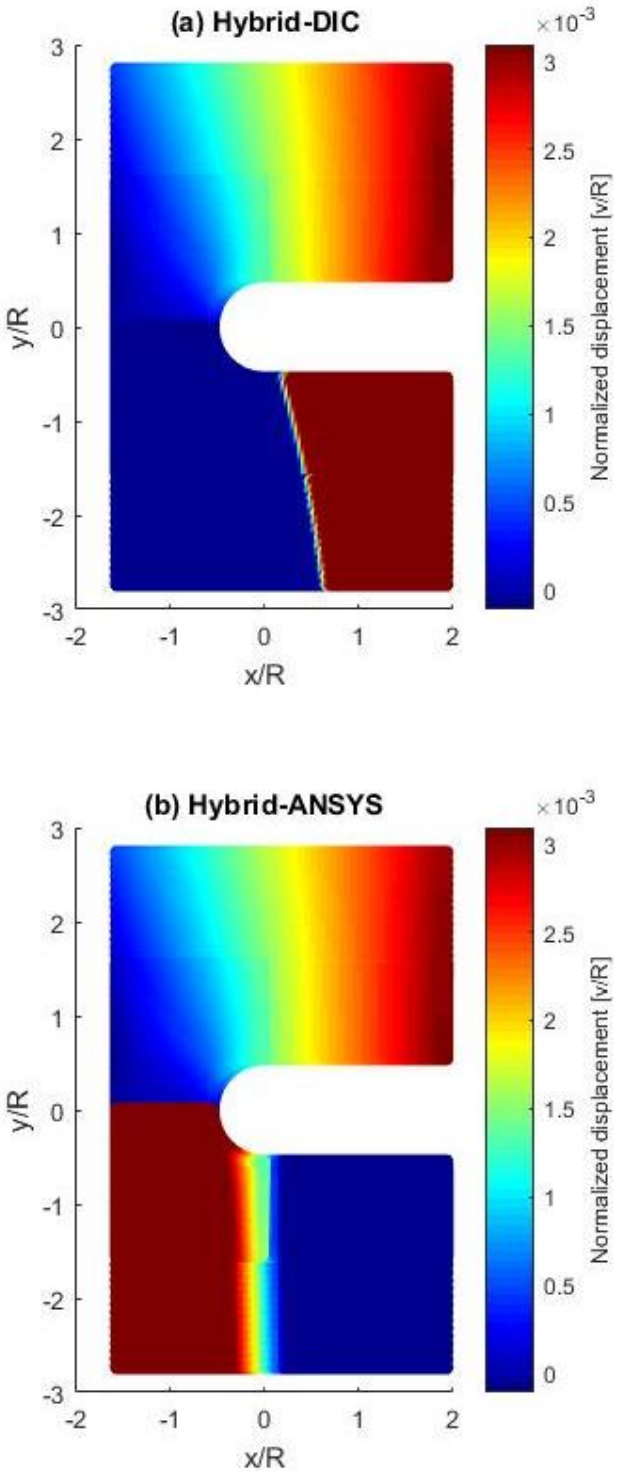

Figure 5.7.6: Vertical displacement with original angle, θ (upper half) and θ+2π (lower half)

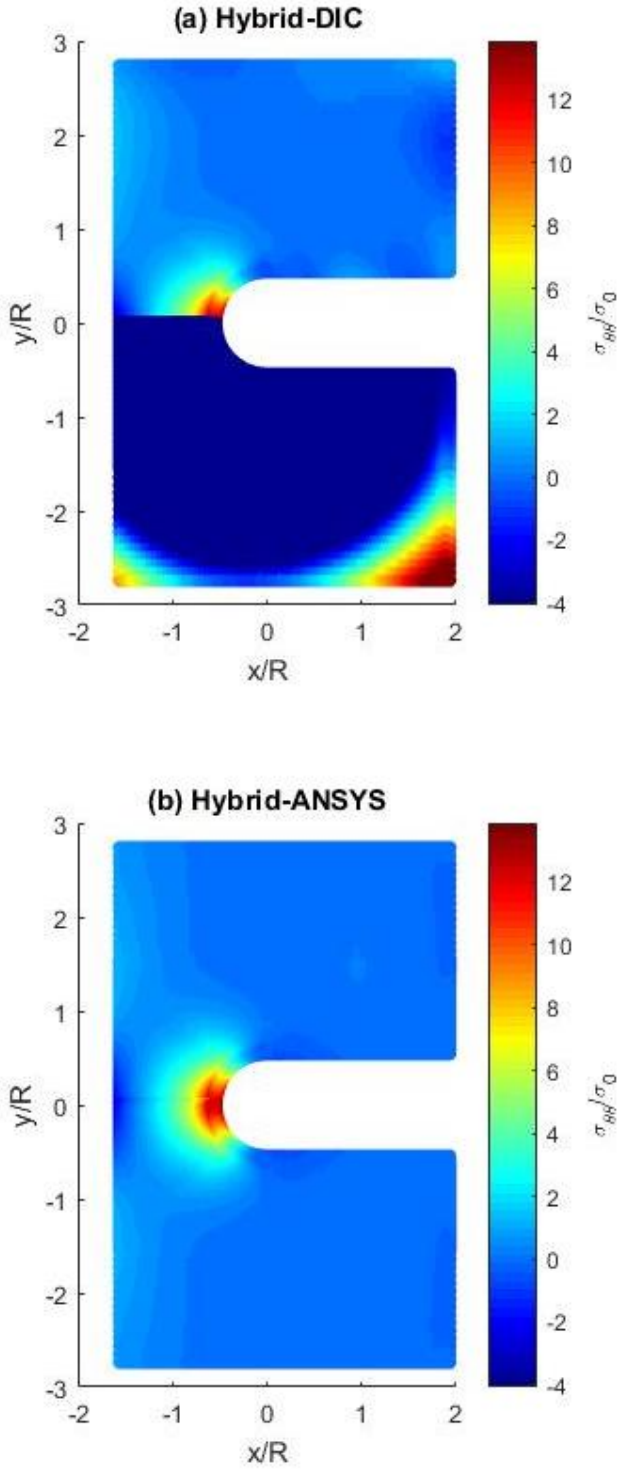

Figure 5.7.7: Tangential stress with original angle, θ (upper half) and $\theta+2\pi$ (lower half)

5.8 Summary, Discussion and Conclusions

The individual stresses on and near the edge of a deeply grooved finite plate are determined by synergizing the DIC-recorded and ANSYS-simulated displacement data with an Airy stress function. Employing more measured input values than unknown coefficients smooths the results. Cases A, B, and C of Chapter 4 are studied and only Case C can reconstruct both components of displacement. Unlike Chapter 3, which only utilizes input of vertical displacement to reconstruct both components of displacement, inputs of both components of displacement are necessary here. This might be due to both components of input displacement values are relatively similar in magnitude to each other while input vertical displacement values of Chapter 3 are much larger than input horizontal displacement values. Case C with inputs of both components of displacement can reconstruct here the upper half of displacements and individual stresses although it cannot reconstruct the other half. A theoretician might adversely view this inability of Case C to provide reliable stresses in both the two halves of this mechanically and geometrically symmetrical structure. However, this is probably not a practical concern since one can visually flip the results of the half plate containing the experimental input data to the other half of the plate. Appendix A5.1 includes results using full-plate input displacement values with Case C. Also, results of this Case C do not produce single-valued values.

Chapter 6. Determining Constitutive Properties and TSA Calibration Coefficients of Orthotropic Materials from Recorded Thermoelastic Information

6.1 Introduction

The mechanical response of elastically loaded plane orthotropic composites is controlled by the magnitudes of the four constitutive properties (E_{11}, E_{22}, G_{12} and v_{12}) whereas the values of the thermal calibration coefficients (K_1 and K_2) relate stress to the thermal-mechanical behavior. Persons have traditionally evaluated these six quantities from recording the stress-strain and stress-thermal response of uniaxially loaded coupons aligned in the 1- and 2-directions of material symmetry. Determining G_{12} additionally involves loading stress-strain coupons at 45 degree to these axes of symmetry. Testing these coupons is time-consuming and less than ideal. The task necessitates preparing separate coupons which presupposes having adequate material. Collecting the constitutive data necessitates recording the loaded coupon strains with strain gages, extensometer or optically (DIC, moiré, etc.). Thermal calibration requires loading those coupons on the same day, at the same frequency, same paint condition and at similar temperature and humidity as the tested structure. The ability to evaluate E_{22} of highly orthotropic materials can be hampered by low transverse strength, and the response of 90- and 45-degree coupons can become nonlinear at low stresses/strains. Employing a stress function and numerical optimization, Alshaya et al [79] recently developed an inverse method to evaluate the four constitutive quantities from

DIC-recorded displacements of a loaded structure. Acknowledging the convenience of the thermoelastic method of stress analyzing engineering structures, particularly if one does not have to prepare and test individual calibration specimens, the present objective is to extend the contribution by Alshaya et al [79] to enable the determination of the four constitutive properties and the two thermal-mechanical calibration coefficients from recorded thermal data of the structure of interest. In addition to not actually requiring the constitutive properties, and unlike displacement-based techniques such as DIC, TSA enjoys the advantage of not having to differentiate the recorded information.

As with Alshaya et al [79], double-notched tensile specimens are presently employed. Four orthotropic composites (two different glass/epoxy laminates, a graphite/epoxy laminate and Loblolly pine wood) are analyzed.

This research is a cooperative effort involving Dr. Considine of the USDA Forest Products Laboratory, Madison, Professor Alshaya, Kuwait University, Kuwaiti and myself. My contribution was to prepare and TSA test the four materials, evaluate their respective thermos-mechanical properties, assemble the experimental information and send it to Professor Alshaya. Professor Alshaya and Dr. Considine will oversee processing the provided experimental data with a stress function and applying the optimization scheme to evaluate the six (four mechanical and two thermal) quantities.

6.2 Materials

Four different orthotropic materials were tested: a graphite/epoxy laminate, glass/epoxy laminates of two different stacking sequences and Loblolly pine. Table 6.1 contains material details (i.e., stacking sequence) and constitutive values.

Table 6.1.1: Constitutive Properties

Material	E_{11} (GPa)	E_{22} (GPa)	G_{12} (GPa)	υ_{12}
$[0_{13}/90_5/0_{13}]$ Gr/Epoxy [80]	100.1	24.89	2.8	0.152
Gl/Epoxy (thin)	?	?	?	?
$[0/90/0_{10}/90/0]$ Gl/Epoxy (thick) [81]	34.2	14.2	3.4	0.22
Loblolly Pine [82]	12.3	13.9	1.01	0.33

6.3 Specimens, Dimensions, Preparation and Loading

Figure 6.3.1 contains the dimensions of the double-notched tensile specimens while figure 6.5.1 is a photograph of such a specimen. Dimensions of the various rectangular TSA thermal calibration coupons/specimens are included in Table 6.3.1. All notched and TSA calibration specimens were initially polished extremely lightly with 400 grid emery cloth. A coating of Krylon Ultra-Flat black paint was then applied to the surface to be scanned. This provides an enhanced and uniform thermal emissivity when loaded. Precautions were taken during polishing the face of a plate not to round-off the edges as this could further erode the quality of adjacent thermal information. Specimens were tensile loaded via hydraulic grips in a 20 kip capacity MTS hydraulic testing machine, figures, 6.3 through 6.5. All notched specimens and calibration coupons were loaded cyclically at 20 Hz when recording the load-induced TSA data.

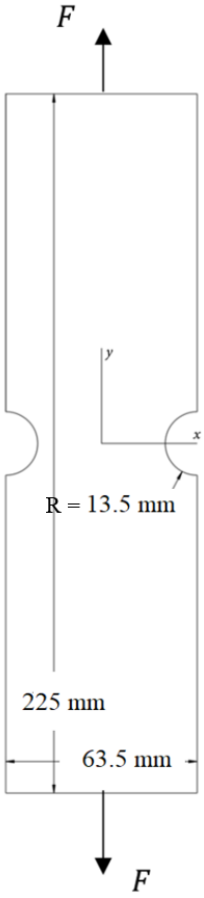

Figure 6.3.1: Schematic of double-notched tensile orthotropic plate

Table 6.2: Dimensions of calibration coupons and testing conditions of humidity and temperature

Material	Coupon Dimensions					Test Conditions	
	Orientation	Length	Width	Thickness	Area [in^2]	%RH	Temp, F
[0_{13}/90_5/0_{13}] Gr/Epoxy	0-deg	11"	0.82"	0.21"	0.1785	35	69
	90-deg	11"	0.5"	0.21"	0.105	35	69
Gl/Epoxy (thin)	0-deg	11"	0.75"	0.095"	0.071	22	69.7
	90-deg	11"	0.75"	0.095"	0.071	22	69.7
[0/90/0_{10}/90/0] Gl/Epoxy (thick)	0-deg	11"	0.75"	0.125"	0.094	22	69.2
	90-deg	11"	0.75"	0.125"	0.094	22	69.2
Loblolly Pine	0-deg	11"	0.75"	0.22"	0.165	10	69.2
	90-deg	5.5"	0.51"	0.22"	0.112	10	69.2

6.4 Thermoelastic Stress Analysis.

Since the theory behind/basis of thermoelastic stress analysis has been covered in Chapters 2 and 4 of this thesis, the details will not be repeated here. It is sufficient to note that for orthotropic materials under plane stress,

$$S^* = K_1\sigma_1 + K_2\sigma_2 \tag{6.1}$$

where σ_1 and σ_2 are the stresses in the directions of material symmetry, K_1 and K_2 are thermal mechanical coefficients and S^* is the recorded system signal. It is advantageous to process the recorded information with the help of complex variable stress functions and available boundary conditions. Equation (6.1) assumes adiabatic response. A DeltaTherm DT1400TSA system (Stress Photonics, Madison, WI) was used. The camera employs an indium antimonide (InSb) focal-plane array which responds in the 3–5 μm range with a peak response at a wavelength of 5.3μm. Camera detectors are cooled to 77 K with liquid nitrogen. The camera records at 1000 frames/second and the system provides images of surface temperature variations with a resolution of 0.001ºC. In mechanical terms, TSA has a resolution comparable to that of commercial metal foil strain gages. TSA images were captured and averaged over two minutes durations, and then exported to Excel to convert each pixel into a data point, i.e., 256 by 256 matrix, 65,536 data points. Pixel size is 0.46 mm (0.018″). Recognizing the unreliable thermoelastic data on or near an edge, no recorded TSA information was used within at least two-pixel positions (0.92 mm) of a boundary. All reported results are based on testing at 20 Hz. The phase information was also monitored to ensure that adiabatic conditions prevailed at this condition.

6.5 Testing

Figure 6.5.1 is a photograph of a one of the double-notched tensile specimens considered and figure 6.5.2 shows the thermal data of a specimen being recorded while the latter is cyclically loaded in a 20-kip MTS closed-loop testing machine. Figure 6.5.3 is an over-view of the testing setup, including the TSA camera and the mechanical testing system and its controls. Thermal calibration coefficients were evaluated from testing uniaxial tensile specimens as illustrated in figure 6.5.4. Unlike the specimen of figure 6.5.1, the surface of those in figures 6.5.2 through 6.5.4 had been painted with the flat black paint. Figures 6.5.5 and 6.5.6 illustrate representative TSA images (from the computer screen) in a tensile notched or uniaxial coupon recorded with the equipment of figures 6.5.2 through 6.5.4. Figures 6.5.7 through 6.5.10 show raw TSA image of graphite epoxy, thinner glass epoxy, thicker glass epoxy, and loblolly pine double notched plate.

All TSA calibration coupons of a particular notched orthotropic tensile plate were painted using the same technique, on the same day and tested on the same day as the associated double-notched specimen. Table 6.2 includes the dimensions of the coupons and the %RH and temperature (^{o}F) conditions at which the various tensile notched plates and their respective coupons were tested.

Figure 6.5.1: Double notched Loblolly pine specimen (before applying black paint)

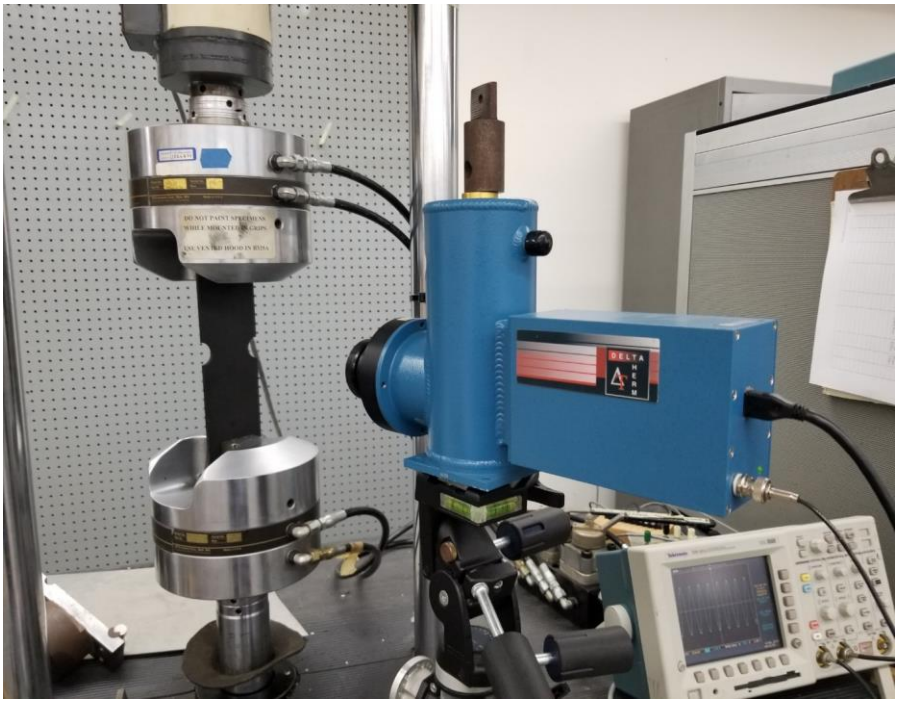

Figure 6.5.2: Recording thermal data in tensile loaded double-notched composite specimen with infrared camera

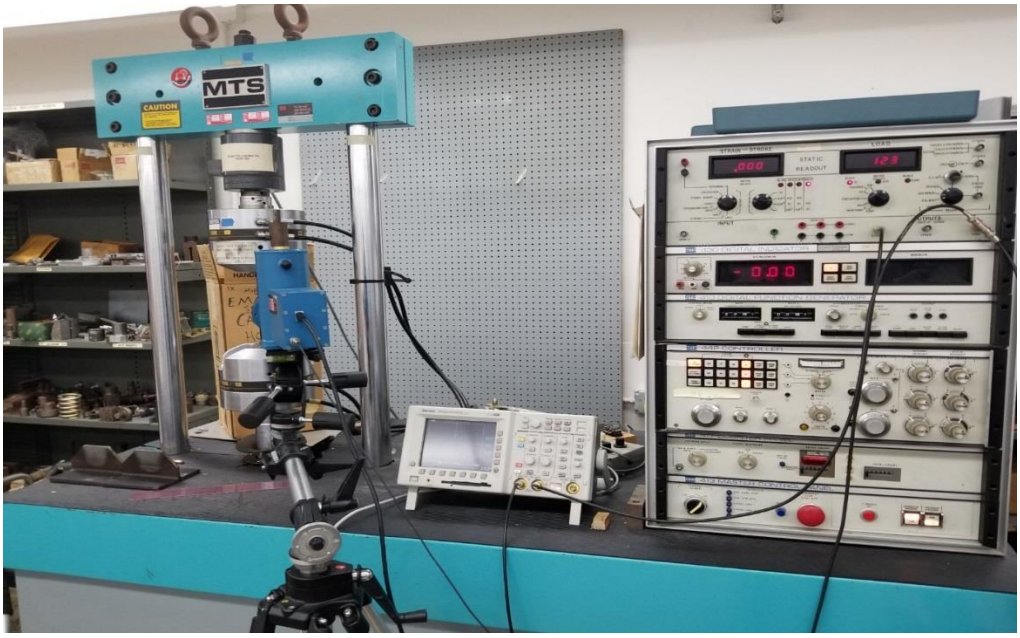

Figure 6.5.3: Over-view of testing setup.

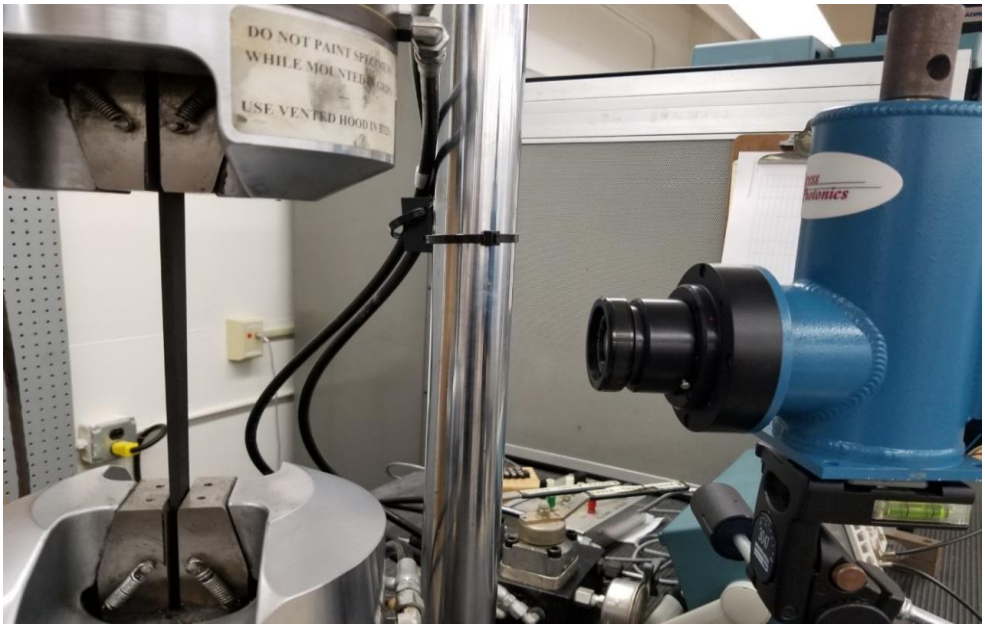

Figure 6.5.4: Recording thermal data in uniaxial tensile coupon with infrared camera

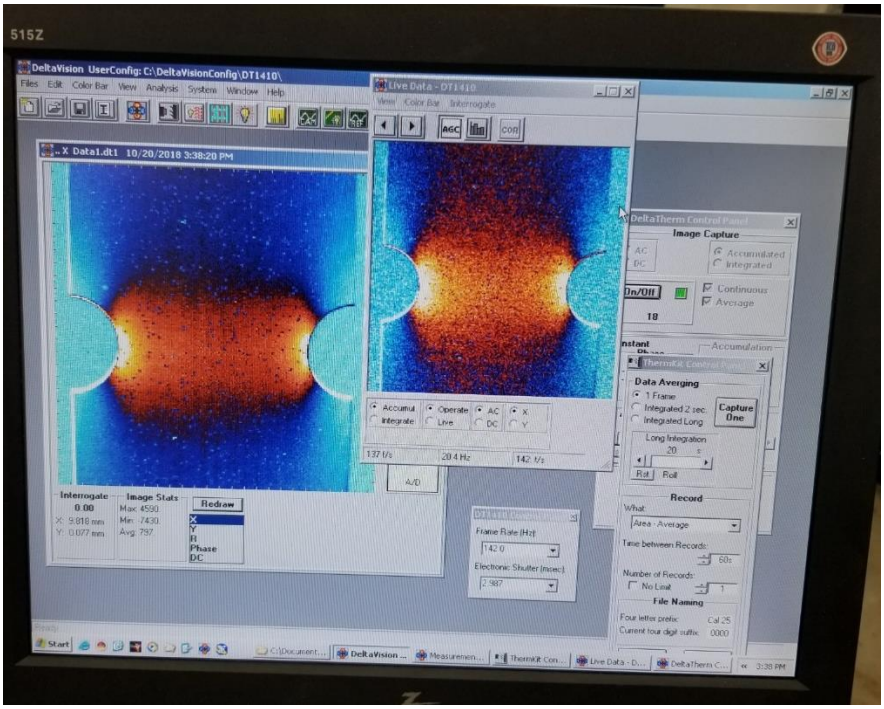

Figure 6.5.5: TSA image in a representative double-notched composite tensile plate

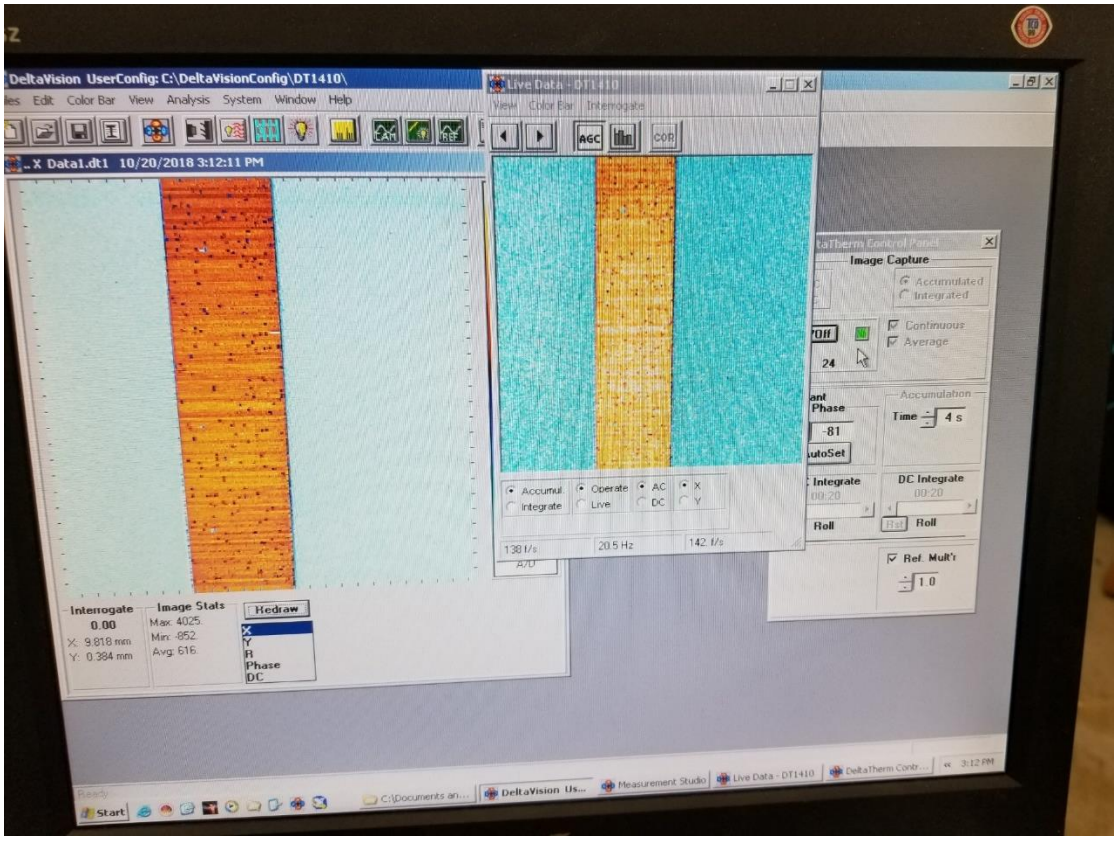

Figure 6.5.6: TSA image in a representative double-notched composite tensile plate

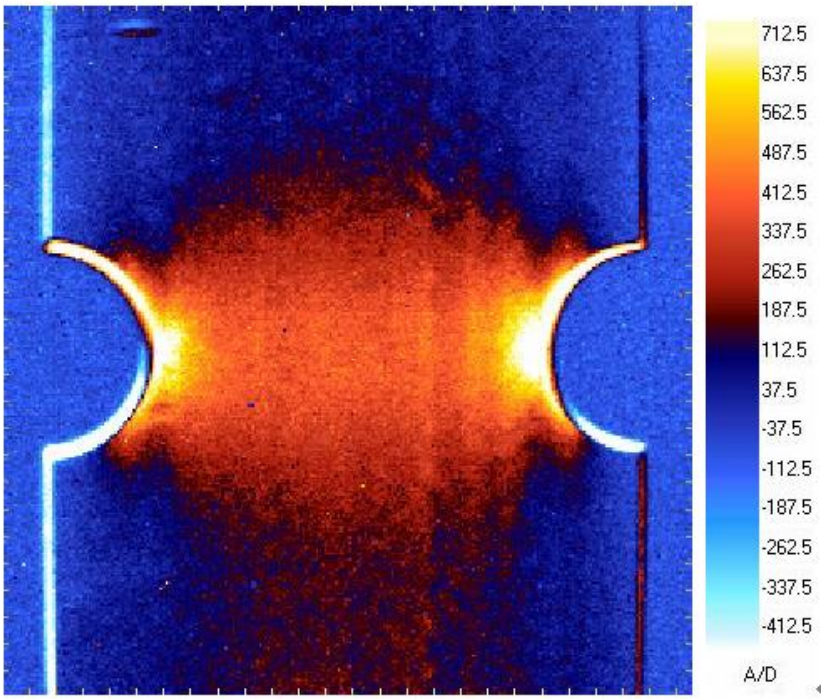

Figure 6.5.7: Raw TSA image of Graphite epoxy

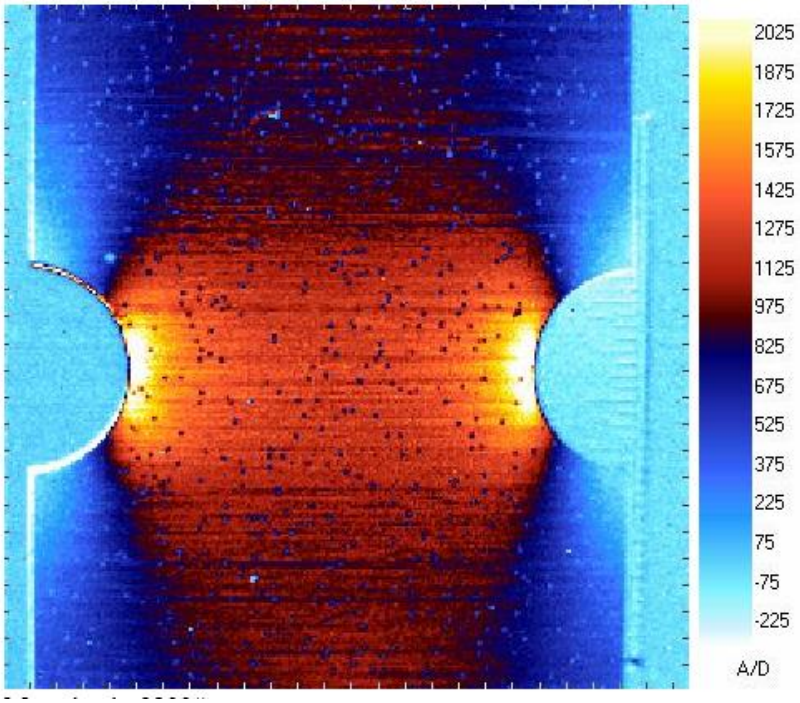

Figure 6.5.8: Raw TSA image of thinner Glass epoxy

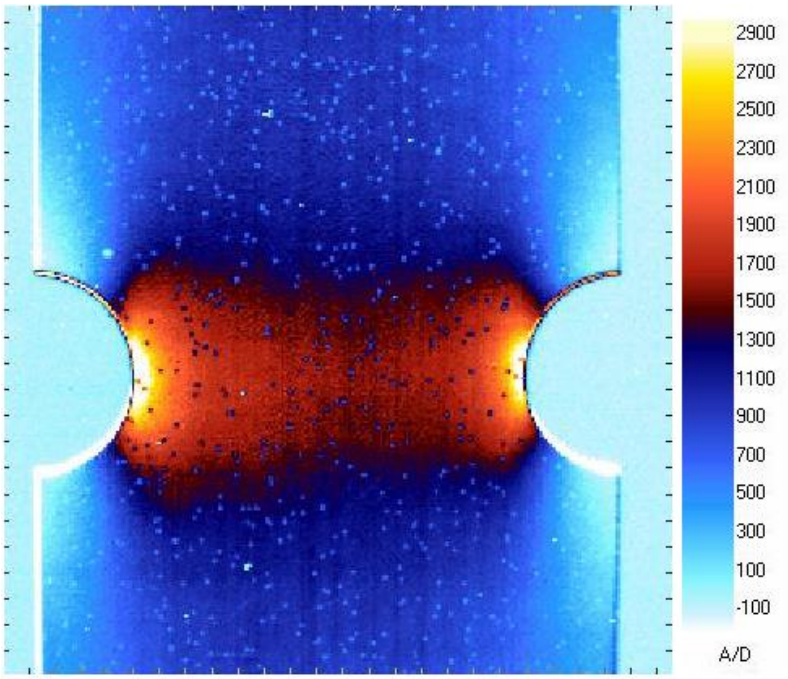

Figure 6.5.9: Raw TSA image of thicker Glass epoxy

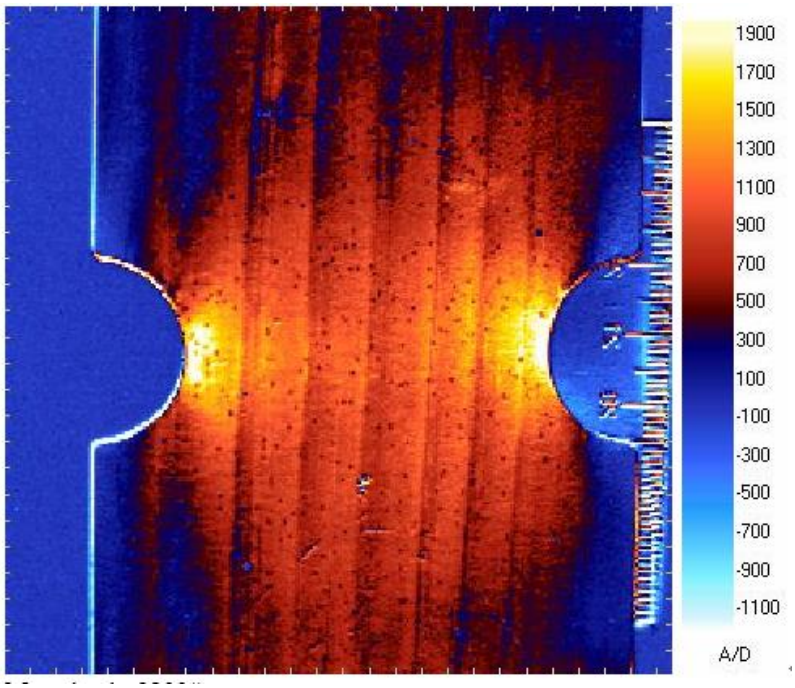

Figure 6.5.10: Raw TSA image of Loblolloy pine

6.6 Thermal Calibration Coefficients

Based on equation (6.1) and testing uniaxial coupons of Table 6.2 in each of the 1- and 2-directions of material symmetry, values of K_1 and K_2 were determined, Table 6.3 in units of U/psi, where the unit U is used to signify the raw TSA output is in uncalibrated signal units. Since the Loblolly pine coupons were damaged by the MTS hydraulic grips, values K_1 and K_2 were not obtained for the wood. The Appendix A6.1 contains quantitative details of these tests.

Table 6.3: Values of Thermal Calibration Coefficients

Material	Coefficients	Values
$[0_{13}/90_5/0_{13}]$ Gr/Epoxy	K_1	0.102
	K_2	1.179
Gl/Epoxy (thin)	K_1	1.037
	K_2	1.277
$[0/90/0_{10}/90/0]$ Gl/Epoxy (thick)	K_1	0.960
	K_2	1.263

A double-edge notched tensile plate is employed here. However, one could potentially use a diametrally-loaded disk or ring. An advantage of a ring or disk specimen is that by loading it but under different orientations of the principal materials directions relative to the direction of loading, one would be able to obtain several sets of values which can be averaged from the single specimen.

APPENDICES

Appendix A4.1: Ensuring plane stress condition on deep notched aluminum plate

Since TSA assumes plane stress condition, 2D and 3D FEM models were created by ANSYS before machining the specimen of figures 4.1.1 and A4.1.1. For both models, a very fine FEM mesh was used in the neighborhood of the notch to ensure reliable results. Element size was decreased was until the ANSYS results at the notch did not vary more than 2% from successive mesh changes. For the 3D model, stresses were computed at the middle of the plate and on the external flat surfaces of the plate and compared with results of the 2D model to assess plane stress condition for the given geometrical dimensions. Figure A4.1.2 plots normalized tangential stresses ($\sigma_{\theta\theta}/\sigma_0$) along arc BC of figure A4.1.1. The results are certainly sufficiently uniform through the plate thickness (i.e., sufficiently plane stress) for TSA.

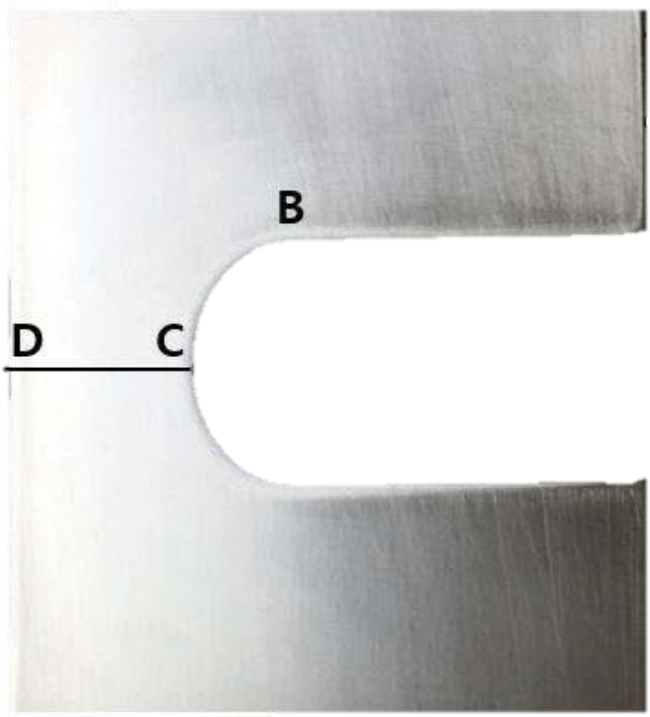

Figure A4.1.1: Line C-D and arc B-C

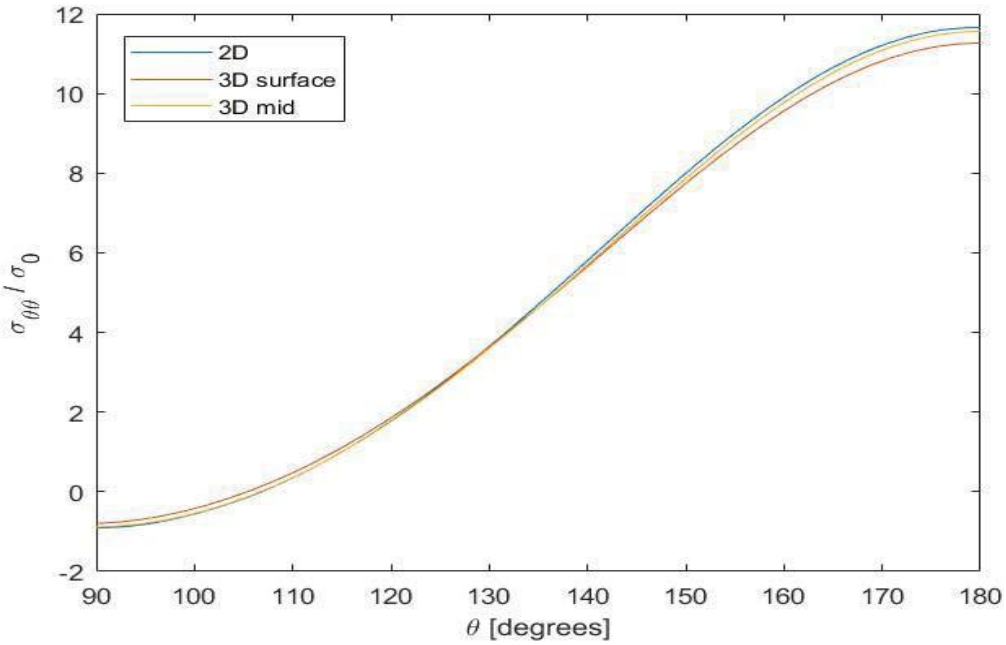

Figure A4.1.2: Normalized tangential stress, $\sigma_{\theta\theta}/\sigma_0$, along arc B-C

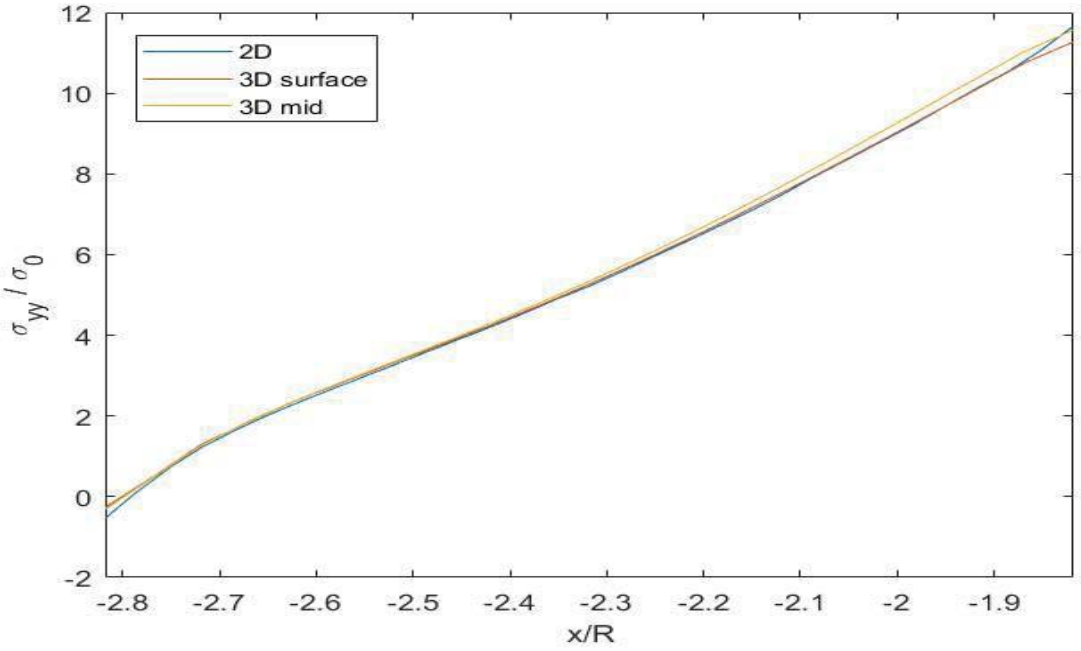

Figure A4.1.3: Normalized vertical stress, σ_{yy}/σ_0, along line C-D

Appendix A4.2: Results using full-plate TSA-signal as input

Instead of evaluating Airy coefficients using only the upper half of the plate having recorded TSA-signal or ANSYS-simulated isopachic stress of Chapter 4, input data from the full plate are used here with Case C (retaining all Airy coefficients). Previous results from Chapter 4 with Case C could reconstruct individual components of stress successfully in the half of the plate containing the input data, but not reconstruct them in the other half of the plate. In this section, when TSA thermal data throughout the full plate is used, ability to reconstruct stresses for the full-plate is studied and is called Case D.

A4.2.1 Data Source Location

A total of 39,738 input values are uniformly distributed throughout the entire plate (averaged recorded TSA values from upper and lower halves of the plate and then used them over the whole plate) as shown in shaded area of figure A.4.2.1.

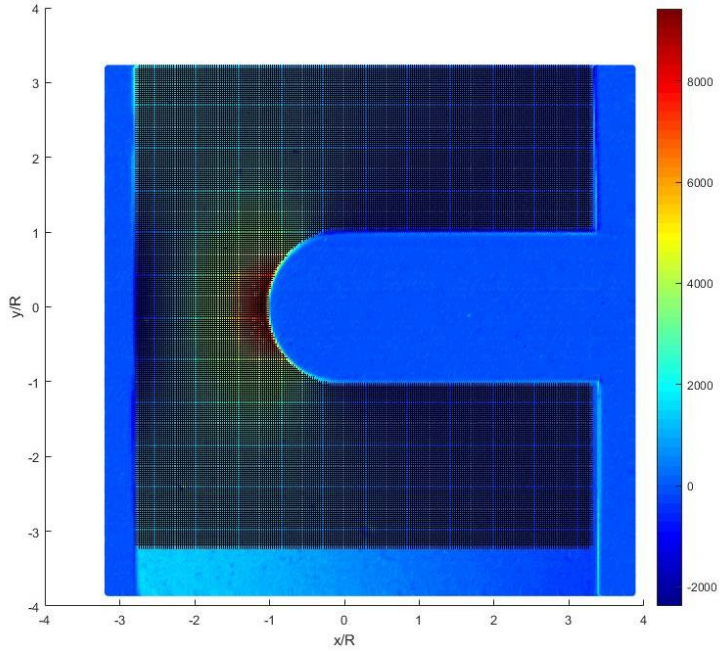

Figure A4.2.1: Source location showing total 39,738 TSA data points

A4.2.2 Boundary Conditions

For the full-plate, additional boundary conditions were applied compared to equation (4.8) and figure 4.3.1. Each of boundary conditions of equation (A4.1) and figure A4.2.2 were applied with 500 discrete locations making total 7,500 imposed boundary values.

$$
\begin{aligned}
&\sigma_{rr}(R,\theta) = \sigma_{r\theta}(R,\theta) = 0, \quad 0.5\pi \leq \theta \leq 1.5\pi \\
&\sigma_{yy}(x,R) = \sigma_{xy}(x,R) = 0, \quad 0 \leq x \leq 1.935 \\
&\sigma_{yy}(x,-R) = \sigma_{xy}(x,-R) = 0, \quad 0 \leq x \leq 1.935 \\
&\sigma_{xx}(-1.56,y) = \sigma_{xy}(-1.56,y) = 0, \quad 0 \leq y \leq 4R \\
&\sigma_{xx}(-1.56,y) = \sigma_{xy}(-1.56,y) = 0, \quad -4R \leq y \leq 0 \\
&\sigma_{xx}(1.935,y) = \sigma_{xy}(1.935,y) = 0, \quad R \leq y \leq 4R
\end{aligned}
\tag{A4.1}
$$

$$\sigma_{xx}(1.935, y) = \sigma_{xy}(1.935, y) = 0, \qquad -4R \leq y \leq -R$$

$$\sigma_{xy}(x, 0) = 0, \qquad -1.56 \leq x \leq -R$$

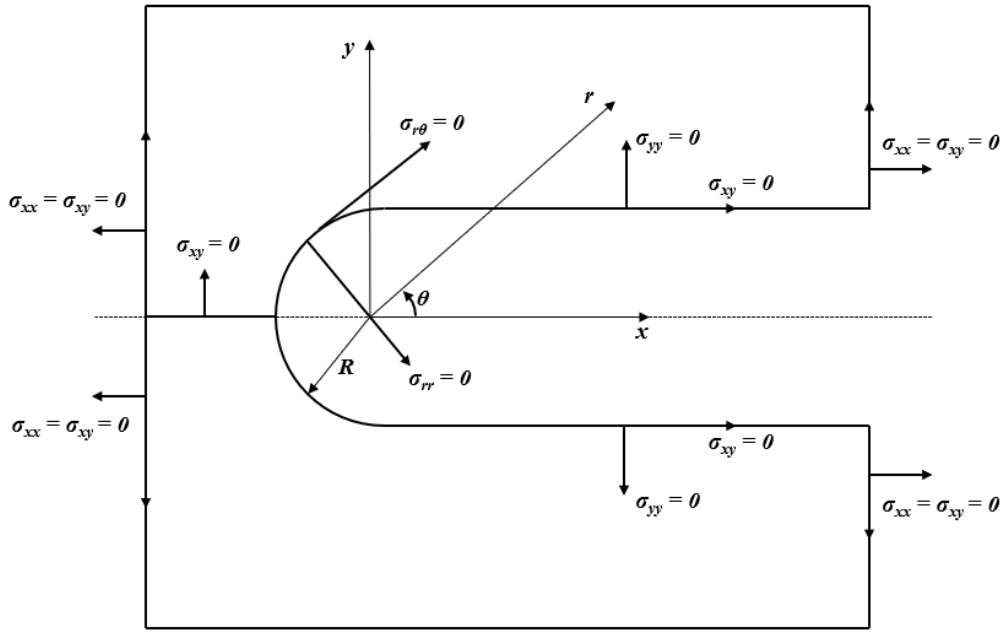

Figure A4.2.2: Imposing traction-free boundary conditions

A4.2.3 *RMS* and Force Equilibrium

Both RMS and force equilibrium method are again used to determine the appropriate terminating index, *N*. Figure A4.2.3 shows *RMS* error between TSA-recorded and reconstructed isopachic stress and figure A4.2.4 shows average value of normalized forces. Using the same arguments of before, $N = 5$ is chosen for Case D.

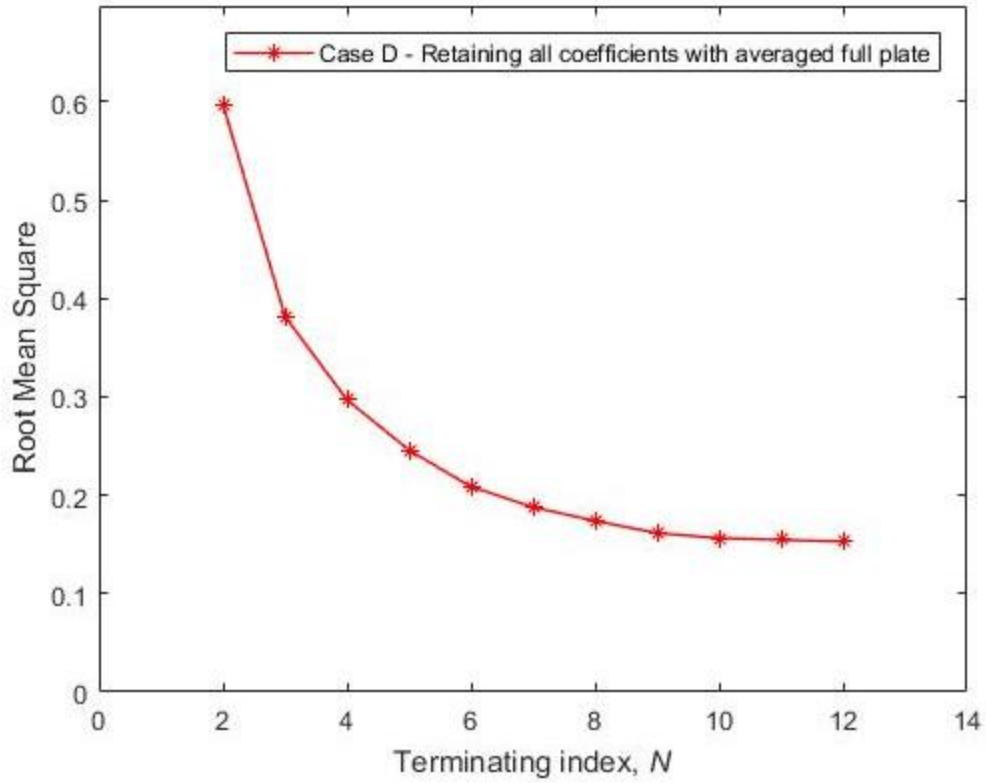

Figure A4.2.3: *RMS* vs Terminating index, *N*

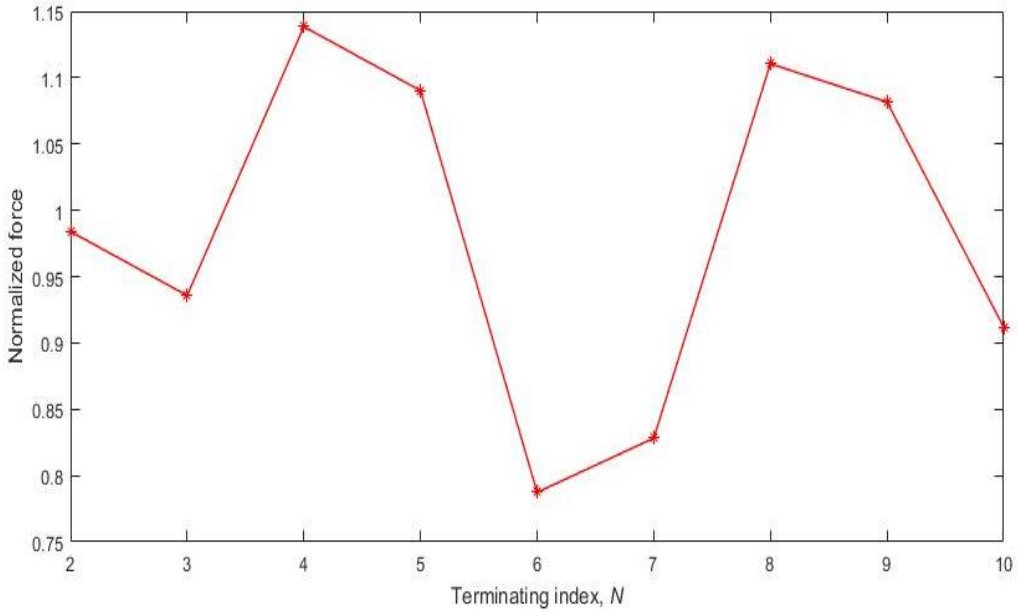

Figure A4.2.4: Average value of normalized forces calculated on the respective horizontal lines of *y*-axis vs terminating index, *N*

A4.2.4 Results

With N=5, the Airy coefficients are evaluated, and individual components of stress are reconstructed with equations (4.1) through (4.6). Figure A4.2.5 compares TSA-recorded and reconstructed with Hybrid-TSA isopachic stress. Unlike Case C of this chapter, Case D can reconstruct the stresses throughout both halves of the plate successfully. Figure A4.2.6 plots normalized tangential stress along the end of the notch (from θ = 90° to 270°) and compares with that from ANSYS. Figure A4.2.7 plots reconstructed radial and shear stresses along the notch. As expected, these are close to zero. Figures A4.2.8 through A4.2.13 compare full-plate individual components of stress from ANSYS and reconstructed with Hybrid-TSA (Case D). Table A4.2.1 lists the values of the Airy coefficients for Case D. Although some of the coefficients associated with symmetry about y = 0 are very small, almost none of them is technically zero.

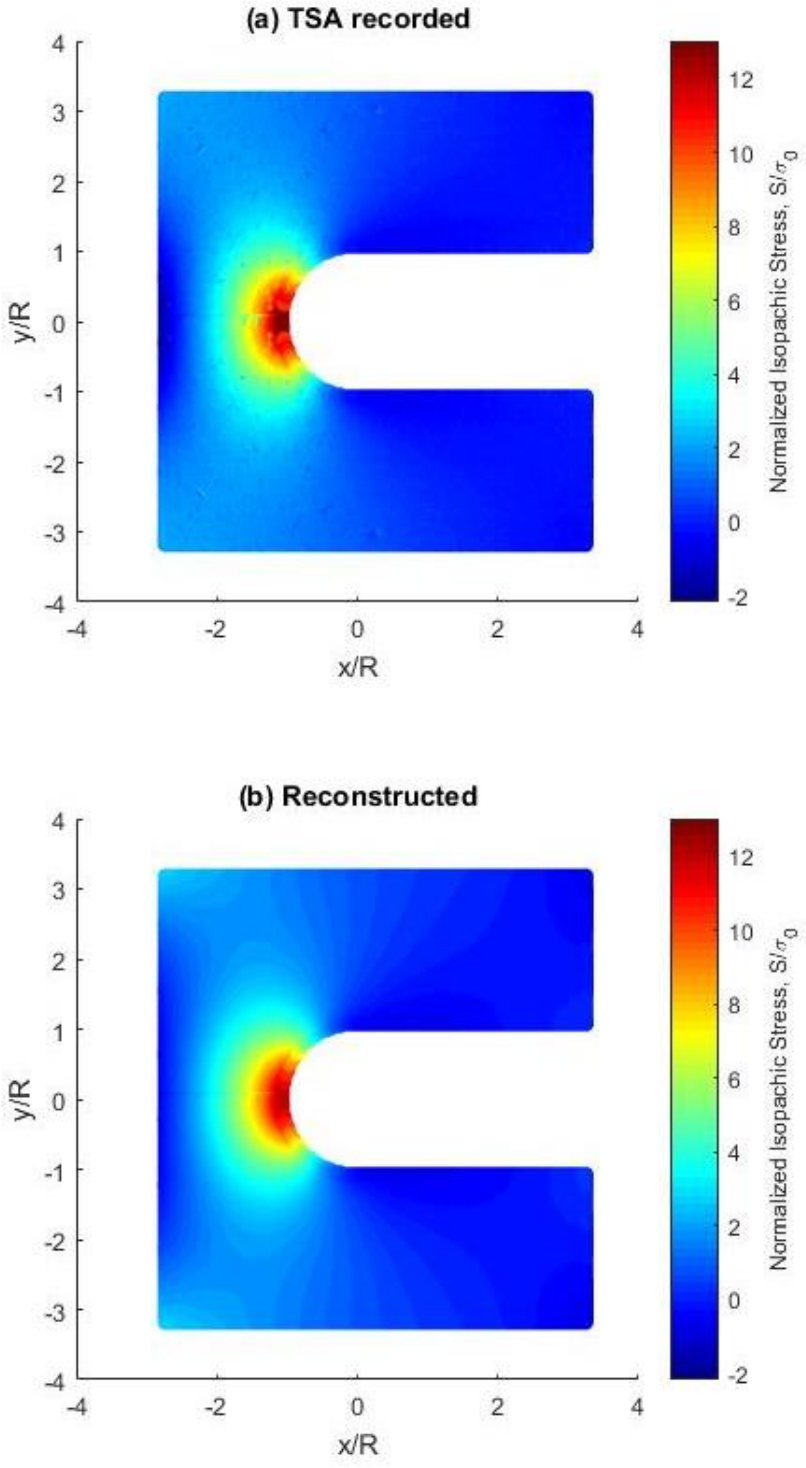

Figure A4.2.5: Normalized isopachic stress, S/σ_0, for TSA-recorded (a) and reconstructed for hybrid-TSA method with N = 5 (b)

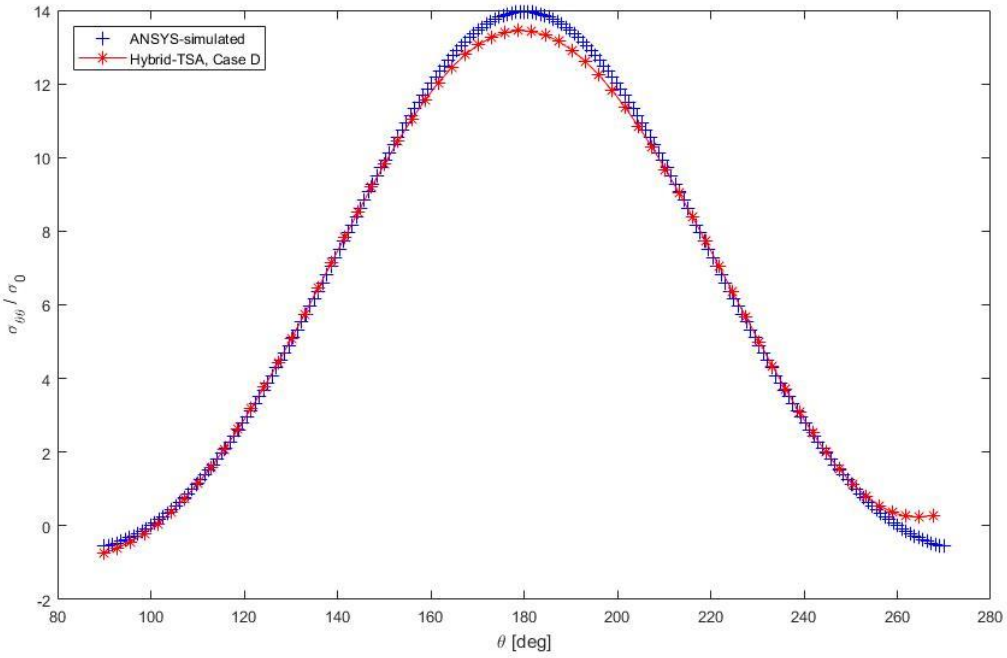

Figure A4.2.6: Normalized tangnetial stress, $\sigma_{\theta\theta}/\sigma_0$, along the edge of the notch

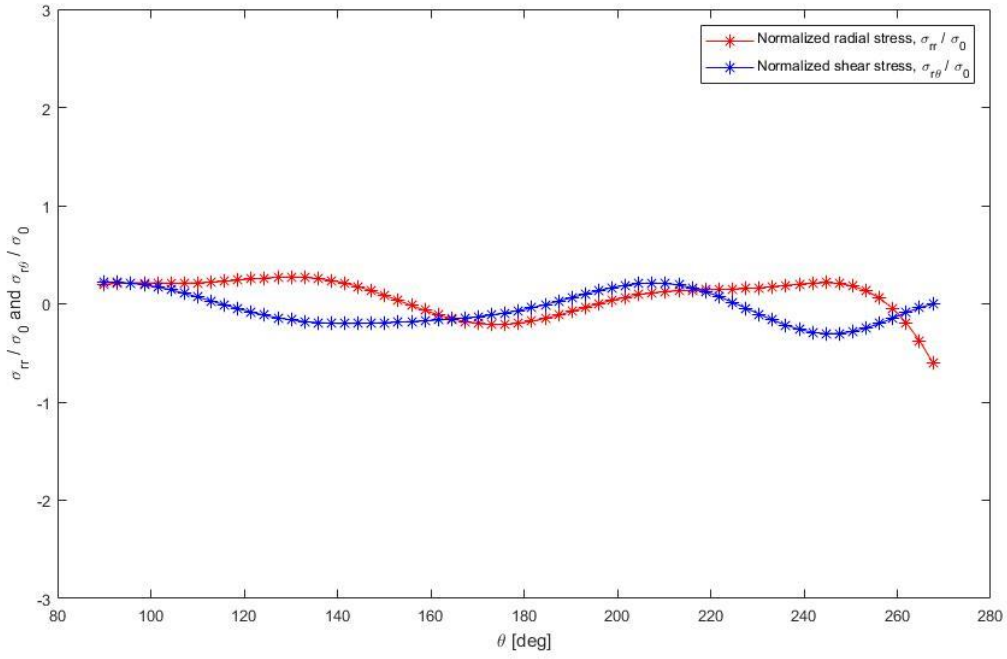

Figure A4.2.7: Normalized radial and shear stress, σ_{rr}/σ_0 and $\sigma_{r\theta}/\sigma_0$, along the edge of the notch

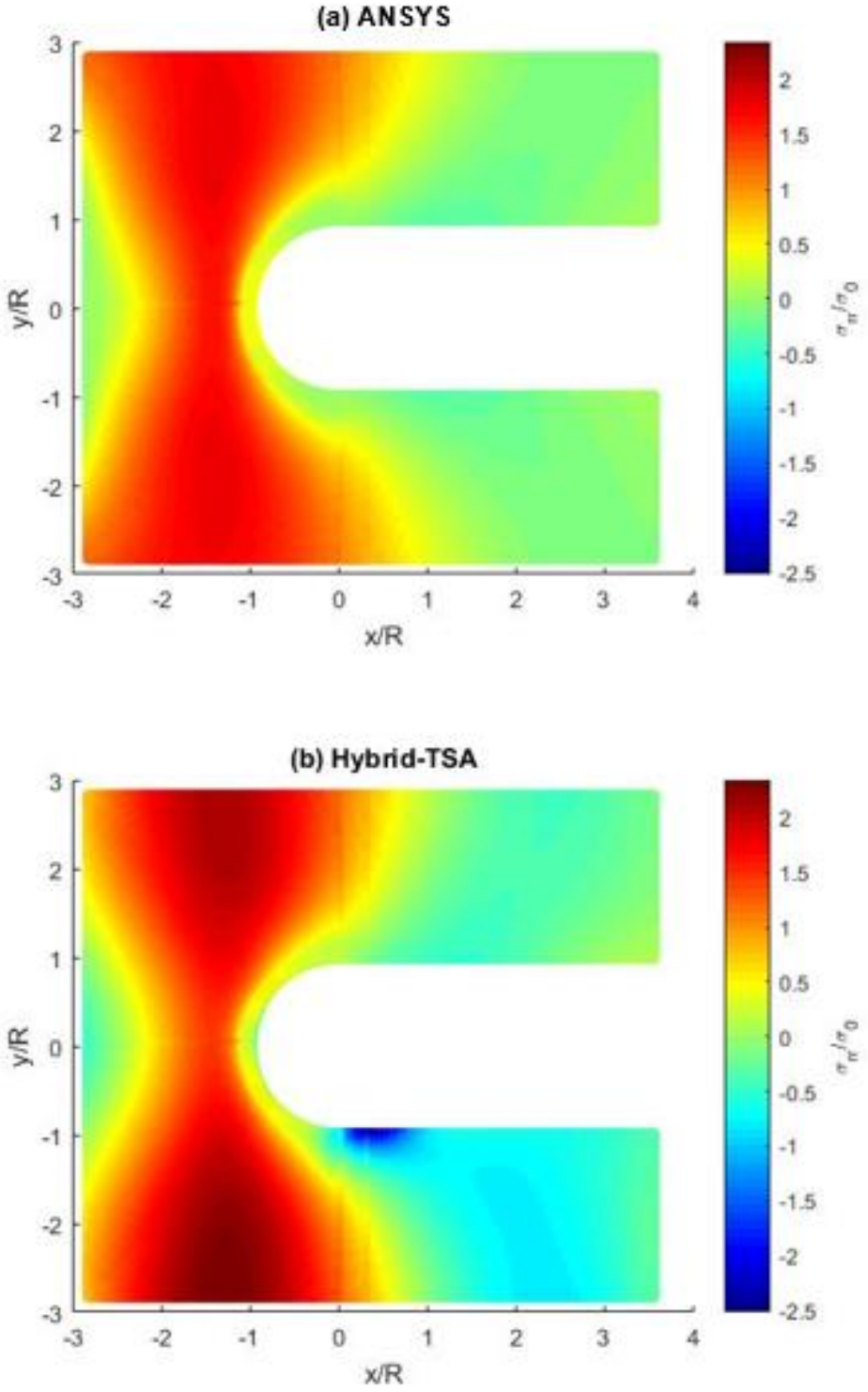

Figure A4.2.8: Normalized radial stress, σ_{rr}/σ_0

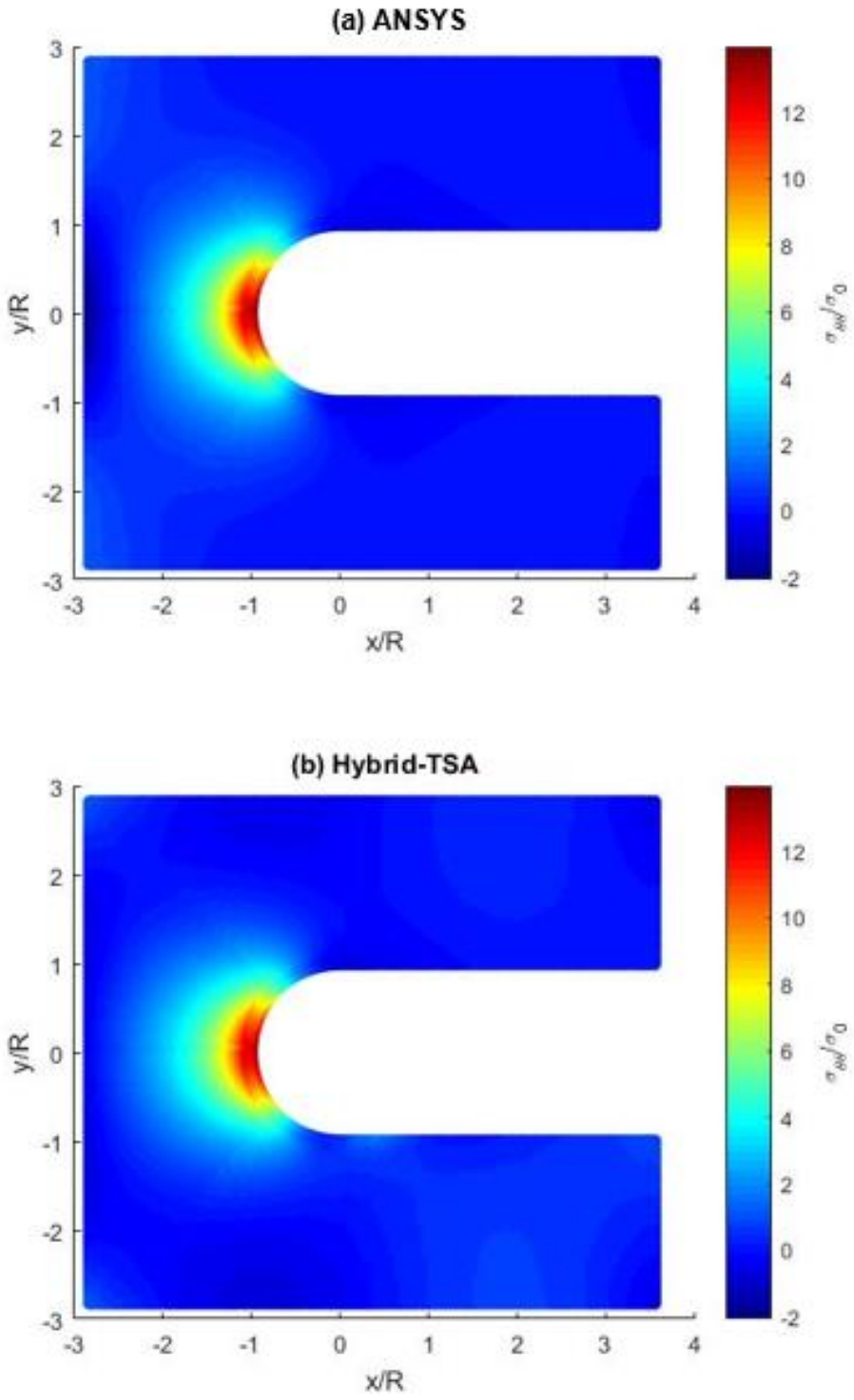

Figure A4.2.9: Normalized tangential stress, $\sigma_{\theta\theta}/\sigma_0$

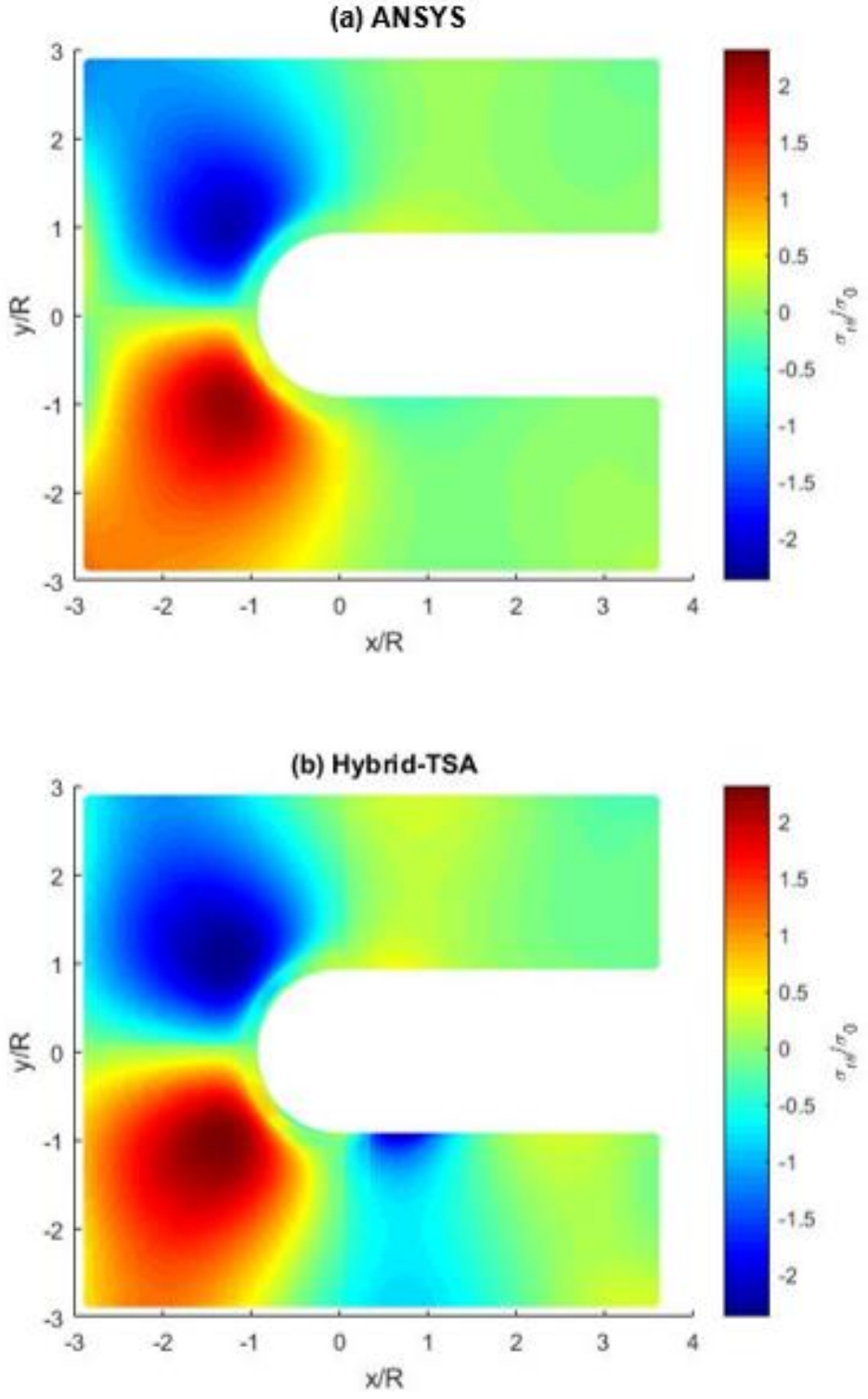

Figure A4.2.10: Normalized shear stress, $\sigma_{r\theta}/\sigma_0$

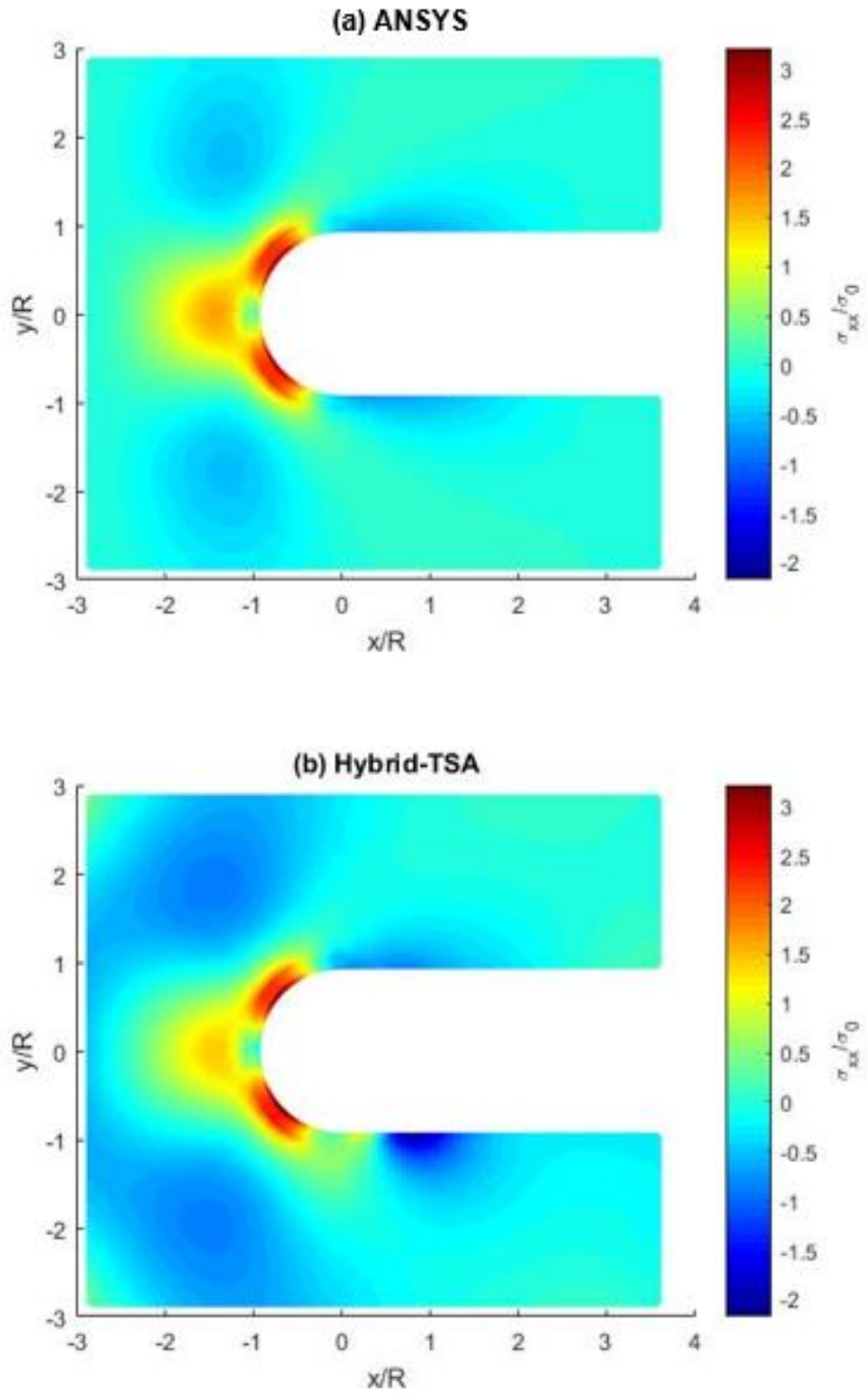

Figure A4.2.11: Normalized horizontal stress, σ_{xx}/σ_0

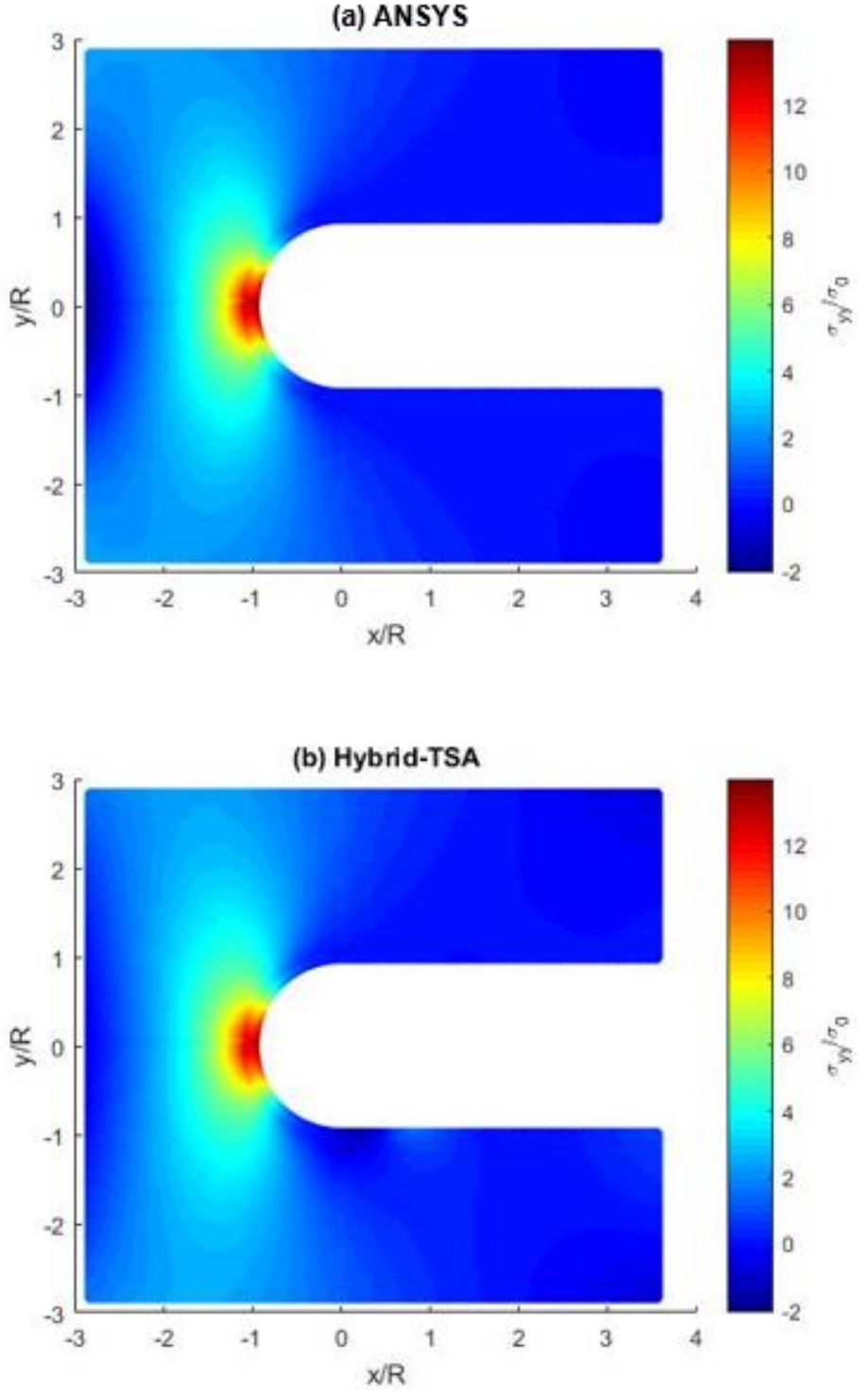

Figure A4.2.12: Normalized vertical stress, σ_{yy}/σ_0

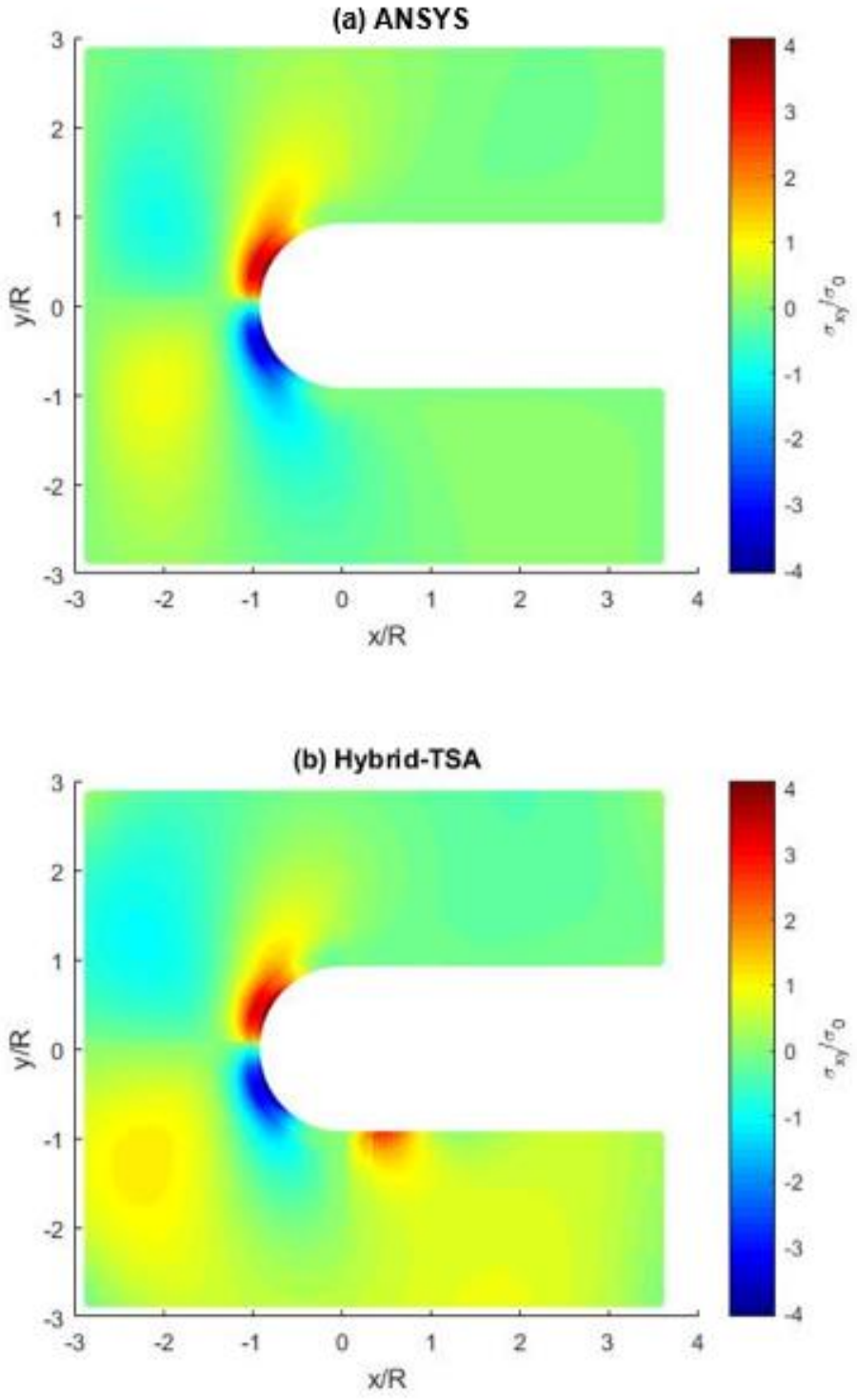

Figure A4.2.13: Normalized shear stress, σ_{xy}/σ_0

Table A4.2.1: Evaluated Airy coefficients based on isopachic stress, *S*, from TSA

c_0	2,354.9	d_3	-5.0	a_3	-0.9
d_0	-1,153.1	d_4	-0.5	a_4	1.2
C_0	-568.6	d_5	0.0	a_5	0.3
D_0	257.6	b'_2	-26.2	c_2	-11.0
b_1	-1,087.3	b'_3	9.3	c_3	-0.4
d_1	47.7	b'_4	-1.6	c_4	0.3
b'_1	-3,107.4	b'_5	0.4	c_5	0.1
d'_1	129.7	d'_2	-187.2	a'_2	424.4
A_1	-176.7	d'_3	16.2	a'_3	-87.2
B_1	-49.3	d'_4	-0.3	a'_4	4.2
A'_1	-95.8	d'_5	-0.3	a'_5	-0.8
B'_1	576.4	b_0	-1,531.4	c'_2	9.8
b_2	3.4	A_0	585.8	c'_3	-8.0
b_3	0.5	B_0	368.4	c'_4	-0.9
b_4	0.0	c_1	-129.3	c'_5	0.0
b_5	0.0	c'_1	-255.1		
d_2	-64.4	a_2	-0.2		

A4.2.5 Single-valueness

To see if the reconstructed stresses for Case D were single-valued, full-plate isopachic and tangential stresses are plotted with (a) original θ and (b) θ+360°. Figures A4.2.14 and A4.2.15 show stresses are not single-valued for Case D.

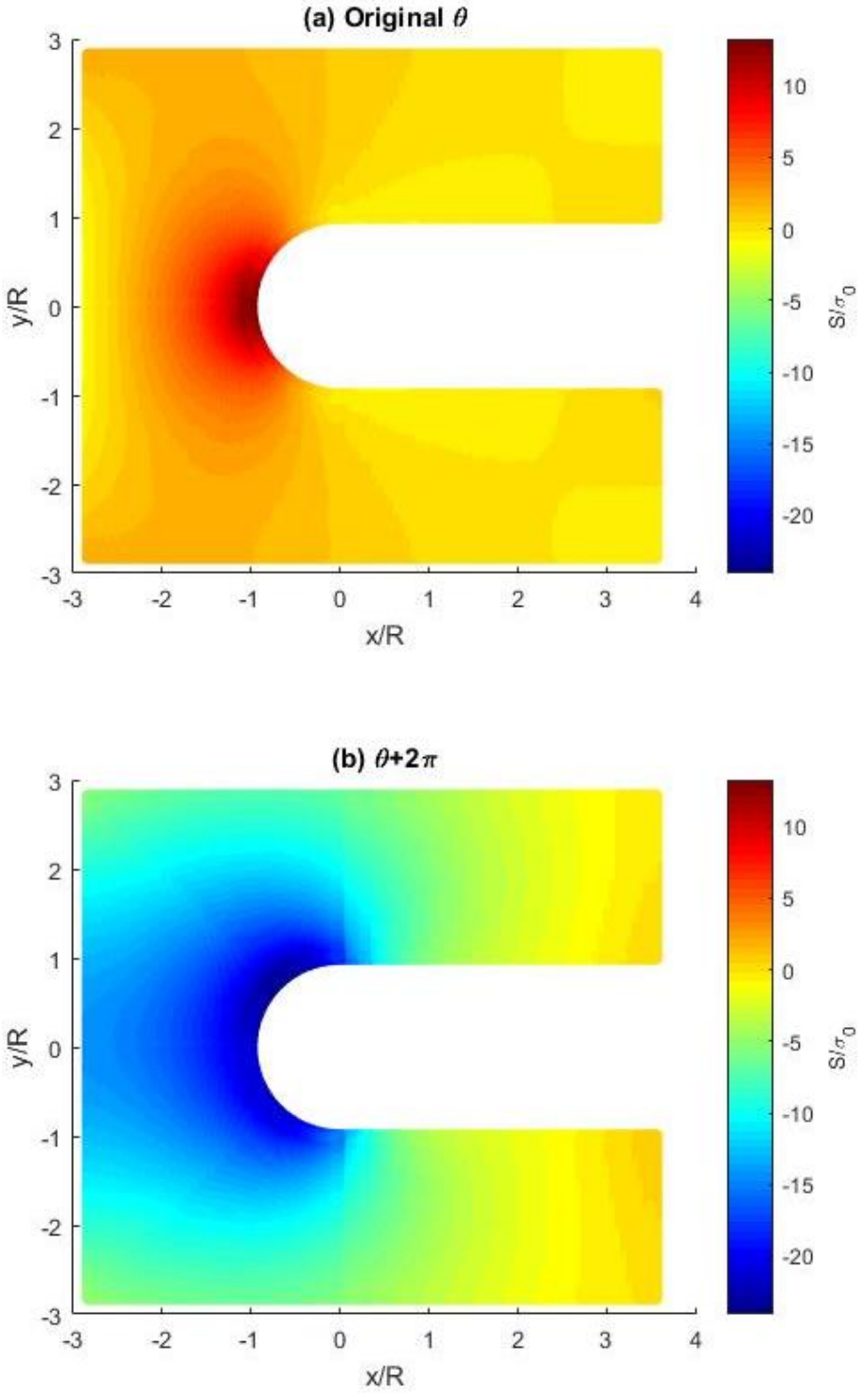

Figure A4.2.14: Normalized isopachic stress, S/σ_0, with (a) original angle, θ and (b) $\theta+2\pi$

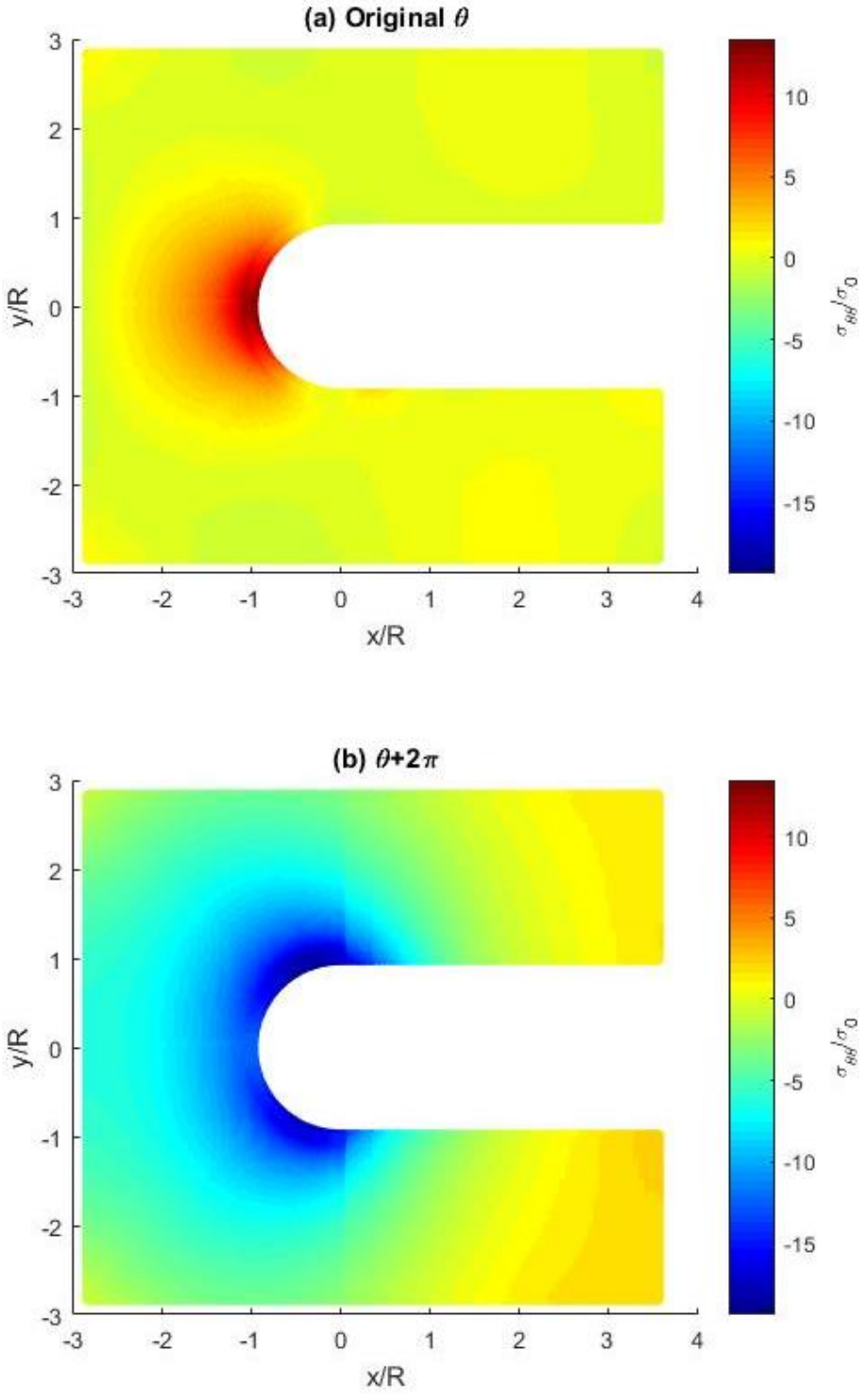

Figure A4.2.15: Normalized tangential stress, $\sigma_{\theta\theta}/\sigma_{\theta_0}$, with (a) original angle, θ and (b) $\theta+2\pi$

Appendix A4.3: Results using full-plate ANSYS-simulated isopachic stress as input

In this section, the Airy coefficients are evaluated for Case D but using ANSYS-simulated isopachic stress instead of TSA-recorded signal. All Airy coefficients are retained, and the same boundary conditions are applied as in Appendix A4.2, i.e., figure A4.2.2. This is the numerical evaluation to accompany the TSA experimental input of Appendix A4.2 (Case D).

A4.3.1 Data Source Location

Figure A4.3.1 shows the locations the ANSYS-simulated isopachis stress used for evaluating the Airy coefficients. A total of 13,559 input values of S were employed.

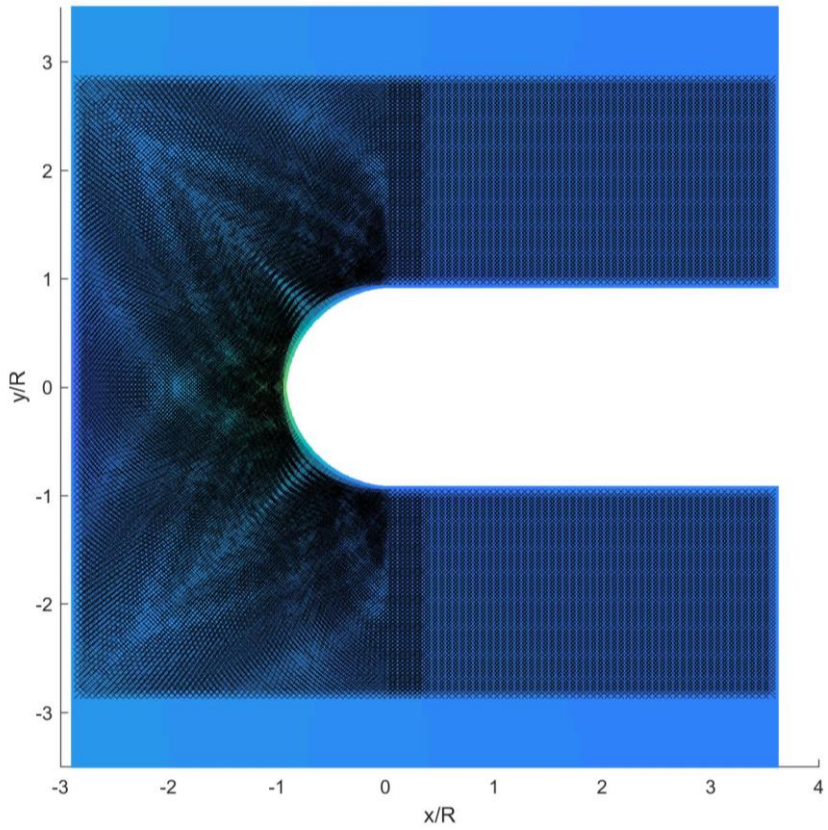

FigureA4.3.1: Source location showing 13,559 ANSYS input data locations

A4.3.2 *RMS* and Force Equilibrium

The *RMS* error between ANSYS-simulated and reconstructed (Hybrid-ANSYS) isopachic stress is shown in figure A4.3.2 for different terminating index, *N*. Figure A4.3.3 shows average forces calculated for each *N*. For this section, $N = 8$.

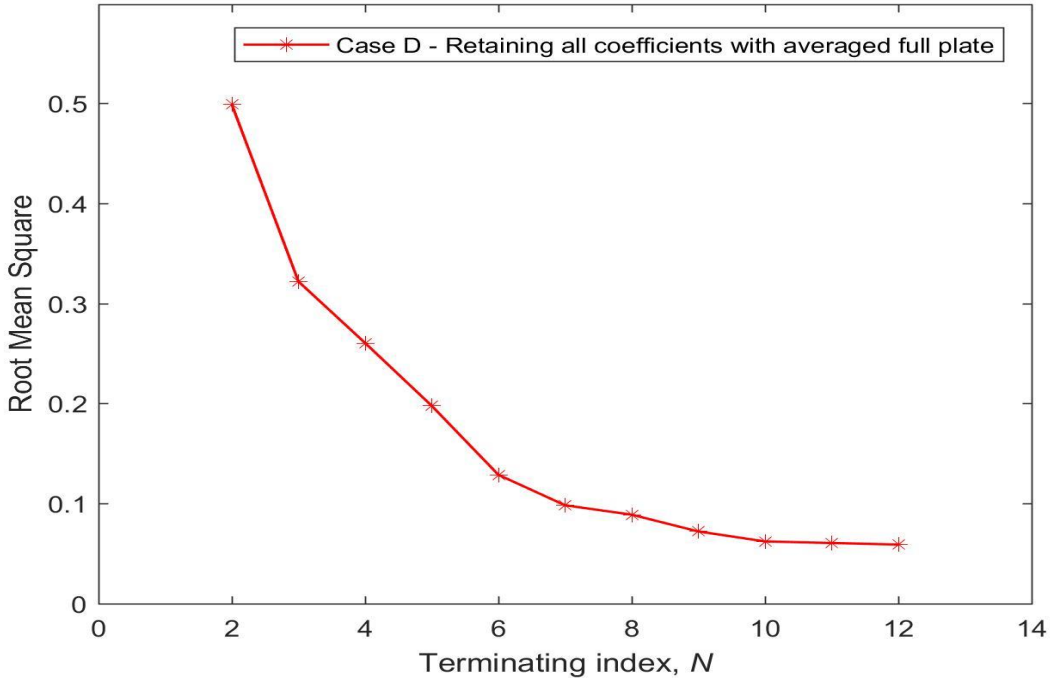

Figure A4.3.2: *RMS* vs Terminating index, *N*

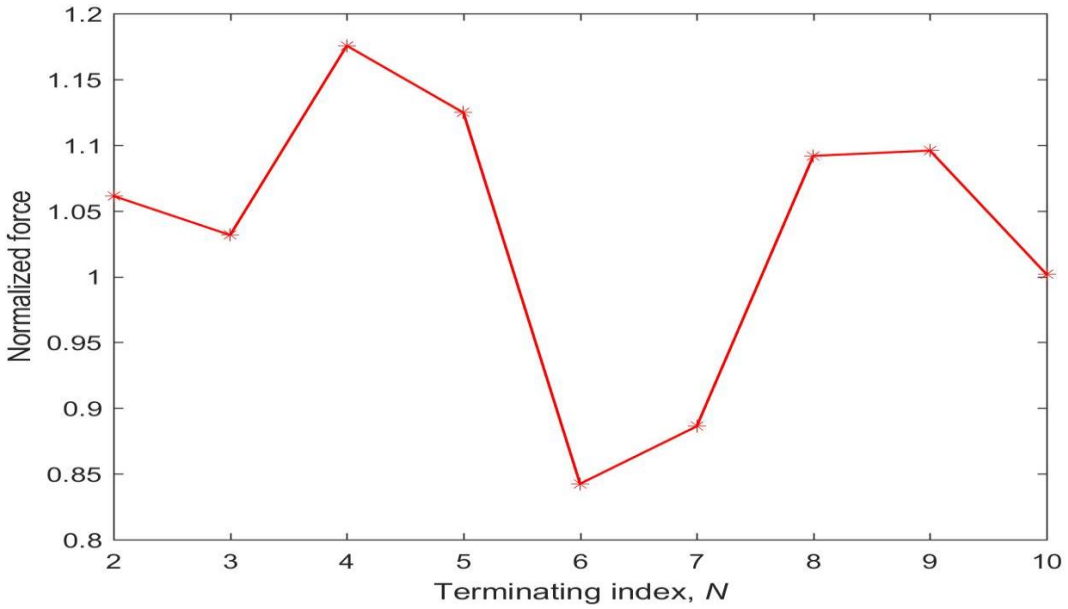

Figure A4.3.3: Average value of normalized forces calculated on the respective horizontal lines of *y*-axis vs terminating index, *N*

A4.3.3 Results

Figure A4.3.4 compares isopachic stress of (a) ANSYS-simulated and (b) reconstructed with N = 8. Figure A4.3.5 plots normalized tangential stress along the notch. They are almost identical to each other. Figure A4.3.6 plots radial and shear stresses along the edge of the notch, and they are almost equal to zero. Figures A4.3.7 through A4.3.12 compare full-plate individual components of stress for (a) ANSYS-simulated, (b) Hybrid-TSA of Appendix A4.2, and (c) Hybrid-ANSYS. Table A3.4.3 contains the values of the Airy coefficients.

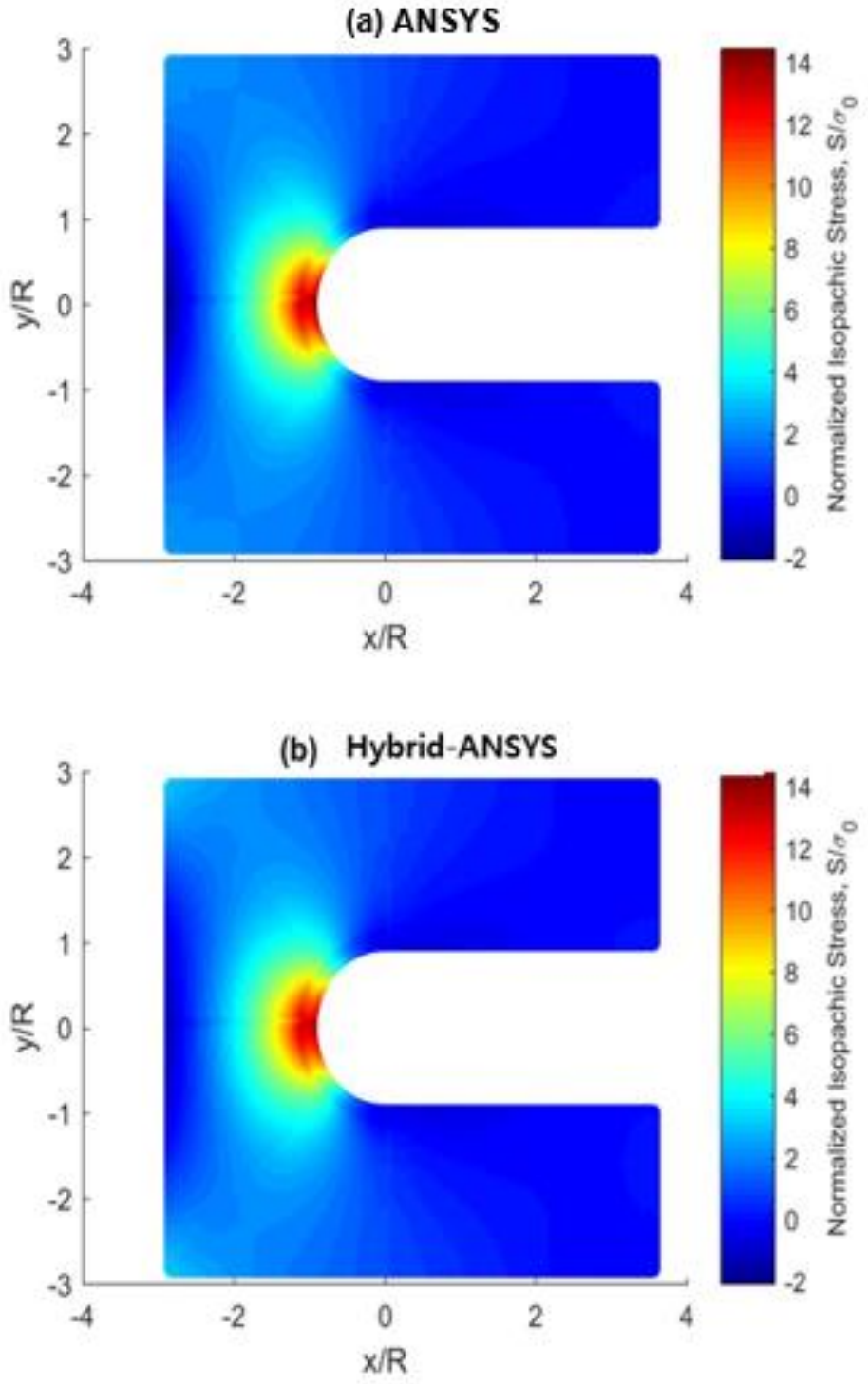

Figure A4.3.4: Normalized isopachic stress, S/σ_0, for ANSYS-simulated (a) and reconstructed for Hybrid-ANSYS method with $N = 8$ (b)

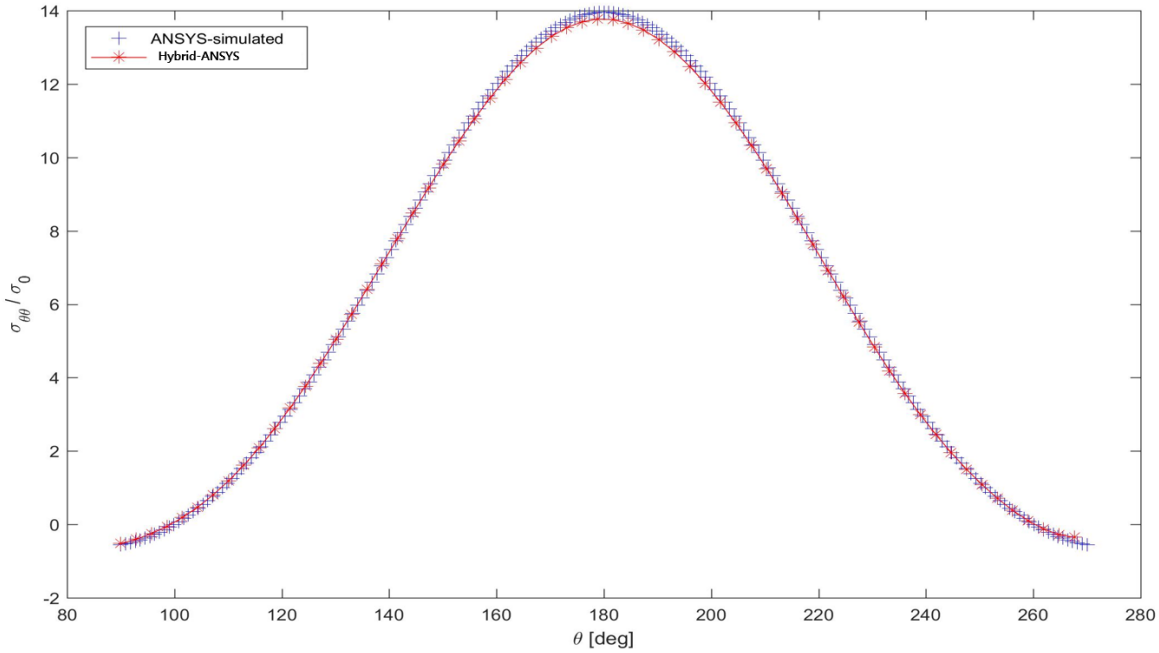

Figure A4.3.5: Normalized tangnetial stress, $\sigma_{\theta\theta}/\sigma_0$, along the edge of the notch

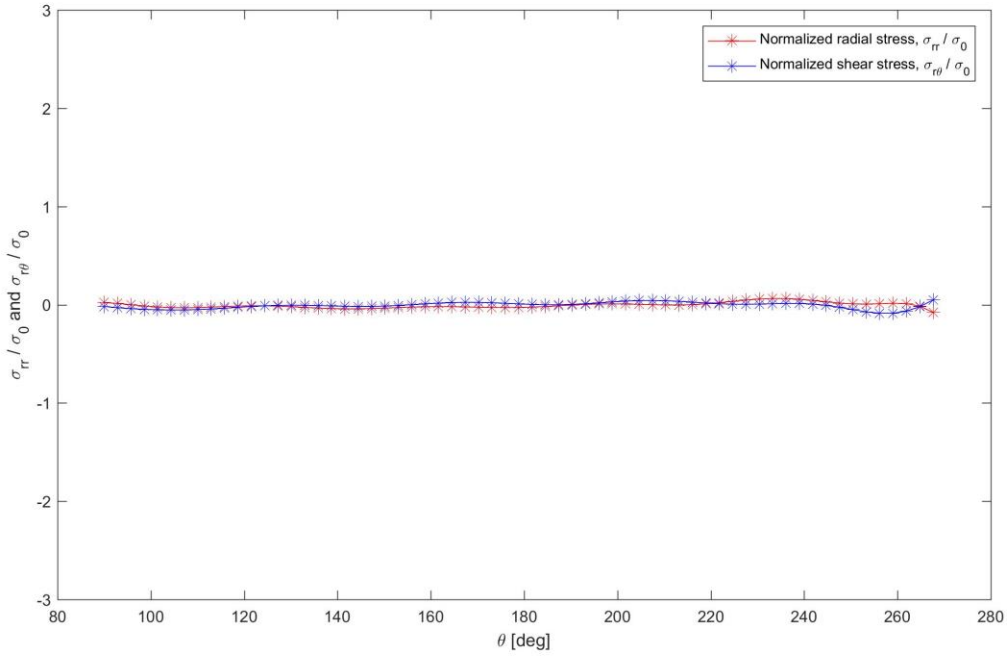

Figure A4.3.6: Normalized radial and shear stress, σ_{rr}/σ_0 and $\sigma_{r\theta}/\sigma_0$, along the edge of the notch

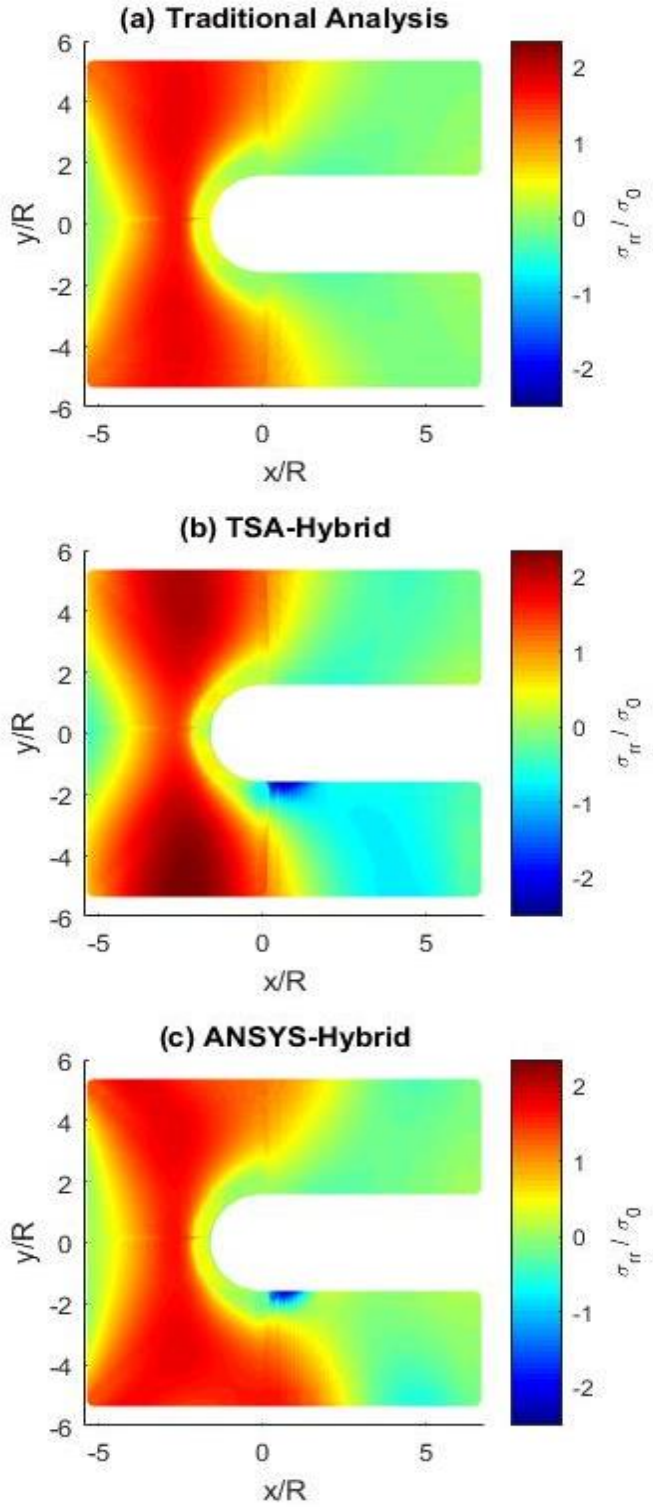

Figure A4.3.7: Normalized radial stress, σ_{rr}/σ_0

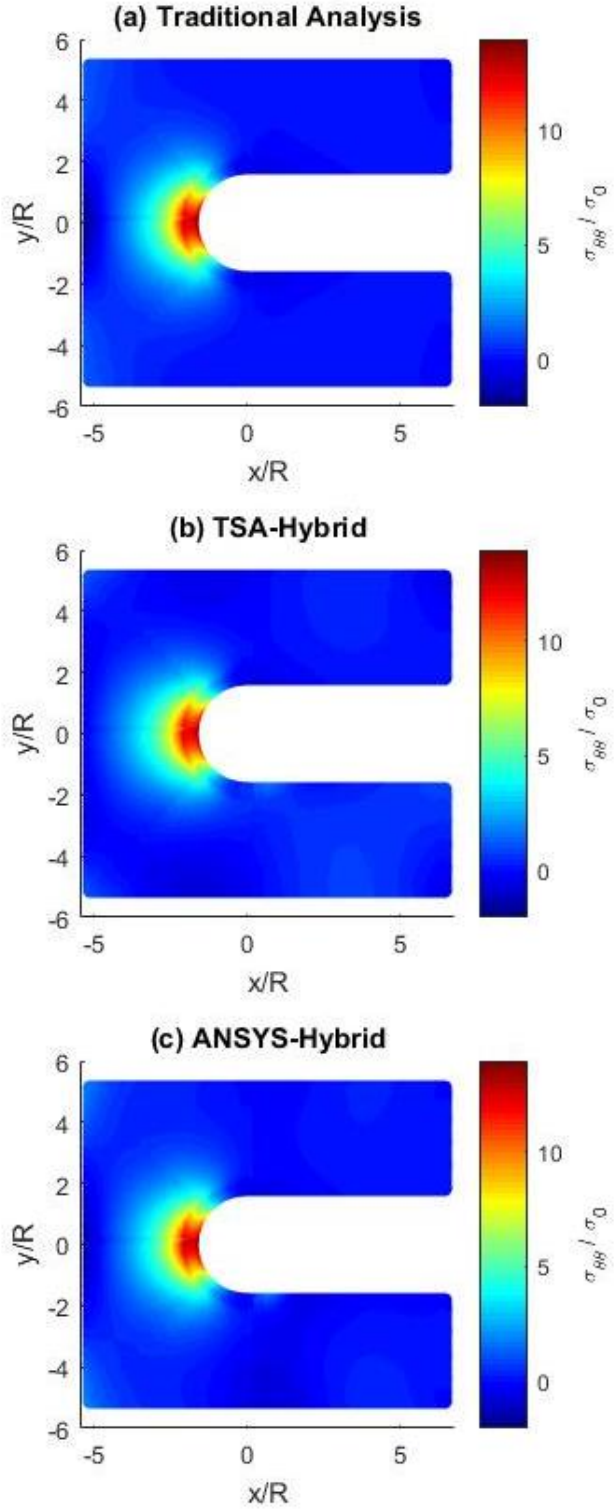

Figure A4.3.8: Normalized tangential stress, $\sigma_{\theta\theta}/\sigma_0$

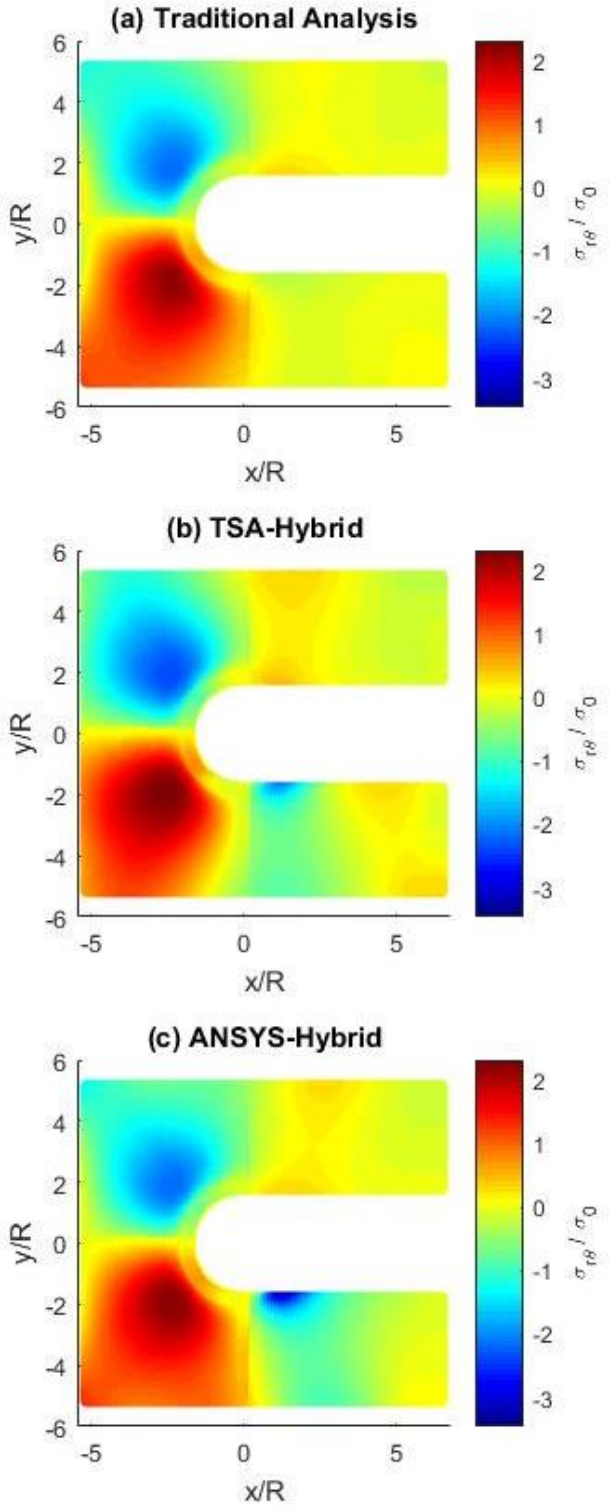

Figure A4.3.9: Normalized shear stress, $\sigma_{r\theta}/\sigma_0$

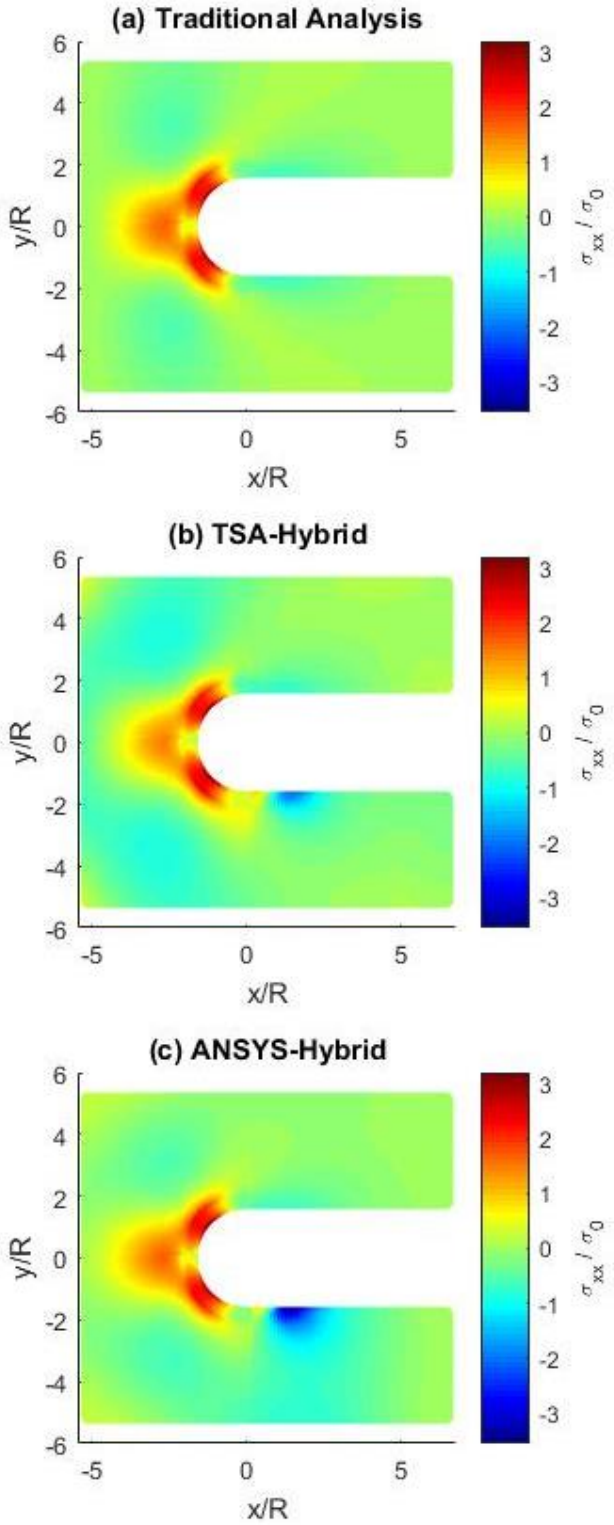

Figure A4.3.10: Normalized horizontal stress, σ_{xx}/σ_0

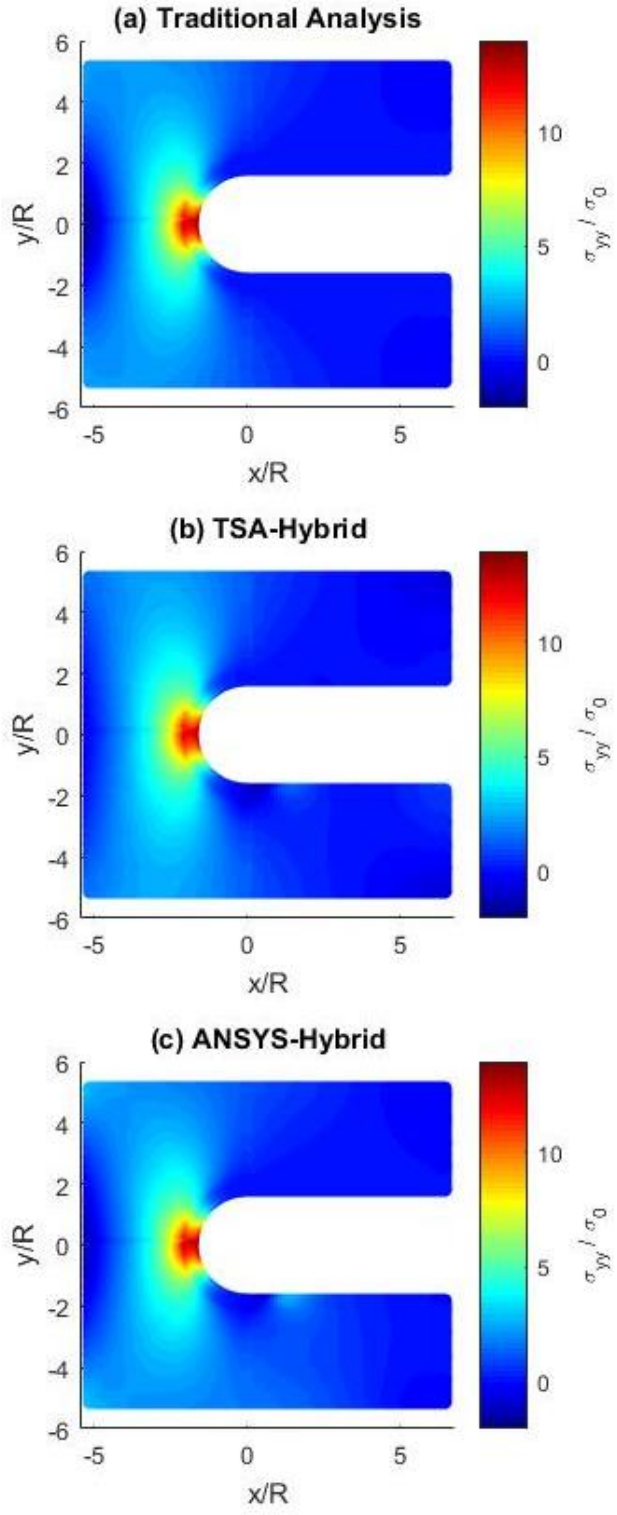

Figure A4.3.11: Normalized vertical stress, σ_{yy}/σ_0

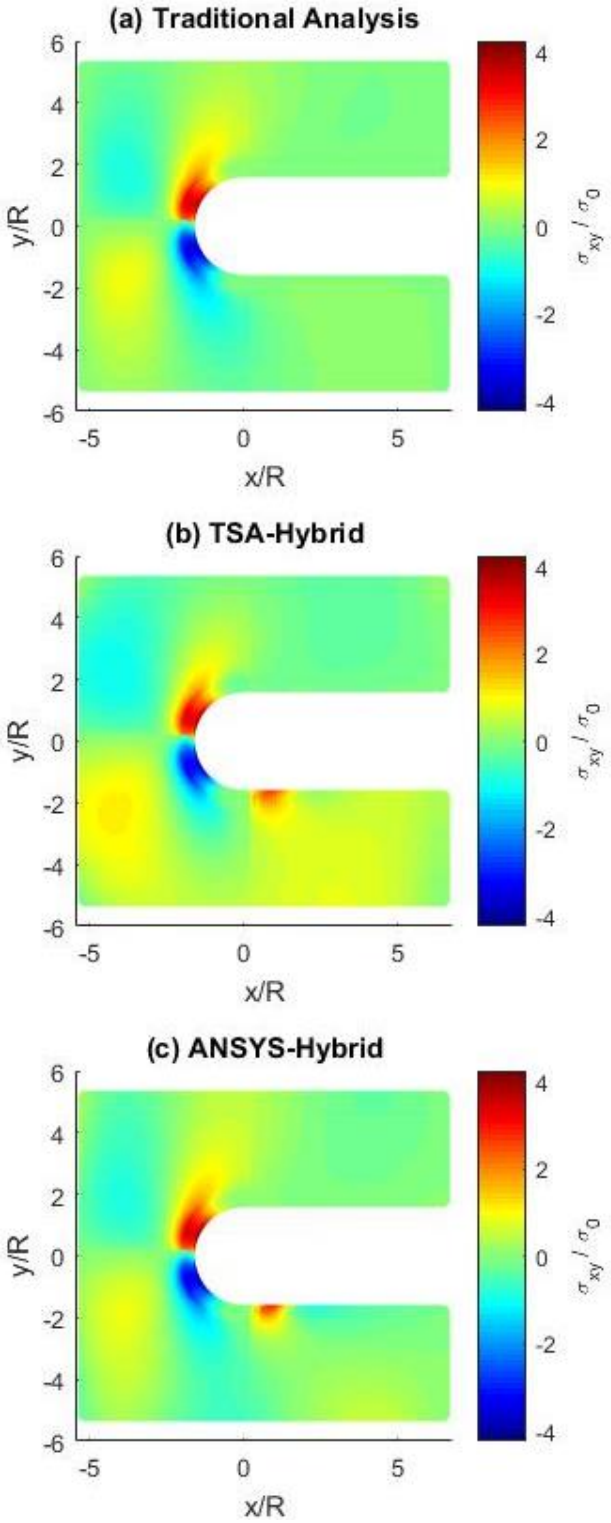

Figure A4.3.12: Normalized shear stress, σ_{xy}/σ_0

A4.3.4 Evaluated Airy Coefficients

Table A4.3.1: Evaluated Airy coefficients based on isopachic stress, *S*, from ANSYS Case D

c_0	21.1	d_8	0.0	a_7	0.0
d_0	-88.2	b'_2	-32.7	a_8	0.0
C_0	232.9	b'_3	9.8	c_2	8.9
D_0	-106.7	b'_4	-2.6	c_3	5.1
b_1	273.7	b'_5	0.7	c_4	2.1
d_1	-22.4	b'_6	-0.1	c_5	0.6
b'_1	-397.2	b'_7	0.0	c_6	0.1
d'_1	110.3	b'_8	0.0	c_7	0.0
A_1	-77.6	d'_2	-158.0	c_8	0.0
B_1	127.3	d'_3	23.6	a'_2	400.6
A'_1	206.5	d'_4	0.0	a'_3	-56.3
B'_1	-252.4	d'_5	0.1	a'_4	5.1
b_2	-2.1	d'_6	0.0	a'_5	-2.8
b_3	-0.3	d'_7	0.0	a'_6	0.3
b_4	0.0	d'_8	0.0	a'_7	0.3
b_5	0.0	b_0	135.1	a'_8	-0.1
b_6	0.0	A_0	-433.6	c'_2	7.0
b_7	0.0	B_0	-159.7	c'_3	-9.2
b_8	0.0	c_1	18.0	c'_4	-0.7
d_2	36.3	c'_1	-272.2	c'_5	0.1
d_3	4.5	a_2	-5.1	c'_6	0.1
d_4	1.2	a_3	-8.1	c'_7	0.0
d_5	0.4	a_4	-1.3	c'_8	0.0

d_6	0.1	a_5	0.5		
d_7	0.0	a_6	0.2		

A4.4 Variations on Previous Cases

Several variations on Cases A through D were evaluated, i.e., cases E through A*. Case E is identical to D except it omits imposing the shear stress along the *x*-axis; Case F resembles D but it employs input data averaged about the *x*-axis projected into only one half of the plate and a modified stress function and Case G is a repeat of Case F but omits imposing the shear stress along the *x*-axis. Case A* is identical to Case A but retains coefficients B_o, C_o, D_o, B_1 and B'_1. Tables A4.4.1 through A4.4.3 contain the magnitude of respective Airy coefficients. None of Cases E through A* is suitable compared with Case D.

Figures A4.4.1 thorough A4.4.3 compare contour plots of reconstructed polar components of stress of Case A*, original Cases A and C. Results of Cases A* and original A are similar but worse than Case C when these are compared to that of ANSYS. Also, results of Case A* cannot reconstruct the other half, meaning utilized Airy coefficients in Case A* are not symmetric, figure A4.4.4. Like Case C, Case A* does not result in single-valued stresses, figure A4.4.5.

Table A4.4.1: Evaluated Airy coefficients based on *S* from TSA Case F

c_0	293	d_3	0	a_3	0
d_0	-227	d_4	0	a_4	0
C_0	89.4	d_5	0	a_5	0
D_0	-41.9	b'_2	-24.7	c_2	0
b_1	0	b'_3	8.28	c_3	0
d_1	0	b'_4	-1.32	c_4	0
b'_1	-979	b'_5	0.32	c_5	0
d'_1	109	d'_2	-189	a'_2	343
A_1	-46.6	d'_3	14.4	a'_3	-78.6
B_1	61.7	d'_4	-1.13	a'_4	2.73
A'_1	-155	d'_5	-0.39	a'_5	-0.49
B'_1	-107	b_0	-445	c'_2	25
b_2	0	A_0	0	c'_3	-3.99
b_3	0	B_0	35.6	c'_4	0.04
b_4	0	c_1	0	c'_5	0.07
b_5	0	c'_1	-221		
d_2	0	a_2	0		

Table A4.4.2: Evaluated Airy coefficients based on *S* from TSA Case G

c_0	282	d_3	0	a_3	0
d_0	-223	d_4	0	a_4	0
C_0	92.4	d_5	0	a_5	0
D_0	-43.2	b'_2	-24.7	c_2	0
b_1	0	b'_3	8.28	c_3	0
d_1	0	b'_4	-1.32	c_4	0
b'_1	-968	b'_5	0.32	c_5	0
d'_1	109	d'_2	-188	a'_2	341
A_1	-45.5	d'_3	14.4	a'_3	-78.6
B_1	62.1	d'_4	-1.13	a'_4	2.73
A'_1	-162	d'_5	-0.39	a'_5	-0.49
B'_1	-112	b_0	-449	c'_2	25
b_2	0	A_0	0	c'_3	-3.97
b_3	0	B_0	37	c'_4	0.04
b_4	0	c_1	0	c'_5	0.07
b_5	0	c'_1	-221		
d_2	0	a_2	0		

Table A4.4.3: Evaluated Airy coefficients based on isopachic stress, *S*, from TSA Case A*

c_0	-15.88	d_3	0.00	a_3	0.00
d_0	0.00	d_4	0.00	a_4	0.00
C_0	238.88	d_5	0.00	a_5	0.00
D_0	-146.68	b'_2	-22.66	c_2	0.00
b_1	0.00	b'_3	7.72	c_3	0.00
d_1	0.00	b'_4	-1.60	c_4	0.00
b'_1	-1234.68	b'_5	0.42	c_5	0.00
d'_1	63.26	d'_2	-338.36	a'_2	555.63
A_1	227.27	d'_3	21.60	a'_3	-100.29
B_1	355.95	d'_4	-5.22	a'_4	17.67
A'_1	0.00	d'_5	0.13	a'_5	-1.97
B'_1	186.86	b_0	-947.39	c'_2	23.49
b_2	0.00	A_0	0.00	c'_3	-7.81
b_3	0.00	B_0	423.85	c'_4	0.47
b_4	0.00	c_1	0.00	c'_5	-0.10
b_5	0.00	c'_1	-447.72		
d_2	0.00	a_2	0.00		

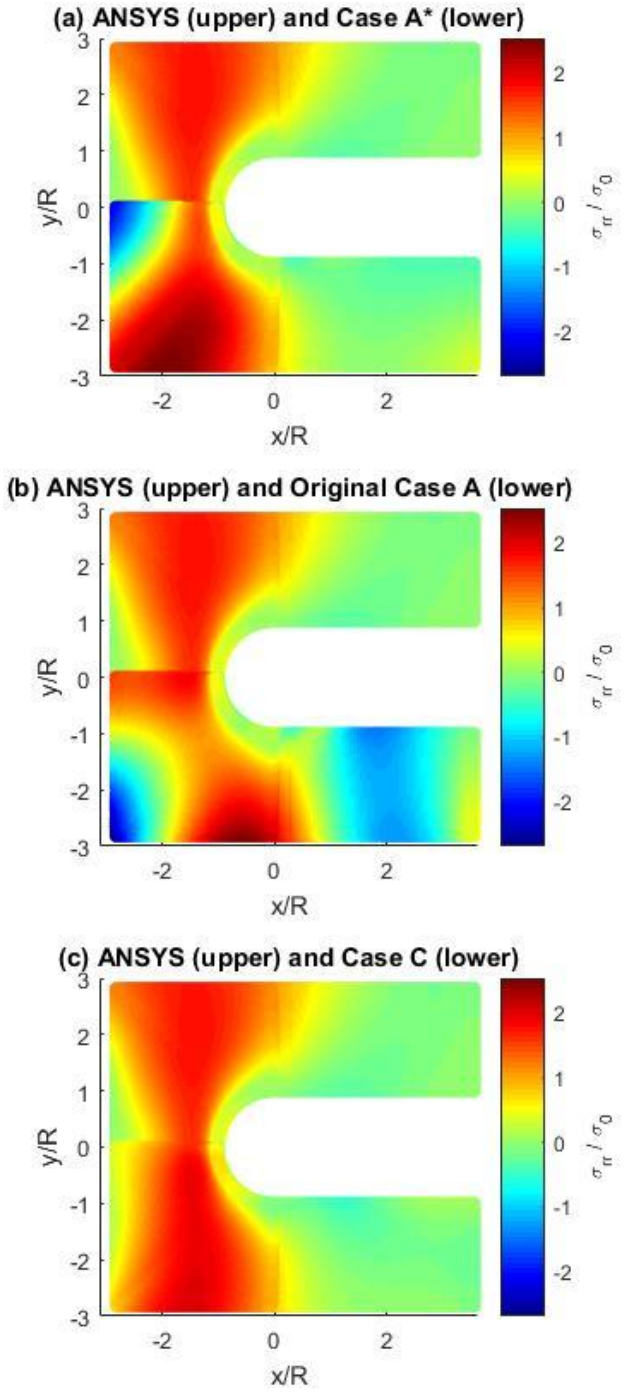

Figure A4.4.1: Normalized radial stress, σ_{rr}/σ_0

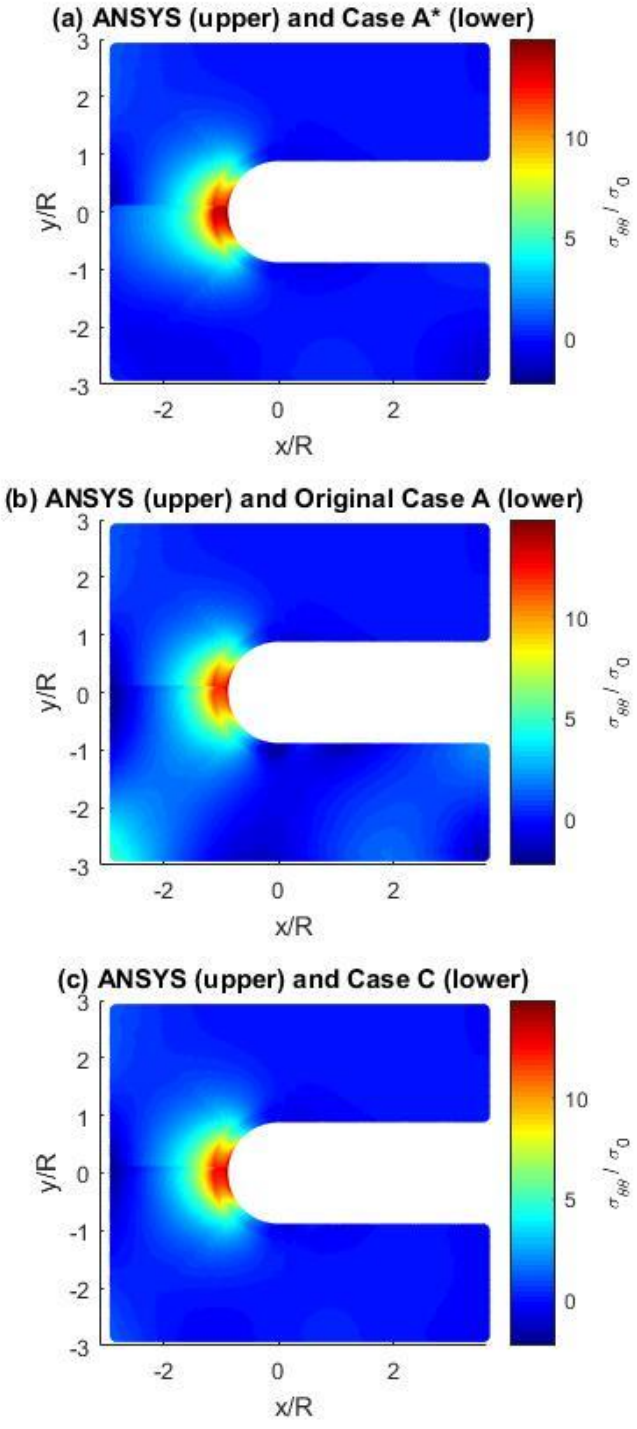

Figure A4.4.2: Normalized tangential stress, $\sigma_{\theta\theta}/\sigma_\theta$

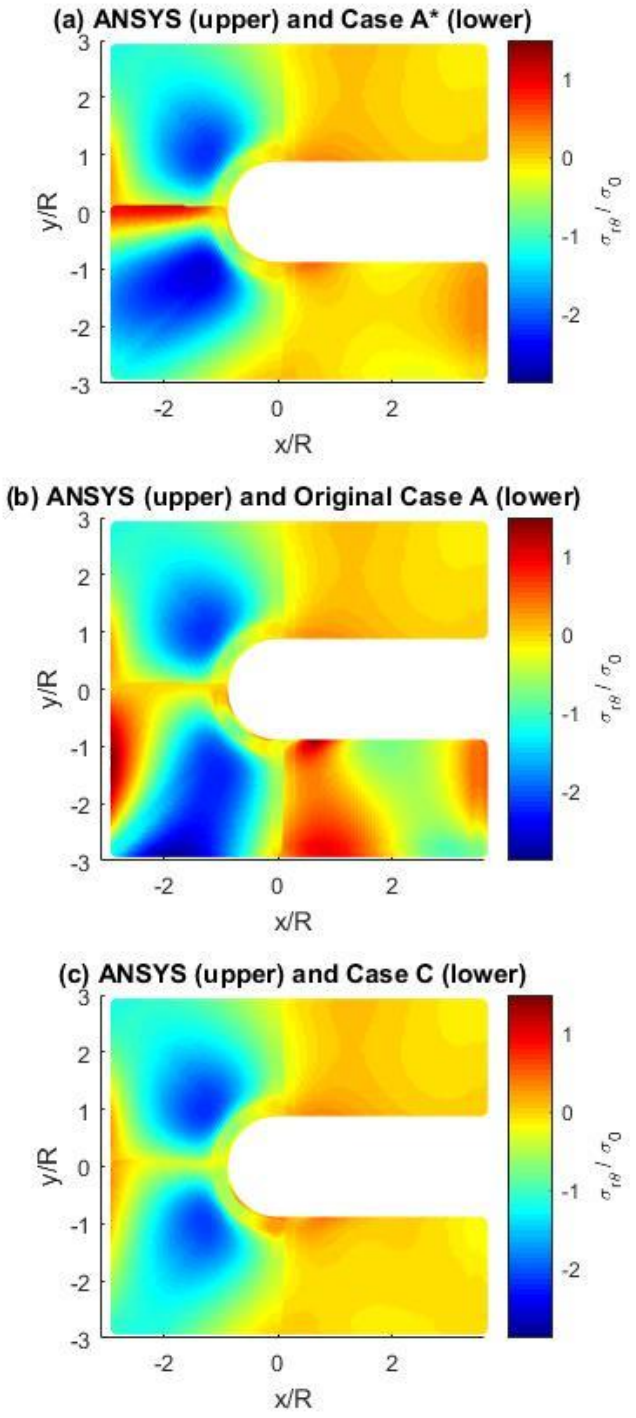

Figure A4.4.3: Normalized shear stress, $\sigma_{r\theta}/\sigma_\theta$

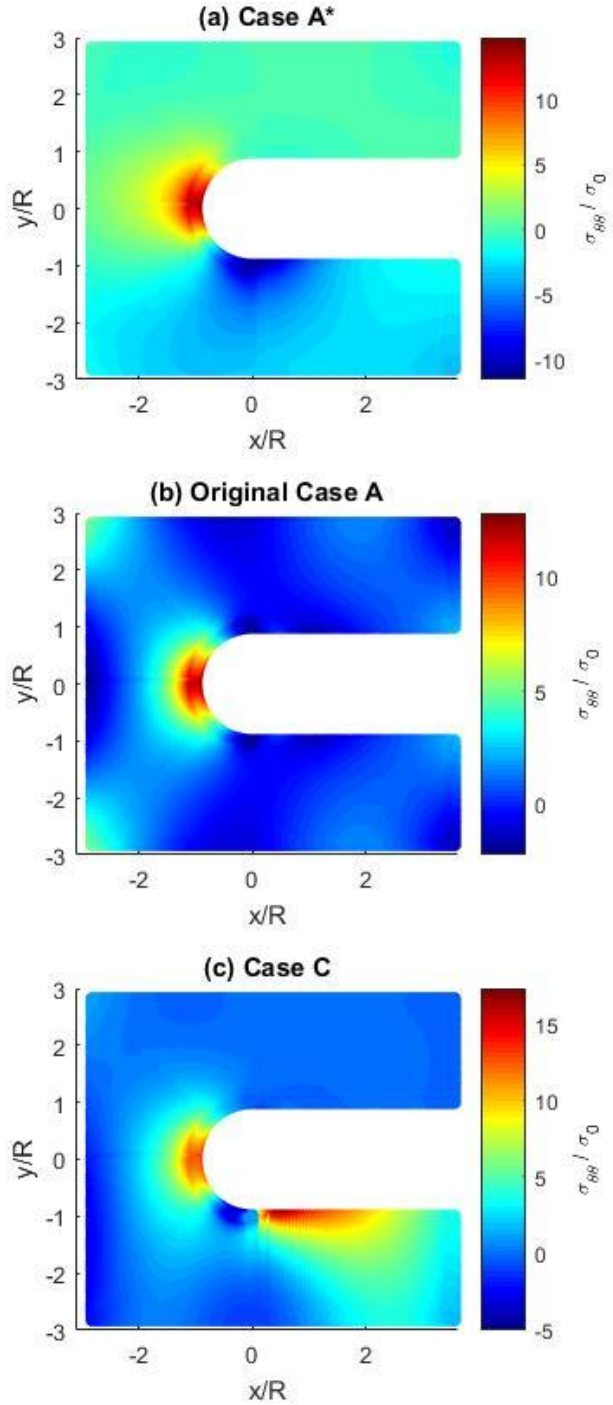

Figure A4.4.4: Normalized tangential stress, $\sigma_{\theta\theta}/\sigma_0$, on entire plate

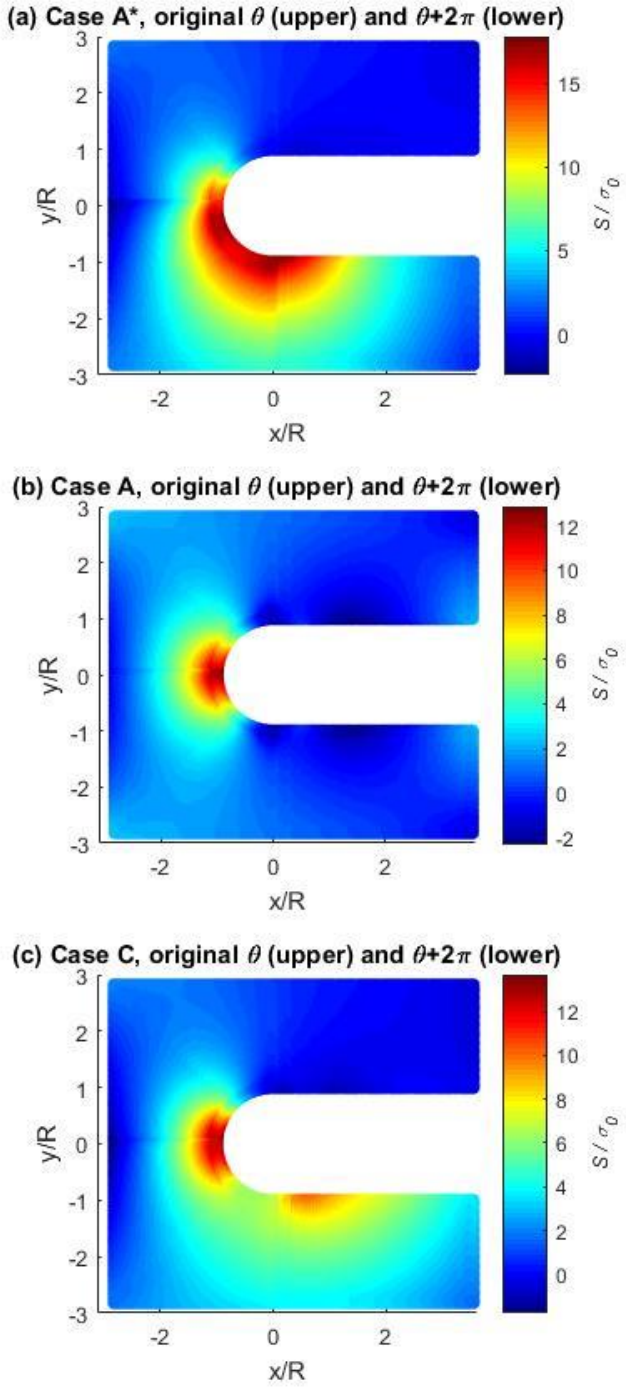

Figure A4.4.5: Normalized isopachic stress, S/σ_0, with original angle, θ (upper) and $\theta+2\pi$ (lower)

Appendix A5.1: Results using full-plate DIC-recorded displacement

Displacement data of DIC and ANSYS of figures 5.5.2 and 5.6.1 are projected to cover the full-plate. A total 27,114 (DIC) or 19,270 (ANSYS) source locations are utilized in the full plate. The same boundary conditions (h = 500 × 2 = 1,000) are applied but now they are applied on full plate as equation (A5.1).

$$\sigma_{rr}(R,\theta) = \sigma_{r\theta}(R,\theta) = 0, \qquad \frac{\pi}{2} \leq \theta \leq \frac{3}{2}\pi \tag{A5.1}$$

To determine appropriate number of Airy coefficients, the same approach is used as in sections 5.3.3 and 5.6.2. Figures A5.1 and A5.2 show *RMS* values of reconstructed vertical displacements and that of input sources (DIC and ANSYS). To see if only using one component of displacement is enough for reconstructing the other displacement, Airy coefficients are evaluated with each case of using only vertical displacement (m = 27,114 for DIC and m = 19,270 for ANSYS) and using both components of displacements as input (m = 54,228 for DIC and m = 38,540 for ANSYS). Both figures A5.1 and A5.2 indicate lower *RMS* values employing input of only vertical displacements. Form these N = 7 is chosen for Hybrid-DIC and N = 11 is chosen for Hybrid-ANSYS.

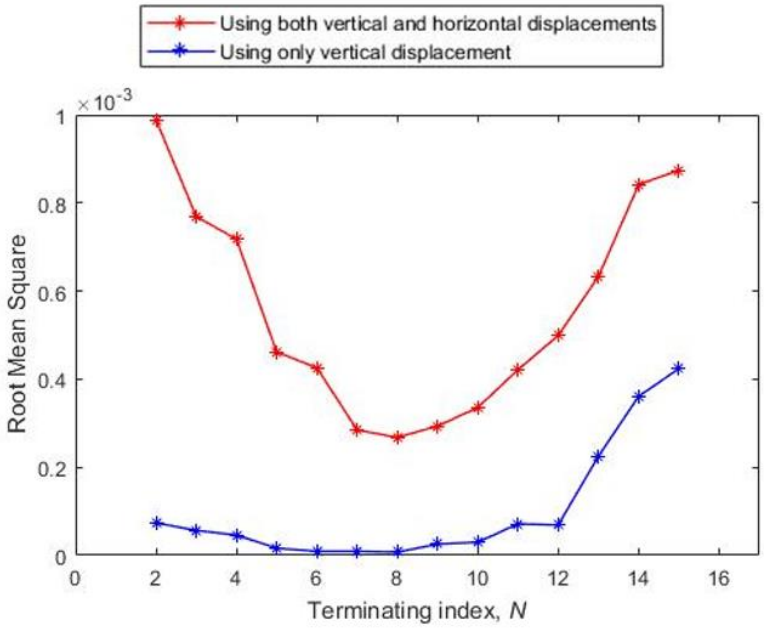

Figure A5.1: *RMS* of reconstrcuted vertical displacement for Hybrid-DIC

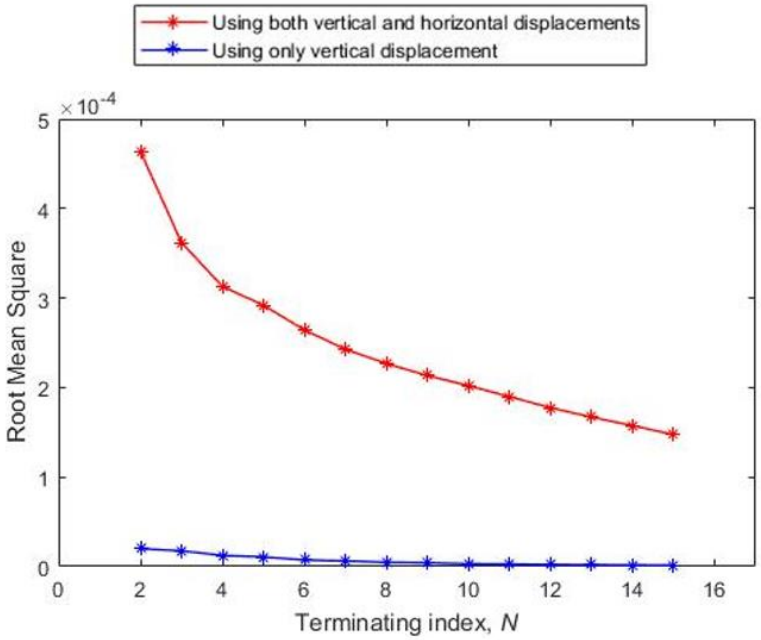

Figure A5.2: *RMS* of reconstrcuted vertical displacement Hybrid-ANSYS

Because figures A5.1 and A5.2 indicate lower *RMS* values for input of only vertical displacement data (m = 27,114 for DIC and m = 19,270 for ANSYS), vertical and horizontal displacements are reconstructed with input of only vertical displacements and with input of both components of displacement (m = 54,228 for DIC and m = 38,540 for ANSYS). Figures A5.3 through A5.6 show reconstructed individual components of displacement compared with that of inputs (DIC or ANSYS displacements). Reconstructed displacements with Airy coefficients evaluated with input of only vertical displacements can reconstruct vertical displacements successfully while it cannot reconstruct horizontal displacements, figures A5.3 and A5.5. However, reconstructed displacement results with evaluated Airy coefficients with inputs of both components of displacement can reconstruct both displacements. Thus, individual polar components of stress are reconstructed with inputs of both components of displacement.

Based on the above number of Airy coefficients and the results of reconstructed displacements, Airy coefficients are evaluated with input of both components of displacements. Using the evaluated Airy coefficients and equations (4.3) through (4.5) of expressions for polar individual stresses, figures A5.7 through A5.9 show reconstructed polar stresses for Hybrid-DIC and Hybrid-ANSYS and compared with that at of ANSYS. Results of Hybrid-ANSYS are almost identical to direct result of ANSYS. Figure A5.10 plots total forces calculated for various horizontal lines of full plate (from y/R = -2.2 to y/R = 2.2 with increment of 0.1). The average normalized force value 1.08 for Hybrid-DIC and 1.02 for Hybrid-ANSYS.

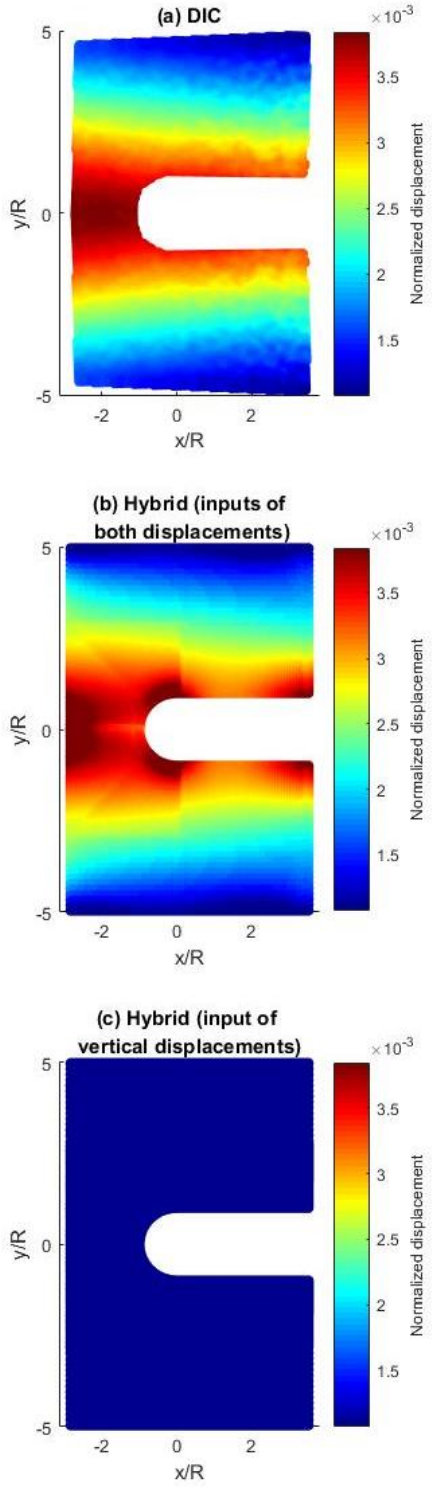

Figure A5.3: Horizontal displacement, *u*, of Hybrid-DIC

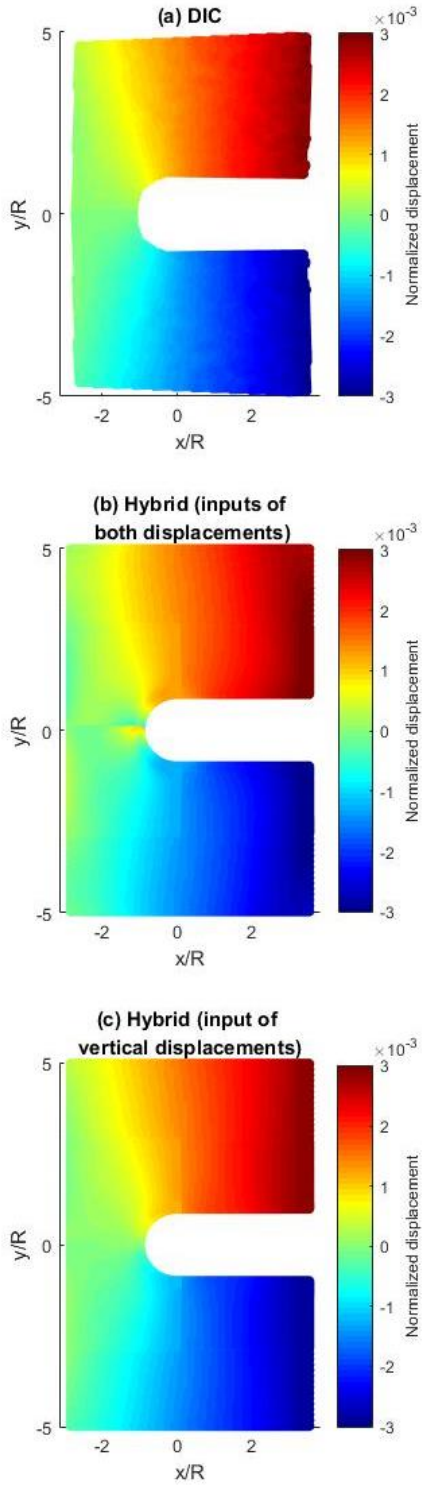

Figure A5.4: Vertical displacement, *v*, of Hybrid-DIC

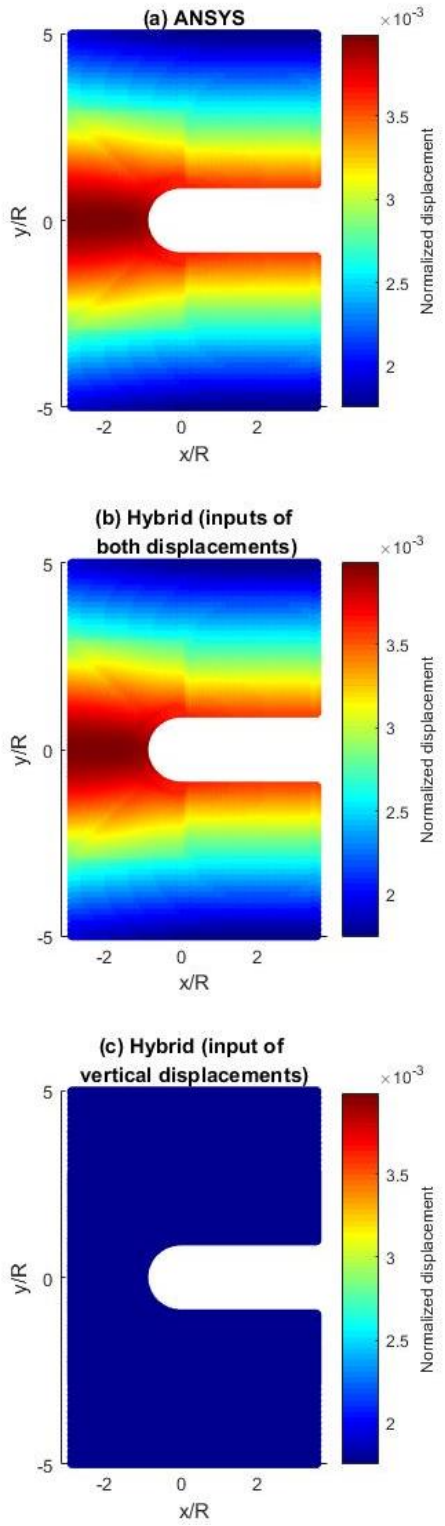

Figure A5.5: Horizontal displacement, *u*, of Hybrid-ANSYS

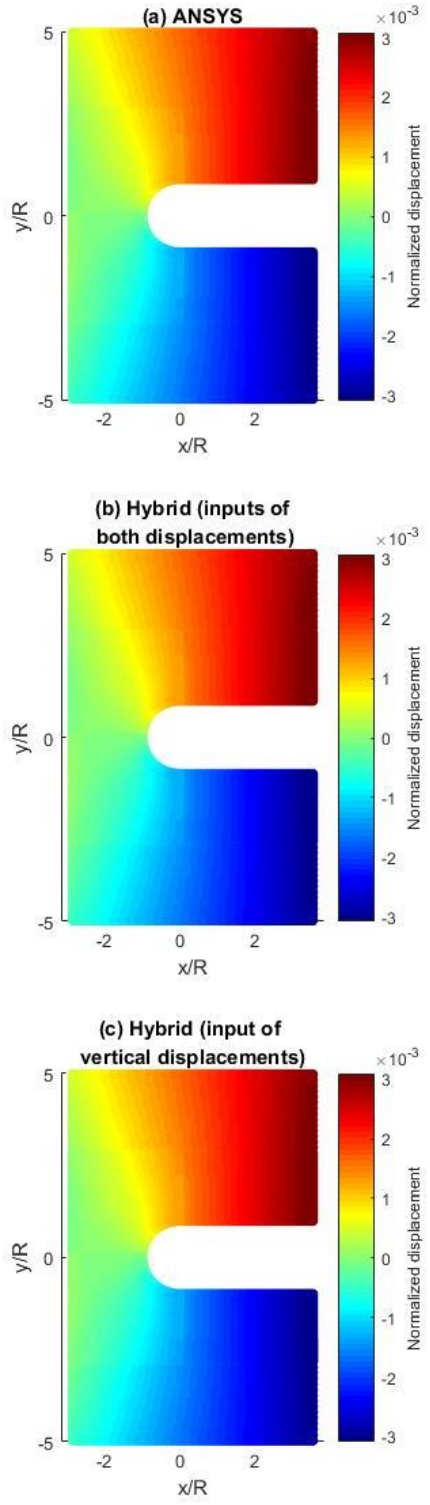

Figure A5.6: Vertical displacement, *v*, of Hybrid-ANSYS

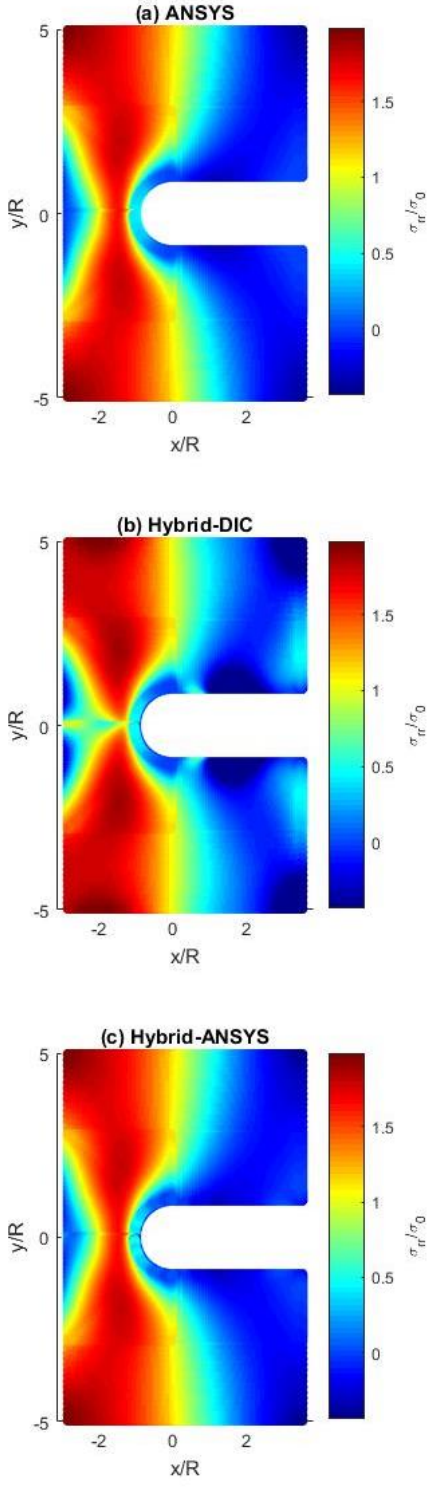

Figure A5.7: Normalized radial stress, σ_{rr}/σ_0

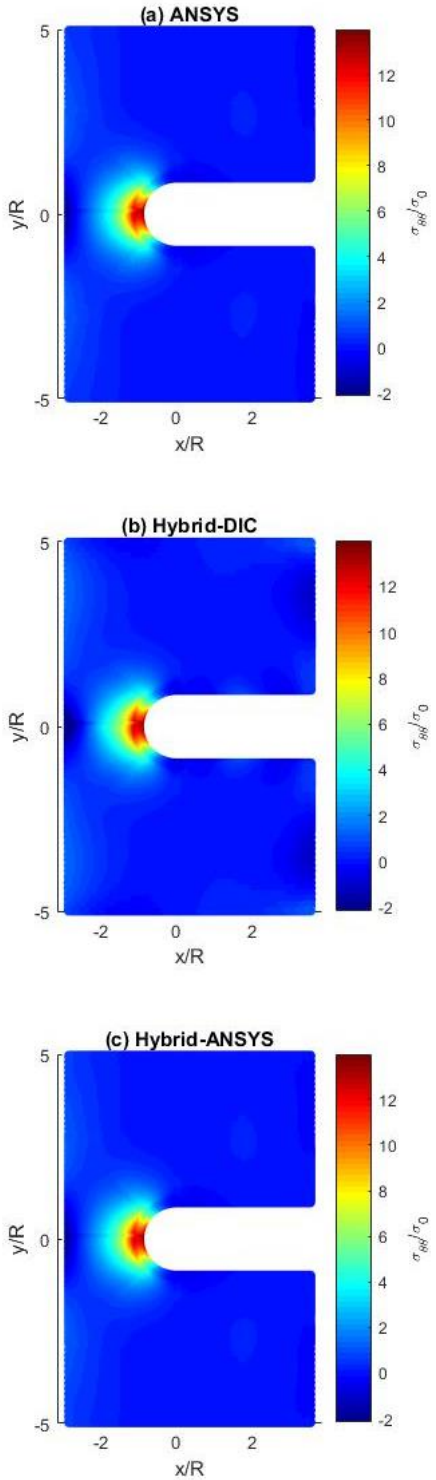

Figure A5.8: Normalized tangential stress, $\sigma_{\theta\theta}/\sigma_0$

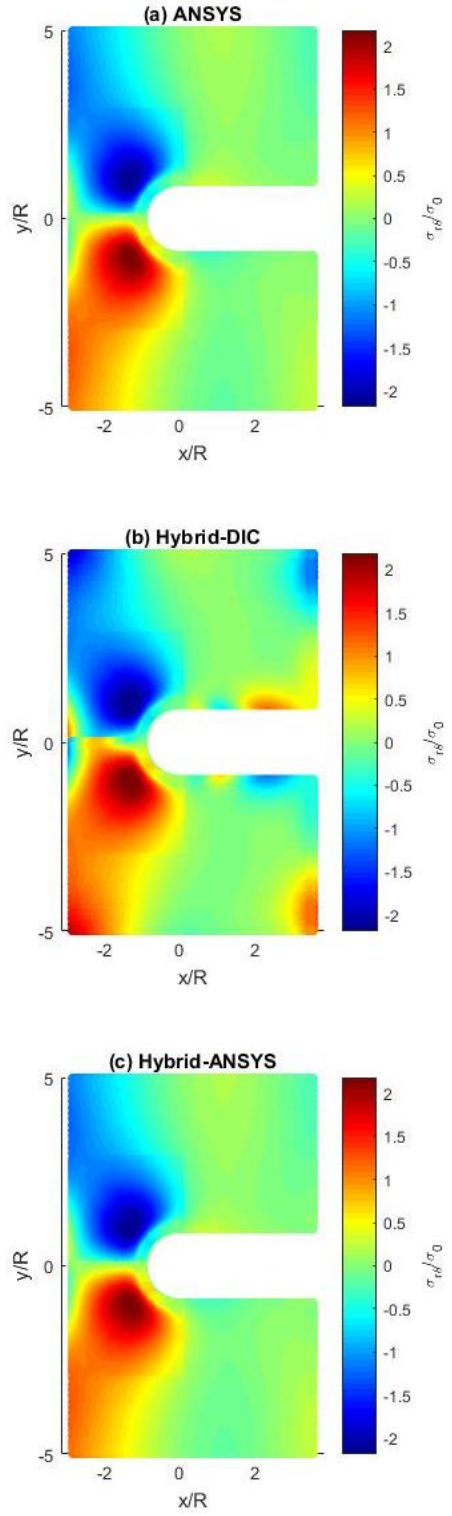

Figure A5.9: Normalized shear stress, $\sigma_{r\theta}/\sigma_0$

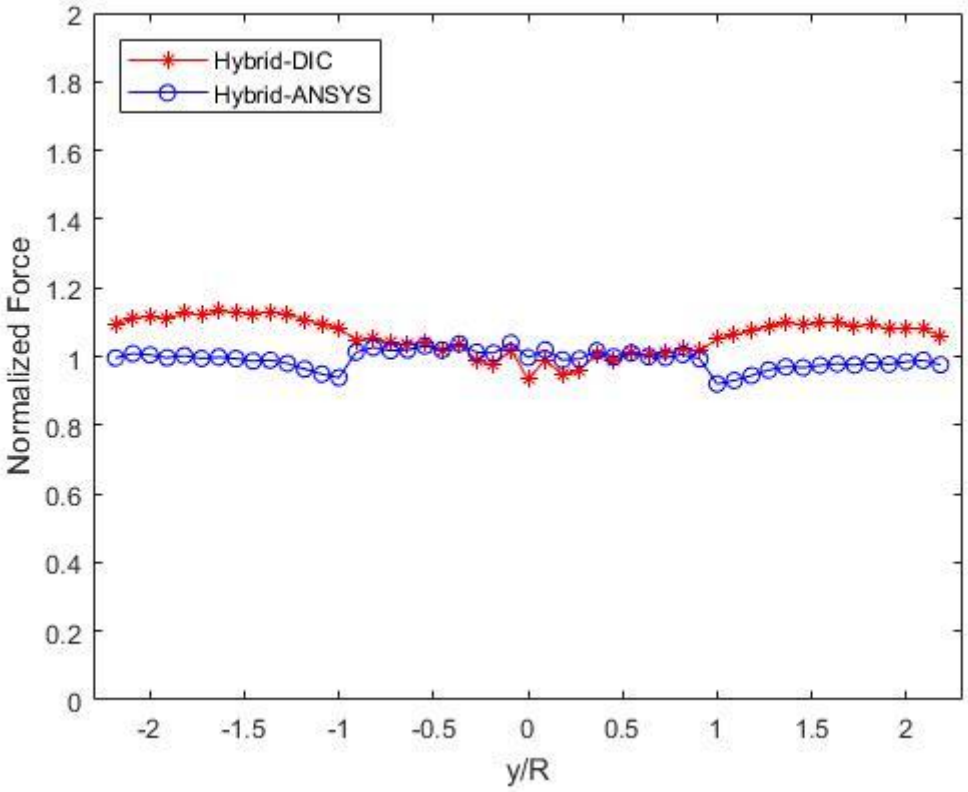

Figure A5.10: Forces on each horizontal line of *y*-axes

Appendix A6.1: Evaluating Properties

A6.1.1: Graphite Epoxy

Sample #1 and #3: width = 0.82”, thickness = 0.208”
Sample #5: width = 0.5”, thickness = 0.208”

Sample #	Mean load (lbs)	Peak-to-peak load (lbs)	K	Averaged K
1	500	600	0.1075	0.1015
	600	800	0.1039	
	800	1200	0.1120	
	1000	1600	0.0920	
3	500	600	0.0961	
	800	1200	0.1037	
	1000	1600	0.0953	
5	150	100	1.1034	1.1785
	200	200	1.1729	
	250	300	1.2593	

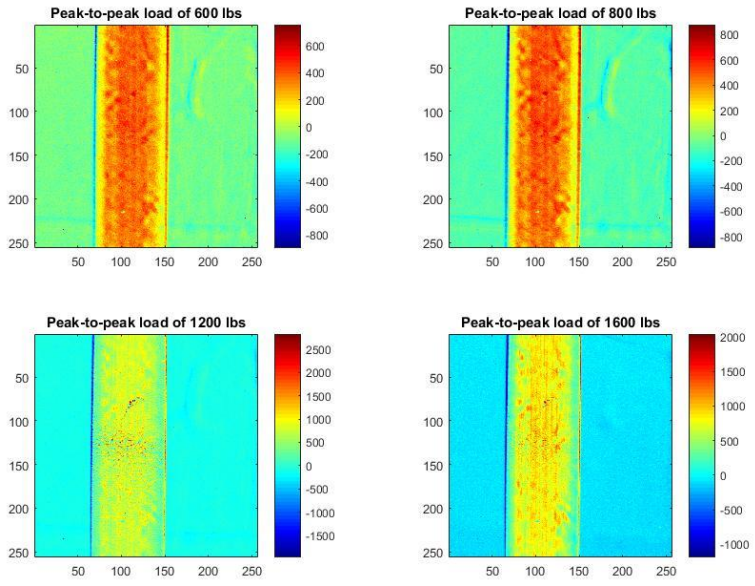

Figure A6.1: Raw TSA recorded signal of Gl/E sample #1

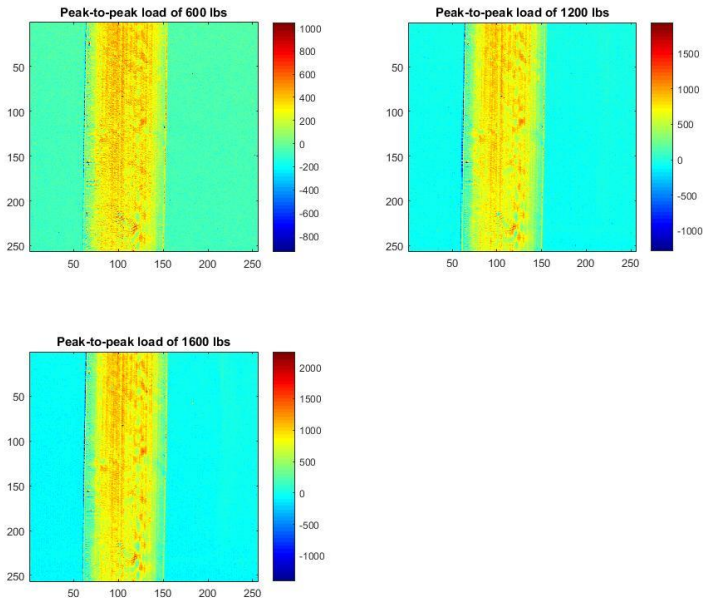

Figure A6.2: Raw TSA recorded signal of Gl/E sample #3

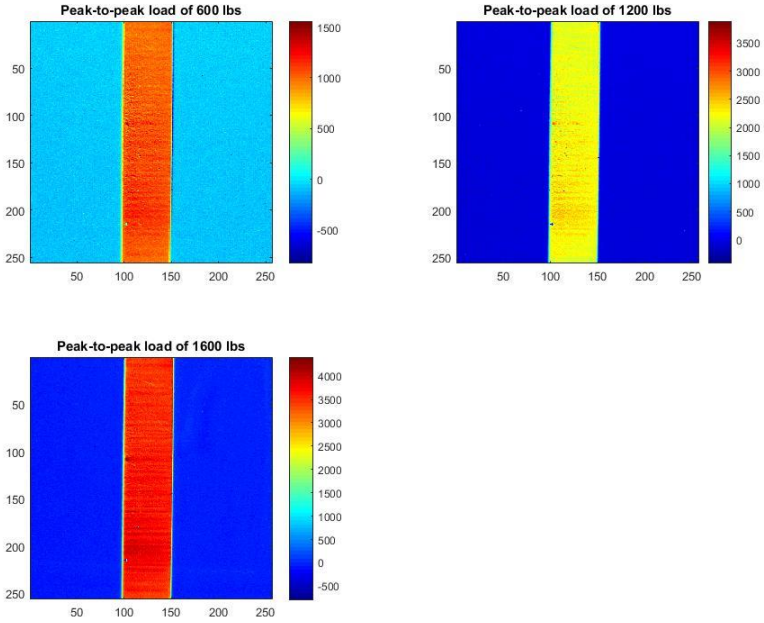

Figure A6.3: Raw TSA recorded signal of Gl/E sample #5

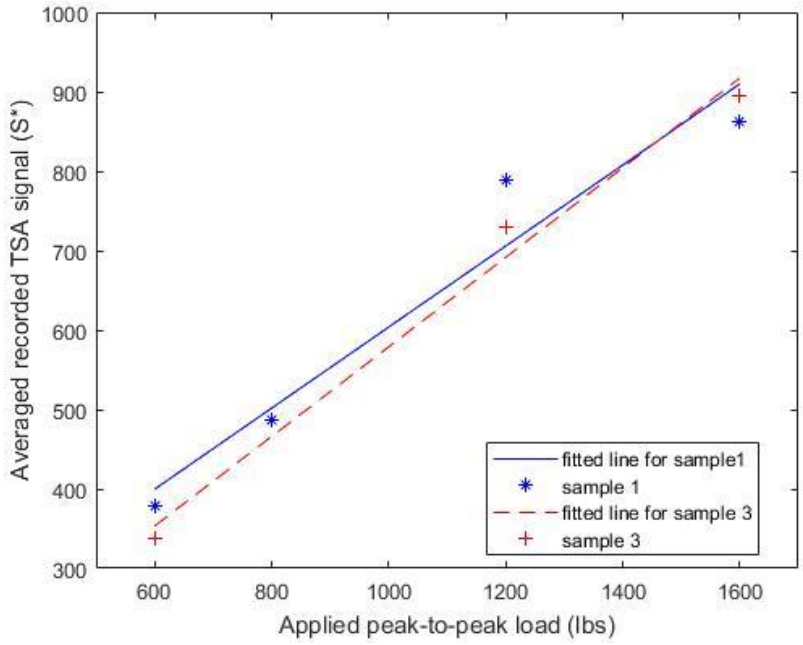

Figure A6.4: Applied load vs averaged TSA signal of Gl/E sample #3

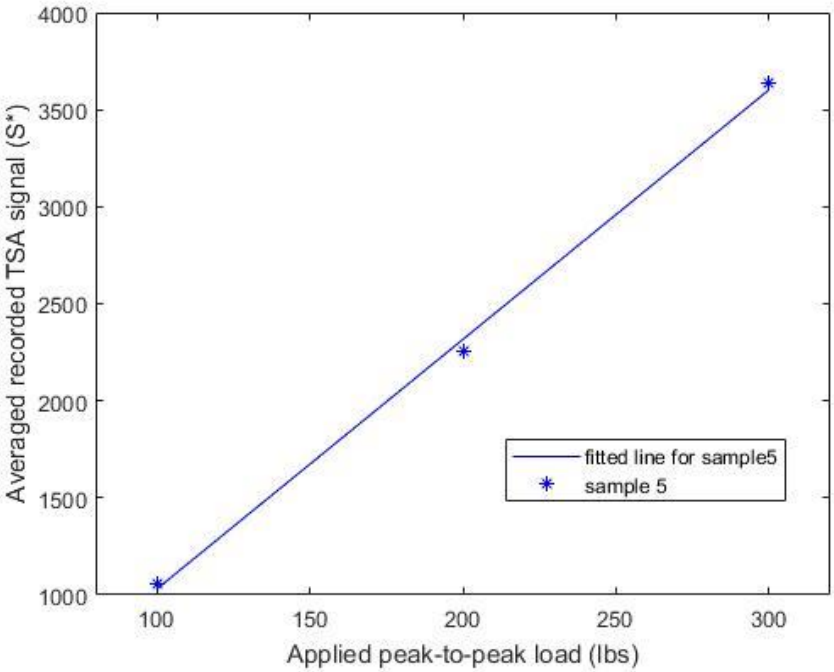

Figure A6.5: Applied load vs averaged TSA signal of Gl/E sample #5

A6.2: Thinner Gl/E

Thickness: 0.095”
Width: 0.75”

Sample #	Mean load (lbs)	Peak-to-peak load (lbs)	K	Averaged K
2	75	50	0.9759	1.0366
	100	100	1.0973	
	125	150	1.2353	Broke
5	100	200	1.2938	1.2770
	200	200	1.2602	

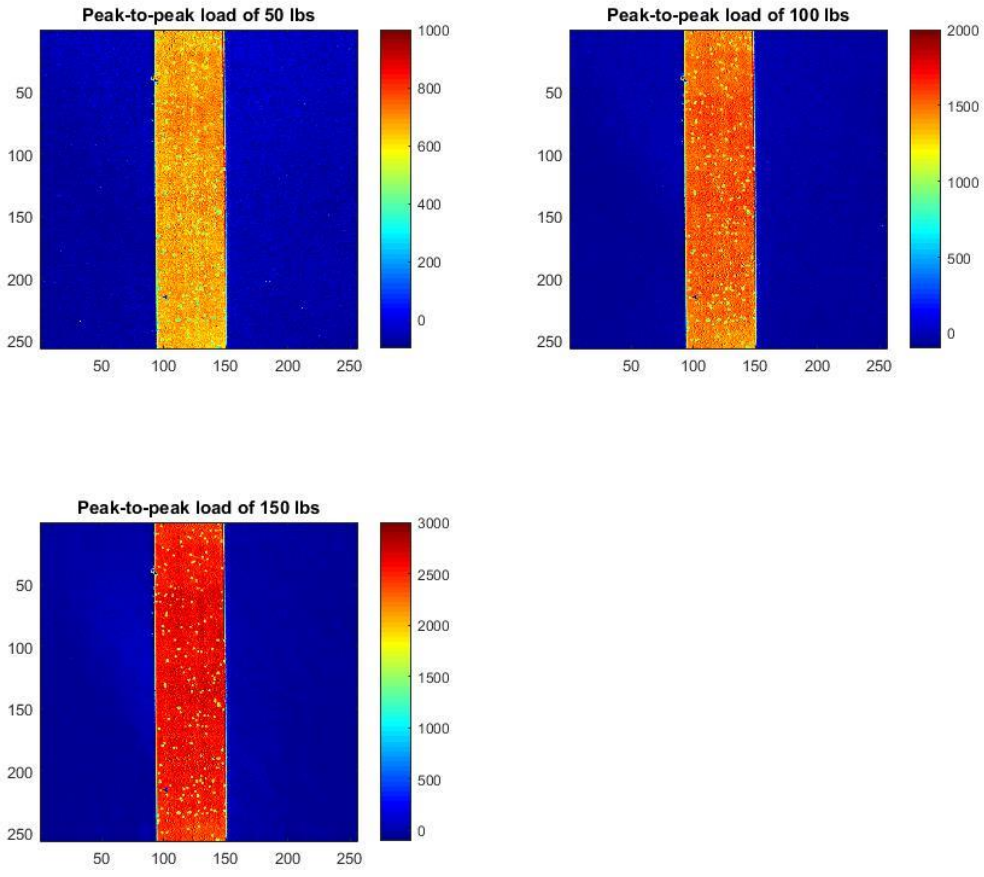

Figure A6.8: Raw TSA recorded signal of Gl/E (thinner) sample #2

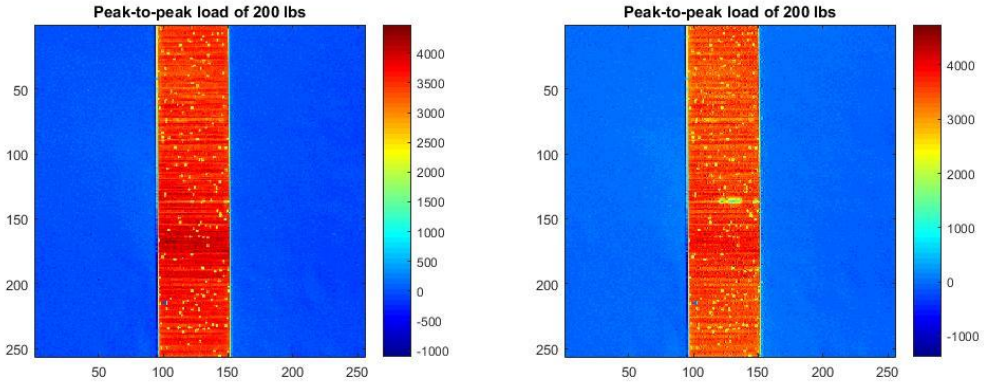

Figure A6.6: Raw TSA recorded signal of Gl/E (thinner) sample #5

A6.3: Thicker Gl/E

Thickness: 0.125”
Width: 0.75”

Sample #	Mean load (lbs)	Peak-to-peak load (lbs)	K	Averaged K
5	300	200	0.9642	0.9599
4	300	200	0.8992	
	400	300	1.0163	
1	75	50	0.8902	Too noisy
	100	100	1.2634	1.2634
	125	150	1.7521	Broke

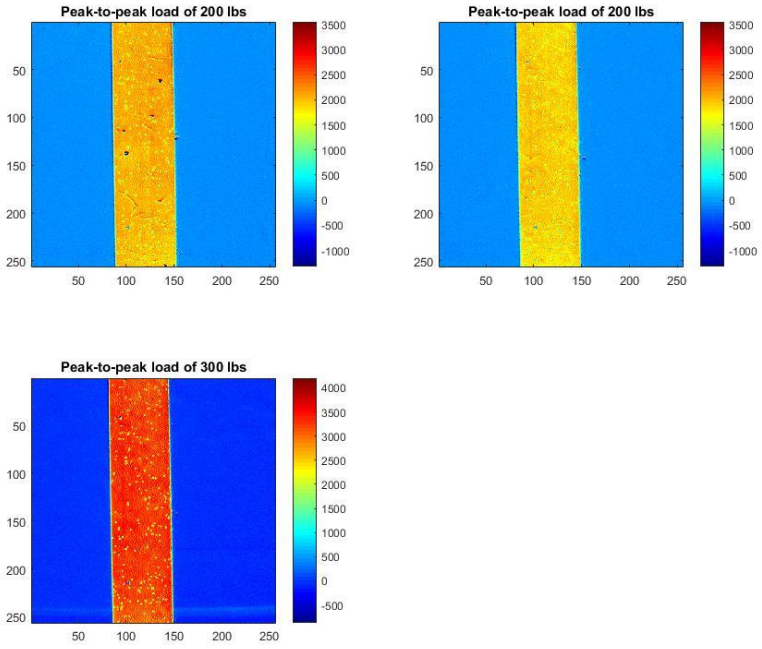

Figure A6.7: Raw TSA recorded signal of Gl/E (thicker) sample #5 and #4

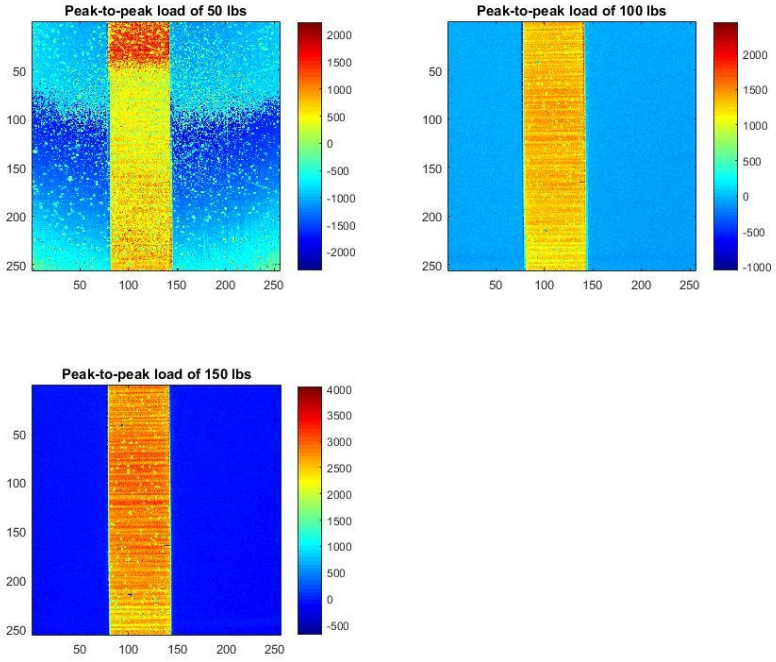

Figure A6.8: Raw TSA recorded signal of Gl/E (thicker) sample #1

References

[1] G. N. Savin, Stress distribution around holes, National Aeronautics and Space Administration, 1970.

[2] R. W. Soutas-Little, Elasticity, Courier Corporation, 1999.

[3] B. Pan, H. Xie and A. Asundi, "Two-Dimensional Digital Image Correlation for In-Plane Displacement and Strain Measurement," *A Review. Meas Sci Technoly,* vol. 20, no. 17, 2009.

[4] L. Yang, Y. Wang and R. Lu, "Advanced Optical Methods for Whole Field Displacement and Strain Measurement," in *Int. Symp. Optomechatronic Technoly*, Toronto, Canada, 2010.

[5] Z. Xu, X. Li, M. Sutton and N. Li, "Drift and Spatial Distortion Elimination in Atomic Force Microscopy Images by the Digital Image Correlation Technique," *J Strain Anal Eng Des,* 2008.

[6] H. Jin, W. Lu and J. Korellis, "Micro-Scale Deformation Measurement using the Digital Image Correlation Technique and Scanning Electron Microscope Imaging.," *J Strain Anal Eng Des ,* p. 43:719–28., 2008.

[7] D. Backman, M. Liao, L. Crinchlow, M. Yanishervsky and E. Patterson, "The Use of Digital Image Correlation in a Parametric Study on the Effect of Edge Distance and Thickness on

Residual Strains After Hole Cold Expansion," *J Strain Anal Eng Des,* 2008;43:781–9..

[8] P. Reu and T. Miller, "The Application of High-Speed Digital Image Correlation," *J Strain Anal Eng Des ,* 2008;43:673–88..

[9] J. Dally and W. Riley, Experimental Stress Analysis, New York: McGraw-Hill, 1991.

[10] A. Shukla and J. W. Dally, Experimental solid mechanics, College House Enterprises Knoxville, 2010.

[11] W. Thomson (Lord Kelvin), "On Dynamical Theory of Heat Transfer," *R. Soc. Edinburg,,* vol. 20, pp. 261-283, 1953.

[12] K. Compton and D. Webster, Temperature Changes Accompanying the Adiabatic Compression of Steel, New York: Physical Review, 1915.

[13] M. Biot, Thermoelasticity and Irreversible Thermodynamics., Buffalo, NY: Cornell Aeronautical Laboratory, 1955.

[14] M. Belgen, Structural Stress Measurements with an Infrared Radiometer, 649–53.: Instrum Syst Autom Soc , 1967.

[15] D. Mountain and J. Webber, Stress Pattern Analysis by Thermal Emission (SPATE), Utrecht, Netherlands: 4th Eur. Electro-Opt. Conf, vol. 0164, 1979.

[16] A. Salerno, A. Costa and G. Fantoni, Calibration of the Thermoelastic Constants for

Quantitative Thermoelastic Stress Analysis on Composites, Rev Sci Instrum, 2009.

[17] R. J. Greene, E. A. Patterson and R. E. Rowlands, "Thermoelastic stress analysis," *Springer handbook of experimental solid mechanics,* pp. 743-768, 2008.

[18] Z. Feng, D. Zhang, R. E. Rowlands and B. I. Sandor, "Thermoelastic determination of individual stress components in loaded composites," *Experimental Mechanics,* vol. 32, no. 2, pp. 89-95, 1992.

[19] S. T. Lin and R. E. Rowlands, "Thermoelastic stress analysis of orthotropic composites," *Experimental Mechanics,* vol. 35, no. 3, pp. 257-265, 1995.

[20] J. Rhee and R. E. Rowlands, "Thermoelastic-numerical hybrid analysis of holes and cracks in composites," *Experimental mechanics,* vol. 39, no. 4, pp. 349-355, 1999.

[21] S.-H. Ju and R. E. Rowlands, "Mixed-mode thermoelastic fracture analysis of orthtropic composites," *International journal of fracture,* vol. 120, no. 4, pp. 601-621, 2003.

[22] S.-H. Ju and R. E. Rowlands, "Thermoelastic determination of KI and KII in an orthotropic graphite–epoxy composite," *Journal of composite materials,* vol. 37, no. 22, pp. 2011-2025, 2003.

[23] B. E. Foust and R. E. Rowlands, "Thermoelastic determination of individual stresses in a diametrally loaded disk," *Strain,* vol. 47, no. 2, pp. 146-153, 2011.

[24] S.-J. K. Lin, Two- and three dimensional hybrid photomechanical-numerical stress analysis,

vol. 68, 2007.

[25] S. Lin, D. R. Matthys and R. E. Rowlands, "Separating stresses thermoelastically in a central circularly perforated plate using an Airy stress function," *Strain,* vol. 45, no. 6, pp. 516-526, 2009.

[26] S. J. Lin, D. R. Matthys and R. E. Rowlands, "Using Airy Function to Thermoelastically Separate Stresses in a Central Circularly Perforated Plate," in *Applied Mechanics and Materials*, 2007.

[27] N. S. Joglekar, Separating stresses using airy's stress function and TSA, effects of varying the amount and source locations of the input measured TSA data and the number of airy coefficients to use, University of Wisconsin--Madison, 2009.

[28] A. A. Khaja and R. E. Rowlands, "TSA Analysis of Vertically-and Incline-loaded Plates containing Neighboring Holes," in *Thermomechanics and Infra-Red Imaging, Volume 7*, Springer, 2011, pp. 117-122.

[29] A. A. Khaja and R. E. Rowlands, "Experimentally determined stresses associated with elliptical holes using polar coordinates," *Strain,* vol. 49, no. 2, pp. 116-124, 2013.

[30] W. Samad, Hybrid Full-Field Stress Analysis of Structures Containing Irregularly-Shaped Cutouts, PhD thesis, University of Wisconsin - Madison, 2013.

[31] W. A. Samad, A. A. Khaja, A. R. Kaliyanda and R. E. Rowlands, "Hybrid thermoelastic stress

analysis of a pinned joint," *Experimental Mechanics,* vol. 54, no. 4, pp. 515-525, 2014.

[32] W. A. Samad and R. E. Rowlands, "Hybrid thermoelastic analysis of an unsymmetrically-loaded structure containing an arbitrarily-shaped cutout," in *Residual Stress, Thermomechanics & Infrared Imaging, Hybrid Techniques and Inverse Problems, Volume 8*, Springer, 2014, pp. 51-57.

[33] A. Alshaya, X. Shual and R. Rowlands, "Thermoelastic stress analysis of a finite orthotropic composite containing an elliptical hole," *Experimental Mechanics,* vol. 56, no. 8, pp. 1373-1384, 2016.

[34] A. A. Alshaya, Experimental, Analytical and Numerical Analyses of Orthotropic Materials and Biomechanics Application. PhD thesis,, Madison: University of Wisconsin - Madison, 2019.

[35] A. Alshaya and R. Rowlands, "Experimental stress analysis of a notched finite composite tensile plate," *Composites Science and Technology,* vol. 144, pp. 89-99, 2017.

[36] Y. H. Ro, J. F. Hunt and R. E. Rowlands, "stress analysis of cellulosic-manure composites," *Wood and Fiber Science, 2017. 49 (2): 231-233.,* vol. 49, no. 2, pp. 231-233, 2017.

[37] A. Khaja and R. Rowlands, "Stresses associated with multiple holes whose individual stresses interact," *The Journal of Strain Analysis for Engineering Design,* vol. 52, no. 3, pp. 162-176, 2017.

[38] A. Alshaya and J. Considine, "Determination of Constitutive Parameters in Inverse Problem Using Thermoelastic Data," *Residual Stress, Thermomechanics & Infrared Imaging, Hybrid Techniques and Inverse Problems,* vol. 7, pp. 25-34, 2019.

[39] B. Kalaycioglu, A. Alshaya and R. Rowlands, "Experimental stress analysis of an arbitrary geometry containing irregularly shaped hole," *Strain,* p. e12306, 2019.

[40] M. A. Sutton, J. J. Orteu and H. Schreier, Image correlation for shape, motion and deformation measurements: basic concepts, theory and applications, Springer Science & Business Media, 2009.

[41] W. Peters and W. Ranson, Digital Imaging Techniques in Experimental Stress Analysis. Opt Eng, 1982.

[42] M. Sutton, W. Wolters, W. Peters, W. Ranson and S. McNeill, Determination of Displacements using an Improved Digital Correlation Method, Image Vis Comput, 1983.

[43] H. Bruck, S. McNeill, M. Sutton and W. Peters, "Digital Image Correlation using Newton-Raphson Method of Partial Differential Correction.," *Exp Mech,* vol. 29, pp. 261-7, 1989.

[44] J. Chen, X. Zhang, H. Zhan and X. Hu, "Deformation Measurement Across Crack using Two-Step Extended Digital Image Correlation Method," *Opt Lasers Eng ,* no. 48, pp. 1126-31, 2010.

[45] C. Davis and D. Freeman, "Statistics of Subpixel Registration Algorithms Based on

Spatiotemporal Gradients or Block Matching," *Opt Eng,* no. 37, pp. 37-9, 1998.

[46] G. Jin, X. Yao and N. Bao, "Applications of Speckle Metrology to Vibration and Deformation Measurements of Electronic Device," in *THERM 2000 Seventh Intersoc. Conf. Therm. Thermomechanical Phenom. Electron. Syst., vol. 2*, Las Vegas, 2000.

[47] B. Pan , A. Asundi, H. Xie and J. Gao, "Digital Image Correlation using Iterative Least Squares and Pointwise Least Squares for Displacement Field and Strain Field Measurements," *Opt Lasers Eng,* no. 47, pp. 865-74, 2009.

[48] B. Pan, "Reliability-Guided Digital Image Correlation for Image Deformation Measurement," *Appl Opt,* no. 48, pp. 1535-42, 2009.

[49] B. Pan and K. Li, "Fast Digital Image Correlation Method for Deformation Measurement.," *Opt Lasers Eng,* no. 49, pp. 841-7, 2011.

[50] B. Pan, K. Li and W. Tong, " Fast, Robust and Accurate Digital Image Correlation Calculation without Redundant Computations," *Exp Mech,* 2013.

[51] N. McCormick and J. Lord, Digital Image Correlation, Mater Today, 2010.

[52] Y. Du, F. Diaz, R. Burguete and E. Patterson, "Evaluation using Digital Image Correlation of Stress Intensity Factors in an Aerospace Panel," *Exp Mech,* no. 51, pp. 45-57, 2011.

[53] X. Zhou, H. Chen, J. Chen, S. Chen and Z. Feng, "High Temperature Full-Field Strain Measurement Based on Digital Image Correlation During Arc Welding," in *2016 IEEE*

Workshop Adv. Robot. Its Soc. Impacts ARSO, Shanhai, 2016.

[54] G. Agarwal, H. Gao, M. Amirthalingam and M. Hermans, " In Situ Strain Investigation During Laser Welding using Digital Image Correlation and Finite-Element-Based Numerical Simulation," *Sci Technol Weld Join,* vol. 23, pp. 134-9, 2018.

[55] J. Zhang, A. Sweedy, F. Gitzhofer and G. Baroud, "A Novel Method for Repeatedly Generating Speckle Patterns used in Digital Image Correlation," *Opt Lasers Eng ,* no. 100, p. 259–66, 2018.

[56] Y. Niu, S. Shao, S. Park and C. Kao, "A Novel Speckle-Free Digital Image Correlation Method for In Situ Warpage Characterization," *IEEE Trans Compon Packag Manuf Technol,* no. 7, pp. 276-84, 2017.

[57] B. Pan, H. Xie, Z. Wang, K. Qian and Z. Wang, "Study on Subset Size Selection in Digital Image Correlation for Speckle Patterns," *Opt Express,* vol. 16, pp. 7037-48, 2008.

[58] Z. Wang, H. Li, j. Tong and J. Ruan, "Statistical Analysis of the Effect of Intensity Pattern Noise on the Displacement Measurement Precision of Digital Image Correlation using Self-Correlated Images," *Exp Mech,* no. 47, pp. 701-7, 2007.

[59] A. A. Khaja, D. R. Matthys and R. E. Rowlands, "Determining all displacements, strains and stresses full-field from measured values of a single displacement component," *Experimental Mechanics,* vol. 54, no. 3, pp. 443-455, 2014.

[60] W. Samad and R. Rowlands, "Nondestructive full-field stress analysis of a finite structure containing an elliptical hole using digital image correlation," in *Proceedings of ISME 2012 Taipei conference on experimental mechanics*, 2012.

[61] S. Paneerselvam, Full-field stress analysis of perforated asymmetrical struc- tures from record values of a single displacement component, Madison: Master's thesis, University of Wisconsin - Madison, 2014.

[62] S. Paneerselvam, W. Samad, R. Venkatesh, K. Song, R. El-Hajjar and R. Rowlands, "Displacement-Based Experimental Stress Analysis of a Circularly-Perforated Asymmetrical Isotropic Structure," *Experimental Mechanics,* vol. 57, no. 1, pp. 129-142, 2017.

[63] N. Fatima and R. Rowlands, "Stress Analysis of a Circularly-Perforated Finite Orthotropic Composite Plate," *Journal of Mechanics Engineering and Automation ,* vol. 7, pp. 20-9-220, 2019.

[64] Y. Ro, J. F. Hunt and R. E. Rowlands, "Cellulosic-Biowaste Composites and Their Stress Determination Using Digital Image Correlation," *Journal of Engineering Materials and Technology,* vol. 141, no. 1, p. 011011, 2019.

[65] "Top dairy producing states in the u.s. based on number of milk cows from 2014 to 2016," Statista, March 2016. [Online].

[66] L. Wang, Y. Li, P. Chen, M. Min, Y. Chen, J. Zhu and R. R. Ruan, "Anaerobic digested dairy manure as a nutrient supplement for cultivation of oil-rich green microalgae Chlorella sp.,"

Bioresource technology, vol. 101, no. 8, pp. 2623-2628, 2010.

[67] A. Kozlosky, Confidence building with contemporary green engineering materials, Madison: Master's thesis, University of Wisconsin - Madison, 2008.

[68] B. E. Foust, Individual stress determination in inverse problems by combining experimental methods and Airy stress functions, Madison: Master's thesis, University of Wisconsin - Madison, 2000.

[69] A. A. Khaja, Experimentally Determined Full-Field Stress, Strain and Displacement Analyses of Perforated Finite Members, Madison: PhD thesis, University of Wisconsin - Madison, 2012.

[70] W. C. Young, R. G. Budynas and A. M. Sadegh, Roark's formulas for stress and strain, vol. 7, McGraw-Hill New York, 2002.

[71] A. P. Boresi, K. Chong and J. D. Lee, Elasticity in engineering mechanics, John Wiley & Sons, 2010.

[72] A. J. Durelli and W. F. Riley, Introduction to Photomechanics, Prentice Hall, 1966.

[73] M. Creager and P. C. Paris, "Elastic field equations for blunt cracks with reference to stress corrosion cracking," *International Journal of Fracture Mechanics,* vol. 3, no. 4, pp. 247-252, 1967.

[74] M. Creager, "The elastic stress field near the tip of a blunt crack," 1966.

[75] O. L. Bowie and D. M. Neal, "The effective crack length of an edge slot in a semi-infinite sheet under tension," *International Journal of Fracture Mechanics,* vol. 3, no. 2, pp. 111-119, 1967.

[76] R. E. Peterson, "Stress Concentration Factors John Wiley & Sons," *New York,* vol. 150, p. 34, 1974.

[77] W. N. Sharpe, Springer handbook of experimental solid mechanics, Springer Science & Business Media, 2008.

[78] R. B. Vieira, S. K. Philip, G. L. G. Gonzáles, J. L. F. Freire, B. Yang and R. E. Rowlands, "Determination of a U-Notch Stress Concentration Factor Using Thermoelasticity," *Journal of Mechanics Engineering and Automation,* vol. 6, no. 2, pp. 66-76, 2016.

[79] A. A. Alshaya, J. M. Considine and X. Tang, "A New Inverse Technique for in-plane Characterization using Stress Function and DIC-displacement Data," under preparation.

[80] N. S. Fatima, Photomechanical Analyses of Isotropic and Orthotropic Composite Structures Containing Various Geometric Discontinuities, Madison: PhD Thesis, University of Wisconsin-Madison, 2019.

[81] T. Baek and R. Rowlands, "Hybrid Stress Analysis of Perforated Composites using Strain Gages," *Experimental Mechanics,* vol. 47 (2), pp. 195 - 203, 2001.

[82] Department of Agriculture, Forest Service, Forest Products Laboratory, Wood Handbook,

Wood as an Engineering Material, General Technical Report FPL-GTR-190, Madison, 2010.

[83] W. A. Samad and R. E. Rowlands, "Full-field thermoelastic stress analysis of a finite structure containing an irregularly-shaped hole," *Experimental Mechanics,* vol. 54, no. 3, pp. 457-469, 2014.

[84] J. Medgenberg and T. Ummenhofer, "Detection of localized fatigue damage in steel by thermography," in *Thermosense XXIX*, 2007.

[85] Y. M. Huang, H. H. AbdelMohsen and R. E. Rowlands, "Determination of individual stresses thermoelastically," *Experimental Mechanics,* vol. 30, no. 1, pp. 88-94, 1990.

[86] J. M. Dulieu-Barton and P. Stanley, "Development and applications of thermoelastic stress analysis," *The Journal of Strain Analysis for Engineering Design,* vol. 33, no. 2, pp. 93-104, 1998.

[87] A. J. Durelli, V. J. Parks, H. C. Feng and F. Chiang, "Strains and stresses in matrices with inserts," in *Mechanics of composite materials*, Elsevier, 1970, pp. 265-336.